Millimeter/Submillimeter Fourier Transform Spectroscopy of Jovian Planet Atmospheres

Thesis by
Eric W. Weisstein

In Partial Fulfillment of the Requirements
for the Degree of
Doctor of Philosophy

California Institute of Technology
Pasadena, California

1996
(Submitted December 4, 1995)

Dedicated to my parents, who supported and nurtured me despite my baffling (but unshakable) preference for science over the arts, and to Susanne, who supported and nurtured me despite my baffling (but unshakable) preference for science over medicine.

Acknowledgments

First and foremost, thanks to my parents. Although you may not have shared in my fondness for math and science, you have supported me in everything I have done. Thanks for all the trips to science museums (when I'm sure you would have much rather been somewhere else), for allowing me the freedom to choose my own direction while at the same time providing just the right amount of guidance, and for instilling in me a love of learning. You spared no effort to provide me with the best education possible, and for that I am eternally grateful.

To Martin Burkhead of the astronomy department at Indiana University, who agreed to let a lowly high school student take his introductory astronomy course, thanks for your engaging teaching style, cheerfulness and, above all, *enthusiasm.* Just look where Astro 110 has taken me! Thanks also to my friends in Dickson Hall and elsewhere at Cornell who helped an introverted, insecure physics major make it through the rigors of a strenuous undergraduate curriculum. Special thanks go out to Jim Houck, who let me tag along with the "big kids" to Hartung-Boothroyd Observatory to take a peek at the heavens with a real CCD camera, and even kept me on for the summer despite my ignorance of infrared astronomy, and to Martha Haynes, who was always there to give support, make helpful suggestions, and keep the astronomy club running smoothly. To John Salzer, who has never forgiven me for switching from astronomy proper to planetary astronomy, thanks for a fun summer working with you in Arecibo. And finally, to my good friends Kim and Brian McLeod, star-mates, jugglers, folk-music fans, and astronomers extraordinaire, I cannot even begin to express what a privilege it has been to interact with you over the years. The memories I have of Fuertes Observatory on cold, Ithaca nights will always be some of my best.

At Caltech, there are also many thanks to go around. My advisor Dewey

Muhleman has supported and encouraged me over my years as a graduate student. He has also offered constructive counsel on many issues related to my academic and research activities, and although I've not always taken his advice, I value it most highly. When my research interests began diverging to shorter wavelengths than his own, he sat out his initial period of skepticism and let me blaze a new trail with an unproven submillimeter FTS. In the process, we have perhaps ended up collaborating less closely than I would have liked, but events seem to have worked out for the best. If anyone got a raw deal in the process, it was Dewey. Thanks for everything, Dewey: your support, good humor (which, although I may be mistaken, seems to have increased markably in the few years since I first met you), well-taught classes, old-fashioned values, and tidbits of wisdom which you let fall in my direction. I hope I was smart enough to pick some of them up.

Since the day I first met him in Tom Phillips' office, Gene Serabyn has been the motivating force behind my involvement with the FTS. Gene is one smart cookie, and although I would still rather use my own computer programs than his, I don't think I will ever be able to come close to his intuitive understanding of most of physics and virtually all of instrumentation. Gene is also the prototypical optimist (although he gets defensive when I accuse him of this to his face and asks me if I'd prefer the alternative), so once he has started doing something, he doesn't let go of it until it's done. Problems and setbacks are simply minor inconveniences to be brushed aside. If I learned no physics from you, Gene (but I sure hope I did), I hope that I learned the power of persistence and the need for thinking things through clearly before going off on a wild goose chase. And besides being a gifted scientist, Gene is also a nice guy who always had time to sit down with me and talk me through just about any difficulty. I feel very lucky to have been able to work so closely with him over the last four years. There are many other things to admire about Gene, such as his excellent

taste in Greek music during observing runs and skepticism about facts which are not amenable to simple explanations, but there isn't room to mention them all here.

All the members of the CSO family have also done much to make this work possible. Antony Schinckel has been available all hours of the night to solve any problem, be it with our instrument or with the CSO itself. (What!? Problems at the CSO!?) I still remember the look on his face when I first came out to Hawaii and assembled various pieces of the FTS using clip leads and duct tape. We've come a long way since then! Ant is also the glue binding the CSO together, and if he were to ever decide to move on, I have a feeling the CSO would fall to pieces in his absence. Raoul Taco Michilvich ("Taco" to his friends and close associates) has been another indispensable resource. Despite the hard time we give him about computer crashes and glitches, things seem to always work smoothly when he's around. We never could have gotten our instrument running without Taco's low-level communication routines and willingness to configure A/Ds, terminal servers, or whatever else came up. While Taco seems to enjoy a love-hate relationship with Hawaii in general and Hilo in particular, the fruits of his devotion to astronomy at the CSO are enjoyed by everyone who uses the telescope. Walt Schaal did a fantastic design job under stressful conditions taking the FTS from sheet metal to finished pieces, and Dave Woody showed lots of patience in trying to use a not-quite ready instrument to do holography and make dish adjustments. Thanks to Tom Phillips, director of the CSO, for giving us so many nights on his wonderful telescope and for his support of the FTS project. Thanks to Thérèse Encrenaz for proposing to observe faint Uranus and Neptune with the FTS, and for making it an enjoyable observing run. Thanks also to Todd Hunter and Dominic Benford for some interesting discussions and more than a few computer tips, and to all the rest of the people associated with the CSO. Finally, thanks to the Hale Pohaku cooks for bringing a unique point of view and more than

a little strangeness to dinner on Mauna Kea.

Thanks to Peter Goldreich for racketball games (which I didn't win nearly as often as I would have liked) and his unstoppable right hook-shot, Yuk Yung and Mark Allen for taking the time to answer some of my more naive questions about atmospheric chemistry, and Andy Ingersoll for his enthusiasm on the basketball court as well as in the classroom. To Kay Campbell, Irma Betters, and Mike Black, who, between the three of them, can answer almost any question, my heartfelt thanks. Mike has gotten me out of more computer jams than I can recall, always with a smile, and always with amazing rapidity. By the way, Mike, that's "Dr." to you!

A very special thank-you also goes to my classmate Mark Gurwell. Mark is a genuinely friendly person who was always willing to put down whatever he is working on in order to help me solve some problem. I made frequent use of his knowledge of numerical radiative transfer, and probably wasted more of his time over the years than was good for him. All the best to you in Boston, Mark, and thanks for everything. Although there's still a Mark sitting at your old desk, no one can take your place. Thanks also go out to Jim Lyons (for his enthusiasm on the basketball court and occasional appearance on the soccer field), Hari Nair (for always having a relevant Monty Python quote handy and, in earlier days, encouraging outdoor breaks for a quick round of hacky-sack), Lyatt Jaegle (for putting up with an office-mate who filled the office with bookshelves and then came close to monopolizing them), Mark Roulston (for listening patiently when I am looking for someone to bug with a dumb question, and also for his unusually fine Welsh sense of humor), and Ian Sammis (for answering computer questions and providing scanning services). I also express my appreciation to everyone who came to Geology soccer games, even when we were in last place. A broken leg and thumb later, we're in first! Former Dewey students Arie Grossman and Mark Hofstadter also need to be mentioned for the help they have

provided through their excellent theses. Arie merits special mention for allowing me to mangle his original radiative transfer code so badly that he probably would have trouble recognizing its pedigree.

Finally, I must express my gratitude to my wife Susanne. How she manages to put up with her often stubborn and frequently moody husband is one mystery I will never be able to fathom. Despite her preference for living somewhere (anywhere?) other than Los Angeles, she came to southern California in order to be together with me. Thanks for giving my life meaning, Susanne, and for giving me a reason to brave the commute home every night. I wish I could learn to enjoy my work as much as you enjoy yours.

Some aspects of Sections 3.11 and 3.12.2 have previously appeared in Serabyn and Weisstein (1995). The 1300 μm observations of the $J = 1 - 0$ PH_3 line in Saturn presented in Chapter 6 have previously been published in Weisstein and Serabyn (1994) (copyright © 1994 by Academic Press, Inc.; all rights of reproduction in any form reserved). The $J = 3 - 2$ PH_3 detection and its interpretation using radiative and photochemical modeling has been submitted for publication (Weisstein *et al.* 1996). The line survey presented in Chapter 7 is currently in press (Weisstein and Serabyn 1996), as is some of the instrumental material in Chapter 3 and the determination of calibrated continuum temperature for Uranus and Neptune using FTS observations (Serabyn and Weisstein 1996). Finally, a separate analysis of the Uranus and Neptune spectra presented in Chapter 8 is also in press (Encrenaz *et al.* 1996).

Abstract

A new Fourier transform spectrometer, built for use at the Caltech Submillimeter Observatory, has been used to observe all four of the jovian planets (Jupiter, Saturn, Uranus, and Neptune) in the millimeter-submillimeter wavelength range (0.3-3.0 mm). These observations have resulted in the detection of the PH_3 $1-0$ rotational line (266.9 GHz) in Saturn, and the PH_3 $3-2$ (800.5 GHz) line in both Jupiter and Saturn. Because PH_3 is a disequilibrium species, it is an important tracer of vertical mixing and upper atmospheric photochemistry, and can therefore be used to derive dynamical and chemical properties of the jovian atmospheres. A jovian planet radiative transfer code has been used to model the observed PH_3 lineshapes. Using the FTS, a spectral line survey covering the entire range of submillimeter frequencies observable from the ground has also been performed on Jupiter at Saturn at a resolution of 200 MHz. This survey has yielded the tentative detection of HCl (and possibly HCN) in Saturn and, again with the aid of radiative transfer modeling, provided a great number of improved upper limits on the concentrations of many other species. Finally, Uranus and Neptune have been observed in the 1300 μm atmospheric window which contains the CO $2-1$ transition. This line was not detected in either planet, placing upper limits on the tropospheric CO mole fraction of 0.5 ppm in Uranus and 1.4 ppm in Neptune.

Table of Contents

List of Figures

List of Tables

Chapter 1

Introduction

> *"A science is said to be useful if its development tends to accentuate the existing inequalities in the distribution of wealth, or more directly promotes the destruction of human life."*
>
> —G. H. Hardy *(A Mathematician's Apology)*

> *"That science is in some respects inhuman may be the secret of its success in alleviating human misery and mitigating human stupidity."*
>
> —E. T. Bell *(Mathematics: Queen and Servant of Science)*

> *"The die is cast, and I write this book. Whether it will be read by my contemporaries or by posterity is not important. If God himself has waited six thousand years for someone to contemplate his works, my book can wait for a hundred."*
>
> —Johannes Kepler *(Harmonice Mundi)*

Spectroscopy is an extremely powerful tool in the study of planetary atmospheres. Using nothing but the radiation emitted from an atmosphere, a variety of constituent molecular species can be detected. Under favorable circumstances—and perhaps with the aid of some simplifying assumptions—the abundances of detected species can also be inferred. This compositional information is useful for intercomparison of the atmospheres of different planets, and also as a means of monitoring atmospheric changes as a function of season or other longer period of time. Furthermore, if enough spectroscopic constraints are available (either from the measurement of multiple lines or from the high resolution determination of spectral lineshapes), then vertical abundance and temperature profiles can be derived as well. Vertical abundance profiles are important because they probe the dynamics and chemistry of an atmosphere, properties which are difficult to study using other means. In the absence of in situ measurements such as the Pioneer Venus and Galileo entry probes or the Viking landers, ground- and spacecraft-based spectroscopy are the *only* technique which can provide direct compositional information on planetary atmospheres.

Over the last few decades, spectroscopic techniques have advanced to the point that virtually the entire electromagnetic spectrum—from the ultraviolet to the

microwave—is now accessible to atmospheric spectroscopy. At the shortest wavelengths (< 0.3 μm), ultraviolet spectroscopy is sensitive to energetic electronic transitions. However, because ozone in the Earth's atmosphere absorbs these wavelengths, ultraviolet spectra can be obtained only from spacecraft and Earth-orbiting satellites. Ultraviolet wavelengths probe the uppermost tenuous regions of planetary atmospheres, generally at the mbar to nbar pressure levels. At the slightly longer wavelengths of 0.3 to 0.8 μm, visible spectroscopy is sensitive to less energetic electronic transitions. Visible spectra can be obtained using ground-based telescopes, but are capable of yielding relatively little quantitative compositional information. The only three molecules detected in the atmospheres of Jupiter and Saturn in the visible portion of the spectrum, for example, are H_2, CH_4, and NH_3. Although it is possible to derive H_2 abundances from visible spectra, these value are actually determinations of the depths of reflecting clouds. Visible observations of NH_3 are also difficult to interpret due to both spatial and temporal variability, as well as the poorly known wavelength dependence of particulate scatters and continuum absorbers. Visible CH_4 observations are similarly complicated by scattering from cloud particles (Prinn *et al.* 1984, pp. 108-112).

At wavelengths of 1-100 μm, infrared spectroscopy is sensitive primarily to molecular vibrational transitions. Since the time of Kuiper's low-resolution prism observations of planetary atmospheres in the mid-1940's, infrared detectors and techniques have advanced by orders of magnitude in sensitivity. Today, infrared measurements provide the majority of the known compositional information for both major and minor constituents of planetary atmospheres. The vibrational transitions of many molecules (e.g., CO, C_2H_2, C_2H_4, C_2H_6, CH_3D, CH_4, H_2O, NH_3, PH_3, AsH_3, and GeH_4) have been detected at infrared wavelengths in both Jupiter (e.g., Ridgway *et al.* 1976, Larson *et al.* 1977, Tokunaga *et al.* 1979, Drossart *et al.* 1982, Knacke

et al. 1982, Kunde *et al.* 1982, Bjoraker *et al.* 1986, Noll *et al.* 1988) and Saturn (e.g., Fink and Larson 1978, Larson *et al.* 1980, Courtin *et al.* 1984, Noll *et al.* 1986, Noll and Larson 1990). In addition, the far-infrared transitions of H_2 have been used to derive the He abundances in the jovian planets. Slightly longer wavelength far-infrared observations can detect energetic rotational transitions of simple molecules. However, measurements at these wavelengths have thus far attained only low signal-to-noise ratios (Haas *et al.* 1985, 1986), sharply limiting their utility.

Microwave wavelength radiation, a spectral region often further divided into the submillimeter (0.3-1.0 mm), millimeter, and centimeter wavebands, has been used at longer wavelengths to measure both rotational and inversion transitions of atmospheric molecules. Centimeter wavelength radiation probes the deep atmospheres of jovian planets and can be used to infer compositional information based on the opacity observed at the several to $\sim$ 90 bar level (e.g., de Pater and Dickel 1982, Hofstadter and Muhleman 1988, de Pater and Richmond 1989, Grossman *et al.* 1989, Hofstadter *et al.* 1990, de Pater *et al.* 1991). The advantage of centimeter wavelengths is their deep atmospheric penetration, which allows them to probe the relatively high temperature regions of jovian atmospheres where clouds form. A disadvantage is that molecules are not detected directly, but instead have their concentrations inferred based on the observed opacity in highly pressure-broadened line wings.

The first millimeter line to be observed in a planetary atmosphere was CO $1-0$ (at 115 GHz = 2.6 mm), which was detected in both Venus and Mars by Kakar *et al.* (1976). In subsequent years, single-dish and synthesis imaging heterodyne spectroscopy at millimeter wavelengths (and, more recently, single-dish heterodyne spectroscopy at *submillimeter* wavelengths) has been used extensively to study the atmospheres of Venus (Clancy and Muhleman 1991, Shah *et al.* 1991, Shah 1992, Lellouch *et al.* 1994, Gurwell *et al.* 1995), Mars (Clancy *et al.* 1983, Lellouch *et al.*

1989, Clancy *et al.* 1990, Clancy and Muhleman 1991, Lellouch *et al.* 1991), Titan (Muhleman *et al.* 1984, Marten *et al.* 1988, Gurwell 1996, Gurwell and Muhleman 1996), and Neptune (Rosenqvist *et al.* 1992, Marten *et al.* 1993) using the first few rotational transitions of CO. However, prior to 1994, the only other atmospheric molecules detected in the microwave region were HCN on Titan (Tanguy *et al.* 1990) and Neptune (Rosenqvist *et al.* 1992, Marten *et al.* 1993, Lellouch *et al.* 1994), HC_3N (cyanoacetylene; Bézard *et al.* 1992) and CH_3CN (acetonitrile; Bézard *et al.* 1993) on Titan, and SO_2 (and potentially SO) on Io (Lellouch *et al.* 1990, 1994). Following the impact of Comet Shoemaker-Levy 9 into Jupiter, stratospheric lines of the molecules CO, CS, OCS (Lellouch *et al.* 1994), and HCN (Owen *et al.* 1994, Marten *et al.* 1995) were also detected near some of the impact sites.

While planetary atmospheres have been extensively studied in the centimeter and millimeter wavebands, the submillimeter spectral region has, until recently, remained largely unexplored. Unlike infrared spectra, spectra taken at millimeter and submillimeter wavelengths contain relatively few spectral lines, which are consequently well separated. Because there is little confusion between the pure rotational lines at millimeter-submillimeter wavelengths, mixing ratios can be retrieved with relative ease. Because rotational lines in general become stronger ($\propto J^3$ for linear molecules) with increasing rotational quantum number J, the highest (and most difficult to observe) submillimeter frequencies usually provide spectra which are the most sensitive to species with small abundances. However, the technical difficulty in constructing radio telescope sized antennas with the precision required for submillimeter observations, combined with the low terrestrial transmission at submillimeter wavelengths, has impeded progress. The recent construction of large and accurately figured telescopes at high, dry sites (such as the 10.4-m Caltech Submillimeter Observatory and the 15-m James Clerk Maxwell Telescope, both located on the summit

of Mauna Kea) has recently opened up the submillimeter spectral range to scrutiny.

In the dense atmospheres of the jovian planets, the full-width at half maximum of collisionally broadened lines can reach several to several tens of GHz at submillimeter wavelengths. In order to detect these highly pressure-broadened lines, a spectrometer with wide frequency coverage is necessary. Heterodyne receivers and bolometers are the most commonly used detectors for millimeter and submillimeter observations (for a recent review, see Carlstrom and Zmuidzinas 1996). Heterodyne receivers provide very high spectral resolution, but only small bandpasses (typically $\leq$ 1 GHz), making them ill-suited to planetary continuum and pressure-broadened line observations. On the other hand, the filters typically used in conjunction with bolometer continuum observations (e.g., Hildebrand *et al.* 1985, Griffin *et al.* 1986, Orton *et al.* 1986, Griffin and Orton 1993) have bandpasses which are much broader than planetary spectral lines, sharply limiting their utility in planetary spectroscopy. A moderate resolution spectrometer which combines a large bandpass with a resolution intermediate to the two cases above is therefore required. A Fourier transform spectrometer provides the necessary combination of a broad passband and moderate resolution required to detect tropospheric absorption features.

In order to study the millimeter and submillimeter spectra of the giant planets at moderate resolution, E. Serabyn and E. Weisstein have built a rapid-scan Fourier transform spectrometer [FTS] for use at the Caltech Submillimeter Observatory. This spectrometer has been used to observe all four of the jovian planets (Jupiter, Saturn, Uranus, and Neptune), in which the expected line widths are well-matched to the maximum available instrumental resolution of 200 MHz. These observations have resulted in the detection of the PH_3 $1-0$ (266.9 GHz) line in Saturn (Weisstein and Serabyn 1994), and the PH_3 $3-2$ (800.5 GHz) line in both Jupiter (Weisstein *et al.* 1996) and Saturn. Because PH_3 is a disequilibrium species, it is an important tracer

of vertical mixing and upper atmosphere photochemistry, and can therefore be used to derive dynamical and chemical properties of the jovian atmospheres. A spectral line survey covering the entire range of submillimeter frequencies observable from the ground has also been performed on Jupiter and Saturn at the full resolution of the FTS. This survey has yielded the tentative detection of HCl (and perhaps HCN) in Saturn, and provided a great number of improved upper limits on the concentrations of many other species. Finally, Uranus and Neptune have been observed in the 1300 μm atmospheric window which contains the CO $2-1$ and PH_3 $1-0$ transitions. Neither molecule was detected in Uranus or Neptune, although the upper limit derived from these observations is consistent with the reported detections of tropospheric CO in Neptune by Guilloteau *et al.* (1993) using three widely separated frequency tunings of the IRAM Plateau de Bure interferometer, and Naylor *et al.* (1994) using a Martin-Puplett FTS located at the James Clerk Maxwell Telescope (Naylor, Clark, and Davis 1994).

Chapter 2

Millimeter/Submillimeter Spectroscopy

"Believe nothing on hearsay. Do not believe in traditions because they are old, or in anything on the mere authority of myself or any other teacher."
—Buddha's last injunction

"The effort to understand the universe is one of the very few things that lifts human life a little above the level of farce, and gives it some of the grace of tragedy."
—Steven Weinberg *(The First Three Minutes)*

2.1. Rotational Transition Formalism

The spectral line features which occur in the millimeter-submillimeter portion of the spectrum result from quantum mechanical molecular rotational transitions. Although rotational transitions can couple with other types of molecular transitions, the Born-Oppenheimer approximation allows a vibrational, rotational, and nuclear spin wavefunction to be separated from the electronic wavefunction. Furthermore, because vibrational energy levels are generally more widely spaced than rotational levels for simple molecules, it is often possible to further separate the vibrational wavefunction from rotational and nuclear spin wavefunctions, and therefore solve the rotational energy eigenvalue problem for an arbitrary given vibrational state (Rosenkranz 1994).

Quantum mechanics allows rotating molecules to possess only discrete quanta of angular momentum. For a rotating rigid diatomic molecule in quantum rotational state $J = 0, 1, 2, \ldots$, the total rotational angular momentum is given by

$$L = \sqrt{J(J+1)}\,\frac{h}{2\pi}, \tag{2.1}$$

where h is Planck's constant. The rotational energy is thus

$$E = \frac{L^2}{2I} = \frac{J(J+1)h^2}{8\pi^2 I}, \tag{2.2}$$

where I is the molecule's moment of inertia. The quantum mechanical selection rule for a diatomic molecule with a nonzero dipole moment is $\Delta J = \pm 1$, so for the $J \rightarrow J-1$ transition,

$$\Delta E = \frac{h^2}{8\pi^2 I}[J(J+1) - (J-1)J] = \frac{h^2}{4\pi^2 I}J. \tag{2.3}$$

(Rotational transitions are quantum mechanically forbidden for molecules which lack both electric and magnetic dipole moments.) The transition frequency is therefore

$$\nu = \frac{\Delta E}{h} = 2BJ, \tag{2.4}$$

where B is the rotation constant defined by

$$B \equiv \frac{h}{8\pi^2 I} \tag{2.5}$$

(Townes and Schawlow 1975). Similar expressions hold true for linear polyatomic molecules, but the situation is slightly more complex for symmetric rotors (which have transition energies dependent on an additional quantum number K as well as J), and significantly more complicated for asymmetric rotors and for molecules which possess nonzero orbital angular momenta (such as the SO molecule, which exists in a $^3\Sigma$ ground electronic state; Gordy and Cook 1984).

For a given rotational transition of a given molecule, the so-called line strength I_{ba} is conventionally defined as the integral of absorption cross-section over the spectral line shape. A quantum mechanical derivation leads to the expression

$$I_{ba}(T_0) = \frac{8\pi^3}{3hc}\frac{\nu_{ba}\, S_{ba}\, \mu^2 (e^{-E_L/kT_0} - e^{-E_U/kT_0})}{Q_{rs}(T_0)}, \tag{2.6}$$

where, following Pickett *et al.* (1992), I_{ba} is taken to have units of nm^2 MHz. In (2.6), Q_{rs} is the rotation-spin partition function

$$Q_{rs}(T) = \sum_{n=0}^{\infty}(2n+1)e^{-hBn(n+1)/kT} = \frac{kT}{hB} + \frac{1}{3} + \frac{1}{15}\frac{hB}{kT} + \ldots \tag{2.7}$$

(for linear molecules), c the speed of light, ν_{ba} the transition frequency, S_{ba} the intrinsic line strength with appropriate degeneracy ($S_{ba} = J_U$ for linear molecules), E_L and E_U the lower and upper state energies relative to ground state, k Boltzmann's constant, T the ambient temperature, and $T_0 = 300$ K the reference temperature. Pickett *et al.* (1992) catalog the logarithm of $I_{ba}(T_0)$ and the upper state energy E'_L in units of cm^{-1} for a wide variety of common (and not so common) molecules and their isotopomers. At a given temperature, the line strength in units of $\mathrm{cm}^{-1}/(\mathrm{molecule\ cm}^{-2})$ can then be well approximated by

$$I_{ba}(T) = \frac{I_{ba}(T_0)}{3 \times 10^{18}} \left(\frac{T_0}{T}\right)^{1+\eta} \exp\left[-\left(\frac{1}{T} - \frac{1}{T_0}\right)\frac{hc}{k}E'_L\right], \tag{2.8}$$

where the factor

$$\eta = \begin{cases} 1 & \text{for linear molecules} \\ \frac{3}{2} & \text{for nonlinear molecules,} \end{cases} \tag{2.9}$$

gives the temperature dependence of the partition function (Pickett *et al.* 1992).

The absorption coefficient k_ν (sometimes denoted α_ν) which has units of cm^{-1} is then given at a pressure p and temperature T in terms of (2.8) by

$$k(\nu, p, T) = \left(\frac{\nu}{\nu_{ba}}\right) I_{ba}(T)\rho(p, T)\phi(\nu, p, T) \tag{2.10}$$

(Van Vleck and Weisskopf 1945, Waters 1976), where ρ is the number density in cm^{-3} and $\phi(\nu, p, T)$ is the lineshape function. Some care must be taken when comparing the above expression with those of other authors, as the ν/ν_{ba} term is frequently absorbed into the lineshape function. However, for lines without extensive wings which have full-widths no greater than $\sim$ 10 GHz at 300 GHz (or $\sim$ 30 GHz at 800 GHz), the ν/ν_{ba} term can be approximated by unity to a good approximation without affecting line wing absorption. (One full width away from line center, the error incurred by dropping this term is only $\sim 4\%$.) For a Lorentzian lineshape, the approximation

$$k(\nu, p, T) = I_{ba}(T)\rho(p, T)\phi(\nu, p, T) \tag{2.11}$$

is therefore frequently used.

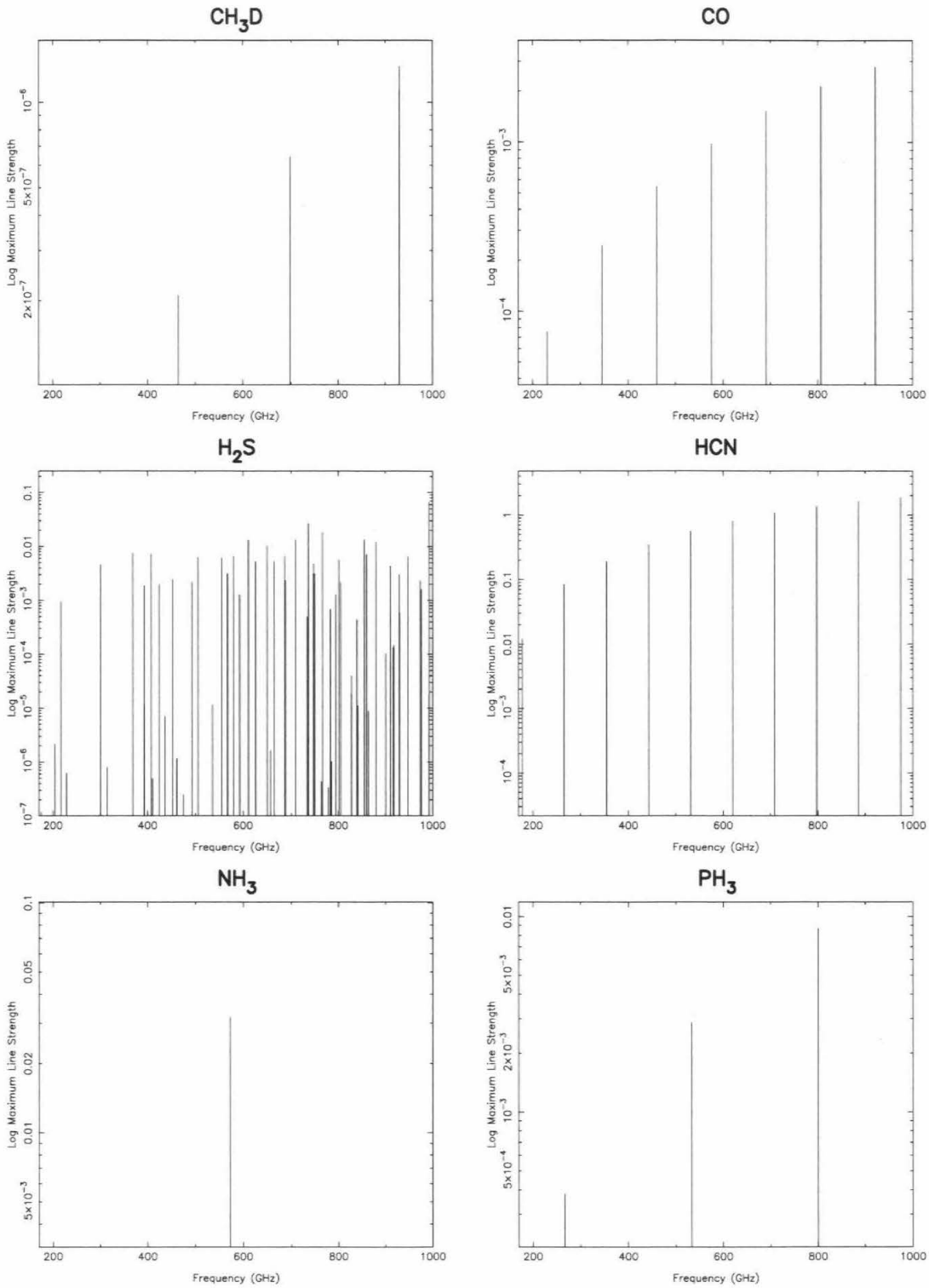

Figure 2.1. Millimeter/submillimeter rotational transitions for a number of molecules of interest. The frequencies and line strengths displayed in these plots were taken from the microwave line catalog of Pickett *et al.* (1992).

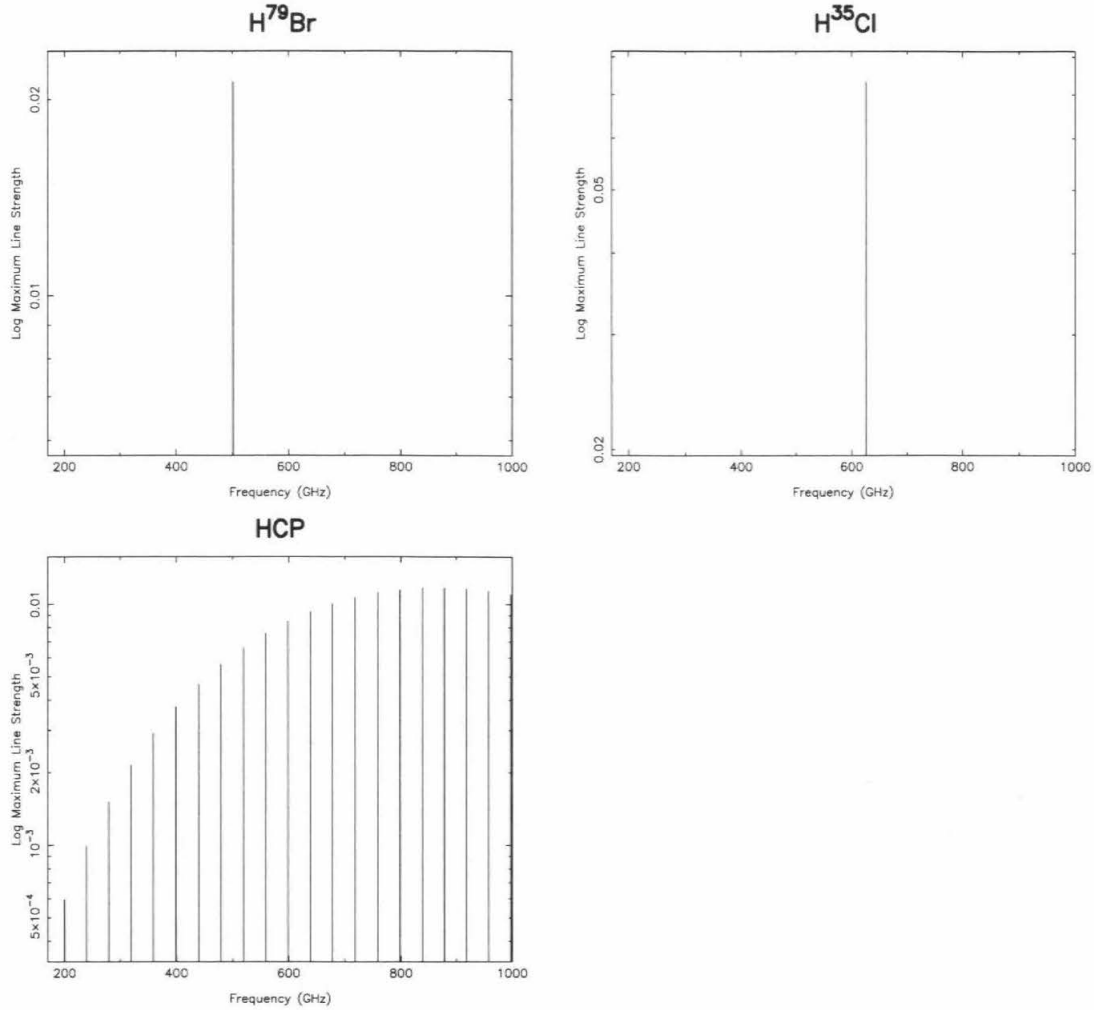

Figure 2.1. Millimeter/submillimeter rotational transitions, con't. The isotopomers of Cl and Br shown here are the ones containing the most abundant halogen isotope. The frequencies of $H^{81}Br$ and $H^{37}Cl$ are very close to the ones shown here in any case.

2.2. Submillimeter Molecular Transitions

The most abundant constituents of jovian atmospheres, H_2 and He, do not have spectral lines in the submillimeter portion of the spectrum. However, the abundant atmospheric molecule NH_3 has its first rotational transition at 575 GHz (0.52 mm), and the relatively abundant NH_3-analog molecule PH_3 (phosphine) has its first three rotational transitions in the millimeter-submillimeter portion of the spectrum (at 267, 534, and 800 GHz). In addition to NH_3 and PH_3, other molecules expected to play an important chemical role in the atmospheres of the jovian planets include

H_2O, H_2S, HCN, HCP, CH_4, CH_3D, and CO. Additional possible constituents include the hydrogen halides HBr and HCl, the alkali hydrides LiH and NaH, and the NH_3 and CH_4-analogs AsH_3 and GeH_4. Fig. 2.1 plots the transition frequencies and line strengths for most of these molecules. Unfortunately, of the molecules just listed, the submillimeter transitions of NH_3, H_2O, GeH_4, and CH_4 cannot be observed from the ground because NH_3 and H_2O are obscured by the Earth's atmosphere and CH_4 and GeH_4 lack dipole moments. Nonetheless, as can be seen from Fig. 2.1, many common or potential jovian atmospheric molecules *do* exhibit strong rotational transitions in accessible portions of the millimeter-submillimeter spectral region, making them attractive targets for spectroscopic investigations.

2.3. Terrestrial Atmospheric Spectrum

The millimeter-submillimeter spectrum of the Earth's atmosphere is an important factor in spectroscopic studies of the planets because the opacity of terrestrial atmospheric rotational transitions obscures significant portions of the sub-THz sky to ground-based observations. The primary source of millimeter-submillimeter opacity in the Earth's atmosphere is water. As a result, observations at submillimeter wavelengths are possible only in a number of atmospheric windows between 150 and 1000 GHz (= 2.0 to 0.3 mm) (Waters 1976, Liebe 1980, 1981, 1985). Fig. 2.2 shows a model of the zenith atmospheric transmission at the 13,200 foot altitude of the Caltech Submillimeter Observatory [CSO] for 1 mm precipitable H_2O, a typical quantity under good observing conditions, generated using the program `AT` (E. Grossman 1989). Under less favorable conditions with higher atmospheric water vapor content, transmission decreases and the high frequency windows effectively close. The deep absorptions are caused by highly pressure-broadened transitions of H_2O and O_2 (the latter of which, although homonuclear, possesses a magnetic dipole moment and therefore has allowed rotational transitions). The many small absorption features are

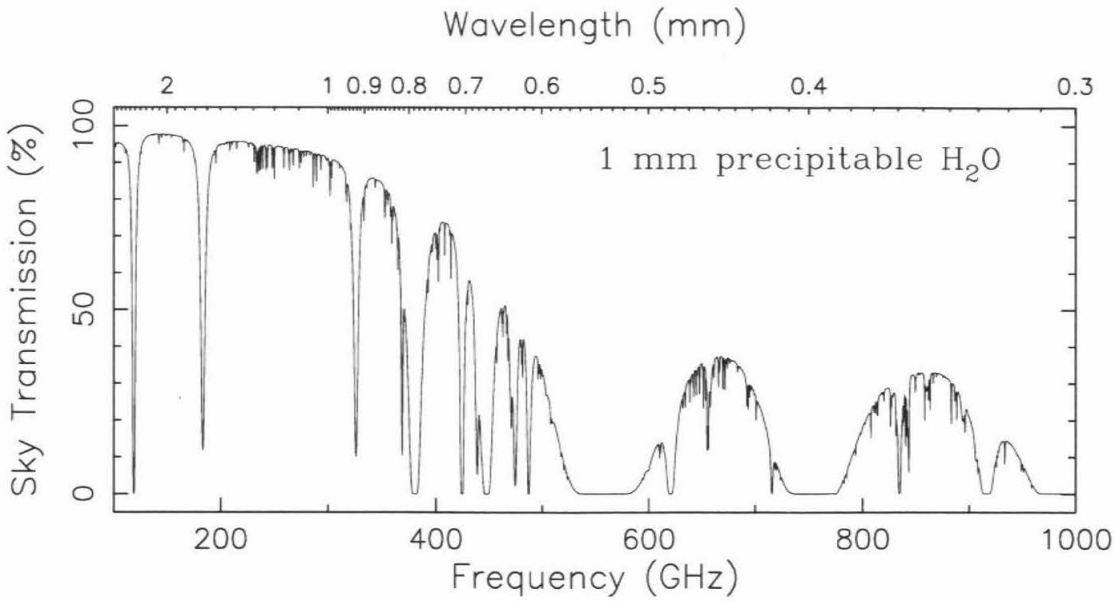

Figure 2.2. Zenith atmospheric transmission at the CSO for 1 mm precipitable H_2O. This plot was generated using the program `AT` (E. Grossman 1989).

primarily due to O_3, although a few $O^{18}O$ lines are also present.

The amount of atmospheric water vapor determines which transmission windows can be used profitably for observations. It is therefore very useful to monitor changing weather conditions in order to make appropriate decisions on filter selection and integration times. The usual technique for monitoring atmospheric transmission is measurement of the change in sky brightness as a function of airmass. A tipping radiometer mounted adjacent to the CSO provides periodic readings of the zenith atmospheric transmission at 225 GHz. A model atmosphere such as the one shown in Fig. 2.2 can then be used to scale this opacity to the submillimeter wavelength of interest. By manually performing skydips using the CSO high-frequency heterodyne receivers, the `AT` model has been found to give results roughly consistent with measurements. However, the measurement of skydips is a rather time-consuming process, so they are generally performed only at the beginning of a night or when significant changes in atmospheric quality are suspected.

Although the details will not be discussed here, the FTS used to obtain the

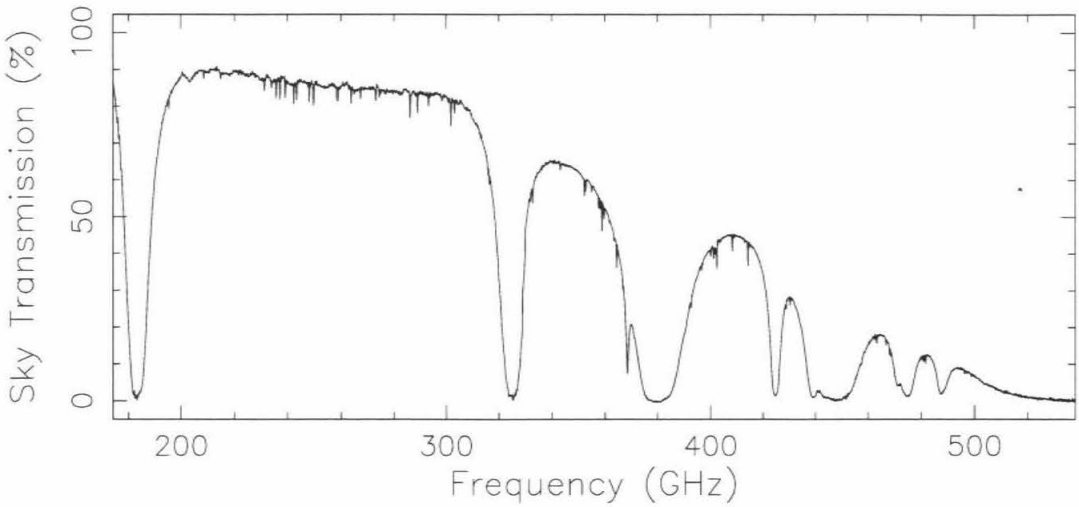

Figure 2.3. Terrestrial atmospheric transmission between 180 and 540 GHz as measured with the FTS. This plot combines data from the 1300, 800, and 600 μm filters. The 1300 μm data was actually obtained on a different night (with a different zenith transmission), and so has been scaled in order to make it join smoothly with the higher frequency data. The minimum time required to obtain a full resolution spectrum in a single window is roughly 10 minutes (the time required for a single pair of hot, cold, and sky scans).

planetary spectra presented in this thesis can also be used to *measure* the atmospheric transmission with great ease and accuracy (Serabyn *et al.* 1993). The technique involves measurement of sky spectra, combined with those of hot (ambient temperature) and cold (liquid nitrogen temperature) loads. By assuming that the hot load and sky are at similar temperatures, the atmospheric optical depth, and hence transmission, can be determined. An example of an atmospheric transmission plot obtained with the FTS using this procedure is shown in Fig. 2.3.

2.4. Jovian Planet Atmospheric Spectra

At millimeter-submillimeter wavelengths, the observed radiation from the jovian planets is emitted thermally from various pressure levels according to the law of radiative transfer. Without the complicating effects of reflected or scattered sunlight or of synchotron radiation (which can be important for long wavelength microwave observations), millimeter-submillimeter jovian spectra are therefore relatively simple.

Spectral features arising from molecular rotational transitions are seen either in emission (if they arise from molecules in the stratosphere) or absorption (if they arise from molecules in the troposphere). While stratospheric lines are narrow ($\lesssim$ 100 MHz), tropospheric lines are quite wide ($\gtrsim$ 1 GHz) due to pressure broadening. In cases where a molecule is found in both the stratosphere and the troposphere, an emission line core may be observed superimposed on top of a broad absorption feature. Because the resolution of our FTS is limited to 200 MHz, we consider mainly tropospheric absorption features.

Although H_2 and He do not have spectral lines in the submillimeter portion of the spectrum, the far wings of their collisionally induced far-infrared transitions do contribute to the millimeter-submillimeter opacity (Goodman 1969, Berge and Gulkis 1976, Birnbaum and Cohen 1976, Cohen *et al.* 1982, Bachet *et al.* 1983, Dore *et al.* 1983, Borysow *et al.* 1988). As already mentioned, the abundant molecule NH_3 has its first ($J = 1 - 0$) rotational transition at 575 GHz. This transition is expected to produce an extremely wide pressure-broadened absorption line in Jupiter and Saturn (de Pater and Massie 1985), but is not observable from the ground due to terrestrial H_2O opacity. The first one or two NH_3 rotational overtones, which fall at wavelengths shorter than the shortest wavelength 350 μm atmospheric window, are also significant opacity sources for determining the high frequency continuum temperatures of the jovian planets. In addition to rotational transitions, NH_3 possesses a strong band of inversion transitions centered at 18-43 GHz (Poynter and Kakar 1975) whose very broad line wings also contribute to the millimeter-submillimeter opacity of jovian atmospheres.

Because of its larger mass, the NH_3-analog molecule PH_3 has its first three rotational transitions in the millimeter-submillimeter portion of the spectrum. Because of PH_3's relatively high abundance and lack of condensation at the tropospheric

temperatures of Jupiter and Saturn, the lines of PH_3 are comparable in strength and width to those of NH_3 in these planets. In Uranus and Neptune, however, both these molecules are expected to condense in the upper tropospheres, so H_2-H_2 and H_2-He collisionally induced dipoles are the most important sources of continuum opacity. On the other hand, the CH_4 molecule is more abundant in the tropospheres of Uranus and Neptune than in Jupiter and Saturn, so collision-induced dipoles of H_2-CH_4 also contribute to the continuum at millimeter wavelengths (Orton *et al.* 1983, Borysow and Frommhold 1986, 1987). As already discussed, various other minor species including CO and HCN have millimeter-submillimeter rotational transitions as well. For all lines, the high pressures found in the thick atmospheres of the jovian planets result in substantial collisional broadening. Finally, although H_2O and H_2S have many millimeter-submillimeter transitions, they are thought to condense out at the relatively low temperature levels probed by millimeter-submillimeter observations, and therefore are not expected to make a significant contribution to opacity.

Model spectra for the jovian planets have previously been generated using radiative transfer models by Encrenaz and Combes (1977), Lellouch *et al.* (1984), Bézard *et al.* (1986), and Encrenaz *et al.* (1995).

Chapter 3

Fourier Transform Spectrometers

"It is more important to have beauty in one's Equations than to have them fit experiment."

—P. A. M. Dirac

3.1. Historical Sketch

In its simplest form, a Fourier transform spectrometer consists of two mirrors located at a right angle to each other and oriented perpendicularly, with a beamsplitter placed at the vertex of the right angle and oriented at a 45° angle relative to the two mirrors. Radiation incident on the beamsplitter from one of the two "ports" is then divided into two parts, each of which propagates down one of the two arms and is reflected off one of the mirrors. The two beams are then recombined and transmitted out the other port. (A schematic drawing illustrating this optical arrangement is shown in the next section.) When the position of one mirror is continuously varied along the axis of the corresponding arm, an interference pattern is swept out as the two phase-shifted beams interfere with each other.

The invention of the Fourier transform spectrometer coincides with A. Michelson's 1880 invention of the Michelson interferometer. In this device, the arms are kept the same length, but interference occurs if the phase velocity in the two arms differs, because the resulting phase advancement experienced by the beams traveling down the two arms is then also different. Using increasingly refined versions of Michelson's original device, Michelson and Morley searched for evidence of the Earth's motion through ether, the medium believed at the time to permeate space and allow the propagation of light through interplanetary space. If a relative motion between the ether and Earth had been present, the speed of light in the two perpendicular arms

would have been different, and the resulting optical paths would therefore also have been different. As a result, an observable change in the brightness (or "visibility") of the recombined interfering beams would have occurred. The absence of a change in the observed visibility for any orientation or time or year marked the death knell for the ether theory and paved the way for the (initially skeptical) acceptance of Albert Einstein's theory of Special Relativity, along with its sometimes counterintuitive implications.

Michelson was fully aware of the spectroscopic potential of his interferometer (Michelson 1891, 1892), but the lack of sensitive detectors (and nonexistence of Fourier transform algorithms capable of being carried out by human calculators) proved insurmountable barriers for its practical implementation. In fact, Michelson's only detector consisted of his own two eyes, and it was not until two decades after the interferometer's invention that Rubens and Wood (1911) published the first true interferogram, recorded with a microradiometer. Because of the continued difficulty in computing Fourier transforms, these early investigators were unable to invert their interferograms directly, but instead guessed a spectrum, computed the inverse Fourier transform, and then compared it to their measured interferogram. The guessed spectrum was then modified to bring it into better agreement with the data, and the process was continued until sufficient agreement was obtained (or the patience of the spectrum guesser wore thin!).

Practical Fourier transform spectroscopy began to come into its own only in the early 1950's when experimental groups at Johns Hopkins University, the Air Force Cambridge Research Laboratories, and elsewhere built and tested high resolution spectrometers. The first astronomical application of Fourier transform spectroscopy occurred in the late 1950's and early 1960's when P. and J. Connes (and others) obtained high resolution and high-quality spectra of the planets. These developments

were greatly aided by the publication of Cooley and Tukey's seminal paper on the "fast Fourier transform" algorithm. The Cooley and Tukey (1965) algorithm allowed Fourier transforms to be computed efficiently using a recursive algorithm which could be implemented easily on primitive electronic computers, reducing the computation time by *several orders of magnitude* and making the timely transformation of long interferograms feasible. (As a historical sidebar emphasizing the often surprising applicability of pure mathematics to real-world problems, it should be noted that the critical factorization step used by Cooley and Tukey in their algorithm had already been recognized and described by Gauss as early as 1805! (Strang 1993).) With numerous computational and instrumental advances of their own devising, Connes *et al.* (1969) published their epic catalog of the near-infrared spectra of Venus, Mars, Jupiter, and Saturn. During this period, commercial Fourier transform spectrometers also began to become widely available.

Today, aided by fast computers which perform Fourier transforms in a flash, visible, infrared, and microwave Fourier transform spectrometers are common laboratory instruments used for spectroscopy in many diverse disciplines.

3.2. CSO Fourier Transform Spectrometer

Since the pioneering work of Connes *et al.* (1969), many infrared spectra of the planets have been obtained by various researchers using Fourier transform spectrometers. However, the astronomical use of FTSes in the millimeter and submillimeter wavebands has been restricted due to the lack of large, high surface accuracy telescopes sited at dry locations. The recent construction of the James Clerk Maxwell Telescope [JCMT] and the Caltech Submillimeter Observatory [CSO] (Woody *et al.* 1994), both located at an altitude of 13,200 feet above sea level near the summit of Mauna Kea (on the island of Hawaii), has removed this impediment, so sub-THz Fourier transform spectroscopy of astronomical sources is now possible.

In order to study the millimeter and submillimeter spectra of the giant planets at moderate resolution, Serabyn and Weisstein (1996) constructed an intermediate resolution ($R \equiv \lambda/\Delta\lambda < 5000$) Fourier transform spectrometer. The screw-driven translation stage on which the moving mirror is mounted provides a maximum total travel of 50 cm. In the default position of the translation stage, a one-sided travel of 46 cm gives a maximum (unapodized) spectral resolution of 200 MHz, while a two-sided travel of 5 cm gives a maximum two-sided resolution of 3.6 GHz. (The one-sided travel plus half the two-sided travel does not quite sum to 50 cm because a small amount of space is left at the ends for limit switches in order to avoid the unpleasant consequences of driving the stage beyond the end of its intended travel; see Fig. 3.3.) The FTS is an upgraded version of an earlier interferometer which was used exclusively for holographic dish surface accuracy measurements (Serabyn *et al.* 1991). During observations, the FTS is mounted at the Cassegrain focus of the 10.4 m CSO telescope. A view of the CSO telescope with its shutter open and dish revealed is shown in Fig. 3.1.

Fourier transform spectrometers (e.g., Connes 1961, Vanasse and Sakai 1967, Schnopper and Thompson 1974, Oepts 1976, Brault 1985) operate by splitting an incoming beam of radiation into two parts, applying a differential phase shift, then recombining the beams. The phase shift is then varied, and an interference pattern known as an interferogram is swept out as a function of phase shift. The phase shift is most commonly produced by translating a reflecting element along one of the beams, thus producing a varying optical path difference. Because the CSO FTS is also used for holographic dish measurements, it is necessary to be able to steer the beam in one of the interferometer arms in azimuth and elevation. This consideration requires that flat surfaces be used for the end-mirrors, which in turn demands use of a dielectric beamsplitter. We therefore built a simple Michelson-type interferometer as opposed

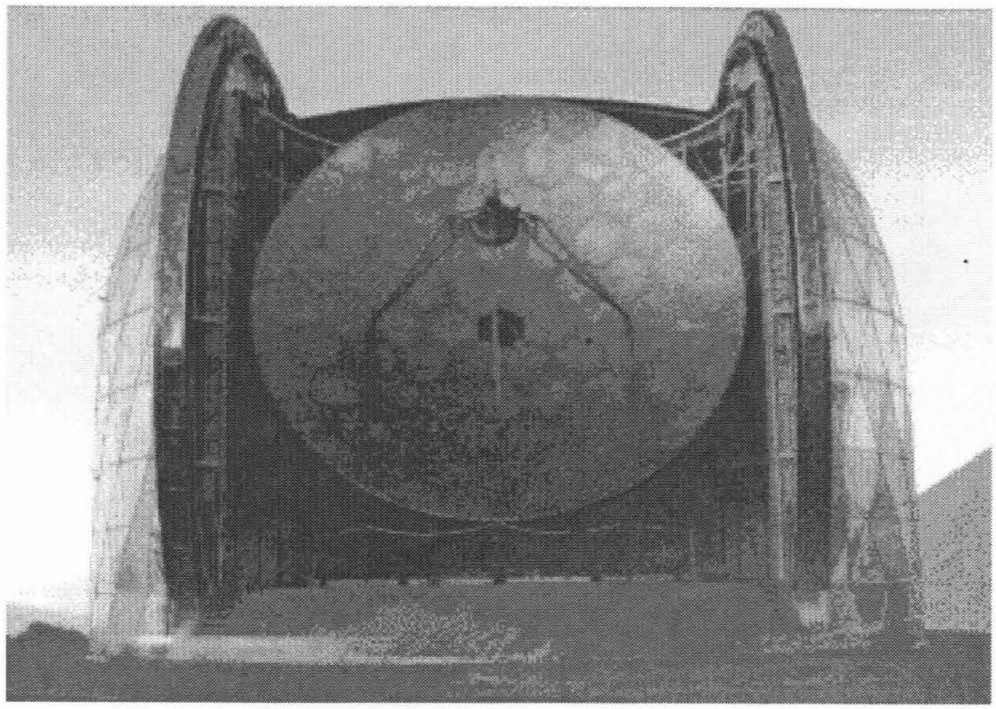

Figure 3.1. The Caltech Submillimeter Observatory.

to a more complicated configuration such as a Martin-Puplett interferometer (Martin 1986) which uses right-angle corner reflectors. While the single input and output port Michelson-type interferometer has a lower sensitivity than a dual-port Martin-Puplett interferometer, its simpler optical configuration is a considerable advantage in allowing rapid alignment and setup at the sometimes mind-numbing altitude of the summit of Mauna Kea.

As shown in Fig. 3.2, our interferometer is decoupled from the F/12.4 beam of the CSO's secondary mirror using two flat mirrors (M1 and M2) placed on either side of the Cassegrain focus. This arrangement folds the beam, allowing it to expand to the necessary size despite space constraints on the underside of the telescope. After reflecting off M2, the radiation is collimated by means of an off-axis paraboloidal mirror (P1), then split into two separate beams using a dielectric mylar beamsplitter (BS). One beam is then reflected off a mirror that is translatable along its normal (I1), and the other reflects off a stationary mirror positioned at right angles to the

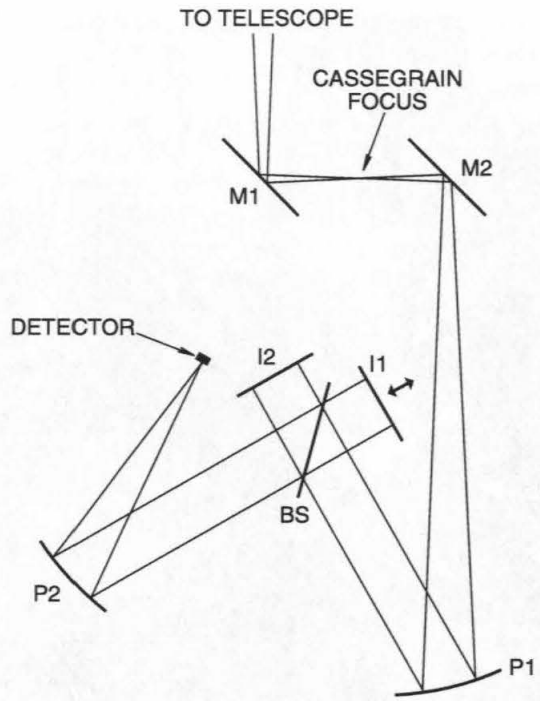

Figure 3.2. Schematic of the FTS optics.

first (I2). The reflected beams are then recombined at the beamsplitter. Finally, the superposed beams are focused onto the CSO facility bolometer by a second off-axis paraboloid (P2). The instrument is aligned by mounting a commercial HeNe laser in place of the bolometer and iteratively adjusting mirrors in order to bring all laser reflections into coincidence. Because FTSes can be operated without cryogenic cooling, the instrument is used at ambient temperature during observations (only the detector must be cooled).

Fig. 3.3 shows an annotated image of the FTS mounted at the CSO Cassegrain focus. The FTS instrument is run using `FTSRUN`, a flexible and (for the most part) user-friendly program which runs on the CSO summit VAXstation. This program allows the near-autonomous collection of data and on-line examination of raw interferograms using a set of predefined observing commands.

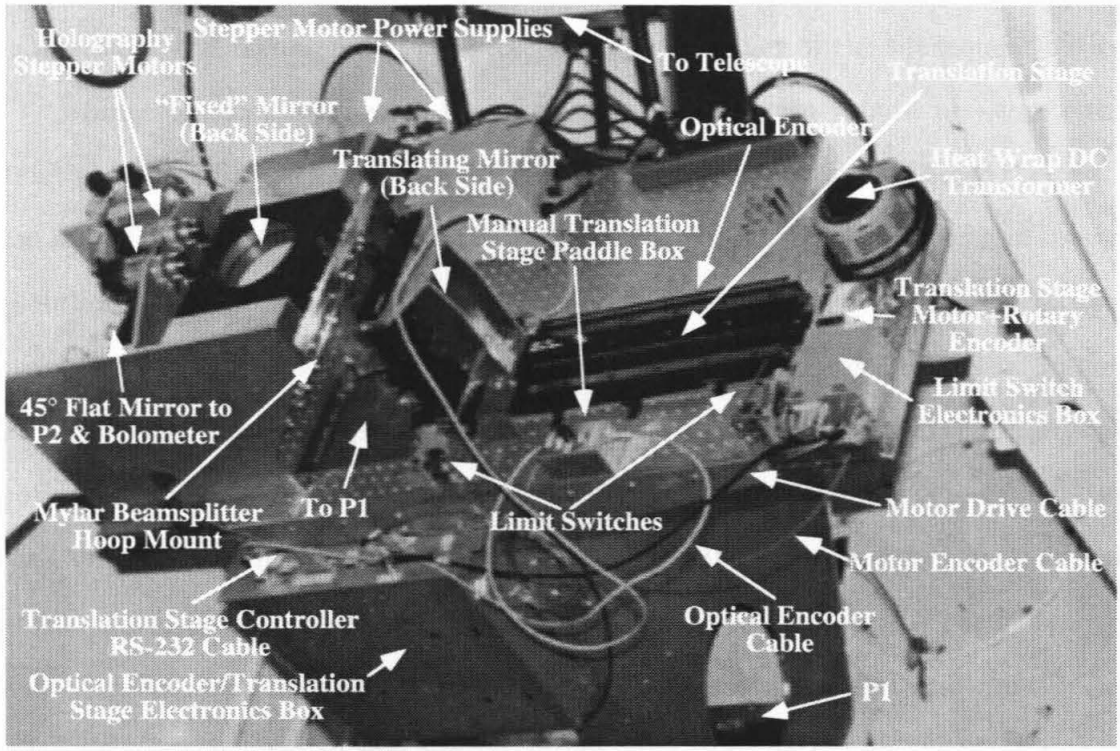

Figure 3.3. An annotated picture of the FTS and its associated gadgetry. The items labeled "holography stepper motors" and "stepper motor power supplies" are used only when the FTS is operated in its shearing mode for holographic dish surface accuracy measurements. For scale, the translation stage is 50 cm long. The FTS is mounted at the Cassegrain focus of the CSO telescope.

3.3. FTS Equations

By smoothly translating one mirror (I1 in Fig. 3.2), the optical path difference [OPD] $x \equiv 2L$ (where x *twice* the distance L traveled by the translating mirror; see Appendix A) between the beams reflecting off the two mirrors is varied continuously, producing an interferogram $I(x)$. The fringe pattern shown in Figure 3.4 is an experimentally measured interferogram for a hot blackbody using the 800 μm CSO filter. A derivation of the specific intensity $I_k(x)$ observed for radiation of a single wavenumber k (Appendix A) gives

$$I_k(x) = J(k)\,\langle T(k)\rangle\,\tfrac{1}{2}[1+\cos(kx)] \tag{3.1}$$

(e.g., Vanasse and Sakai 1967, Schnopper and Thompson 1974), where $J(k)$ is the incident intensity and $\langle T(k)\rangle$ is the beamsplitter transmission function (averaged over

polarizations and combined, in practice, with the efficiency of the subsequent optics).

Since $\cos(kx)$ is an even function, the interferogram should be symmetrical about the white light fringe for a perfectly aligned ideal instrument. Since the resolution of an FTS increases with increasing optical path difference, the maximum spectral resolution is achieved by using the entire available translation distance to measure only one side of the interferogram. However, in order to maximize the signal-to-noise ratio (by avoiding the slight overhead incurred in switching the direction of stage motion), both sides of the interferogram can be measured, yielding a so-called "two-sided" interferogram. Two-sided interferograms contain two measurements of each interferogram point per scan, but can only achieve half the optical path difference (and therefore half the spectral resolution) of one-sided scans. Because one-sided interferograms transform to real spectra, no explicit information on the interferogram phase is available, although phase problems do show up as anomalous spectral baselines. Two-sided interferograms transform to complex spectra (they have two pieces of information per frequency), allowing phase errors to be directly measured as a function of frequency. Two-sided scans are therefore extremely useful for examining (mis-)alignment of the optics and other potential instrumental problems. As already mentioned, a perfectly aligned instrument with no phase errors will produce completely symmetric interferograms whose transform will have zero imaginary part over all frequencies in the passband.

The total intensity measured for a given OPD x from radiation at all wavenumbers is found by integrating (3.1), which is equivalent to applying an inverse Fourier cosine transform $\mathcal{F}_c^{-1}$,

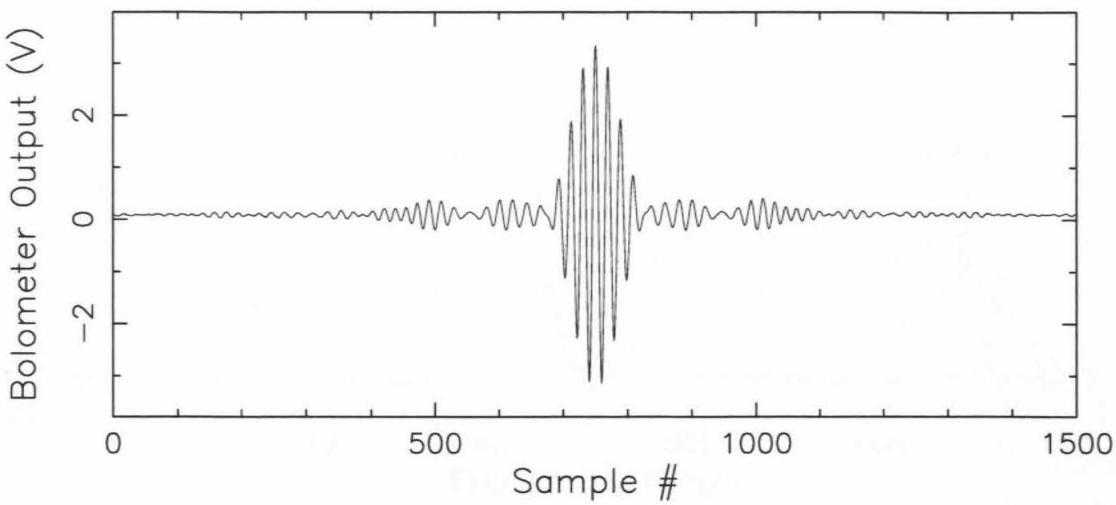

Figure 3.4. A sample interferogram observed for ambient temperature Eccosorb in the 800 μm filter. The interferogram level is (nearly) centered about 0 instead of $I(0)/2$ because the bolometer response is AC coupled to the signal, removing the continuum signal which would otherwise be present. The slight offset from 0, produced by DC offsets in the Bessel filter electronics, is removed prior to Fourier transformation by fitting out a linear baseline.

$$\begin{aligned} I(x) \equiv \int_0^\infty I_k(x)\,dk &= \frac{1}{2}\int_0^\infty [1+\cos(kx)]\,\langle T(k)\rangle\,J(k)\,dk \\ &= \frac{1}{2}\int_0^\infty \langle T(k)\rangle\,J(k)\,dk + \frac{1}{2}\int_0^\infty \cos(kx)\,\langle T(k)\rangle\,J(k)\,dk \\ &= \tfrac{1}{2}I(0) + \frac{1}{2}\int_0^\infty \cos(kx)\,\langle T(k)\rangle\,J(k)\,dk \\ &= \tfrac{1}{2}I(0) + \tfrac{1}{2}\mathcal{F}_c{}^{-1}[\langle T(k)\rangle\,J(k)]. \end{aligned} \tag{3.2}$$

In (3.2), the fact that the intensity of the white light fringe ($x = 0$) can be written

$$I(0) = \int_0^\infty I_k(0)\,dk = \int_0^\infty \langle T(k)\rangle\,J(k)\,dk, \tag{3.3}$$

has been used.

Equation (3.2) can now be inverted for the one-sided case to yield a real spectrum (Fig. 3.5)

$$\langle T(k)\rangle\,J(k) = 2\mathcal{F}_c[I(x) - \tfrac{1}{2}I(0)]. \tag{3.4}$$

Similarly, equation (3.2) can be inverted for the two-sided case to yield a spectrum with both real and imaginary parts (Fig. 3.6).

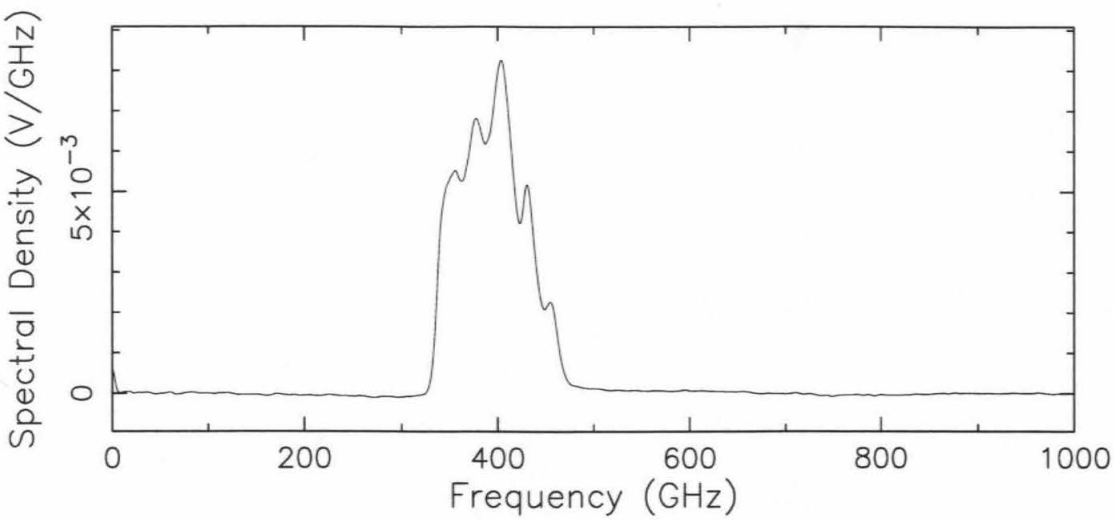

Figure 3.5. One-sided Fourier transform of Fig. 3.4.

3.4. Spectral Resolution

In both the one-sided and two-sided cases, we measure $I(x)$ (an "interferogram") and want to recover $J(k)$ (the "spectrum"). This can be done since both $\mathcal{F}_c^{-1}$ and $\mathcal{F}^{-1}$ are invertible. In practice, we can only measure $I(x)$ out to a finite OPD of $x = 2L$, so we have to multiply the integrand by a rectangle (or "window") function

$$\Pi_{2L}(x) \equiv \begin{cases} 1 & |x| < 2L \\ 0 & |x| > 2L, \end{cases} \tag{3.5}$$

where $\Pi_{2L}(x)$ may be multiplied by an additional apodization function which goes to 0 for $|x| > 2L$ in order to reduce sidelobes. Call the overall apodization function $W_{2L}(x)$, and let

$$S(k) \equiv \langle T(k) \rangle \, J(k) \tag{3.6}$$

$$S_{\text{obs}}(k) \equiv [\langle T(k) \rangle \, J(k)]_{\text{observed}} \tag{3.7}$$

be the actual and observed beamsplitter-attenuated spectral fluxes. Using the con-

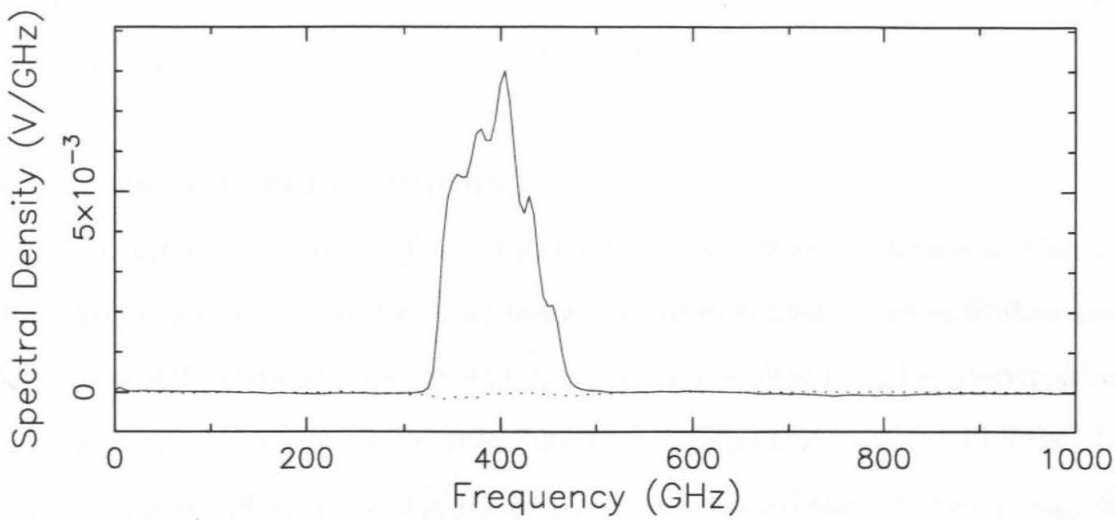

Figure 3.6. Two-sided Fourier transform of Fig. 3.4. The dotted line is the imaginary part of the transform.

volution theorem (Bracewell 1965) then gives

$$S_{\rm obs}(k) = \mathcal{F}_c\{W_{2L}(x)2[I(x) - \tfrac{1}{2}I(0)]\} = \mathcal{F}_c[W_{2L}(x)] \otimes 2\mathcal{F}_c[I(x) - \tfrac{1}{2}I(0)]$$
$$= \mathcal{F}_c[W_{2L}(x)] \otimes S(k), \tag{3.8}$$

where $\otimes$ denotes convolution. If no apodization function is used to weight the data, then $W_{2L}(x) = \Pi_{2L}(x)$ (Schnopper and Thompson 1974), and

$$S(k) = \mathrm{sinc}(2\pi kL) \otimes 2\mathcal{F}_c[I(x) - \tfrac{1}{2}I(0)]. \tag{3.9}$$

The spectral resolution for a one-sided travel of L (giving an OPD of $2L$) is

$$\Delta\nu = \frac{\eta c}{4L}, \tag{3.10}$$

where η is a factor which depends on the width of the apodization function (Thompson *et al.* 1991, p. 239). Note that for a two-sided scan of total length L_2, the one-sided length is $L = L_2/2$. With no apodization, $\eta = 1.20671\ldots$ is defined as $2u/\pi$ where u the HWHM (half width at half maximum) of the sinc instrument function, given by numerically solving

$$\mathrm{sinc}(u) = \tfrac{1}{2}. \tag{3.11}$$

The translation stage on which our moving mirror is mounted has a maximum one-sided travel L of ≈ 46 cm, giving $\Delta\nu = 200$ MHz.

3.5. Interferogram Sampling

Accurately spaced samples are generated every 20 μm of mirror motion (40 μm of OPD) along the interferogram using the pulses output by an optical encoder located along the translation stage (Fig. 3.3). 20 μm sampling provides interferograms which are sampled above the Nyquist rate for all frequencies up to 3.75 THz. Let f_{sample} be the sampling frequency, $f_{\text{fringe, max}}$ the maximum fringe frequency, ν_{max} the maximum sky frequency, and Δx be the spacing of mirror positions at which the interferogram is sampled. Then for the highest submillimeter frequency of 1000 GHz, the oversampling ratio β is given by the expression

$$\beta \equiv \frac{f_{\text{sample}}}{f_{\text{Nyquist}}} = \frac{f_{\text{sample}}}{2f_{\text{fringe, max}}} = \frac{\frac{v}{\Delta x}}{2\left(\frac{2v}{c}\nu_{\text{max}}\right)} = \frac{c}{4\nu_{\text{max}}\Delta x} \tag{3.12}$$

(c.f., equation 3.19). Plugging in the maximum translation speed $v_{\text{max}} = 1.0$ cm s^{-1}, $\nu_{\text{max}} = 1000$ GHz, and $\Delta x = 20$ μm then gives $\beta = 3.75$. However, the additional information provided by oversampling the interferograms is extremely useful for diagnostic purposes, particularly for examining interferograms for symmetry and for accurately determining the positions of white light fringes. The position of the WLF is critical to the inversion of our data because it also corresponds to the first interferogram point to be included in the Fourier transform.

Because the zero path-length difference "white light fringe" [WLF] can fall between two sample positions, our one-sided scans include a short two-sided portion which ensures our interferograms contains several fringes on both sides of the WLF. Fitting the central WLF using a second order polynomial then allows its position to be accurately determined. Sine and cosine transforms of the one-sided portion of the interferogram (or a full complex Fourier transform of the interferogram in its

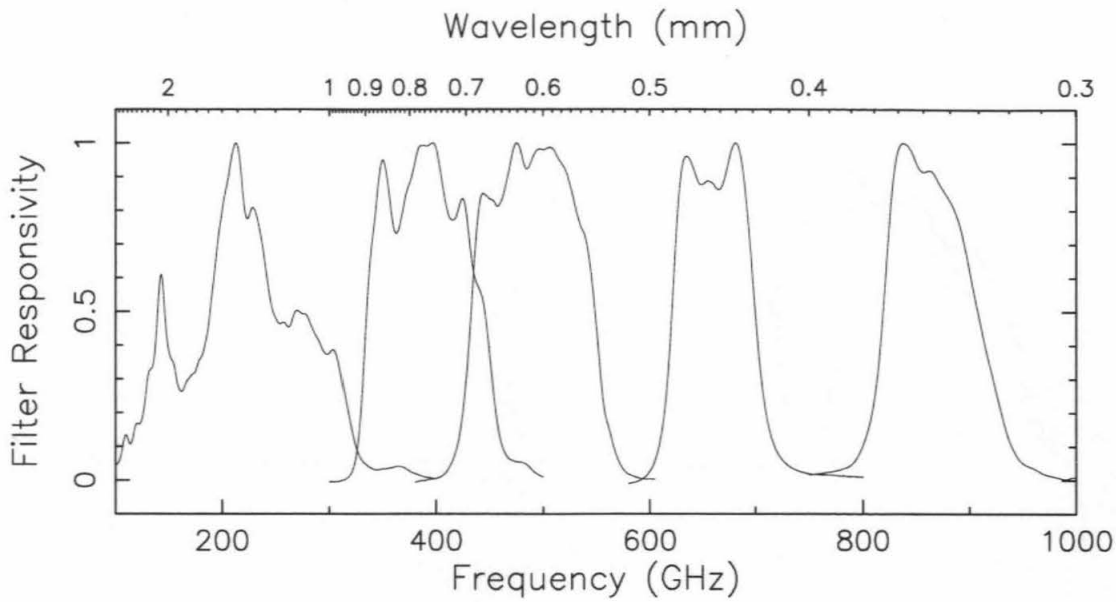

Figure 3.7. The responsivities of the standard suite of CSO filters as measured with the 31″ Winston cone. From left to right, they are referred to as the 1300, 800, 600, 450 (standard), and 350 (standard) μm filters.

entirety for two-sided scans) are then multiplied by a complex phase factor $\epsilon^{i\phi}$ in order to account for the phase shift resulting from the fractional offset of the WLF (Schnopper and Thompson 1974).

3.6. Optical Filters

The spectrometer's bandpass is fixed by a liquid helium cooled metal-mesh filter (Whitcomb and Keene 1980, Holah 1982) located in the CSO bolometer dewar. A selection of $\sim$ 10% bandpass filters matched to the several atmospheric windows between 150 and 1000 GHz is available at the CSO (Figs. 3.7 and 3.8). The available filters are centered at roughly 1300, 800, 600, 450, and 350 μm. (For the lowest frequency 1300 μm filter, the low frequency cutoff is introduced by the waveguide-like cutoff of the Winston cone light concentrator. Winston cones smaller than 30″ cannot be used with this filter.) Because the standard CSO 450 and 350 μm filters did not extend over the entire range of the high-frequency terrestrial atmospheric windows, we acquired two new custom-designed broad bandpass filters. These filters

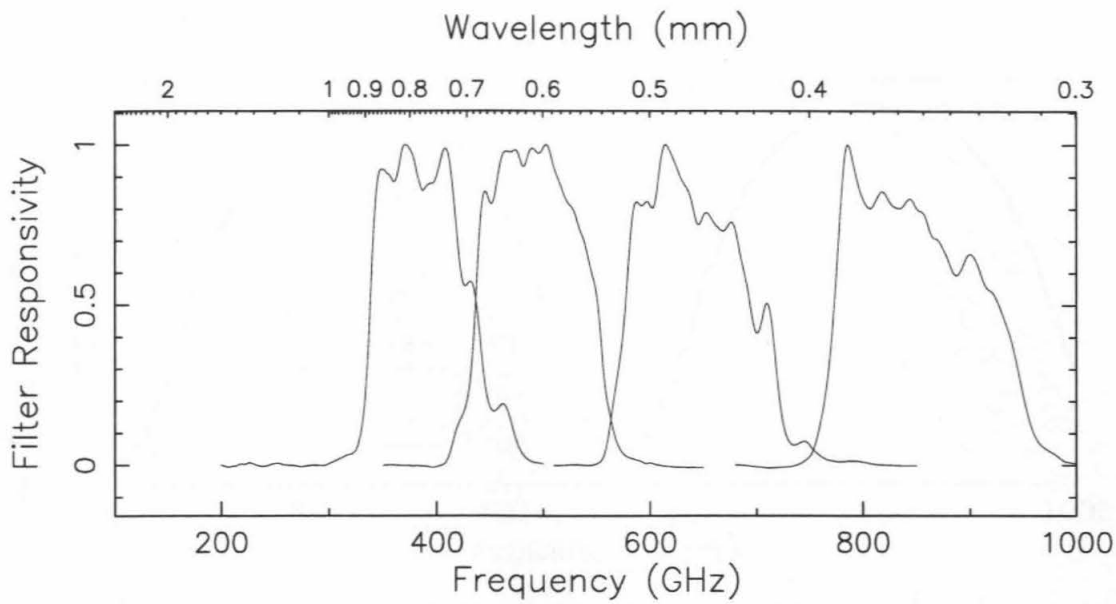

Figure 3.8. The responsivities of the four FTS filters used with the 20″ Winston cone. The two high frequency filters are custom built to cover the entire atmospheric windows. From left to right, they are referred to as the 800, 600, 450 (broad), and 350 (broad) μm filters.

are transmissive from 560 to 750 GHz and 760 to 950 GHz respectively, providing a passband wider than the relevant atmospheric windows (Fig. 3.8).

A cooled filter wheel assembly inside the dewar (Fig. 3.10) allows switching between any one of four filters without having to break the dewar's vacuum and bring it to room temperature, a time-consuming process not undertaken lightly.

3.7. Beamsplitter

Because of the relatively large distance tolerances permitted at millimeter wavelengths, a transparent dielectric material functions as an excellent beamsplitter. However, the thickness of this dielectric beamsplitter d must be matched to the metal-mesh bandpass filter in order to ensure that it is transmissive in the filter's passband. The beamsplitter transmission function (or "beamsplitter efficiency") of a dielectric beamsplitter is given by

$$T_p \equiv \left|\frac{E}{E_0}\right|^2 = \frac{16R_p(1-R_p)^2\sin^2(\frac{1}{2}\delta)}{[(1-R_p)^2+4R_p\sin^2(\frac{1}{2}\delta)]^2}, \tag{3.13}$$

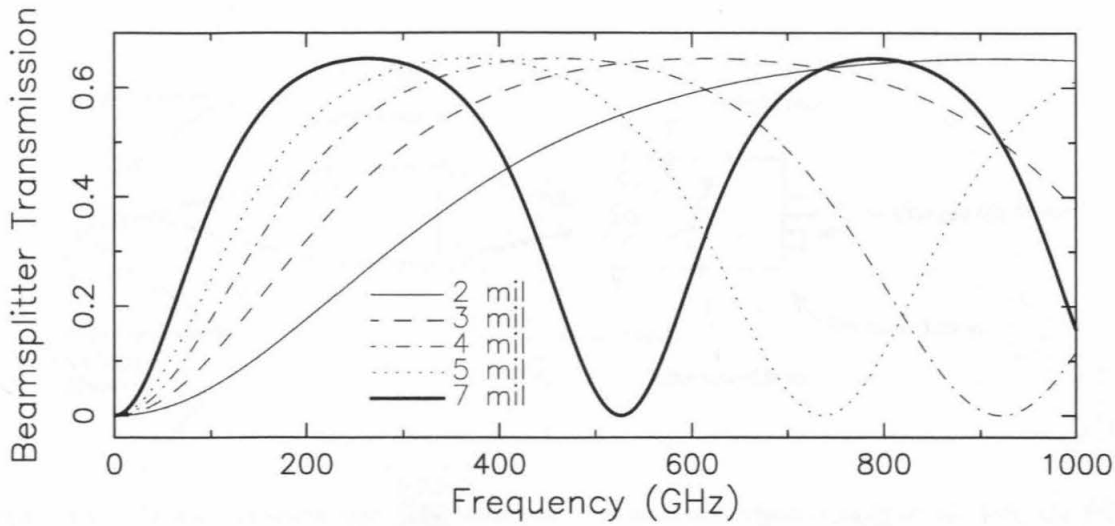

Figure 3.9. Beamsplitter transmission for the selection of mylar thicknesses available in hoop mounts.

where

$$\delta \equiv \frac{4\pi d}{\lambda_0}\sqrt{\left(\frac{n}{n_0}\right)^2 - \tfrac{1}{2}}\,, \tag{3.14}$$

E is the average electric field at the detector, E_0 is the incident electric field, λ_0 is the vacuum wavelength, n and n_0 are the indices of refraction of the beamsplitter and air, respectively, and R_p is the Fresnel reflection coefficient for polarization p either perpendicular or parallel. These formulas are derived in Appendix A. Equation 3.13 is normalized slightly differently than the expression of Chamberlain *et al.* (1966), resulting in an expression twice as large.

Because of its ready availability and low cost, we chose mylar as the dielectric material for our beamsplitters. Thicknesses of 2, 3, 4, 5, and 7 mil mylar are mounted in circular hoops which can be attached onto the instrument using three screws, allowing beamsplitters to be switched within a minute or two. Thompson (1990) discusses currently available commercial varieties of mylar, while Loewenstein and Smith (1971) discuss mylar's optical properties. The index of refraction of mylar has been measured as $n = 1.74$ for the frequency range 500-900 GHz (Whitbourn *et al.*

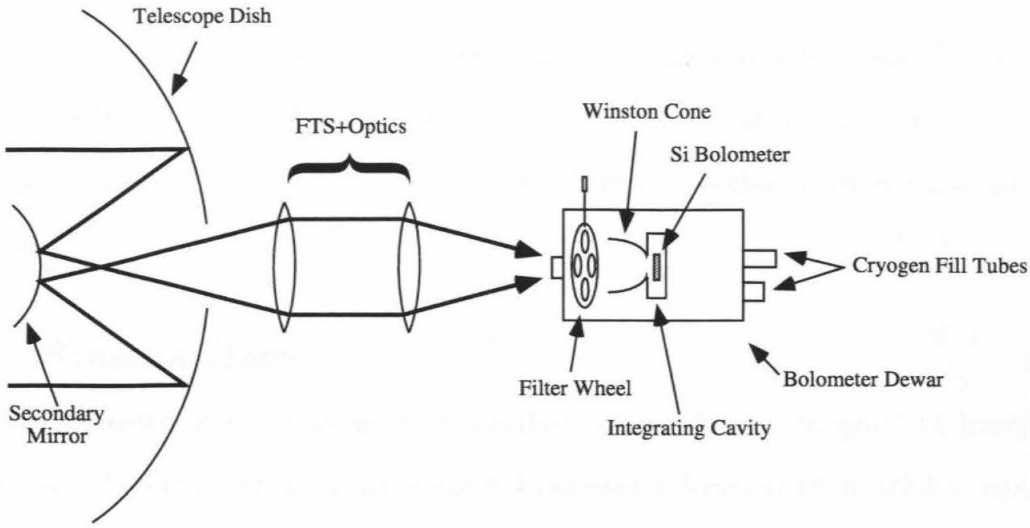

Figure 3.10. Bolometer schematic. The telescope dish is drawn schematically to the left, the FTS assembly in the middle, and the bolometer itself to the right.

1988) and $n = 1.70 \pm 0.02$ at 740 GHz (Bowden *et al.* 1991). Plots of the beamsplitter transmission as a function of frequency computed using (3.13) and (3.14) are shown in Figure 3.9.

3.8. Detector

After entering the cryogenically cooled IR Labs bolometer dewar, incident radiation from the FTS reaches a focus at the entrance aperture of a Winston cone, which concentrates it into an integrating cavity. After perhaps undergoing several bounces inside the cavity, the incident radiation is then detected by a single-element liquid ^{3}He-cooled Si bolometer (Boyd 1983) with noise equivalent power of $\sim 10^{-14}$ W Hz$^{-1/2}$. A schematic of the dewar layout is shown in Fig. 3.10. The bolometer is mounted to the FTS assembly using plastic screws on top of a rubber annulus in order to electrically isolate it from the telescope and the spectrometer. The output voltage from the bolometer is sampled and digitized by a 16-bit analog-to-digital converter after low-pass Bessel filtering to remove high frequency electrical noise. The choice of a Bessel filter (Horowitz and Hill 1990) is mandated by the requirement that the

filter response to the interferogram have a constant phase as a function of frequency. Our 6-pole Bessel filter is located just prior to the A/D, and is conventionally set to a low-pass cutoff of 80 Hz in order to prevent aliasing of high-frequency noise into the bandpass.

3.9. Winston Cone

A Winston cone is an off-axis parabola of revolution designed to maximize collection of incoming rays within some field of view (Winston 1970, Hildebrand and Winston 1982, Hildebrand 1985, Welford and Winston 1989). Winston cones are nonimaging light concentrators intended to funnel all wavelengths passing through the entrance aperture out through the exit aperture. They maximize the collection of incoming rays by allowing off-axis rays to make multiple bounces before passing out the exit aperture. Even so, there are certain families of off-axis rays which are rejected back out the entrance aperture. In addition, since diffraction effects become important for radiation wavelengths similar to the cone's physical dimensions, Winston cones exhibit a waveguide-like cutoff at low frequencies.

These waveguide-like non-geometric properties of Winston cones can lead to nonideal behavior, and in particular to multiple reflections, resulting in the possible generation of standing waves. Uncalibrated spectra taken with the FTS all contain ripples (Fig. 3.11) which change amplitude and period depending on the size of the cone, the geometric size of the source being observed, and the filter being used. Observed ripples typically have periods of $\sim$ 2-6 GHz. Fortunately, because the instrument has a nearly linear response, the ripple can be approximately divided out of planetary spectra during the differencing/ratioing procedure used to convert our raw interferograms to atmospheric transmission-corrected spectra.

The equations describing the geometry of a Winston cone are derived in Appendix B, together with the the algebraic equations connecting their various param-

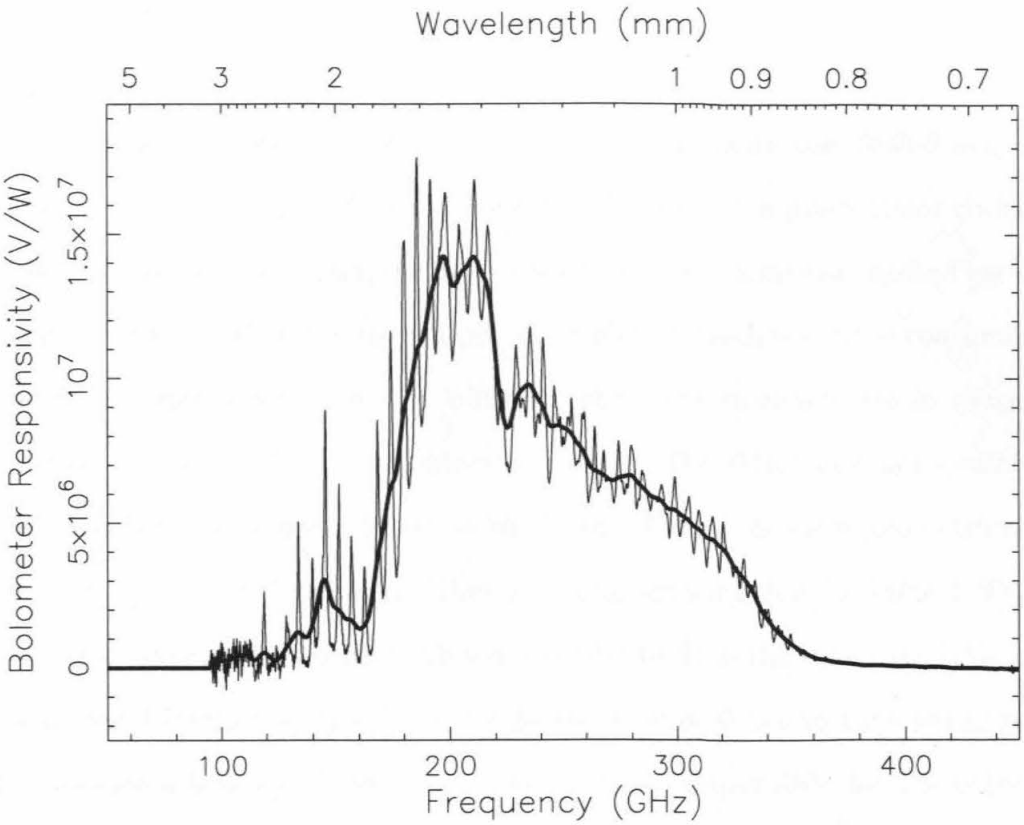

Figure 3.11. Responsivity of the CSO bolometer detector with the CSO's 30″ Winston cone and "1300 μm" wire-mesh filter. The thin solid curve is the measured responsivity at full resolution; the thick solid curve is the responsivity measured at lower resolution. At full resolution, interference ripples produced by multiple reflections inside the Winston cone are quite prominent.

eters. As shown in Appendix B, a Winston cone is completely specified by its length L and geometric field of view Θ_G. The field of view of the Winston cone on the *sky* is computed from

$$\Theta = 2\tan^{-1}\left(\frac{a}{f'}\right) = 2\tan^{-1}\left(\frac{a}{F'D}\right) \approx \frac{2a}{F'D}, \tag{3.15}$$

where f' is the effective focal length of the telescope+optics, $F' \equiv f'/D$ is the corresponding F-number, and D is the telescope diameter. For the CSO, $D = 10.4$ m and the optical setup is designed to give $F' = 4.4$, so

$$\Theta = \frac{2a}{45.76\text{ m}}\text{ radians} = 4.5''\left(\frac{2a}{\text{mm}}\right). \tag{3.16}$$

The entrance aperture required to produce a given field of view on the sky is therefore

given by (3.16).

Since the Winston cone is physically mounted inside the cooled evacuated bolometer dewar, only single Winston cone may be used at a given time. Switching cones therefore requires bringing the bolometer to ambient temperature and pressure, replacing the cone, and re-cooling—a process which is much too time consuming to be performed during observations. A Winston cone is therefore selected in advance in order to best match the size of the object of interest. The Winston cones available at the CSO have fields of view on the sky of 10, 20, or 30″, and the same geometrical field of view ($\theta \approx a'/a = 0.114$ radians). They are summarized below in Table I. The 30″ cone has been truncated a length of 22 mm in order to fit in the space available inside the bolometer. (Truncation results in the degradation of Winston cone performance, and the complications which result may be partially responsible for the extremely large ripple observed with this cone in Fig. 3.11. It should also be noted that use of the 10″ cone requires a repositioning of the bolometer by 1 cm in order to bring the vertical position of the focus into coincidence with the entrance aperture of this short cone.)

Table I. CSO Winston Cones.

Θ	$d_1 \equiv 2a$ (mm)	$d_2 \equiv 2a'$ (mm)	L (mm)
30″	6.6	0.75	32 (truncated to 22)
20″	4.4	0.50	21
10″	2.2	0.25	11

3.10. Beam Coupling

The response of the FTS to incoming radiation is not isotropic, but is given by the primary beam of the telescope convolved with the Winston cone's field of view on the sky. The analytic computation of this convolution is discussed in Appendix C, where the telescope's primary beam is approximated as a Gaussian with standard

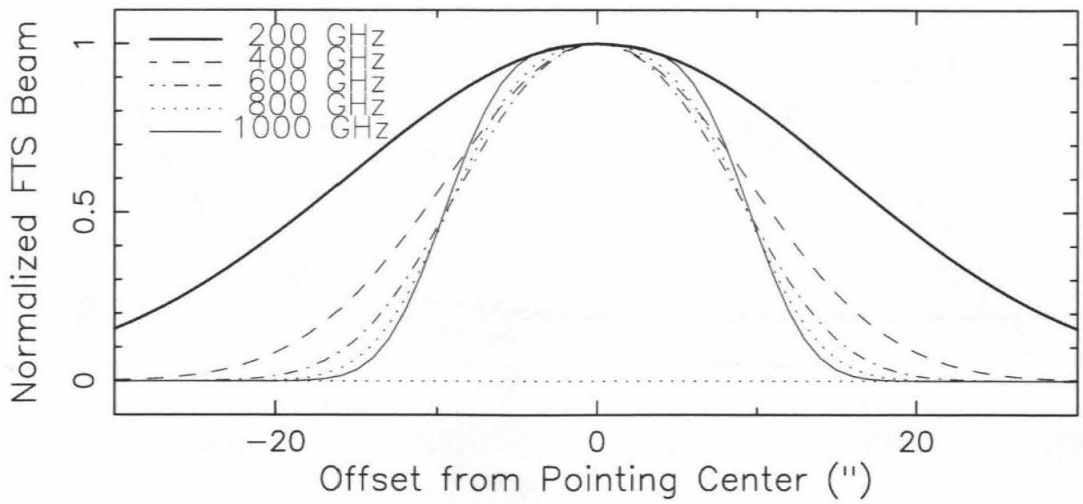

Figure 3.12. FTS beam shape as a function of frequency. These curves, normalized to unity, give the response of the instrument to a point source located a given angular distance away from the pointing center. Note the transition from a Gaussian shape at low frequencies to a rectangle function at high frequencies.

deviation σ. Because of the frequency dependence of σ,

$$\sigma \propto \lambda \propto \frac{1}{\nu}, \tag{3.17}$$

the response function of the FTS changes as a function of frequency. A plot of the instrumental response as a function of pointing center offset is given in Fig. 3.12 for a range of frequencies from 200-1000 GHz. At low frequencies, the main beam is large compared to the field of view, so the response is nearly Gaussian. At greater frequencies, the geometric field of view becomes the dominant factor and the response approaches a flat-topped rectangle (window) function.

The effect of the changing beam shape as a function of frequency is most simply expressed in terms of the half-power beamwidth [HPBW] (also called the full-width at half power). Figure 3.13 shows the half-power beamwidth as a function of frequency, computed with the equations derived in Appendix C (solid line) for a Winston cone field of view of 20″. Also plotted are the half widths computed using a more realistic Airy beam pattern (dotted line), in which the integrations must be done numerically

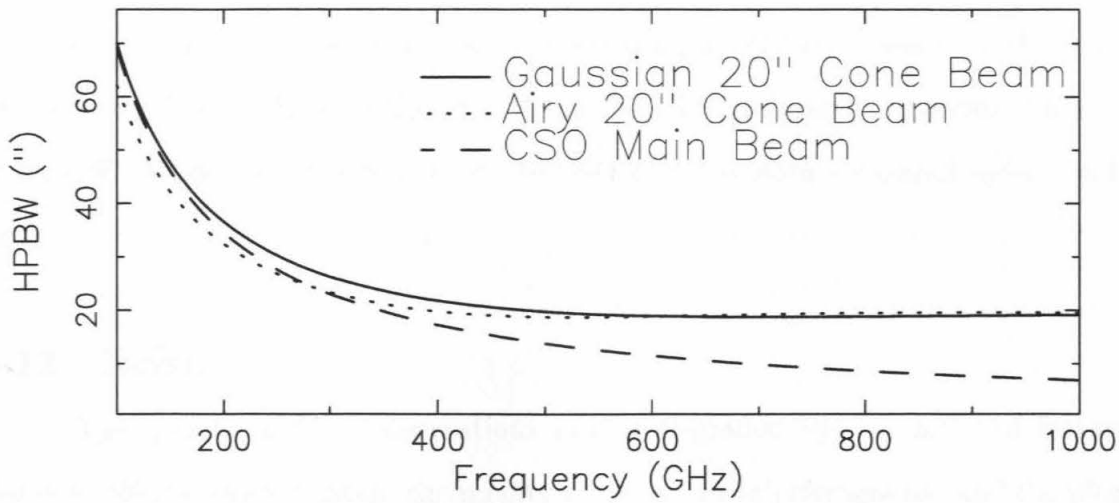

Figure 3.13. Half-power beamwidths for the CSO main beam and the FTS Winston cone field of view convolved with the CSO main beam. Beamwidths have been computed assuming both Airy and Gaussian beam shapes for the CSO main beam.

from the outset, and for a Gaussian main beam with an infinite field of view (dashed line). It is apparent that for frequencies $\gtrsim$ 400 GHz, the half power beamwidth of the instrumental beam (solid and dotted curves) is very nearly constant. As shown by the dashed curve, the CSO's main beam HPBW varies from 34.5″ at 200 GHz to 6.9″ at 1000 GHz.

3.11. Dish RMS

In addition to the variations of the telescope HPBW with frequency, the power lost from the main beam due to surface irregularities is a strong function of frequency. The fractional power in the main beam is given by

$$P_{\text{main beam}} = \epsilon^{-(4\pi\epsilon/\lambda)^2} \eta_{\text{Moon}}, \tag{3.18}$$

where η_{Moon} is the "Moon efficiency" (the ratio of the full Moon's antenna temperature to its physical temperature) and ϵ is the RMS telescope surface error (Ruze 1966, Serabyn and Weisstein 1996). The power scattered out of the main beam is not

actually lost, but forms a broad, flat "error pattern" surrounding the main beam. This power is therefore recovered when measuring a very large source such as the Moon, but otherwise falls on the sky. Using the FTS in its shearing mode (Serabyn *et al.* 1991, Woody *et al.* 1994), ϵ for the CSO dish has been measured to be $\epsilon \approx 15$ μm.

3.12. Noise

The quality of FTS observations can be degraded by a number of factors. Random effects which degrade the quality of measured interferograms (and therefore reduce the quality of the associated spectra) are discussed in this section, while systematic effects which can be corrected post-observationally during the processing of interferograms are discussed in the following chapter.

3.12.1 Sky Fluctuations

Even on the summit of Mauna Kea, variations in sky transmission and ground-level atmospheric humidity during or between individual spectrometer scans can have a deleterious effect on the quality of data obtained. In order to minimize the effects of sky fluctuations, the FTS is operated in rapid-scan mode. By rapidly scanning the translating mirror, it is possible to modulate sky variations, which occur at typical frequencies of a few Hz, so that they transform to spectral frequencies which fall outside the bandpass of interest. The relationship between electrical, or "fringe," frequencies (f) and spectral frequencies (ν) for a rapid-scan FTS is given by

$$f = \frac{2v}{c}\nu, \tag{3.19}$$

where $c = 30$ cm GHz is the speed of light and v is the speed of the translation stage. The FTS is typically run with translation speeds between $v = 0.9$ and 0.45 cm s^{-1} (depending on the filter being used), resulting in electrical fringes with frequencies $f \sim$

6-30 Hz. Sky-induced noise (with typical frequencies < 1 Hz under good observing conditions or $\lesssim 5$ Hz in poor weather) is therefore mostly transformed away to low spectral frequencies. Although high scan speeds are desirable in order to reduce longer-term sky variations which could occur between sets of "on" and "off" scans, lower speeds are required for the high-frequency 450 and 350 μm filters in order to avoid microphonics (vibrations induced in the bolometer by motion of the stage, which typically occur at $f > 30$ Hz), as well as the ever-present residual 60 Hz pickup.

3.12.2 Detector Noise

For high submillimeter frequencies, the atmospheric thermal background dominates over detector noise. However, the detector noise limit is reached first at the lower frequencies. The predicted RMS noise in a spectrum obtained by averaging N on-off pairs is given by

$$\sigma = \frac{4\,NEP}{k}\sqrt{\frac{v}{c\Delta\nu N}} \tag{3.20}$$

(Serabyn and Weisstein 1995), where NEP is the detector noise equivalent power, k is the Stefan-Boltzmann constant, v is the scan speed, and $\Delta\nu$ is the resolution (in frequency units). But the number of scans acquired in a time t is just

$$N = \frac{t}{\frac{L}{v}} = \frac{tv}{L}, \tag{3.21}$$

so solving (3.10) for $1/L$ gives

$$\frac{1}{L} = \frac{4\Delta\nu}{\eta c}. \tag{3.22}$$

Combining (3.22) with (3.21) results in

$$N = \frac{4tv\Delta\nu}{\eta c}, \tag{3.23}$$

and plugging this into (3.20) gives finally

$$\sigma = \frac{2\eta^{1/2}NEP}{k\Delta\nu\sqrt{t}}. \tag{3.24}$$

For $NEP \sim 10^{-14}$ W Hz$^{-1/2}$, this simplifies to

$$\sigma \approx \frac{2}{\Delta\nu_{\mathrm{GHz}}\sqrt{t}}. \tag{3.25}$$

Therefore, for a given scan length, the detector noise integrates down as $t^{-1/2}$. This result has been verified experimentally by observing the CO 3−2 line in M82 (Serabyn and Weisstein 1995).

3.12.3 Electrical Pickup and Microphonics

Any noise occurring at a fixed electrical frequency during measurement of interferogram fringes will appear as a noise spike at the corresponding spectral frequency given by (3.19). As already mentioned, special care must be taken to avoid 60 Hz electrical pickup, which appears in spectra as a large spike (at 900 GHz for a scan speed of 1 cm s^{-1}).

An additional source of noise spikes is microphonics. These vibrations of the bolometer can be induced by the motion of the stage or telescope. Stage-induced microphonics, are reduced by mounting the bolometer on top of an annulus of soft rubber. However, some vibrations are still transmitted through the rubber as well as through the plastic mounting screws. Their effect on spectra is seen as a series of narrow noise spikes at fairly well-defined frequencies (> 700 GHz in Fig. 3.14). While microphonics cannot be completely eliminated, they can be moved out of the spectral range of interest by picking a stage velocity which modulates them so that they transform out of the filter bandpass. Speeds of 0.9, 0.75, 0.7, 0.45, and 0.45 cm s^{-1} have been found experimentally to give microphonics-free spectra in the 1300, 800, 600, 450, and 350 μm filters, respectively.

3.12.4 Ghosts

If the sampling of an interferogram is modulated at a definite frequency instead of being uniformly sampled, spurious spectral features called "ghosts" are produced

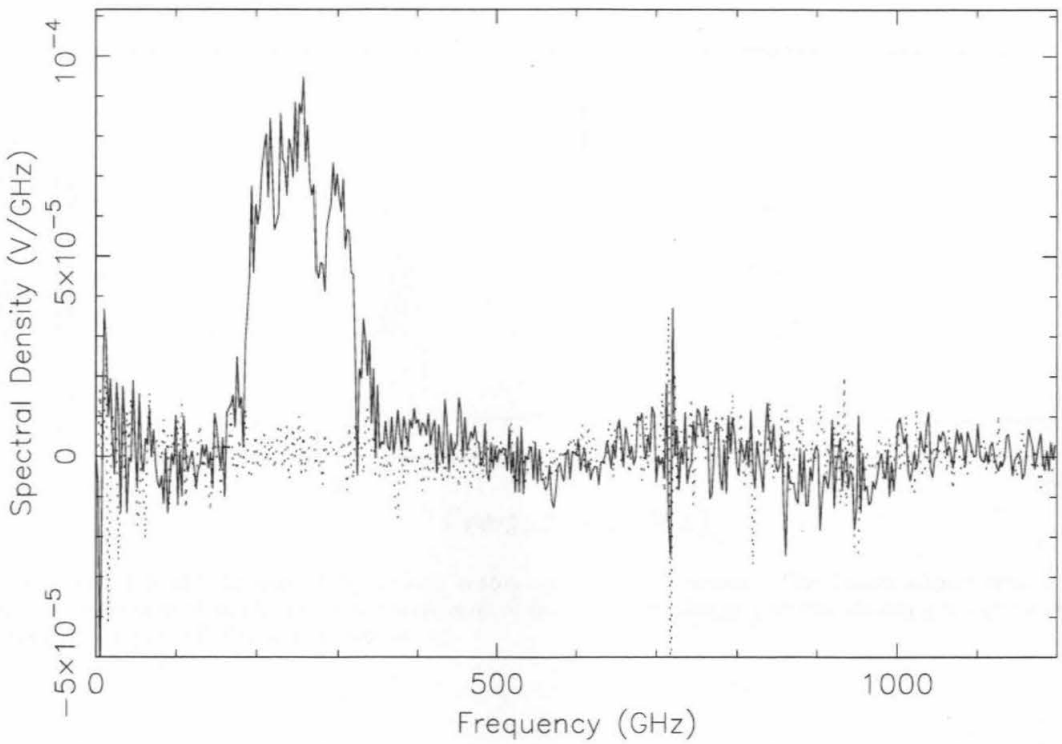

Figure 3.14. Microphonics visible in a two-sided Uranus-Off difference spectrum as real and imaginary spikes at $\nu > 700$ GHz. Note also the flatness of the imaginary part within the filter bandpass.

(Brault 1985). The translating mirror of the CSO FTS is driven by a precision screw which is turned at a constant angular velocity. However, periodic errors in the ruling of the screw (commonly introduced in the manufacturing process) can and do introduce a modulation superposed on top of the expected fringe pattern due to uniform stage translation. Because modulation is a multiplicative process, spurious features are generated in spectral space at the sum and difference of the true fringe and ghost fringe frequencies, thus throwing power out of its spectral band.

Ghosts are copies of the actual spectrum, but appear at reduced strength. Figure 3.15 shows the power spectrum for a pure sinusoidal signal sampled by translating the FTS stage at constant speed. In order for a ghost to appear, the process producing it must exist for most of the interferogram. However, if the ruling errors are not truly sinusoidal but vary across the length of the screw, a longer travel path

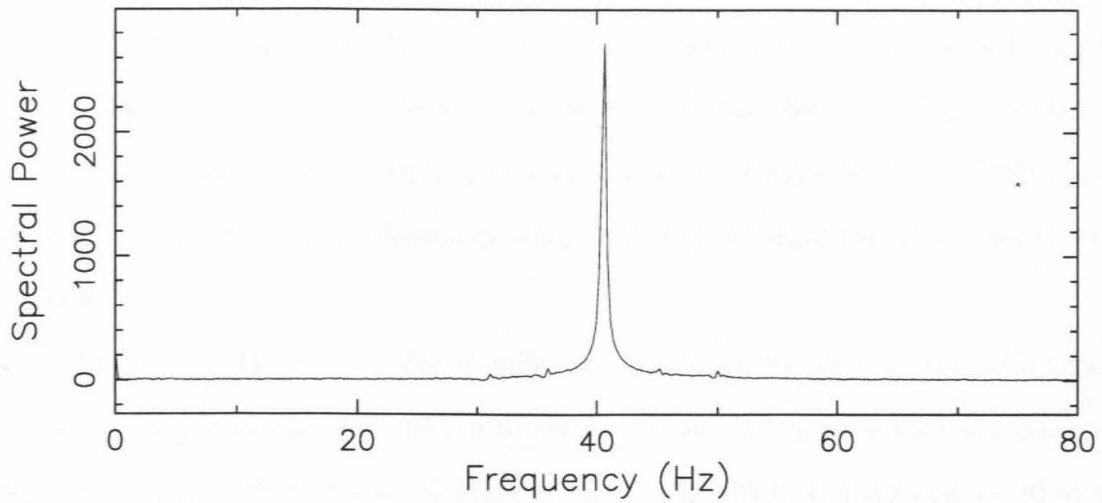

Figure 3.15. Ghosts produced by ruling errors on the FTS screw. The input signal was a pure $\sim$ 40.5 Hz sinusoid, but the Fourier transform of the detected fringe pattern shows a series of ghosts symmetrically placed about this frequency.

could reduce their effect. Unfortunately, the only way to remove ghosts is by replacing the offending screw with one manufactured to higher precision.

3.13. Frequency Calibration

The frequency scale in spectral space is determined solely by the number of points in a scan and the number of points sampled (or the total number of points if an interferogram is padded with 0s to a power of 2 in length for an FFT). In order to verify that the optical encoder provided pulses correctly spaced by 20 μm, we examined the central frequencies of narrow O_3 lines in the Earth's atmosphere, as well as the frequencies of the many narrow strong lines in the Orion Molecular Cloud core, which has a very small radial velocity relative to the Earth (Serabyn and Weisstein 1995). In both cases, the central frequencies of features were found to correspond to their tabulated transition frequencies to within small fractions of a resolution element, demonstrating the accuracy of the optical encoder sampling interval and data reduction software. The instrumental frequency calibration was

estimated more precisely by fitting the narrow CO 2−1 line observed in Venus. A fit to this line using an exponential lineshape and linear baseline yielded a central frequency of 230.543 GHz, compared to the actual frequency (in the absence of Doppler shift) of 230.538 GHz (Pickett *et al.* 1992). The surprisingly good agreement of 5 MHz is only 2% of a resolution element, demonstrating that instrumental frequency uncertainty is negligible.

Frequency (Doppler) shifts of molecular transition frequencies caused by radial motion of the jovian planets relative to the Earth are unimportant for our analyses. Since $(v_{\oplus}/c)_{\mathrm{max}} \approx 10^{-4}$, $\Delta\nu \sim 30$ MHz at 300 GHz, which is small compared to the resolution of the FTS.

Chapter 4

Data Reduction

> *"It is a profoundly erroneous truism... that we should cultivate the habit of thinking of what we were doing. The precise opposite is the case. Civilization advances by extending the number of important operations which we can perform without thinking about them. Operations of thought are like cavalry charges in battle—they are strictly limited in number, they require fresh horses, and must be made only at decisive moments."*
>
> —Alfred North Whitehead

Although the relationship between a measured interferogram and the corresponding spectrum is that of a simple Fourier (or cosine) transform, the determination of astronomical spectra from many interferograms measured over the course of an observing run requires both scan alignment and some additional processing. After the interferograms are suitably aligned, systematic problems such as cosmic ray hits on the detector or spurious trigger pulses must be identified and the affected scans discarded or corrected. During the processing of scans, data massaging procedures such as dechirping and apodization may also be performed. Finally, the observed interferograms must be combined in order to derive a hot-spillover and atmospheric absorption corrected source antenna temperature T_A^*.

In planetary observations, pairs of scans are taken alternately "on" the source and "off" the source on blank sky. Following completion of the "on" scans, we offset the telescope so that it tracks over the same sky positions previously traversed by the planet. These "off" scans provide a sky measurement at an atmospheric opacity which is nearly identical to that of the "on" scans. Depending on the strength of the source, many on-off pairs may be required to obtain a usable spectrum. Since on-source observations suffer from atmospheric attenuation, an additional measurement is taken of a "hot" (i.e., ambient temperature) emitter (in our case, a small sheet of Eccosorb placed over the spectrometer's collecting mirror) to provide an unattenuated

blackbody spectrum. Hot scans are therefore periodically interspersed with on/off pairs. Suitable processing of these three sets of scans allows atmospheric absorption, hot spillover, and emission from the interferometer's "output port" which is reflected back through the interferometer to be eliminated. In addition, the ratioing procedure we describe below is effective at removing reflective standing waves in the spectra which are produced inside the Winston cone.

FTS data are reduced using the program `FTSPEC`, which has been specifically written for the CSO FTS. All the processing steps described in this chapter (as well as many not mentioned here) are implemented in this program.

4.1. Planetary Observations

In order to obtain planetary spectra from individual "on," "off," and "hot" scans, the equations of radiative transfer are used (Penzias and Burrus 1973). To a good approximation, the Earth's atmosphere can be treated as an absorber/emitter with optical depth τ. The opacity of the Earth's atmosphere attenuates flux from astronomical sources by a factor $e^{-\tau}$, producing a transmitted brightness $B_{\rm pla}e^{-\tau}$ for a source with disk-averaged brightness $B_{\rm pla}$, where B is the Planck function. In addition to attenuating the source flux, the Earth's atmosphere also emits. By Kirchhoff's Law, if the atmosphere were in equilibrium emitting $B_{\rm sky}$, it would emit radiation in order to exactly balance the radiation it absorbed, giving atmospheric radiation with flux $B_{\rm atm} = B_{\rm sky}(1 - e^{-\tau})$.

In practice, a sky efficiency $\eta_{\rm sky}$ must be inserted appropriately to account for the telescope's hot spillover (that fraction of the beam intercepted by ambient temperature surfaces—such as the feedlegs). In addition, because the telescope's beam becomes less responsive away from the pointing center, a frequency-dependent beam coupling efficiency $\eta_{\rm c}$ modifies the $B_{\rm pla}$ term (Ulich and Haas 1976, Kutner and Ulich 1981, Kutner *et al.* 1984). Finally, a temperature $B_{\rm port\ 2}$ must be *subtracted* to

account for emission entering the interferometer from its second input port (Brault 1985) which, for our instrument, is reflected back to the detector.

The equations describing our observations are therefore

$$V_{\rm off} = G[\eta_{\rm sky} B_{\rm sky}(1 - e^{-\tau}) + (1 - \eta_{\rm sky}) B_{\rm hot} - B_{\rm port\ 2}] \tag{4.1}$$

$$V_{\rm on} = G[\eta_c \eta_{\rm sky} B_{\rm pla} e^{-\tau} + \eta_{\rm sky} B_{\rm sky}(1 - e^{-\tau}) + (1 - \eta_{\rm sky}) B_{\rm hot} - B_{\rm port\ 2}] \tag{4.2}$$

$$V_{\rm hot} = G(B_{\rm hot} - B_{\rm port\ 2}), \tag{4.3}$$

where V is the detected voltage, G is the instrumental gain, and all other terms are defined above. In practice, the factor $B_{\rm port\ 2}$ should really be written

$$B_{\rm port\ 2} = \eta_{\rm hot} B_{\rm hot} + \eta_{N_2} B_{N_2} + \eta_{\rm He} B_{\rm He} + \eta_{^3{\rm He}} B_{^3{\rm He}} \tag{4.4}$$

(Serabyn and Weisstein 1996), where $T_{\rm hot}$, 77 K, 4 K, and 0.3 K are the temperatures of the surfaces subtended by the port 2 beam (hot spillover, liquid nitrogen shield, liquid helium cooled interior, and liquid helium-3 cooled detector) and the η's their corresponding efficiencies, normalized according to $\sum \eta = 1$. However, since the same port 2 emission is measured in all spectra and therefore subtracts away (see below), and because the efficiencies are not in practice known in any case, we need not consider the details of (4.4) further. Dividing [(4.2)−(4.1)] by [(4.3)−(4.1)] gives

$$\frac{V_{\rm on} - V_{\rm off}}{V_{\rm hot} - V_{\rm off}} = \frac{\eta_c \eta_{\rm sky} B_{\rm pla} e^{-\tau}}{\eta_{\rm sky}[B_{\rm hot} - B_{\rm sky}(1 - e^{-\tau})]} = \frac{\eta_c B_{\rm pla}}{B_{\rm sky}} \frac{1}{1 + e^{\tau}\left(\frac{B_{\rm hot}}{B_{\rm sky}} - 1\right)}. \tag{4.5}$$

Rearranging, we obtain

$$\eta_c B_{\rm pla} = \left[\frac{V_{\rm on} - V_{\rm off}}{V_{\rm hot} - V_{\rm off}} B_{\rm sky}\right]\left[1 + e^{\tau}\left(\frac{B_{\rm hot}}{B_{\rm sky}} - 1\right)\right]. \tag{4.6}$$

If we now take $B_{\rm hot} \approx B_{\rm sky}$, this simplifies to

$$\eta_c B_{\rm pla} = \frac{V_{\rm on} - V_{\rm off}}{V_{\rm hot} - V_{\rm off}} B_{\rm sky}. \tag{4.7}$$

The concept of antenna temperature is usually encountered in temperature and frequency regimes where the Planck function can be well approximated by the Rayleigh-Jeans law. It is therefore convenient to define a so-called Rayleigh-Jeans brightness temperature T_B corresponding to an observed flux B_ν by

$$T_B \equiv \frac{c^2 B_\nu}{2k\nu^2}. \tag{4.8}$$

Plugging (4.7) and (4.8) into the definition of the antenna temperature corrected for atmospheric absorption and hot spillover (as well as port 2 emission in our case)

$$T_A^* \equiv \eta_c T_{\rm pla} \tag{4.9}$$

(Penzias and Burrus 1973, Ulich and Haas 1976) then gives

$$T_A^* = \frac{h\nu/k}{e^{h\nu/kT_{\rm sky}} - 1} \frac{V_{\rm on} - V_{\rm off}}{V_{\rm hot} - V_{\rm off}}. \tag{4.10}$$

This quantity, computed using on, off, and hot interferograms and the measured ambient temperature, has units of K and is the one used to display most of the spectra presented in this thesis. In the Rayleigh-Jeans limit, $h\nu/kT_{\rm sky} \ll 1$, and (4.10) simplifies to

$$T_A^* = T_{\rm sky} \frac{V_{\rm on} - V_{\rm off}}{V_{\rm hot} - V_{\rm off}}. \tag{4.11}$$

4.2. Scan Registration

For weak sources such as Uranus and Neptune, individual on−off interferograms may have insufficient signal-to-noise ratios for their WLFs to be identified. As a result, it is necessary to be able to align the WLFs of interferograms regardless of signal strength. This is achieved using a reference pulse provided by the optical encoder. In addition to providing sample pulses, the encoder also provides an absolute reference mark which is generated upon motion of the translation stage past a fixed point on the encoder. The position of the reference pulse is measured and recorded

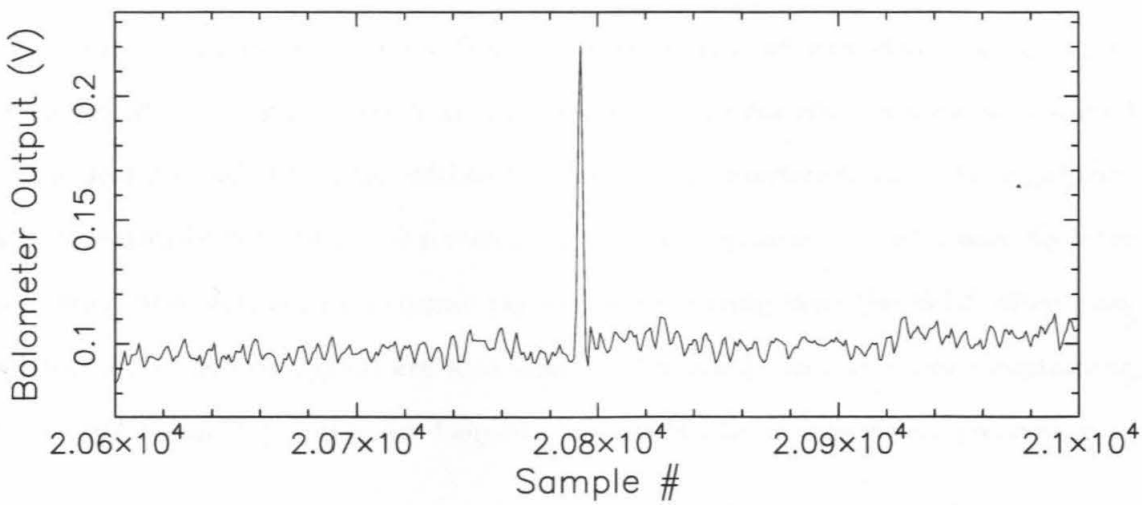

Figure 4.1. Cosmic ray spike in a raw interferogram. The reason no fringes are seen in this interferogram fragment is that only low-power, high-frequency spectral terms have fringes at large OPDs such as the region shown here. Before transforming, the high frequency fringes appear to be swamped by noise, but Fourier transformation reveals the entire interferogram to contain modulated spectral information.

for each interferogram so that all scans can be properly aligned for processing even if there is some offset in the position of the stage between scans.

For diagnostic purposes (and because the fractional position of the WLF differs in the two directions), scans in the two directions of mirror motion are aligned and processed separately.

4.3. Rejection of Bad Scans

4.3.1 Cosmic Rays

At the high altitude of Mauna Kea, cosmic ray strikes on the detector are a relatively common occurrence. One cosmic ray hit is generally seen every 5-10 minutes, making its presence known in the form of a 0.1-0.2 V spike in an interferogram. The observed spikes are a few sample points wide, corresponding to the *RC* falloff time of the bolometer preamp. An example of a cosmic ray hit in the middle of an interferogram is shown in Figure 4.1.

It is important to remove cosmic ray spikes from interferograms before Fourier transforming. Otherwise, since the Fourier transform of a delta function is a sine wave, the spikes will appear in spectra as high frequency ripples with periods determined by the positions of the spikes within the individual interferograms. An algorithm for automatically detecting and removing cosmic ray spike is currently used to filter them out. However, because cosmic ray spikes appearing near the WLF often pass undetected, all interferogram are also examined visually, and any scans containing undetected cosmic ray spikes are flagged and omitted from subsequent processing.

4.3.2 Spurious Trigger Pulses

Extra trigger pulses are sometimes generated by the optical encoder during motion of the translation stage. These spurious pulses offset an entire portion of an interferogram beyond the position of the extra pulse, as illustrated in Fig. 4.2. Spurious pulses are most likely caused by slight vibrations of the translation stage which, on rare occasions (no more often than $\sim$ once an hour), cause it to backtrack just enough in order to pass over a previous ruling on the optical encoder and generate an additional pulse. Alternatively, spurious pulses could also be caused by electrical pickup from the noisy telescope environment. Although the recurrence rate of spurious pulses seems to vary as a function of translation stage speed, it is not uncommon for entire nights to pass without the occurrence of a single spurious pulse. Because of the relative rarity of spurious trigger pulses, we have not yet been able to completely diagnose and fix the problem in hardware.

As a result, interferograms which are offset by extra pulses must be identified and excluded (or fixed) before Fourier transformation in order to avoid contamination. For interferograms with an extra pulse near the WLF, the consequences of accidentally including this data in computing an average spectrum could be particularly undesirable. Fortunately, shifted interferograms can be identified easily by

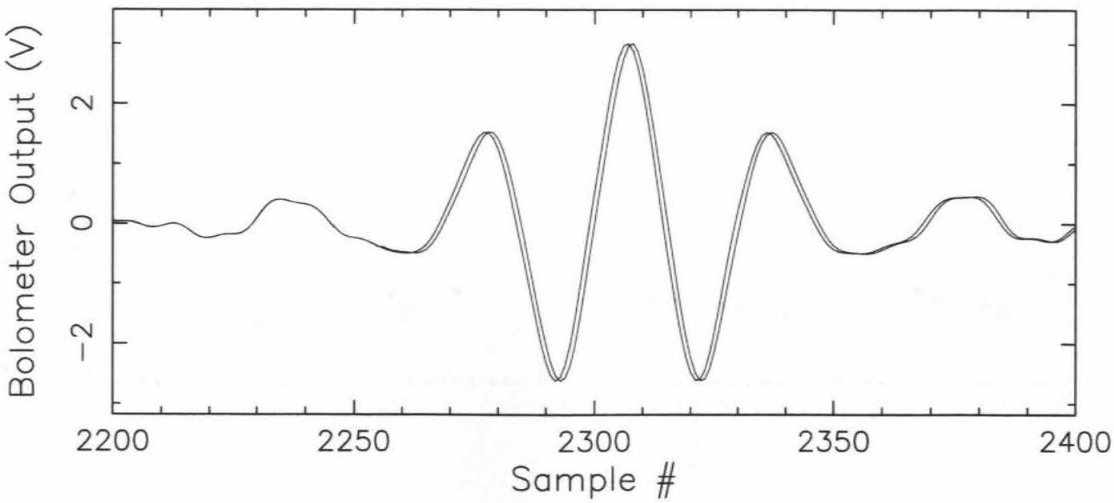

Figure 4.2. One of the two interferograms in this plot contains a spurious trigger pulse which shifts it by one sample point beginning near sample number 2255. Scans so affected must be eliminated before Fourier transformation since their fringes are not correctly modulated.

comparison with a "template" interferogram which must, of course, itself be free of spurious triggers. By aligning two interferograms using the recorded reference position and taking the sum of square differences between points, bad scans stand out prominently due to their anomalously large RMS residuals. A plot of the residuals for several hours worth of data is shown in Fig. 4.3. In the plot, the bad scan shown in Fig. 4.2 is immediately evident.

In addition to providing a mechanism for detecting shifted interferograms, comparison using a template also provides a means for monitoring sky variations. This is possible because the increased noise in interferograms accompanying changing atmospheric transmission appears as a secular increase in RMS deviation as a function of time. In fact, on nights when transmission was known to degrade and then later improve, a corresponding rise and fall of the interferogram RMSes compared to a template interferogram is seen clearly (Serabyn and Weisstein 1996).

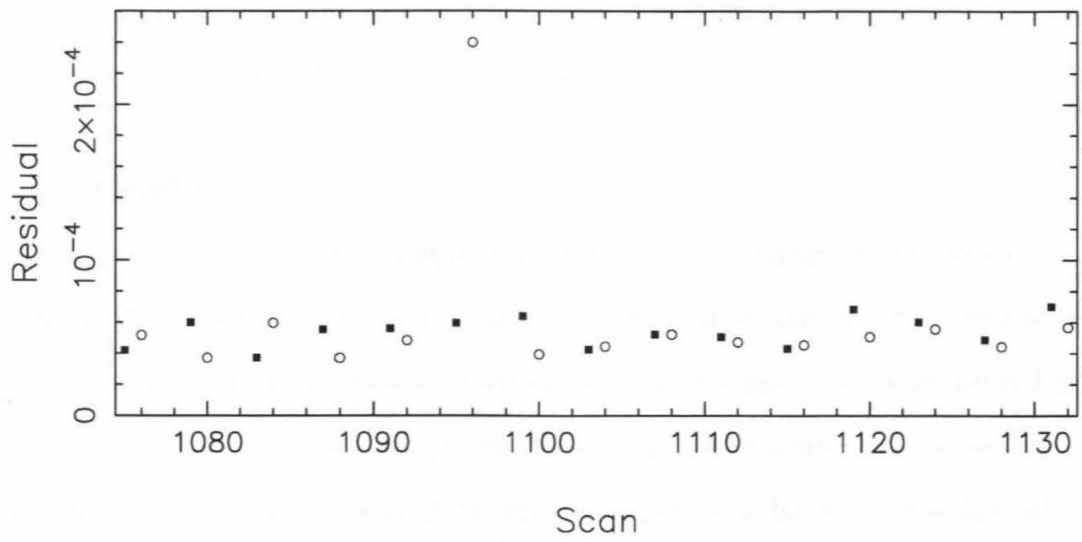

Figure 4.3. Comparison of the RMS residuals obtained by comparing a sequence of scans with a "template" scan. Downward-going scans (odd-numbered) are shown as solid squares (▪) and upward-going (even-numbered) scans are shown as outlined circles (o). Scan 1096, the scan with a spurious trigger pulse shown in Fig. 4.2, stands out clearly due to its anomalously large RMS residual.

4.4. Dechirping

The presence of phase errors between the two arms of an FTS can result in asymmetric two-sided interferograms. Instrumental misalignment is the simplest source, but other instrumental effects (such as frequency-dependent phase shifts in data recording equipment or dispersion in the beamsplitter) can also produce phase errors (Schnopper and Thompson 1974). An asymmetric interferogram resulting from frequency dependent phase errors is said to be "chirped." Loewenstein (1963), Forman *et al.* (1966), Mertz (1967), Sakai *et al.* (1968), and Schnopper and Thompson (1974) have all considered methods of "dechirping" such interferograms. The simplest approach is to use a short two-sided portion of a scan to determine the phase dependence on frequency at low resolution, then use this information to correct the high resolution one-sided interferogram (after Fourier transforming). The `FTSPEC` program can implement dechirping, but the high quality of the interferograms obtained with our FTS combined with the unimportance of dispersion in the mylar beamsplitter

renders this procedure unnecessary. Observed interferograms are almost completely symmetrical without any additional processing.

4.5. Apodization

Apodization, sometimes also called tapering, is a mathematical technique used to reduce the Gibbs phenomenon "ringing" which is produced in a spectrum obtained from a truncated interferogram. Since interferograms can only be measured out to some finite distance, all laboratory interferograms are truncated. As shown by (3.8), the observed spectrum is related to the true spectrum by a convolution with the "instrument function" (or "apparatus function") obtained by Fourier transforming the apodization function. The instrument function corresponding to the simplest apodization—the rectangle function produced by a finite-length interferogram—is a sinc function. Because of the large sidelobes of this function, it is sometimes desirable to multiply the original interferogram by some other function which goes smoothly to zero at the end of the interferogram (e.g., Schnopper and Thompson 1974). Table II lists the most commonly used apodization functions and their transforms, both of which are plotted in Fig. 4.4.

While apodization suppresses sidelobes, it also results in a broadening of spectral features (Thompson *et al.* 1991, p. 239). Table III lists the widths, peak, and peak sidelobes of the apodization functions in Table II. For a given application, these two factors must be balanced when selecting an appropriate apodization function. Spectra obtained with the CSO FTS have been processed using a variety of apodization functions. For planetary interferograms, apodization made no discernible difference. This is true because the broad width of planetary features smears out the ringing of the instrument functions, averaging out their effect. Furthermore, because the signal levels in our interferograms are very weak near the maximum optical path difference, the interferograms are effectively "self-apodized" by noise, making additional

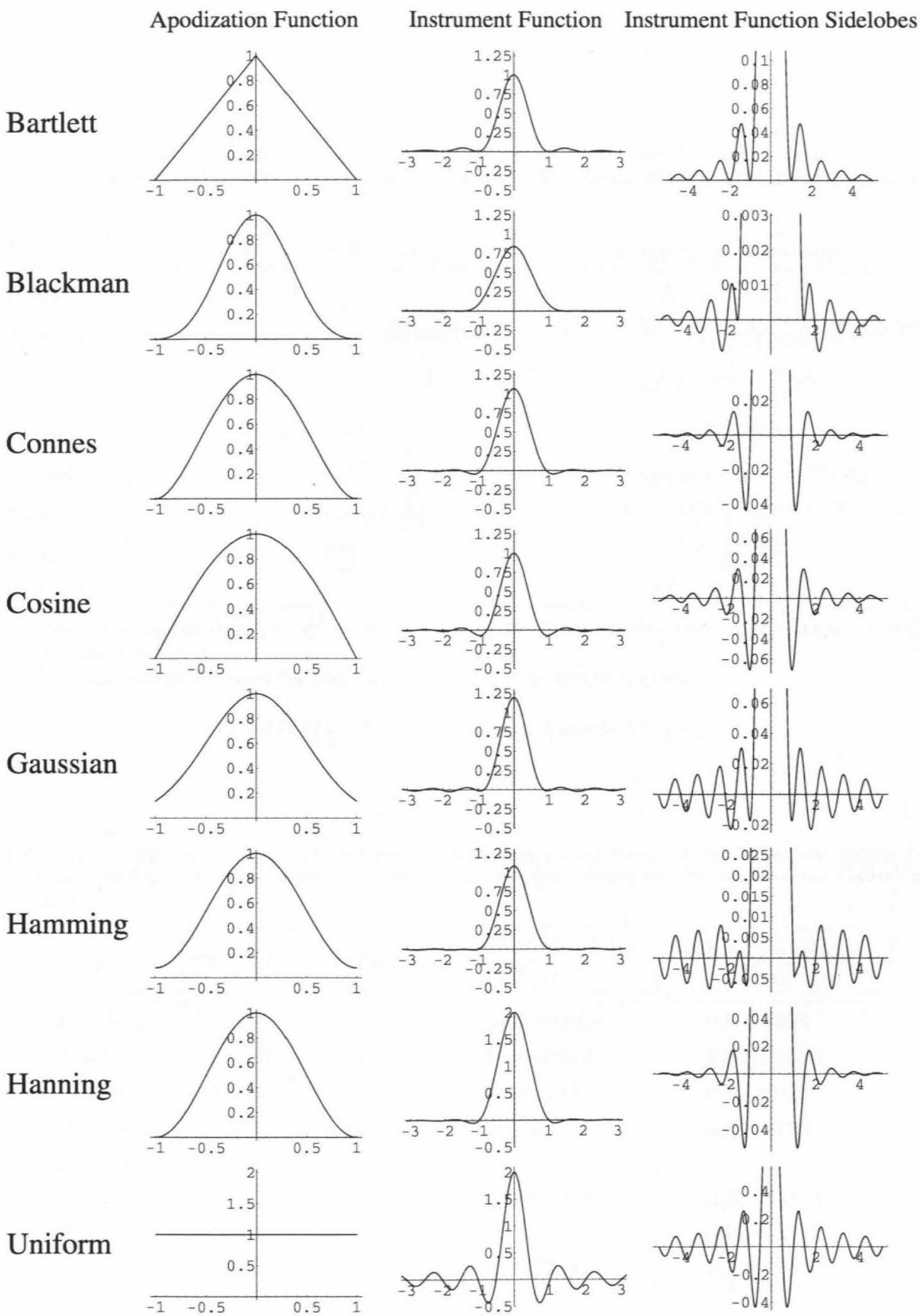

Figure 4.4. Apodization functions, their instrument functions, and blowups of the first few sidelobes.

Table II. Various commonly used apodization functions and their corresponding instrument functions as illustrated in Fig. 4.4. L is the length of the one-sided portion of an interferogram (in sample numbers).

Type	Apodization Function	Instrument Function
Bartlett	$1 - \frac{\lvert x\rvert}{L}$	$L\,\mathrm{sinc}^2(\pi kL)$
Blackman	$0.42 + 0.5\cos\left(\frac{\pi x}{L}\right) + 0.08\cos\left(\frac{2\pi x}{L}\right)$	$\frac{L(0.84-0.36L^2k^2-2.17\times10^{-19}L^4k^4)\,\mathrm{sinc}(2\pi Lk)}{(1-L^2k^2)(1-4L^2k^2)}$
Connes	$\left(1-\frac{x^2}{L^2}\right)^2$	$8L\sqrt{2\pi}\,\frac{J_{5/2}(2\pi kL)}{(2\pi kL)^{5/2}}$
Cosine	$\cos\left(\frac{\pi x}{2L}\right)$	$\frac{4L\cos(2\pi Lk)}{\pi(1-16L^2k^2)}$
Gaussian*	$e^{-x^2/(2\sigma^2)}$	$2\int_0^L \cos(2\pi kx)e^{-x^2/(2\sigma^2)}\,dx$
Hamming	$0.54 + 0.46\cos\left(\frac{\pi x}{L}\right)$	$\frac{L(1.08-0.64L^2k^2)\,\mathrm{sinc}(2\pi Lk)}{1-4L^2k^2}$
Hanning†	$\cos^2\left(\frac{\pi x}{2L}\right)$	$\frac{L\,\mathrm{sinc}\,(2\pi Lk)}{1-4L^2k^2}$
Uniform	1	$2L\,\mathrm{sinc}\,(2\pi kL)$

*For Gaussian apodization, σ^2 is the variance of the Gaussian function, which can be chosen independently of L.

†The instrument function for Hanning apodization can also be written

$$a[\mathrm{sinc}(2\pi kL) + \tfrac{1}{2}\,\mathrm{sinc}(2\pi kL - \pi) + \tfrac{1}{2}\,\mathrm{sinc}(2\pi kL + \pi)].$$

Table III. Width, peak value, and peak positive and negative sidelobes for the instrument functions illustrated in Fig. 4.4. The values for Gaussian apodization depend on the choice of the Gaussian variance σ^2.

Type	FWHM	PSF Peak	$\frac{\text{Peak }(-)\text{ Sidelobe}}{\text{Peak}}$	$\frac{\text{Peak }(+)\text{ Sidelobe}}{\text{Peak}}$
Bartlett	1.77179	1	0.00000000	0.0471904
Blackman	2.29880	0.84	−0.00106724	0.00124325
Connes	1.90416	$\frac{16}{15}$	−0.0411049	0.0128926
Cosine	1.63941	$\frac{4}{\pi}$	−0.0708048	0.0292720
Gaussian	—	1	—	—
Hamming	1.81522	1.08	−0.00689132	0.00734934
Hanning	2.00000	1	−0.0267076	0.00843441
Uniform	1.20671	2	−0.217234	0.128375

apodization unnecessary. Even for fairly narrow lines such as those in the Orion Molecular Cloud core (Serabyn and Weisstein 1995), only a single sidelobe of ringing was evident for the strongest CO lines. In this case, the desire for the highest possible resolution precluded the use of apodization.

4.6. Scan Weighting

Over the course of an observing run, there are a number of time-varying factors which affect the quality of the data. In addition to changing airmass, the atmospheric opacity, ground-level humidity, and ground temperature all change over the course of a night. These factors are monitored by CSO meteorological instruments, and their values are stored to the header of each interferogram. As a result, scans taken under more favorable conditions can be given a higher weighting in the final processing. Since the quality of planetary spectra should, to first order, be proportional to atmospheric transmission at the time of their observation, the weighting

$$w(\tau_0, \mathrm{AM}) \propto e^{-\tau_0/\mu} = e^{-\tau_0 \cdot \mathrm{AM}}, \tag{4.12}$$

where τ_0 is the zenith atmospheric optical depth at 225 GHz as measured by the on-site water vapor radiometer, μ is the cosine of the emission angle, and AM is the airmass, is usually used. In practice, τ_0 should really be scaled to the relevant frequency of observations. However, on good nights during which conditions do not change very much, uniform weighting gives indistinguishable final spectra. Some care is also required on nights when the CSO tipping radiometer is acting up, a not uncommon occurrence. Under circumstances understood only by the radiometer, it is quite capable of producing a time series for tau which is punctuated by abrupt (and spurious) spikes.

4.7. Shifting and Transforming

The recording of a reference pulse allows alignment of interferograms according

to their absolute position on the translation stage. However, the position of the WLF is really what is required for proper scan alignment. Knowledge of the WLF position is also needed to determine the zero point for Fourier transformation. In order to find the offset between the WLF and reference pulse position, we intersperse measurements of planetary sources with scans on an ambient temperature (or "hot") reference blackbody. Because the hot load shows a strong and easily identifiable WLF (whereas interferograms of weak astronomical source might not), the position of the WLF relative to the reference pulse can be found for the reference scans, and then this offset applied to the remainder of the scans. Because phase delays in the amplifier circuitry give different reference–WLF offsets in the two directions of mirror motion, the offsets must be determined separately for the two directions.

Frequent measurement of reference scans also allows the monitoring of secular shifts which occur in the position of the WLF during the course of observations. Such shifts can be produced by thermal expansion/contraction or by instrumental flexure as a function of zenith angle, and are generally fairly small in size (~ 0.3 of a sample channel, or ~ 12 μm of OPD over an entire night). However, Fourier transformation of interferograms using an incorrectly positioned WLF introduces a phase shift $e^{i\Delta\phi}$ which produces step-function-like behavior in the spectral baselines (they are pulled low on one side of the passband and pushed high on the other). This phenomenon is highly undesirable for measurements requiring accurate continuum levels, especially for weak sources such as Uranus and Neptune. The reference scans can therefore be used to fit a smooth function through the WLF offsets over the course of the night (with the scan number, zenith angle, or other observing parameter as the free variable), which can then be used to interpolate the measured WLF offsets to the non-reference scans.

In order to apply the above procedure, it is necessary to either (1) Fourier

transform each pair of on–off scans separately and then apply the instantaneous $e^{i\phi_n}$ phase shift derived from the reference scans, or (2) interpolate and shift the interferograms to a common WLF position (again using the fit to the reference scans), do the on–off subtraction, and then perform a single transform with no phase shift. The latter approach is less robust since the large OPD portion of the interferogram is noisy and cannot easily be interpolated (although the strong central few fringes can). It is also much more time consuming (at least in its current implementation), since a direct 20,000 point polynomial interpolation is considerably slower than a fast Fourier transform. A third approach is to use the reference scans to compute the *average* reference–WLF difference for an entire set of scans, co-add interferograms in position space using the integer part of the average reference–WLF difference to determine alignment, Fourier transform, then use the fractional part of the average WLF for phase shifting by $e^{i\langle\phi\rangle}$.

For large data sets, this latter approach is many times faster than the previous two methods since no interpolation of interferograms is used and only one Fourier transform need be computed for the entire set of "on" and "off" scans in a given direction. Processing in position space also allows the on–off difference interferograms to be directly examined, giving a good indication of the quality of the data before it is even transformed. In practice, all three of these techniques are found to give nearly identical results. The position space approach is therefore used while observing at the telescope in order to allow rapid on-line processing of data as it is acquired, and the frequency space approach is used off-line for the final processing of the data.

Chapter 5

Radiative Transfer Modeling

"Remote from human passions, remote even from the pitiful facts of nature, the generations have gradually created an ordered cosmos, where pure thought can dwell as in its natural home and where one, at least, of our nobler impulses can escape from the dreary exile of the actual world."

—Bertrand Russell

"When they come to model Heaven
And calculate the stars, how they will wield
The mighty frame, how build, unbuild, contrive
To save appearances, how grid the sphere
With centric and eccentric scribbled o'er
Cycle and epicycle, orb in orb."

—John Milton *(Paradise Lost)*

All radiative transfer modeling is ultimately based on the fundamental equation of radiative transfer, which relates the change in radiation intensity I_ν along a ray path to local absorption k_ν and volume emission j_ν,

$$\frac{1}{k_\nu}\frac{dI_\nu}{ds} = -I_\nu + \frac{j_\nu}{k_\nu}. \tag{5.1}$$

For a nonscattering atmosphere in local thermodynamical equilibrium, j_ν/k_ν equals the Planck function B_ν at the local temperature T. The solution to (5.1) is then given by

$$I_\nu(s_0) = I_\nu(0)e^{-\int_0^{s_0} k_\nu(s)\,ds} + \int_0^{s_0} k_\nu(s)B_\nu(T(s))e^{-\int_s^{s_0} k_\nu(s')\,ds'}\,ds \tag{5.2}$$

(Chandrasekhar 1960), where s_0 is the optical path above the surface and $I_\nu(0)$ is the surface brightness. For observations of emission from planetary atmospheres, the integration is instead begun at the top of the atmosphere and continued downward until either the surface or some very large optical depth is reached. In the latter case, the "surface emission" term can be neglected.

For numerical evaluation of the absorption due to multiple absorbers in a real

atmosphere divided into N layers, it is useful to rewrite (5.2) in a discretized form,

$$I_\nu = \sum_{i=1}^{N} B_\nu(T_i)(1 - e^{-\Delta\tau_i/\mu_i})e^{-\sum_{j=1}^{i}(\Delta\tau_j/\mu_j)}, \tag{5.3}$$

where T_i is the temperature of layer i,

$$\Delta\tau_i \equiv \int k_\nu(p)\frac{dz}{dp}\,dp \tag{5.4}$$

is the total optical depth in layer i, $k_\nu(p)$ is the absorption coefficient at pressure level p due to all contributing species (with units of cm^{-1}), and

$$\mu \equiv \cos\theta = \frac{dz}{ds} \tag{5.5}$$

is the cosine of the emission angle θ (the angle between the local vertical and the line-of-sight).

In our atmospheric model, the opacity is computed starting at some top pressure level. The equations of radiative transfer are then applied to find the contribution to the brightness temperature and optical depth from this level. Calculation then proceeds to the next pressure level, and so on, until a specified (large) optical depth is reached. The atmospheric levels are treated as locally spherical for the purposes of the radiative transfer model (since spheroidal layers become geometrically unmanageable for oblique ray paths), but a full Darwin-de Sitter spheroid formalism (Zharkov and Trubitsyn 1978) is used for calculating the net gravitational acceleration at each layer. In order to compute μ, the planetocentric latitude is converted to planetographic latitude as in de Pater and Massie (1985).

It is often useful to view (5.3) as a sum of contributions of various atmospheric layers to the total radiation emitted at the top. This can be done by defining the so-called weighting function (Clancy and Muhleman 1994) by

$$W_i \equiv (1 - e^{-\Delta\tau_i/\mu_i})e^{-\sum_{j=1}^{i}(\Delta\tau_j/\mu_j)}. \tag{5.6}$$

Then (5.3) can be written in the particularly simple form

$$I_\nu = \sum_{i=1}^{N} W_i B_\nu(T_i), \tag{5.7}$$

and a plot of W_i versus altitude immediately shows the atmospheric levels from which the majority of the observed flux originates.

In order to calculate the radiation emitted by an atmosphere, it is necessary to specify the temperature and compositional structure as a function of altitude. For the jovian planets, the temperature profiles are well known from both radio occultation and infrared emission measurements. Unfortunately, because not much is known about the deep cloud-forming regions of the jovian planets, compositional effects involving condensation and chemical equilibria between species must be analyzed using models. The opacity of the constituent species as a function of frequency must also be known, which requires extensive laboratory measurements to determine these species' behavior as a function of temperature and pressure in an atmosphere containing various other components. For the jovian planets, such measurements can involve inconveniently high pressures or low temperatures, as well as dangerous chemicals (such as explosive H_2 and neurotoxic PH_3). And while many experiments have been performed in order to provide atmospheric modelers with accurate opacities, there are still major uncertainties in such important areas as the NH_3 inversion and rotation lineshapes and the low-temperature saturation vapor pressure curves for minor constituents such as HCN and PH_3.

The radiative transfer model used to calculate the synthetic spectra with which we interpret our millimeter-submillimeter spectra is based on the code of A. Grossman (Grossman *et al.* 1989, Grossman 1990), which in turn is a synthesis of the classic review paper of Berge and Gulkis (1976) and previous modeling work by Atreya and Romani (1985) and de Pater and Massie (1985). Model spectra of the jovian planets containing a range of mole fractions for a variety of molecules have been previously

generated by Encrenaz and Combes (1977), Lellouch *et al.* (1984), Bézard *et al.* (1986), and Encrenaz *et al.* (1995).

5.1. Pressure-Temperature Profiles

The pressure-temperature profiles used in this model are the radio occultation results summarized in Lindal (1992). For Neptune, however, we use the profile of Gautier *et al.* (1995) instead of that of Lindal (1992), resulting in slightly cooler temperatures. A summary of the extant jovian radio occultation profiles, together with profiles obtained for the lower stratospheres and upper tropospheres of Jupiter, Saturn, and Neptune from infrared measurements (Orton *et al.* 1992, Courtin *et al.* 1984, Gautier *et al.* 1995) is given in Table IV. For pressures greater than those probed by the radio occultation measurements, temperatures were adiabatically extrapolated downward to several tens of bars (Fig. 5.1). A wet adiabat including condensation of CH_4, NH_3, H_2S, and H_2O was used for the extrapolation (Atreya and Romani 1985, Briggs and Sackett 1989), where the formalisms used to compute latent heats and treat chemical equilibrium between H_2S and NH_3 were adopted from Grossman (1990). In order to ensure that the opacity remained reasonably small in each layer, the pressure-temperature profiles were interpolated to small logarithmically spaced layers in pressure.

Table IV. Summary table of extant measurements of the temperature profile as a function of pressure for the jovian planets.

Planet	$p_{\max}$ (bar)	Source	Latitude	Reference
Jupiter	1000	Voyager 1 egress	0°	Lindal *et al.* 1981, Lindal 1992
	977	Thermal IR emission	9 – 15° N	Orton *et al.* 1992 (quoted in Marten *et al.* 1994)
Saturn	1298	Voyager 2 ingress	36.3° N	Lindal *et al.* 1985, Lindal 1992
	1000	Thermal IR emission	36.5° N	Courtin 1984
Uranus	2309	Voyager 2 ingress	2 – 6° S	Lindal *et al.* 1987, Lindal 1992
Neptune	6268	Voyager 2 ingress	59 – 62° N	Lindal 1992
	~ 6000	Thermal IR emission	?	Gautier *et al.* 1995

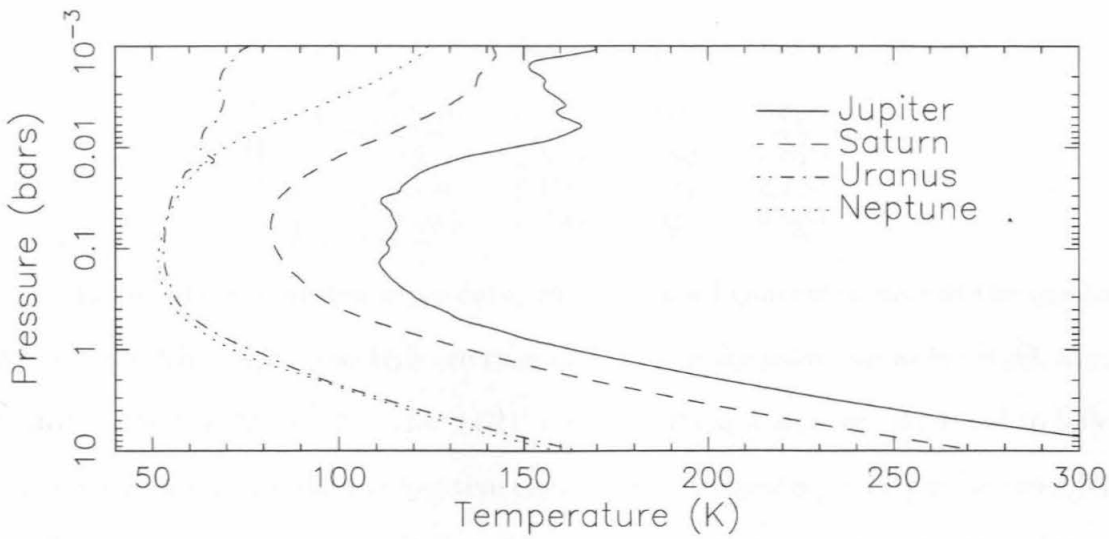

Figure 5.1. Pressure-temperature profiles obtained from the Voyager radio occultation experiment.

The heat capacity of H_2 gas depends on its *ortho* to *para* ratio (Massie and Hunten 1982, Gierasch 1983, Conrath and Gierasch 1984, Baines *et al.* 1995, Smith and Gierasch 1995), with the most significant difference occurring at temperatures $\lesssim$ 250 K. Grossman (1990, p. 87) plots the heat capacity of H_2 for the so-called intermediate-frozen, equilibrium, normal, *para,* and *ortho* cases. In our model, we adopt the "frozen" value for the heat capacity of hydrogen for all the jovian planets. The specific heats of He, CH_4, H_2O, NH_3, and H_2S used in the adiabatic extrapolation are taken from Grossman (1990).

5.2. Composition

Table V summarizes the composition of the major species H_2, He, and CH_4 used in the model. For Jupiter, the values were obtained by rescaling the least-squares fits from various observations given by Fegley (1994) to obtain a sum of unity. Mole fractions in Saturn represent the best values obtained by Voyager IRIS measurements (Conrath *et al.* 1984, Courtin *et al.* 1984). Data for Uranus are taken from Lindal *et al.* (1987) and data for Neptune from Lindal (1992).

Table V. Major atmospheric constituents for the jovian planets used in the radiative transfer model.

Species	Jupiter	Saturn	Uranus	Neptune
H_2	0.897	0.963	0.850	0.810
He	0.100	0.030	0.127	0.170
CH_4	0.003	0.004	0.023	0.020

In the absence of definitive data, the sub-cloud concentrations of the condensible species NH_3, H_2O, and H_2S are taken to assume the solar values for N, O, and S of 1.676×10^{-4}, 1.328×10^{-3}, and 3.621×10^{-5}. NH_3 and H_2O are assumed to follow a saturation law above their respective clouds, the chemical equilibrium between NH_3 and H_2S is used to obtain the H_2S saturation law, and all species other than H_2 and He are assumed to be cutoff above the tropopause.

In addition to the species listed above, a great many disequilibrium species have been detected in the jovian planets, primarily using infrared spectroscopy. CO, PH_3, GeH_4, and AsH_3 have all been detected in Jupiter and Saturn (e.g., Larson *et al.* 1977, Bjoraker *et al.* 1986, Noll *et al.* 1986, Noll *et al.* 1988, Noll *et al.* 1989, Noll and Larson 1990). In addition, PH_3 has been detected in the millimeter-submillimeter in both Jupiter and Saturn (Weisstein and Serabyn 1994, Weisstein *et al.* 1996) and HCl (and possibly HCN) has been tentatively identified in Saturn (Weisstein and Serabyn 1996; see Chapter 7). In the following, the concentrations of minor species considered in various models are discussed on an individual basis.

5.3. Opacity Sources

The opacity sources included in this model are emission from H_2 dipoles induced by H_2-H_2, H_2-He, and H_2-CH_4 collisions, the band of NH_3 inversion lines centered at centimeter wavelengths, the three NH_3 rotational lines at 572.4, 1168.5, and 1215.2 GHz, and the strong PH_3 rotational lines with frequencies less than 1200 GHz. In addition, opacity due to the species CO, H_2O, H_2S, HBr, HCl, HCN, HCP, LiH,

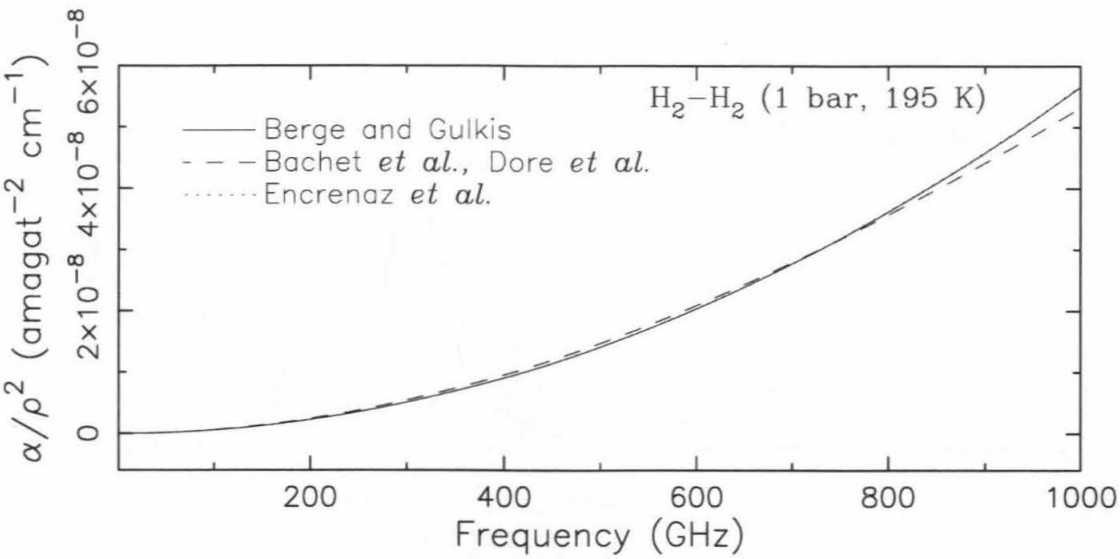

Figure 5.2. Comparison of H_2-H_2 formalisms. Predicted absorption coefficients are virtually identical, except for a small discrepancy for frequencies greater than 800 GHz.

NaH is included in the code.

5.3.1 H_2-H_2

The opacity contributed by spontaneous dipole formation induced by the collisions of H_2-He and H_2-H_2 can parameterized using the empirical formalism of Goodman (1969) as discussed in Berge and Gulkis (1976). Goodman's equation extrapolates the values computed by Trafton (1965) and gives opacity as a function of temperature and H_2 and He partial pressures. A similar, slightly simpler empirical formalism is used by Encrenaz *et al.* (1995). However, in our model, we use instead the quantum mechanically derived (but still requiring insertion of an empirical intensity function) formulas of Bachet *et al.* (1983) and Dore *et al.* (1983), as summarized in Hofstadter (1992). As can be seen in Fig. 5.2, a comparison of all three formalisms reveals them to be virtually identical in the entire sub-THz band. A fourth formalism derived by Meyer *et al.* (1989) is not considered here.

Fig. 5.3 plots the H_2-H_2 absorption coefficient calculated using the formalism of Bachet *et al.* (1983) for temperatures of 77, 195, and 297 K.

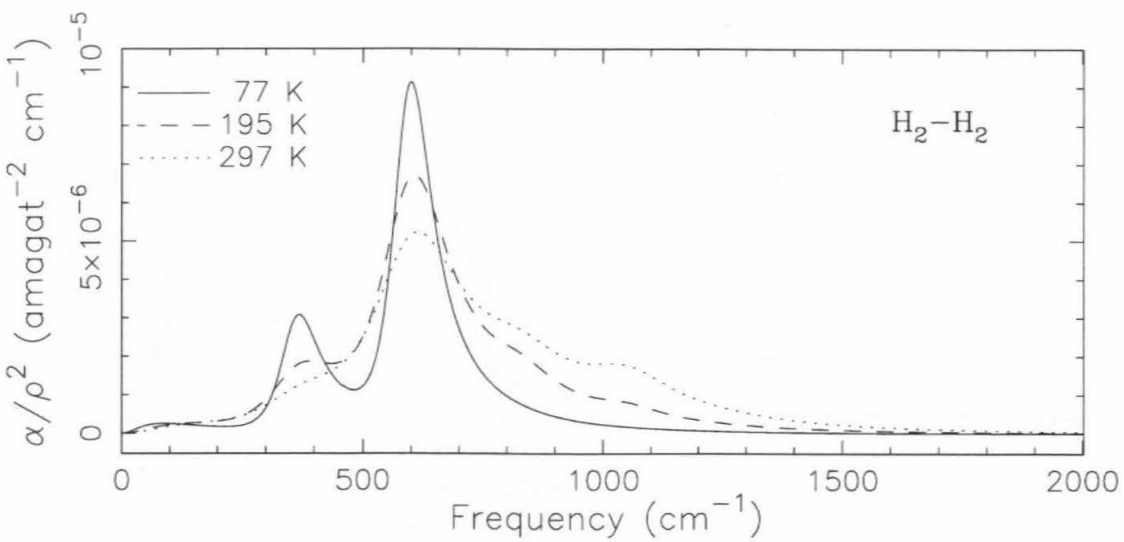

Figure 5.3. H_2-H_2 absorption calculated using the formalism of Bachet *et al.* (1983).

5.3.2 H_2-He

Berge and Gulkis (1976) and Encrenaz *et al.* (1995) use empirical expressions to calculate absorption due to He-H_2 collisions as well as H_2-H_2 collisions. In this work however, we follow Hofstadter (1992) in using instead the quantum mechanically derived expressions of Birnbaum and Cohen (1976) and Cohen *et al.* (1982). An alternative formalism due to Borysow *et al.* (1988) is not considered here. Fig. 5.4 plots the absorption coefficient calculated using the formalism of Cohen *et al.* (1982) for temperatures of 77, 195, and 297 K.

5.3.3 H_2-CH_4

Formalisms for the opacity contributed by spontaneous dipole formation induced by the collisions of H_2-CH_4 (which is especially important in Uranus and Neptune) have been developed by Orton *et al.* (1983) and Borysow and Frommhold (1986, 1987). We again follow Hofstadter (1992), utilizing the formalism of Orton *et al.* (1983). Fig. 5.5 plots the absorption coefficient calculated using this formalism for temperatures of 77, 195, and 297 K.

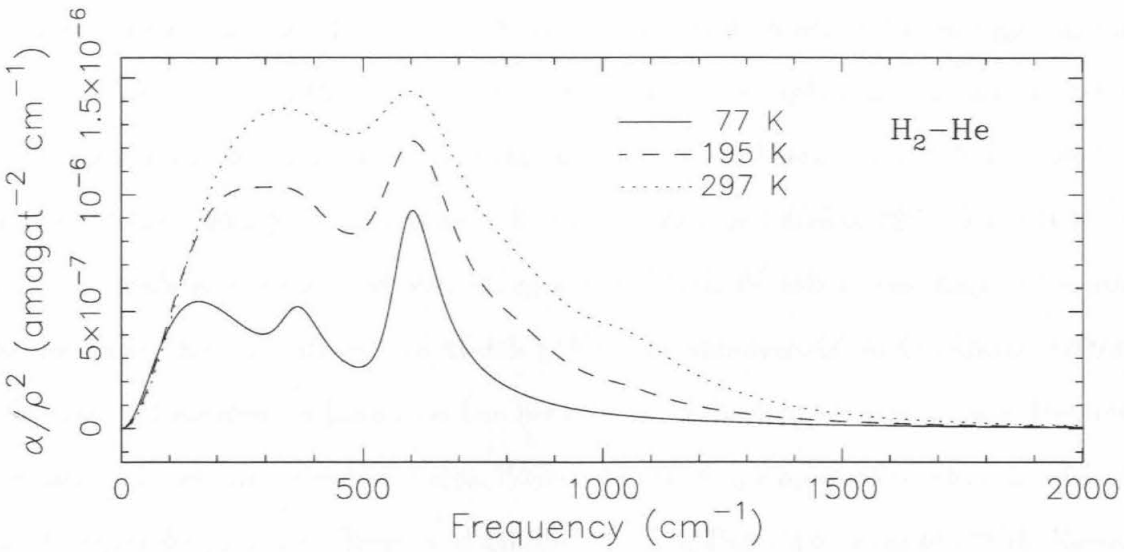

Figure 5.4. H_2-He absorption calculated using the formalism of Cohen *et al.* (1982).

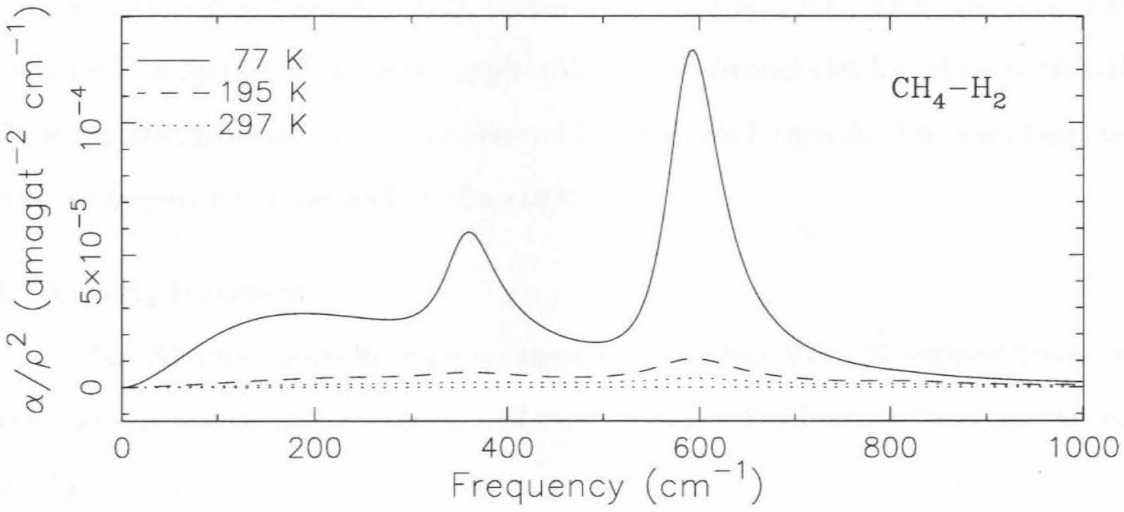

Figure 5.5. H_2-CH_4 absorption calculated using the formalism of Orton *et al.* (1983).

5.3.4 NH_3 Inversion

The NH_3 molecule resembles a triangular-base pyramid, with the three hydrogen atoms at the corners of the base and the nitrogen atom at the apex. However, quantum mechanical tunnelling of the nitrogen atom allows it to pass through the pyramid base to the other side, overcoming the potential barrier which should prevent

such a feat (Townes and Schawlow 1975). A transition in which the nitrogen atoms flips the orientation of the pyramid is distinct from a simple rotation, and is called an inversion transition since it "inverts" the pyramid. There are 119 NH_3 inversion lines with wavelengths longer than 1.3 cm (Poynter and Kakar 1975, Pickett *et al.* 1992), and these are summed over using a Van Vleck-Weisskopf lineshape according to the formalism of Wrixon and Welch (1970), as summarized in Grossman (1990). Although a Ben-Reuven lineshape has been found to best-fit observations at frequencies less than 30 GHz, the Van Vleck-Weisskopf line shape appears to provide a better fit at higher frequencies (Berge and Gulkis 1976, de Pater and Massie 1985). Recent measurements, however, indicate that both the Van Vleck-Weisskopf and Ben-Reuven lineshapes may provide an inadequate description of observations at centimeter and shorter wavelengths (Spilker 1993). Unfortunately, a new NH_3 lineshape formalism developed by Spilker is currently applicable only to frequencies less than $\sim$ 50 GHz (T. R. Spilker, pers. comm.). An alternate Ben-Reuven formalism, not used here, has been developed by Joiner and Steffes (1990).

5.3.5 NH_3 Rotation

The NH_3 rotational lines are assumed to have a Van Vleck-Weisskopf lineshape. The relevant functional form for each of these lines is taken from de Pater and Massie (1985).

5.3.6 PH_3

The pressure broadening coefficients for the $J = 1-0$ (266.945 GHz) rotational transition of PH_3 in He and H_2 are taken from the room temperature laboratory measurements of Pickett *et al.* (1981),

$$\Delta\nu = (4390 \text{ MHz/bar})p_{H_2} + (2240 \text{ MHz/bar})p_{He}. \tag{5.8}$$

Because the PH_3 molecule is a symmetric top, the $J = 3 - 2$ PH_3 line is a triplet

composed of $K = 0$, 1, and 2 levels. These three components are comparable in line strength and are separated by a total of $\sim$ 100 MHz (Pickett *et al.* 1992), a very small offset compared to the expected pressure-broadened line widths in jovian planets. Because laboratory measurements of the pressure broadening coefficient for the $J = 3 - 2$ triplet in hydrogen-helium atmospheres do not exist, our model uses the pressure broadening coefficients of the $J = 1 - 0$ transition measured by Pickett *et al.* (1981).

There are no published determinations of the temperature broadening exponent for any PH_3 rotational lines. The only extant laboratory measurements are for vibrational transitions at 1950-2150 cm^{-1} (Levy *et al.* 1994) which suggest $n = 0.73$. Because the temperature broadening exponent has not been measured, we adopted $n = 0.67$ for both $1 - 0$ and $3 - 2$ transitions—the same value as given by Berge and Gulkis (1976) for NH_3. We also adopt a Lorentzian lineshape for all PH_3 transitions.

5.3.7 H_2O

At millimeter-submillimeter wavelengths, radiation does not penetrate the atmospheres of the jovian atmospheres deeply enough to encounter water vapor or liquid H_2O. Even though H_2O opacity is unimportant for millimeter-submillimeter observations, it is implemented in the radiative transfer code in order to extend the model's applicability to centimeter wavelengths (where it can be compared with the models of Grossman 1990 and Hofstadter 1992). Three different H_2O formalisms, one proposed by Goodman (1969) (summarized in Berge and Gulkis 1976) and two proposed by Waters (1976), are implemented. Waters gives expressions valid at frequencies $\nu < 300$ GHz for the opacity due to the 10 strong H_2O transitions with frequencies < 450 GHz. He also gives an expression valid for frequencies $\nu < 100$ GHz which includes only the lowest frequency 22.235 GHz H_2O transition. These expressions have been found to agree with laboratory data for N_2/O_2 atmospheres and pressures

≤ 1 bar, but have not been tested for jovian atmospheres. Berge and Gulkis (1976), on the other hand, give a formalism explicitly valid for H_2-He atmospheres, but which includes only the 22 GHz H_2O line.

The opacity of suspended water droplets is also included in the model. An expression given by Liebe (1985) is used, where the dielectric constants (valid for frequencies $\nu < 300$ GHz) are taken from Chang and Wilheit (1979). These formulas are discussed in Grossman (1990).

5.3.8 Minor Species

The frequencies, line strengths, and energies for all minor species were taken from Pickett *et al.* (1992). They were all modeled with a Lorentzian line shape. Temperature exponents and widths, when available, were taken from a variety of sources.

5.4. Lineshapes

The millimeter and submillimeter continua of the giant planets are produced by the far wings of NH_3 inversion lines (Poynter and Kakar 1975), the fundamental NH_3 $J = 1 - 0$ rotational transition at 572 GHz and its first few overtones, the first few rotational transitions of PH_3, and transitions of collisionally induced dipoles in molecular hydrogen. These spectral lines are spread out by temperature and pressure broadening mechanisms. However, at the tropospheric levels probed by our observations, pressure broadening is far more important because of the high pressures and relatively low temperatures present there.

The simplest treatment of collisional broadening gives a Lorentzian lineshape, while more detailed treatments give complicated profiles such as the Ben-Reuven, Van Vleck-Weisskopf, and kinetic lineshapes. Although the more complicated lineshapes do not differ substantially from the Lorentzian near the line center, the discrepan-

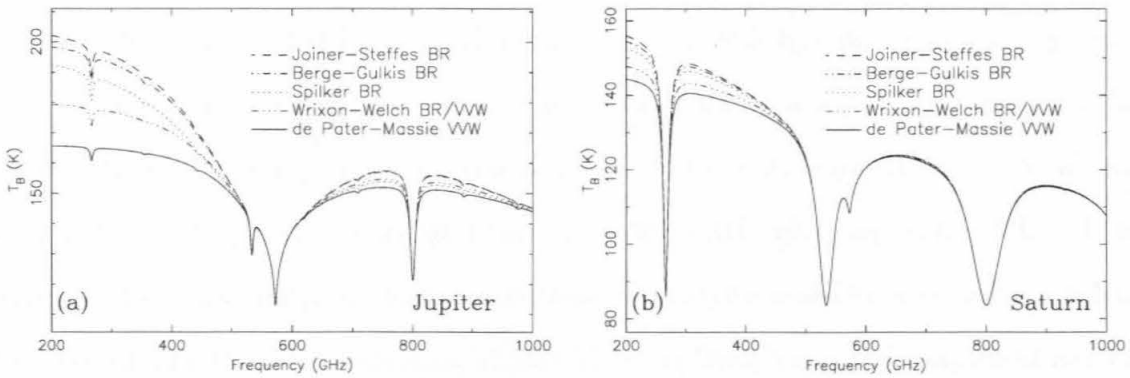

Figure 5.6. 1-D radiative transfer models for (a) Jupiter and (b) Saturn for various published NH_3 lineshape formalisms. BR stands for Ben-Reuven and VVW for Van Vleck-Weisskopf.

cies can be significant in the far linewings. As a result, in order to obtain the correct opacities at frequencies far from line center, the Ben-Reuven, Van Vleck-Weisskopf, or kinetic lineshape must usually be employed for species which have strong lines or are present high concentrations. Since the agreement (or lack thereof) between a given theoretical lineshape and the actual measured profile must be established empirically, the choice of the correct line broadening parameters rests on careful laboratory measurements under the appropriate ambient conditions of planetary atmospheres. Fig. 5.6 shows 1-D model spectra of Jupiter and Saturn for various NH_3 inversion lineshapes. At low frequencies, the deviation in the predicted brightness temperatures is quite large, emphasizing the importance of having accurate lineshape information.

5.4.1 Doppler Lineshape

Doppler line-broadening results from the random motion of radiating molecules, and is therefore dependent on temperature. The Doppler lineshape takes the form of a Gaussian,

$$\phi(\nu) = \frac{1}{\alpha_D}\sqrt{\frac{\ln 2}{\pi}}\, e^{-(\ln 2)(\nu-\nu_0)^2/{\alpha_D}^2}, \tag{5.9}$$

where the Doppler half-width is given by

$$\alpha_D \equiv \frac{\nu_0}{c}\sqrt{\frac{2\ln 2RT}{M}} = 1.131 \times 10^{-8}\sqrt{\frac{T}{M}}\,\nu_0 \tag{5.10}$$

(Townes and Schawlow 1975, pp. 337-338). In (5.10), R is the universal gas constant, T is the thermal temperature, M is the mean molar mass (in kg), and c is the speed of light. Plugging values appropriate for Jupiter's tropopause ($T \sim 120$ K and $M \sim 2.2 \times 10^{-3}$ kg) into (5.10) at 1 mm ($\nu = 300$ GHz) gives $\alpha_D = 0.8$ MHz. This value is very small compared to pressure broadening (discussed below) and much less than the maximum FTS resolution of 200 MHz, so Doppler broadening need not be considered in our models.

5.4.2 Voigt Lineshape

The Voigt profile is the spectral line shape which results from a superposition of independent Lorentzian and Doppler line broadening mechanisms (e.g., Armstrong 1967). It is given by the expression

$$\phi(\nu) = \frac{1}{\alpha_D}\sqrt{\frac{\ln 2}{\pi}}K(x,y), \tag{5.11}$$

where $K(x,y)$ is the "Voigt function"

$$K(x,y) \equiv \frac{y}{\pi}\int_{-\infty}^{\infty}\frac{e^{-t^2}}{y^2+(x-t)^2}\,dt. \tag{5.12}$$

In (5.12),

$$y \equiv \frac{\alpha_L}{\alpha_D}\sqrt{\ln 2} \tag{5.13}$$

is the ratio of Lorentz to Doppler widths and

$$x \equiv \frac{\nu-\nu_0}{\alpha_D}\sqrt{\ln 2} \tag{5.14}$$

is the frequency scale in units of Doppler half-width α_D.

Since Doppler broadening is negligible compared to pressure broadening for jovian tropospheric lines, consideration of a Voigt profile is also unnecessary for modeling of our spectra.

5.4.3 Lorentzian Lineshape

Pressure broadening results from collisions between molecules in a gas. It is the most important source of broadening when pressures are high. The simplest treatment of pressure broadening produces a Lorentzian lineshape centered at the transition frequency ν_0 and given by the functional form

$$\phi(\nu) = \frac{1}{\pi} \frac{\alpha_L}{(\nu - \nu_0)^2 + {\alpha_L}^2} \tag{5.15}$$

(Townes and Schawlow 1975, pp. 338-339), where α_L is the Lorentzian half-width. This simplest of all collisional lineshapes has the additional attractive property of being area-normalized to unity. While more complicated formalisms may be needed for species which are major atmospheric constituents, a Lorentzian is used in our model for the rotational lines of all species other than H_2, He, CH_4, and NH_3.

5.4.4 Ben-Reuven Lineshape

The quantum mechanical treatment of collisional broadening is formally similar to the effect of collisions on a classical oscillator. Considering changes in the amplitude, phase, orientation, and momentum of a classical oscillator upon collision, a very general function called the Ben-Reuven lineshape can be derived (Waters 1976). It is given by the expression

$$\phi(\nu) = \frac{2}{\pi} \left(\frac{\nu}{\nu_0} \right) \frac{(\gamma - \xi)\nu^2 + \gamma\xi[(\nu + \nu_0 + \delta)^2 + \gamma^2 - \xi^2]}{[(\nu_0 + \delta)^2 - \nu^2 + \gamma^2 - \xi^2]^2 + 4\nu^2\gamma^2}, \tag{5.16}$$

where γ, ξ (or ζ), and δ are the pressure-broadened line width, coupling element, and pressure shift terms (which, practically speaking, must be measured in the lab for a given gas). The Ben-Reuven lineshape has been used to describe NH_3 inversions (Wrixon and Welch 1970, Berge and Gulkis 1976, Joiner and Steffes 1990, Spilker 1993) and H_2S rotational lines (DeBoer and Steffes 1994), but is not used in our model. Under certain assumptions, the Ben-Reuven lineshape simplifies to the Van Vleck-Weisskopf or kinetic lineshape.

5.4.5 Van Vleck-Weisskopf Lineshape

The Van Vleck-Weisskopf lineshape (Van Vleck and Weisskopf 1945) is given by

$$\phi(\nu) = \frac{1}{\pi}\left(\frac{\nu}{\nu_0}\right)\left[\frac{\gamma}{(\nu-\nu_0)^2+\gamma^2} + \frac{\gamma}{(\nu+\nu_0)^2+\gamma^2}\right]. \tag{5.17}$$

It is a special form of the Ben-Reuven lineshape under the assumptions that there are no momentum-reversing collisions and that collision-induced phase shifts are random, in which case $\zeta = 0$ and $\delta = 0$ (Waters 1976). The Van Vleck-Weisskopf lineshape has been used to describe NH_3 inversion and rotational lines (Wrixon and Welch 1970, Wrixon *et al.* 1971, de Pater and Massie 1985), and is used for this purpose in our model.

5.4.6 Kinetic Lineshape

The kinetic lineshape (also called the Gross or Zhevakin-Naumov lineshape) is given by

$$\phi(\nu) = \frac{1}{\pi}\frac{4\nu\nu_0\gamma}{({\nu_0}^2-\nu^2)^2+4\nu^2\gamma^2}. \tag{5.18}$$

It is a special form of the Ben-Reuven lineshape under the assumption that only momentum reversing collisions take place, in which case $\gamma = \zeta$ and $\delta = 0$ (Waters 1976). The kinetic lineshape has been used for modeling H_2O lines in the Earth (Liebe 1981) and NH_3 lines in Jupiter and Saturn (Marten *et al.* 1980), but is not used in our model.

5.5. Pressure and Temperature Exponents

The width of a pressure-broadened spectral line depends on the temperature and pressure of the surrounding gas. The width is usually parameterized by the expression

$$\Delta\nu = (\Delta\nu)_0\left(\frac{p}{p_0}\right)^m\left(\frac{T_0}{T}\right)^n, \tag{5.19}$$

where $(\Delta\nu)_0$ is the width at some standard temperature T_0 and pressure p_0, m is the pressure broadening exponent (usually ~ 1) and n is the temperature broadening exponent (usually 0.5-1.0). Laboratory measurements of m and n (as well as $(\Delta\nu)_0$!) are spotty at best. m is often taken as 1 in the absence of information to the contrary, but published values of n are somewhat easier to come by for important molecules. $n = 0.5$ corresponds to "hard" collisions (Townes and Schawlow 1975, p. 368), and experimental temperature exponents for microwave transitions of molecules possessing typical intermolecular forces commonly lie in the range 0.7-1.0 (Waters 1976).

5.6. Condensation

At any given temperature, a certain amount of vapor exists in equilibrium with a liquid. The partial pressure of vapor existing in this equilibrium is called the saturation vapor pressure for a given substance. At colder temperatures, the saturation vapor pressure decreases, causing gaseous constituents to condense as liquid (or solid) aerosols. Condensation occurs whenever the partial pressure of a given substance exceeds the empirically determined saturation vapor pressure over the solid or liquid form of that substance. Atmospheric regions containing liquid aerosols are called clouds, and the deepest pressure level at which condensation can occur is called the cloud base. In regions of rapid convection, aerosols should be fully saturated, but subsaturated cloud with relative humidities less than 100% and supersaturated clouds with humidities greater than 100% are also possible. Table VI gives the pressure levels of jovian planet cloud bases under the assumptions of solar N, O, and S mole fractions, using the saturation vapor pressure curves plotted in Fig. 5.7.

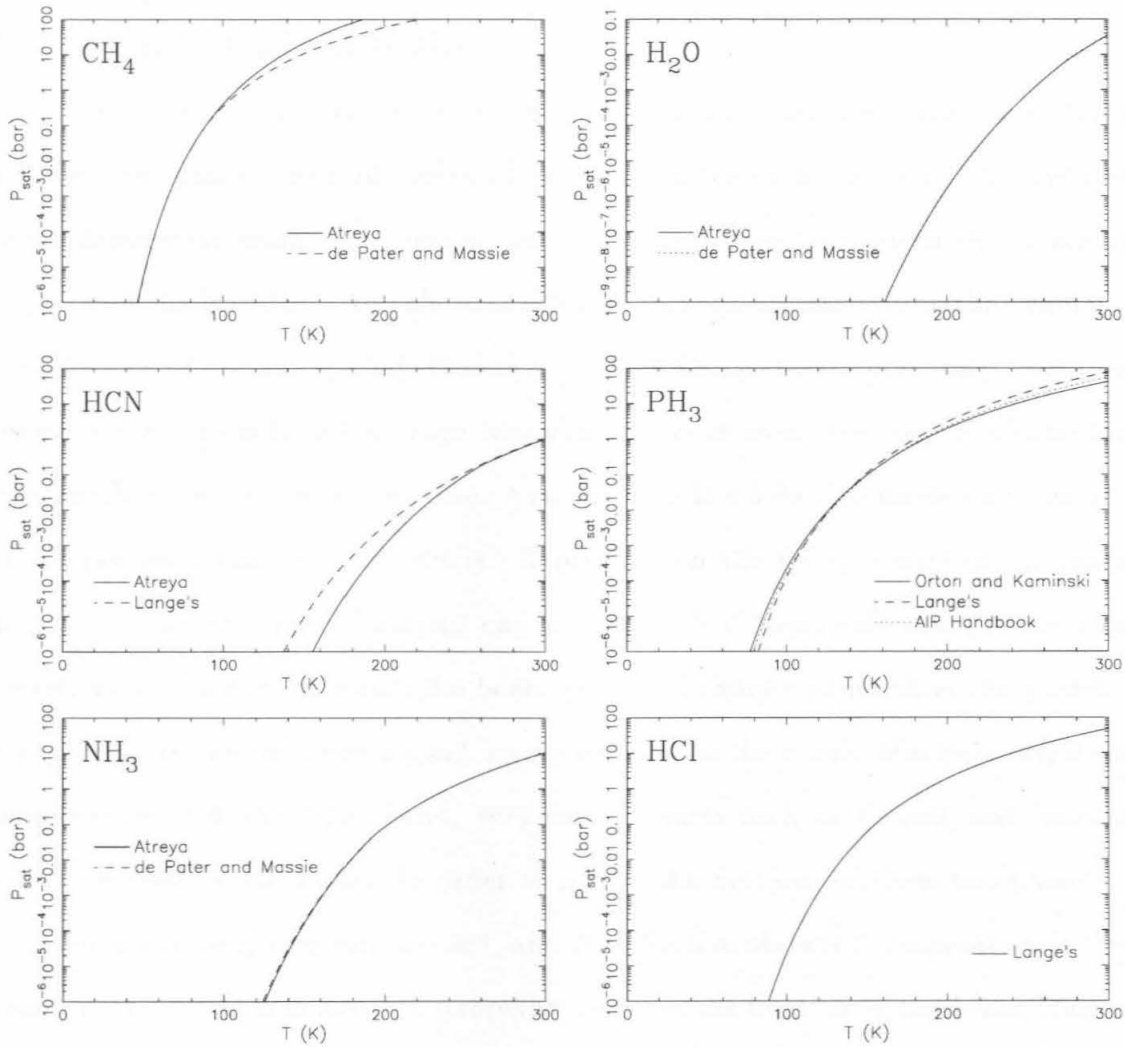

Figure 5.7. Saturation vapor pressures from American Institute of Physics Handbook, Atreya (1986), de Pater and Massie (1985), Dean (1985) ["Lange's"], and Orton and Kaminski (1989).

Table VI. Cloud base pressures for the jovian planets (in bar). Solar NH_3 (1.328×10^{-3}), H_2O (1.676×10^{-4}), and H_2S (3.621×10^{-5}) mole fractions have been assumed below the saturation level. The sub-cloud HCN mole fractions have been taken to be 0.3 ppb, 0.1 ppb (upper limits from Weisstein and Serabyn 1996), 0.1, and 1.0 ppb (upper limit and best fit to stratospheric measurements of Marten *et al.* 1993). The sub-cloud PH_3 mole fractions were taken as 0.6, 3.0, 1.0, and 1.0 ppm.

Molecule	Jupiter	Saturn	Uranus	Neptune
CH_4	—	—	1.2	1.3
PH_3	—	—	1.4	1.8
HCN	0.3	0.8	5.0	5.7
NH_3	0.8	1.5	10.1	11.4
NH_4SH	2.3	4.7	22.8	28.4
H_2O	5.9	12.9	105	109

5.7. Whole Disk Modeling

Because of the decreasing emission angle away from the center of a planetary disk, the atmospheres of jovian planets experience limb darkening. In addition, the instrumental beam (the convolution of the telescope beam with the geometric response of the Winston cone) shows a falloff in its response away from the beam center. Because of the low spatial resolution of the FTS, measured planetary brightness temperatures are actually average temperatures over some fraction of a planetary disk weighted by the beam response. As a result, 2-D whole disk models are required for proper modeling of observations. Depending on the relative sizes of the planet and beam, various approximations can be made. For "resolved" submillimeter observations of Jupiter, in which the beam is several times smaller than the planet, a 1-D disk center model gives a good approximation to the actual observed brightness temperature. On the other hand, very small planets such as Uranus and Neptune are unresolved by the beam. In order to model observations of these two planets, a uniform beam weighting can be used, and the effective observed temperature is then given by the whole disk average temperature times the fraction of the beam filled by the planet ($\propto D^2$, where D is the angular diameter). In intermediate cases where the size of the beam is comparable to that of the planet, full averaging over disk temperatures and beam weighting must be computed.

Whole disk models can either be calculated directly by laying down a grid of points on the projection of a planet, or by calculating temperatures at a series of radial steps and then appropriately averaging them together. The direct approach allows for arbitrarily complicated asymmetric observing geometries (e.g., planetary oblateness, obliquity, latitudinal structure, rings), while the use of radial steps can give an excellent approximation for planets with near azimuthal symmetry using far less computational effort.

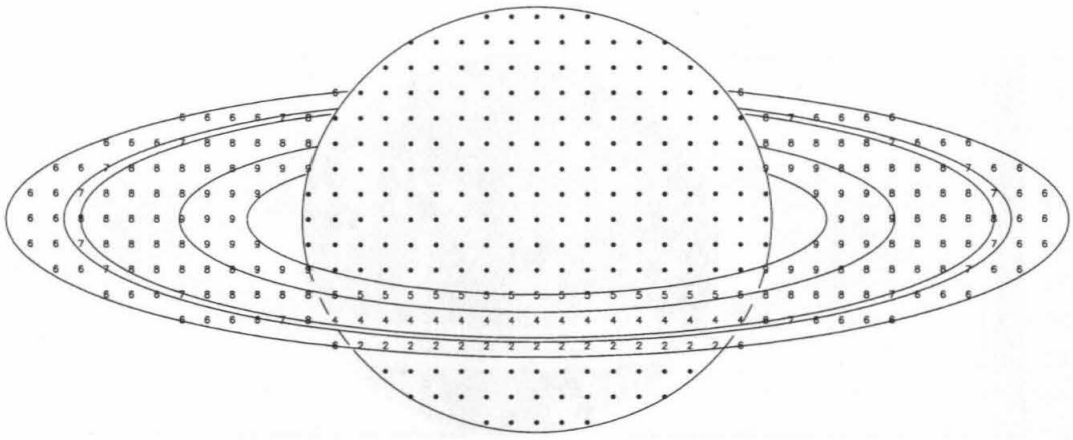

Figure 5.8. A projection of Saturn and its rings onto the sky for a ring opening angle of $\phi = 15°$. The effective temperatures for various regions of Saturn and its ring system (indicated using a numerical label) are given in Table VII.

5.7.1 Gridded Calculation

To compute whole disk models for an arbitrary planetary geometry, the projection of an oblate spheroidal planet to yield an elliptical "disk" is performed, and each grid point lying in the ellipse is converted to the corresponding latitude and longitude. After 1-D brightness temperatures are computed at each grid point, they are either averaged together and expressed as an equivalent disk brightness temperature (for unresolved planets), or weighted by the beam response at each point and then summed (for resolved planets). Planets for which latitudinal structure can be neglected need only be modeled in one of the two east-west hemispheres, saving a factor of two in computation time.

For Saturn, the geometry of the A, B, and C rings and Cassini Division is fully accounted for in the whole disk model (Fig. 5.8). Attenuation of Saturn's flux by the ring cusps and thermal emission from the ring ansae (Table VII) are modeled using ring "brightness" temperatures and optical depths. Because the thermal emission of the rings increases appreciably with frequency in the millimeter-submillimeter portion of the spectrum (Esposito *et al.* 1984), a linear slope in frequency was fit to the

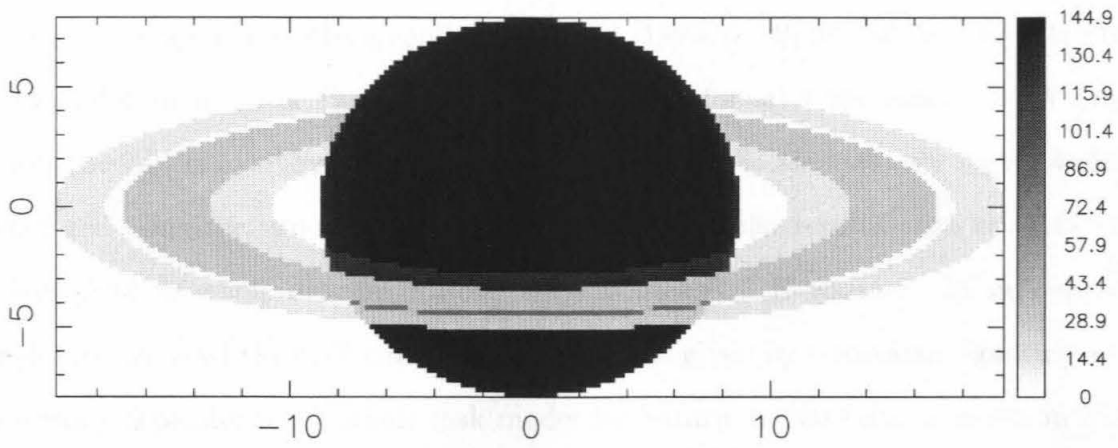

Figure 5.9. Gridded whole disk model for Saturn at 200 GHz with beam weighting omitted. The grid size was taken as 0.2″ and the ring opening angle was set to $\phi = 15°$. The vertical bar at right gives the model brightness temperature scale in units of K.

brightness temperatures of the combined A and B rings measured between 90 and 300 GHz by Epstein *et al.* (1984), Muhleman and Berge (1982), Dowling *et al.* (1987), Ulich (1974), Grossman (1990), and Werner *et al.* (1978). The slope was then used to extrapolate the brightness temperatures derived for the individual rings by Grossman (1990, p. 52) at 150 GHz.

Table VII. Regions of a planet projection considered in calculating a gridded whole disk model of Saturn. For other planets, only points on and off the disk must be distinguished.

Region #	Name	T_{eff}
•	Disk	T_p
2	A ring cusp	$T_A + T_p(1 - e^{-\tau_A})$
3	Cassini Division cusp	$T_{\text{Cd}} + T_p(1 - e^{-\tau_{\text{Cd}}})$
4	B ring cusp	$T_B + T_p(1 - e^{-\tau_B})$
5	C ring cusp	$T_C + T_p(1 - e^{-\tau_C})$
6	A ring ansae	T_A
7	Cassini Division ansae	T_{Cd}
8	B ring ansae	T_B
9	C ring ansae	T_C

The optical depth of the combined A+B+C rings is observed to be independent of wavelength from the UV to a wavelength of 6 cm (Dowling *et al.* 1987). While the optical depths of the individual rings are not expected to be wavelength-independent,

not many values have been published at millimeter wavelengths. We therefore ran models using optical depths given by Grossman (1990, p. 59) at 2.01 cm and 6.17 cm. Optical depths at these two frequencies are similar for all rings except the A ring, where the 2.01 cm value given by Grossman appears to be anomalously high. Models generated using the two sets of optical depths gave similar results, with the 6.17 cm values yielding whole disk brightness temperatures $\sim$ 3 K warmer. In subsequent modeling, we used the 6.17 cm ring optical depths given by Grossman, ignoring any frequency dependence. A whole disk model for Saturn at 200 GHz is shown in Fig. 5.9.

5.7.2 Radial Step Calculation

For an azimuthally symmetrical planetary disk of angular radius R and with brightness temperature as a function of radius given by $T(r)$, the disk average temperature is given by the integral

$$\langle T \rangle = \frac{2\pi \int_0^R T(r) r \, dr}{2\pi \int_0^R r \, dr} = \frac{2 \int_0^R T(r) r \, dr}{R^2}. \tag{5.20}$$

This expression can be approximated by calculating the 1-D brightness temperature at N points (plus the origin) spaced across the disk. Since limb darkening become increasingly important near the edge of a planetary disk, it is convenient to allow the spacings of the points to be specified by the power law

$$r_n = \left(\frac{n}{N}\right)^p, \tag{5.21}$$

where p is a specified constant and r_n is a fraction of the planetary radius. The integral (5.20) can then be approximated using a trapezoidal rule. Interpolating linearly between adjacent points T_n and T_{n+1} calculated at radii r_n and r_{n+1} gives

$$T(r) = T_n + \frac{T_{n+1} - T_n}{r_{n+1} - r_n}(r - r_n) \equiv T_n + \gamma_n (r - r_n) = (T_n - \gamma_n r_n) + \gamma_n r, \tag{5.22}$$

for $r_n \leq r \leq r_{n+1}$, where $\gamma_n \equiv \Delta T_n / \Delta r_n$. Integrating over the annulus then gives

$$\Delta T_n = 2 \int_{r_n}^{r_{n+1}} [(T_n - \gamma_n r_n) + \gamma_n r] r \, dr = [(T_n - \gamma_n r_n) r^2 + \tfrac{2}{3} \gamma_n r^3]_{r_n}^{r_{n+1}}, \qquad (5.23)$$

and summing the results yields

$$\langle T \rangle = \sum_{n=1}^{N} \Delta T_n. \qquad (5.24)$$

5.8. Weighting Functions

At submillimeter wavelengths (1.0-0.3 mm = 300-1000 GHz), the observed fluxes of the jovian planets are produced by thermal blackbody emission from their atmospheres. The equations of radiative transfer can be used to calculate the radiation emitted by such an atmosphere after passing through overlying absorbing/emitting layers on its journey outward. The useful radiative transfer concept of the weighting function (5.6) is frequently used to quantify the fraction of emitted radiation arising from various pressure levels. For frequencies sufficiently far from strong rotational transitions, the submillimeter continuum weighting functions for the jovian planets lie in the range $\sim$ 0.5-1.6 bar for Jupiter and Saturn, or $\sim$ 0.2-3.0 bar for Uranus and Neptune, as illustrated in Fig. 5.10. In the models used to generate these weighting functions, NH_3 follows a saturation law up to the tropopause and PH_3 is uniformly mixed up to cutoff pressures of 250 and 100 mbar in Jupiter and Saturn, respectively.

5.9. Chi Squared Formalism

If the appropriate spectral line and broadening parameters are known for a given species, a non-detection can be used to obtain an upper limit for the atmospheric abundance of that molecule. Upper limits can be computed by determining the smallest concentration of a molecule required to produce an observable spectral absorption feature at a frequency where no such feature was actually observed. To

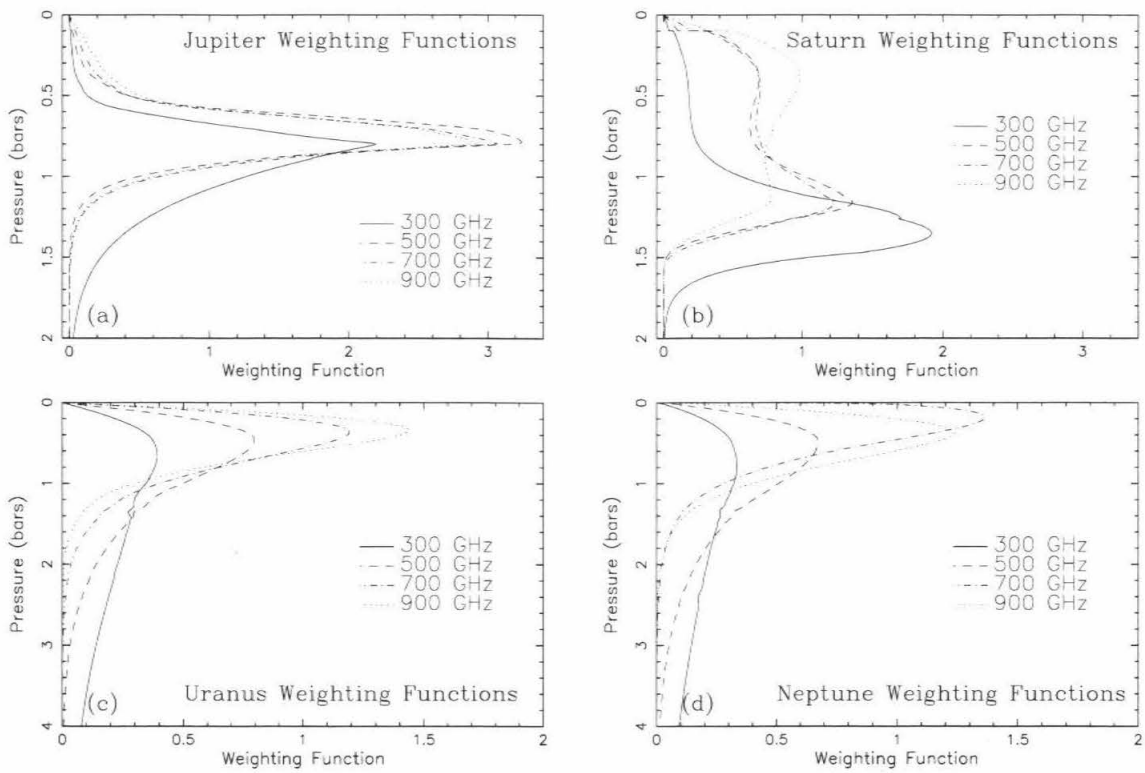

Figure 5.10. Submillimeter weighting functions for (a) Jupiter, (b) Saturn, (c) Uranus, and (d) Neptune. The weighting functions are given for frequencies of 300, 500, 700, and 900 GHz. Jupiter's weighting function is dominated by NH_3. The bimodal appearance of Saturn's weighting functions arises because the wings of both PH_3 and NH_3 are important, and their peak contributions originate at different pressure levels. The most important contribution to weighting functions for Uranus and Neptune is H_2-H_2 collisionally induced dipoles.

determine this limiting concentration, we compute a "template" spectrum $T_0(\nu)$ for a model atmosphere containing zero concentration of a molecule, then a series of spectra $T_m(\nu)$ for a range of tropospheric mole fractions m. The model spectra are generated using our radiative transfer code and then convolved to the instrumental resolution of the observations. Because the modeled lines are much wider than a single channel due to pressure broadening, we compute the weighted sum over model frequency channels of the square deviations between the model spectra $T_0(\nu)$ and $T_m(\nu)$,

$$R_m{}^2 \equiv \sum_{\nu} w_m(\nu)[T_0(\nu) - T_m(\nu)]^2 \tag{5.25}$$

for each undetected molecular transition. The weights $w_m(\nu)$ are chosen to be proportional to the line absorption at a given frequency, thus weighting the central

absorption channel most highly and de-emphasizing the continuum channels in which no line absorption would be present. Symbolically, the weights are given by

$$w_m(\nu) \equiv \frac{|T_0(\nu) - T_m(\nu)|}{\sum_\nu |T_0(\nu) - T_m(\nu)|}. \tag{5.26}$$

${R_m}^2$ gives the expected squared deviation from the continuum that a molecular mole fraction m would produce. When divided by the mean square noise σ^2 of the data, a normalized χ^2 statistic is obtained. This statistic can provide an estimate of the probability that a weak feature of a given strength would have been detected in a measured spectrum in the presence of noise,

$${\chi_m}^2 \equiv \frac{1}{\sigma^2} \sum_\nu w_m(\nu)[T_0(\nu) - T_m(\nu)]^2. \tag{5.27}$$

The mole fraction which produces a χ^2 value equal to the 3σ Gaussian confidence level (99.73%) can then be identified as the 3σ upper limit.

Chapter 6

PH_3 Observations

"The experiment I pursued with dogged persistence for more than a year... represented a compulsive dividing line between kid's stuff and adult stuff. It was the preparation of phosphine... The delicious trouble with phosphine was that it would explode on contact with air... Taking care that my parents were out..., I slipped in the Bunsen and let things cook, retreating to a safe distance myself. Things went as planned. There was a soft explosion..., whereupon I rushed out of my hiding place... Pretty soon the phosphine started to bubble up through the water, and there were my smoke rings... I repeated the experiment two or three more times. My mother really did protest strenuously about it, because the decay of phosphine stank out her kitchen terribly and took surely a week to clear itself."

—Fred Hoyle *(Home Is Where the Wind Blows)*

"Every attempt to employ mathematical methods in the study of chemical questions must be considered profoundly irrational and contrary to the Spirit of Chemistry. If Mathematical Analysis should ever hold a prominent place in chemistry—an aberration which is happily almost impossible—it would occasion a rapid and widespread degeneration of that science."

—Auguste Comte *(Philosophic Positive)*

6.1. Introduction

Because of the strength of its spectral lines, the PH_3 molecule is a valuable probe of the upper atmospheres of Jupiter and Saturn. Thermodynamic equilibrium models of these atmospheres indicate that PH_3 forms at appreciable concentrations only at the relatively high temperatures ($\gtrsim$ 500 K) of the deep tropospheres, and that the PH_3 abundance decreases rapidly with height as solid phosphorus precipitates are formed at the cooler ($\lesssim$ 150 K) temperatures of the upper troposphere (Fegley and Lodders 1994, Borunov *et al.* 1995). Surprisingly, appreciable quantities of PH_3 were detected two decades ago in the upper atmospheres on Jupiter and Saturn using infrared spectroscopy. The presence of observable quantities of PH_3, in the absence of a stratospheric source, therefore reveals the existence of rapid vertical mixing from deeper, warmer levels (Prinn and Lewis 1975, Ridgway *et al.* 1976, Larson *et al.* 1980). Because PH_3 is rapidly depleted via photodissociation by solar UV pho-

tons upon reaching the upper atmospheres of the Jupiter and Saturn (Strobel 1977, Kaye and Strobel 1984, Atreya 1986), observations of PH_3 can provide constraints on photochemical/transport models, making PH_3 an important chemical and dynamical probe of these atmospheres. (In Uranus and Neptune, PH_3 condenses in the cold upper tropospheres and so is not expected to be observable.) However, because of difficulties in inverting infrared spectra, this potential has yet to be fully exploited.

After PH_3 was detected in Jupiter and Saturn, phosphorus compounds were proposed as potential chromophores in these atmospheres (Prinn and Lewis 1975). However, Saturn's more subdued coloration relative to Venus despite its larger observed PH_3 abundance, and the lack of PH_3 enrichment in Jupiter's Great Red Spot (Kim and Owen 1983, Drossart *et al.* 1990, Griffith *et al.* 1992) revealed by more recent measurements, call this suggestion into question.

Infrared measurements have already provided estimates of the PH_3 abundances in Jupiter and Saturn (Bregman *et al.* 1975, Ridgway *et al.* 1976, Larson *et al.* 1980, Drossart *et al.* 1982, Kunde *et al.* 1982, Courtin *et al.* 1984, Drossart *et al.* 1990, Noll and Larson 1990). However, infrared spectra of the giant planets are littered with thousands of overlapping ro-vibrational transitions, making comparison of infrared measurements with atmospheric models difficult, especially when combined with several other complicating factors such as scattering by haze and clouds, and confusion with overlapping NH_3 lines (Courtin *et al.* 1984, Noll *et al.* 1988, Noll *et al.* 1989, Noll *et al.* 1990, Noll and Larson 1990). Uncertainties in PH_3 line strengths at infrared frequencies also impose significant limitations on the retrieval of mixing ratios for other species (Noll and Larson 1990).

It is therefore fortunate that the PH_3 molecule has two strong observable rotational transitions in the millimeter-submillimeter portion of the spectrum ($J = 1 - 0$ at 267 GHz and $J = 3 - 2$ at 800 GHz). (The $J = 2 - 1$ transition at 534 GHz is

obscured by telluric H_2O.) Because there is little confusion between the pure rotational lines at millimeter-submillimeter wavelengths, mixing ratios can be retrieved with relative ease. However, the extremely large pressure-broadening experienced by PH_3 prevented its detection using heterodyne submillimeter spectroscopy in Jupiter and Saturn. Using the moderate resolution and wide bandpass of the CSO Fourier transform spectrometer, we were able to detect strong PH_3 rotational transitions in both planets. Our first observations were in the low frequency 1300 μm window, which resulted in the detection of the $1-0$ line in Saturn, but not in Jupiter. Subsequently, we observed using a wide filter in the 350 μm window and detected the $3-2$ line in both Jupiter and Saturn. In the following sections, PH_3 detections and their implications are discussed first for Jupiter and then for Saturn.

6.2. Jupiter PH_3 1-0 Observations

Fig. 6.1 shows a spectrum of Jupiter obtained using the 1300 μm filter and 30″ Winston cone on Sept. 19, 1995. The data were collected at a spectral resolution of 3 GHz under favorable weather conditions, with an average zenith atmospheric optical depth of $\tau_{225\ \mathrm{GHz}} = 0.034$, as measured by the on-site water vapor radiometer. A total of 10 pairs of "on" scans were obtained over a period of 20 minutes while Jupiter varied in airmass from 1.6 to 1.7. In Fig. 6.1, the spectrum has been rescaled from T_A^* units to an absolute brightness temperature using a model continuum provided by a radiative transfer model. This continuum level is in good agreement with the measured continuum brightness temperatures of Jupiter at the relevant millimeter wavelengths (as summarized in Joiner and Steffes 1990) of 158 $\pm$ 10 K (Courtin *et al.* 1977) and 166-175 K (Joiner *et al.* 1992) at 214-215 GHz, and 165 $\pm$ 8 K (Ulich *et al.* 1984) and 169-197 K (Joiner *et al.* 1992) at 227-230 GHz. A moderate filter ripple is present, causing adjacent channels to alternate between high and low values across the spectrum. However, there is clearly no trace of a prominent absorption

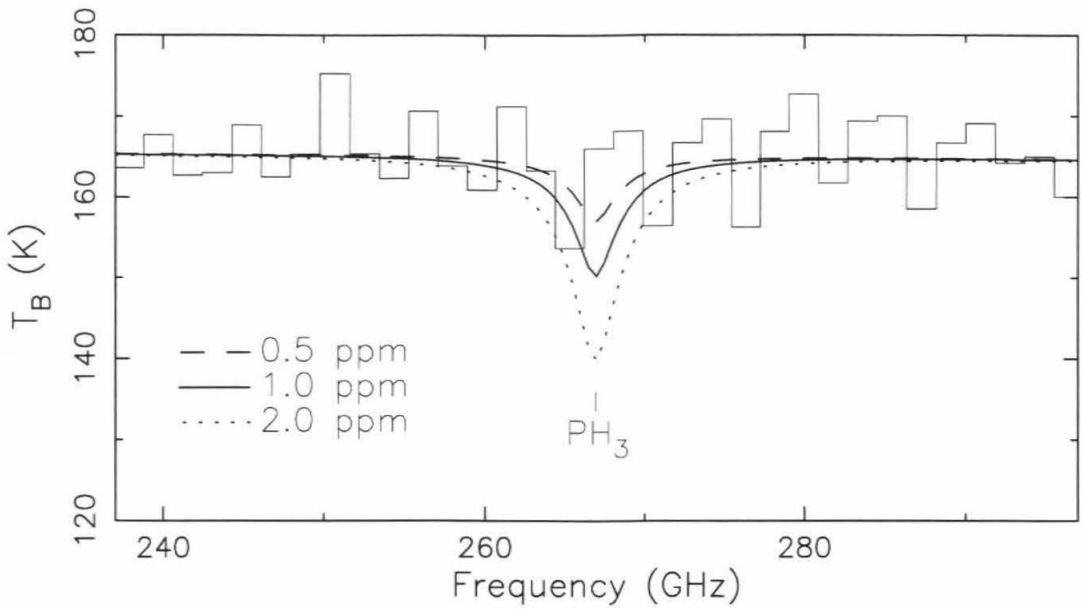

Figure 6.1. Jupiter spectrum obtained in the 1300 μm filter. Model spectra containing 0.5, 1.0, and 2.0 ppm PH_3 are superposed, and the transition frequency of the PH_3 $1-0$ is marked.

feature in the vicinity of the 267 GHz $J = 1 - 0$ PH_3 line.

To estimate the phosphine abundance required to produce an observable line, we ran radiative transfer models assuming a constant PH_3 mixing ratio with no photochemical cutoff. Our models indicated that a PH_3 mole fraction of 1.0 ppm would yield a line observable above the noise and filter ripple at the 3σ level. Unfortunately, this limit is a factor of 1.4-2.5 times larger than the 0.4-0.7 ppm mole fraction derived from infrared spectroscopy. In order to improve in the PH_3 $1-0$ result, it was necessary to either reduce the instrumental ripple at low frequencies, or go to the higher frequency $3-2$ transition at 800 GHz. After attempts to reduce reflections inside the bolometer dewar and to eliminate off-axis rays by stopping down the FTS mirrors proved insufficient to eliminate filter ripples, new high-frequency measurements were undertaken.

6.3. Jupiter PH_3 3-2 Observations

Because the $J = 3 - 2$ line falls very near a strong terrestrial H_2O feature, it was necessary to first acquire a filter wide enough to transmit the 350 μm window in its entirety (since the standard CSO filter was not wide enough for this purpose). It was hoped that the rise in line strength with increasing rotational quantum number J would overcome the difficulty of attempting to observe on the edge of an atmospheric water line. We therefore observed Jupiter at the CSO using a custom-designed broad bandpass 350 μm filter on June 21-22, 1994 (UT). The metal-mesh filter was transmissive from 760 to 950 GHz, providing a passband wider than the relevant atmospheric window. For these observations, the instrumental field of view was defined by a 20″ Winston cone. The CSO's main beam HPBW varies from is 8.6 to 7.7″ for frequencies from 800 to 900 GHz, giving the FTS a spatial resolution of 19″ over this frequency range for the 20″ cone. The size of Jupiter during the observations was $41.3'' \times 38.6''$. Because the on-site water vapor radiometer was under repair at the time of our observations, the terrestrial atmospheric optical depth was not measured. However, the quality of our spectra indicated that opacity was quite good on June 21, but poorer on June 22. We therefore used data exclusively from the June 21 in our analysis.

After conversion to the T_A^* scale, the Jupiter spectrum was divided by a spectrum of the Moon obtained over a similar airmass range. This ratioing procedure mostly eliminated residual terrestrial ozone features not completely removed by the usual on−off calibration procedure (which works perfectly only for an isothermal atmosphere). Division of the 350 μm Jupiter spectrum by the Moon yielded a spectrum with a smooth continuum and strong absorption feature near 800.5 GHz (Fig. 6.2), corresponding to the $J = 3 - 2$ transition of PH_3. The FWHM of the prominent PH_3 line is 9.6 GHz, and its depth is 20%. The negative slope apparent in the continuum of Fig. 6.2 may be intrinsic to Jupiter, but may also be produced by a falloff in tele-

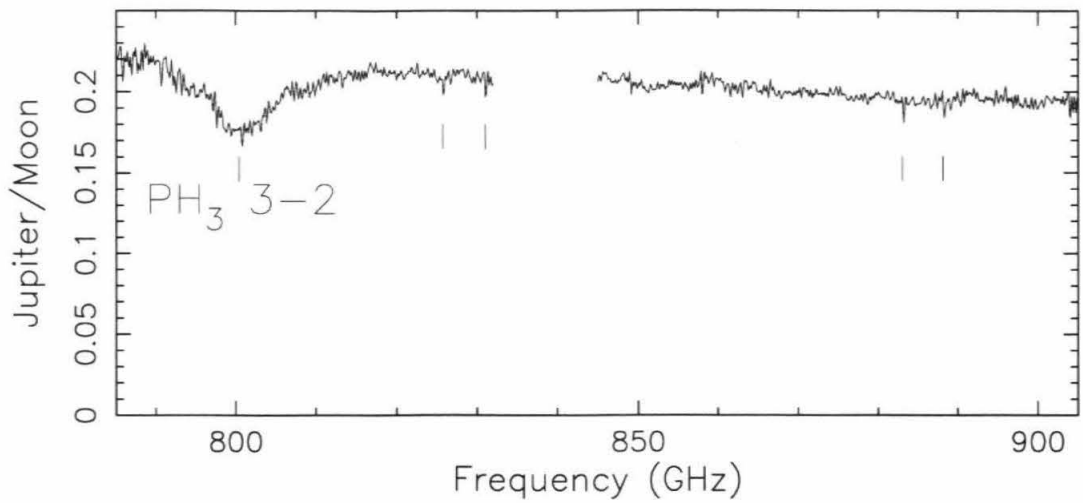

Figure 6.2. Ratio of Jupiter/Moon spectra (both in uncalibrated T_A^* units) at 800 GHz. The $J = 3 - 2$ PH_3 transition is marked, and a number of residual O_3 lines not removed by the division are ticked. A portion of the spectrum near 835 GHz has been blanked where it is contaminated by a terrestrial O_2 feature.

scope efficiency at high frequencies. Small residual ozone features not removed by the Moon division have been ticked for clarity, but do not adversely affect the spectrum.

Because weather prevented completion of beam coupling measurements necessary to directly convert our observations to an absolute brightness temperature scale, we instead performed the scaling from the Jupiter/Moon ratio spectrum using the continuum level provided by our radiative transfer model. Because the spatial resolution of our observations was roughly half the planetary diameter, limb darkening reduced beam-weighted whole-disk brightness temperatures by only $\lesssim 2$ K compared to a simple 1-D model. We fit a first-order polynomial baseline to the continuum in Fig. 6.2, and a second-order baseline to the synthetic spectrum given by our model. We then rescaled the observed spectrum by the ratio of the baseline polynomials so that the continuum level of the data was forced to match that of the model. This procedure preserves the line/continuum ratio, since beam coupling affects the spectrum at each frequency by a given scaling factor which is independent of the relative

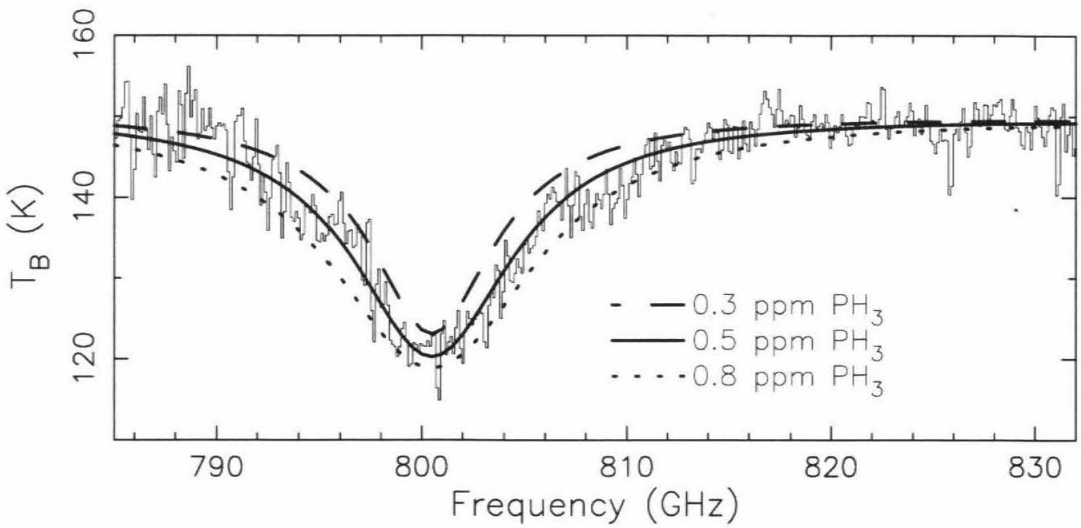

Figure 6.3. Jupiter spectrum converted to brightness temperature units using a radiative transfer model. Models for 0.3, 0.5, and 0.8 ppm PH_3 assuming a constant mixing ratio and cutoff pressure $p_c = 0.25$ bar are overlaid.

importance of line absorption and continuum emission at that frequency. The resulting scaled spectrum (now with a model-derived continuum temperature) is shown in Fig. 6.3 on an expanded horizontal scale, together with several fits to the data.

The continuum weighting function determines the deepest level to which our observations probe. As shown in Fig. 6.4a, continuum emission six half-widths away from the PH_3 line center (6α, where α is the half-width at half-maximum) has a weighting function which peaks near 0.8 bar. Continuum contributions to the weighting function extend to a maximum pressure of $\sim$ 1.1 bar, which is the thus deepest level to which our observations are sensitive. The strong PH_3 line therefore arises from tropospheric absorption at $p < 1.1$ bar. Fig. 6.4b illustrates how the weighting function varies as a function of frequency offset from the PH_3 line center for the Model A profile discussed below. Near the PH_3 line center ($\Delta\nu = 0$), optical depth unity is reached very high up (near the cutoff pressure p_c), while far away from the line center ($\Delta\nu = 6\alpha$), the weighting function is composed almost entirely of the NH_3 contribution. The near line wings therefore contain the most useful information

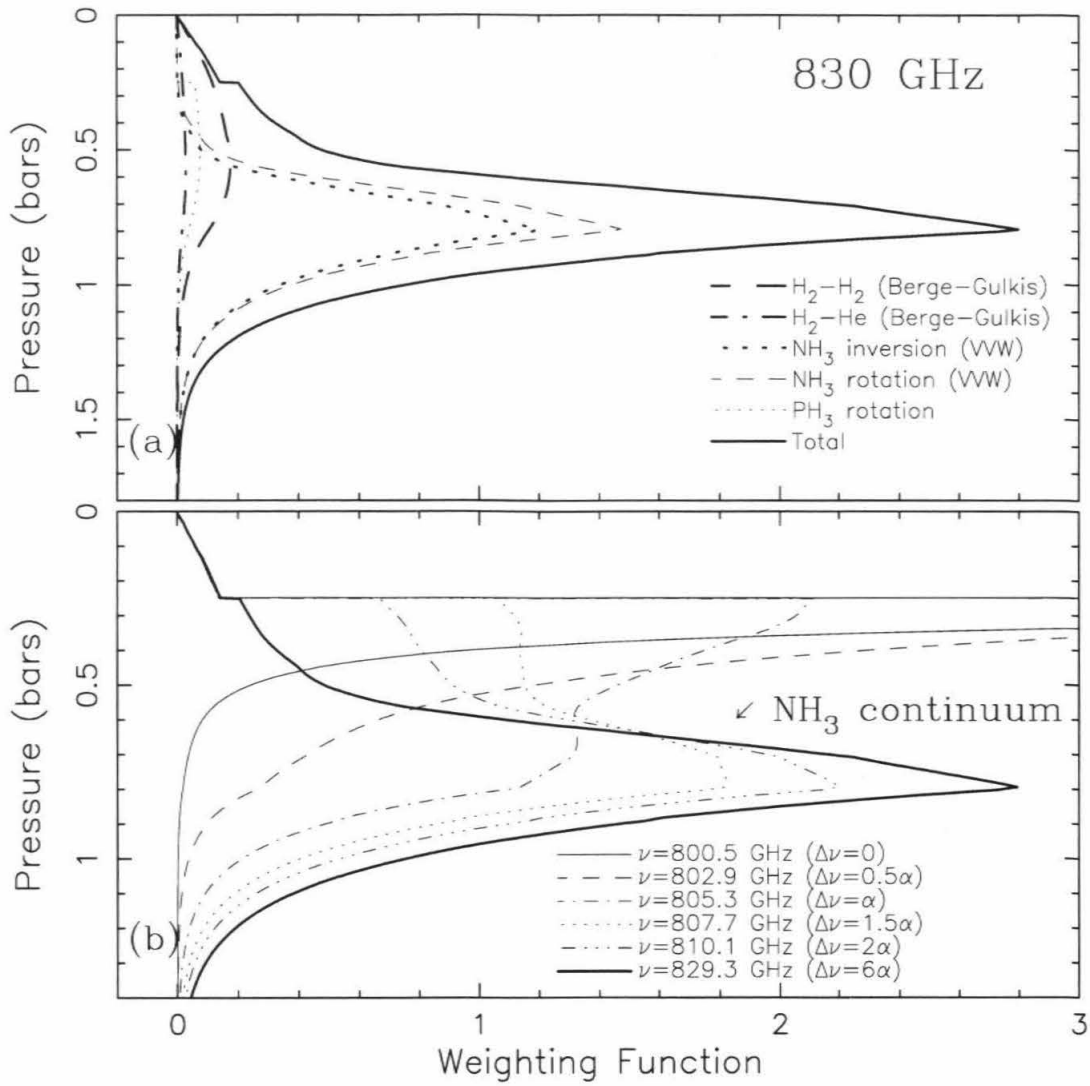

Figure 6.4. Jupiter weighting functions. (a) Continuum weighting functions for Jupiter at 830 GHz. The small slope discontinuity at 0.25 bar results from a contribution by the line wings of PH_3, which has been modeled with a constant mole fraction up to a cutoff at this level. The weighting function peaks near 0.8 bar, but has appreciable contribution down to $p \lesssim 1.2$ bar. (b) Weighting functions for various frequency offsets from the PH_3 line center. The upper peak is due to PH_3, and the lower peak is due to NH_3 continuum emission.

about the vertical distribution of PH_3 in Jupiter's troposphere, and inversion of the broad PH_3 line is most sensitive to PH_3 arising from $p \lesssim 0.6$ bar.

The absence of an emission core at our 200 MHz resolution (Fig. 6.3) demonstrates that little or no PH_3 is present above the cold trap (140 mbar) in Jupiter, consistent with the upper tropospheric depletion inferred by Encrenaz *et al.* (1978,

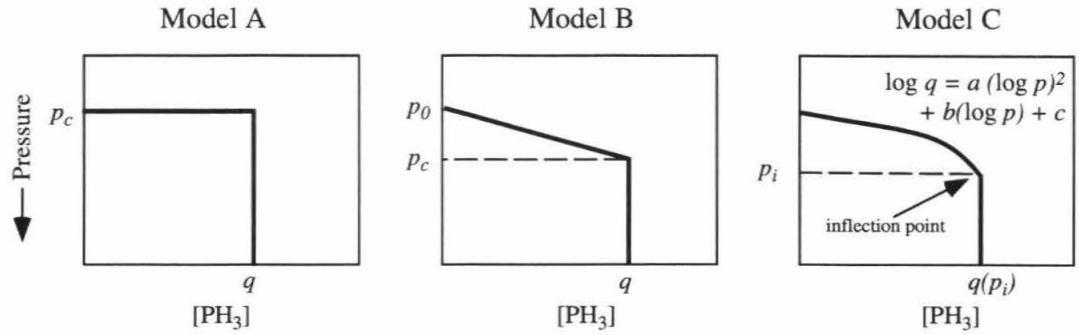

Figure 6.5. Functional forms for the three PH_3 models described in the text.

1980) and Tokunaga *et al.* (1979). The lack of an emission core places a 3σ upper limit of $\sim$ 60 ppb on the stratospheric PH_3 mole fraction (assumed to be constant) in Jupiter. This result is virtually independent of the PH_3 mole fraction profile used to match the tropospheric absorption line. It is also consistent with the lack of an observed line core in high resolution 267 GHz heterodyne spectra by Lellouch *et al.* (1984) and confirmed at the CSO by our own heterodyne measurements.

The PH_3 $3-2$ line profile was modeled in several ways using our radiative transfer model. We began with a simple rectangular model (Model A) in which PH_3 was assumed to have a constant mole fraction q for pressures p greater than some cutoff pressure p_c (Fig. 6.5a). This model provides only a first approximation to the actual PH_3 profile, which is expected to be roughly constant at deep levels and to fall off to zero near the top of the atmosphere due to UV photodissociation (Kunde *et al.* 1982). For $p < p_c$, the mole fraction of PH_3 was set to zero. A simultaneous nonlinear least squares inversion for q and p_c yielded a best fit of $q = 0.55$ ppm and $p_c = 0.25$ bar for the nominal Lindal *et al.* (1981) pressure-temperature profile. To examine the sensitivity of this fit to the PH_3 mole fraction, models were also run for $q = 0.30$ and 0.80 ppm, keeping $p_c = 0.25$ bar. These models, displayed in Fig. 6.3, constrain the PH_3 mole fraction to within an estimated uncertainty of $\sim$ 0.10 ppm. We also investigated the sensitivity of Model A inversions to the assumed

temperature structure of the atmosphere. Using temperature profiles shifted upward and downward by 5 K, the corresponding inversions gave (p, q) = (0.72 ppm, 0.26 bar) and (0.43 ppm, 0.24 bar), respectively. These profiles have essentially the same p_c, but the resultant variation in the best-fit PH_3 mole fraction gives a further uncertainty of $\sim$ 0.15 ppm. Finally, we investigated sensitivity of the inversion to the temperature exponent for values between $n = 0.5$ and 0.9 and obtained mole fractions within $\sim$ 0.1 ppm of the nominal $n = 0.67$ case. Adding all these uncertainties in quadrature, we derive a PH_3 mole fraction in Jupiter of 0.55 ± 0.21 ppm for Model A.

Because of the non-physical nature of the vanishing PH_3 scale height in the simple Model A, we also considered more general PH_3 profiles which allowed a more gradual falloff. In Model B, we allowed q to increase linearly from zero with pressure increasing from p_0 to p_c, and constrained it to remain constant for $p > p_c$ (Fig. 6.5b). By specifying various values of p_0 and determining the best-fit values of p_c and q, we obtained a series of inversions giving a deep PH_3 value of 0.60 ± 0.05 ppm. The profiles obtained using Model B are shown in Fig. 6.6a, where they appear as the first three curves listed in the key. Although these profiles show differing falloff slopes, they all give roughly the same deep PH_3 mole fraction. In contrast, determination of the "best" PH_3 falloff is precluded by the fact that the sums of square residuals for Model A and all three Model B fits are comparable. However, note that the profile obtained for $p_c = 250$ mbar reproduces exactly that obtained with Model A. Allowing for uncertainties in the temperature exponent and temperature profile as before, we estimate a total uncertainty in the deep PH_3 mole fraction of ± 0.2 ppm.

In an attempt to choose the optimal value of dq/dp from among the family of profiles obtained with Model B, our final model (Model C) parameterized log q as a second order polynomial in log p in the upper troposphere (using three free parameters instead of the two in Model A and two free plus one fixed parameter in

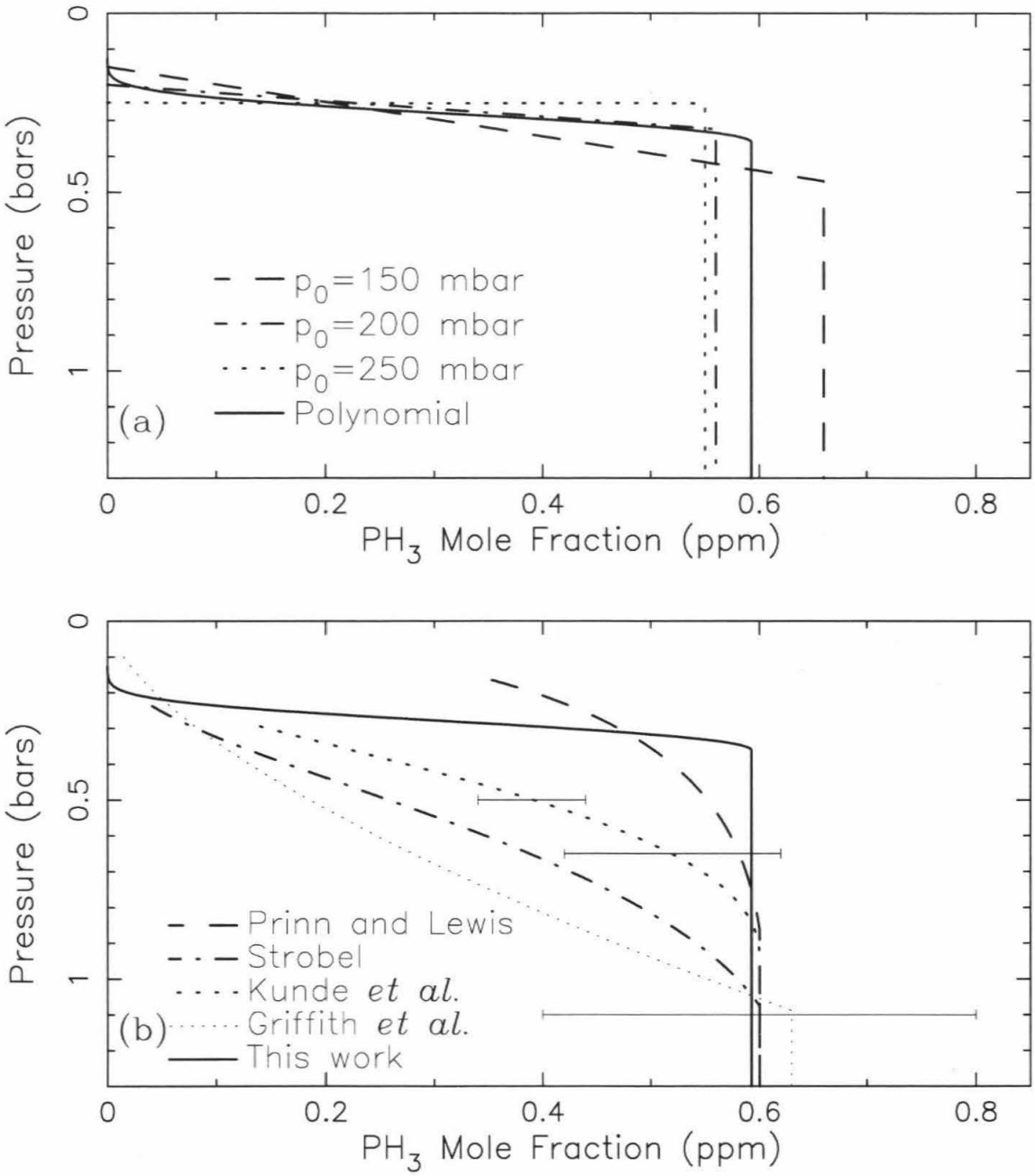

Figure 6.6. PH_3 mole fraction profiles in Jupiter. Model spectra computed using these profiles are shown in Fig. 6.7. (a) Radiative transfer model profiles discussed in the main text. (b) Photochemical and infrared-derived profiles. The "Prinn and Lewis" and "Strobel" curves are photochemical model predictions of Prinn and Lewis (1975) and Strobel (1977), while the Kunde *et al.* (1982) and Griffith *et al.* (1992) curves were obtained from inversion of Voyager IRIS data. The Griffith *et al.* (1992) curve corresponds to an average of their "STZ Hot" and "STZ Cold" cases. Error bars are those given by Kunde *et al.* (1982) for their PH_3 inversion.

Model B). Model C was further constrained to approach a constant mole fraction in the deep atmosphere below its inflection point (Fig. 6.5c). Inversion using Model C yielded the solid curve shown in Fig. 6.6a, again giving a deep PH_3 abundance of 0.6 ppm. Note that in the falloff region ($\sim$ 0.2-0.4 bar), the polynomial slope is nearly linear and the curve is virtually indistinguishable from the Model B profile. The Model C synthetic spectrum, shown as the solid line in Fig. 6.7, matches our observed spectrum to within the noise, as do all three Model B spectra. However, because the sum of square residuals for Model C was comparable to those obtained for Model B, Model C does not provide an improvement over Model B. It therefore appears that the family of trapezoidal profiles obtained with Model B provides an adequate sampling of parameter space available to the PH_3 profile subject to the constraints of our observations, giving a deep PH_3 mole fraction for $p \gtrsim 0.5$ bar of 0.6 ± 0.2 and a steep falloff with slope $\lesssim 2$ ppm/bar occurring at $p \sim 0.3 \pm 0.1$ bar.

6.4. Conclusions on PH_3 in Jupiter

High-frequency FTS measurements have succeeded in detecting PH_3 in Jupiter and resolving its lineshape, allowing a direct determination of its mole fraction and vertical distribution. No emission core was present at our 200 MHz resolution, placing an upper limit of 60 ppb on the stratospheric PH_3 mole fraction. Because the PH_3 lineshape is quite sensitive to the distribution of PH_3 in the upper troposphere, we were able to derive information about the molecule's vertical distribution. Using a radiative transfer model with a smooth PH_3 vertical profile constrained to approach a constant mixing ratio in the "deep" ($\gtrsim 0.6$ bar) atmosphere, we derived a PH_3 mole fraction which falls off with increasing height. Our best-fit deep PH_3 mole fraction of 0.6 ± 0.2 ppm is consistent with infrared results, but the slope of the PH_3 falloff in the upper troposphere is steeper than that inferred from both infrared measurements and previous photochemical models.

Table VIII summarizes previous PH_3 determinations in Jupiter, arranged in order of decreasing pressure of the peak observational sensitivity. Kunde *et al.* (1982) and Griffith *et al.* (1992) derived their concentrations from inversion of Voyager IRIS spectra. Kunde *et al.* (1982) normalized their model profiles to their derived deep mole fraction of 0.6 ± 0.2 ppm and obtained a best-fit profile shown as the heavy dotted line in Fig. 6.6b. Griffith *et al.* (1992) used a PH_3 profile in which the logarithm of the mole fraction decreased linearly with the logarithm of pressure (constrained to a constant deep mole fraction of 0.63 ppm). We averaged their "South Tropical Zone Hot" and "South Tropical Zone Cold" profiles together to obtain a profile representative of the disk average. This profile, shown as the light dotted line in Fig. 6.6b, is depleted in PH_3 compared to Kunde *et al.* (1982).

Table VIII. Published Jupiter PH_3 abundances.

Mixing Ratio (ppm)	Pressures (bar)	λ (μm)	Author
0.54	5	4.8	Larson *et al.* 1977
0.7 ± 0.1	2-5	4.8	Bjoraker *et al.* 1986
0.6 ± 0.2	1-4	4.6	Kunde *et al.* 1982
0.41 ± 0.15	1-2	4.5	Drossart *et al.* 1982
0.54	1	9.0	Ridgway *et al.* 1976
0.54 ± 0.10	0.65	4.6	Kunde *et al.* 1982
$0.30^{+0.23}_{-0.17}$	0.6	8.9	Griffith *et al.* 1992
0.75 ± 0.18	0.1-1.0	9.0	Knacke *et al.* 1982
0.37 ± 0.05	0.50	4.6	Kunde *et al.* 1982
0.1-0.2	0.2-0.6	8.3-11.6	Encrenaz *et al.* 1978, 1980
0.09-0.18	≤ 0.6	10.2-13.4	Tokunaga *et al.* 1979
0.6 ± 0.2	≤ 1.2	380	This work

There are a number of factors which collectively make an unambiguous estimate of minor species mixing ratios based on infrared measurements very difficult. First of all, because infrared observations often suffer from a lack of prominent features (this is especially true for PH_3), it is difficult to separate emission from a given line from that due to other continuum sources. Secondly, infrared observations may also

be sensitive to reflected solar flux from the few hundred millibar level, as well as thermal radiation from several bars. Finally, infrared abundance inversions are sensitive to assumptions about cloud heights and structure. Because millimeter-submillimeter observations are immune from these difficulties, they should, in principle, be able to provide more definitive mixing ratios for species which exhibit strong rotational lines.

While our best "deep" PH_3 mixing ratio of 0.6 ± 0.2 agrees well with those obtained by Ridgway (1976), Drossart *et al.* (1982), Kunde *et al.* (1982), and Knacke *et al.* (1982) at deep levels, our best-fit smooth PH_3 profile requires more PH_3 in the upper troposphere than found by these authors at the same levels. We also find significantly more PH_3 in the upper troposphere than derived from the measurements of Encrenaz *et al.* (1978, 1980), Tokunaga *et al.* (1979), and Griffith *et al.* (1992). We have no reason to believe that temporal variations are responsible for this discrepancy, especially since changes on a global scale would be required to produce an appreciable effect over our large beam. However, observations at 5 μm may indicate that the PH_3 abundance in Jupiter is spatially variable by a factor of up to two (Drossart *et al.* 1984, Bjoraker 1985, Drossart *et al.* 1990).

Our FTS measurements also show a much more rapid falloff than the profiles of Kunde *et al.* (1982) and Griffith *et al.* (1992), or the photochemical models of Prinn and Lewis (1975) and Strobel (1977) (Fig. 6.6b). The discrepancy with the infrared-derived profiles may result from errors in the treatment of reflected solar flux or scattering by haze layers in infrared models. However, the relatively small error bars given by Kunde *et al.* (1982) at the 0.5 bar level ($\sim \pm 0.05$ ppm) would seem to suggest that a genuine discrepancy exists between our measurements and theirs. On the other hand, it should also be noted that the upper tropospheric error bars also fail to overlap the profile derived by Griffith *et al.* (1992) from observations at longer infrared wavelengths! While we are not entirely sure what the source of discrepancy

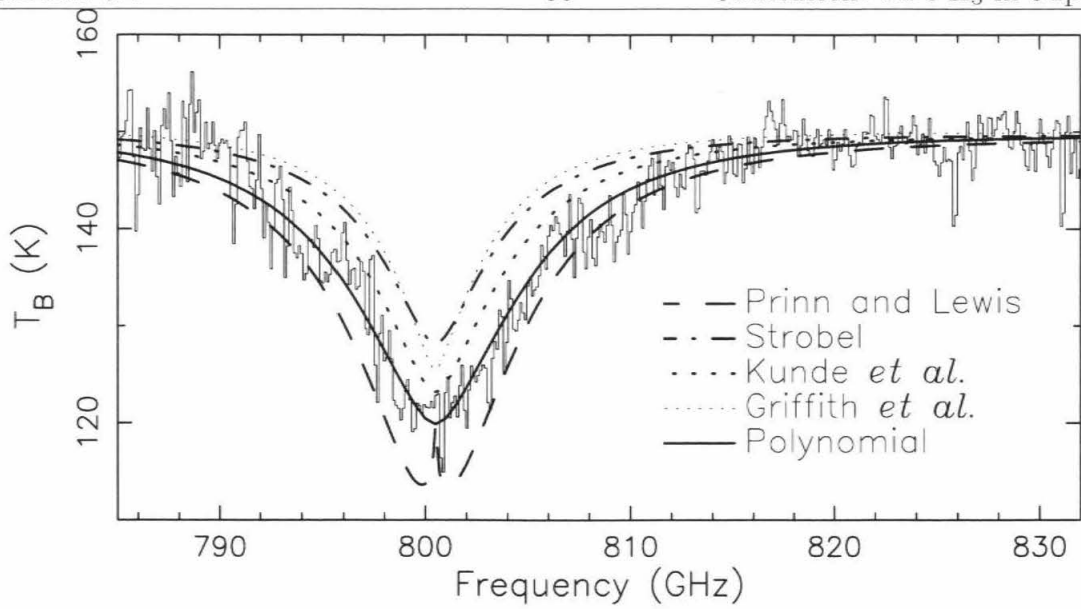

Figure 6.7. Model spectra obtained using the PH_3 profiles of Fig. 6.6b. The spectrum from Fig. 6.3 is superposed for comparison. The polynomial PH_3 model fits the data to within experimental noise.

among the infrared measurements and between the infrared measurements and our own may be, the simpler nature of submillimeter radiative transfer modeling and spectra (note the clear distinction in line depth and width between the spectra shown in Fig. 6.7 which are derived from the various profiles) lend confidence to our result. Unfortunately, given the factor of ~ 2 discrepancy between the photochemical models of Prinn and Lewis (1975) and Strobel (1977) together with the rather primitive nature of these early models, it appears that they cannot be used to distinguish among the various observational PH_3 profiles in Fig. 6.6b.

In order to examine the consequences of the rapid PH_3 falloff in the upper troposphere, we are currently preparing to use the newly updated version of the Caltech/JPL photochemical model (Landry *et al.* 1991). This model includes UV photodissociation of PH_3, chemical reactions of the dissociation products, radiative transfer (including Rayleigh scattering), and eddy diffusion. Based on preliminary results using an earlier version of the photochemical model, we believe it is possible that the sudden PH_3 falloff marks a transition between rapid and slower eddy diffusion

regimes, and furthermore that this transition is connected with Jupiter's radiative-convective boundary.

The radiative-convective boundary is expected to occur at the point where the atmospheric temperature lapse rate first decreases from the convectively unstable adiabatic rate to a sub-adiabatic value. The atmospheric level at which this transition occurs delineates the boundary between the well-mixed troposphere and the overlying stably stratified stratosphere. The radiative-convective boundary thus marks the true dynamical boundary between the tropopause and stratosphere, although it occurs slightly deeper than the temperature inversion (which occurs at $\sim$ 140 mbar in Jupiter). The pressure of the radiative-convective boundary suggested by our modeling of the PH_3 lineshape is slightly smaller than that predicted by radiative-convective models of Appleby and Hogan (1984), which suggest the boundary occurs in the range 500-700 mbar. However, the radiative-convective boundary can also be estimated as the pressure level corresponding to the observed "effective" infrared temperature of Jupiter. Combining the of 124.4 ± 0.3 K temperature observed by Voyager (Hanel *et al.* 1981a) with the pressure-temperature profile of Lindal *et al.* (1981) gives a pressure of $\sim$ 360 mbar, in excellent agreement with the pressure level for the radiative-convective boundary suggested by our measurements.

Because the microscopic processes responsible for atmospheric mixing are too complex to model in detail, atmospheric modelers generally treat atmospheric mixing as a macroscopic "eddy" diffusion process. In this approach, the diffusion rate at each pressure level is parameterized by a quantity known as the eddy diffusion coefficient K (Chamberlain and Hunten 1987, pp. 75 and 90). In practice, eddy diffusion coefficients are difficult to determine experimentally, so a range of theoretical values are normally considered by modelers. A small eddy diffusion coefficient in the upper troposphere, as implied by our inverted PH_3 profile, has important chemical

implications for the upper atmosphere of Jupiter, since a stagnant (low K) region in the upper troposphere can also produce enhanced abundances in chemically inactive species which flow downward through the stratosphere with a constant flux. Landry *et al.* (1991) have shown that this process is capable of producing concentrations which are comparable to those generated by rapid upward mixing from the deep troposphere. A decrease in the upper tropospheric eddy diffusion rate over the value at deeper levels as suggested by our PH_3 analysis is therefore compatible with possibility that stratospheric photochemical production may provide a substantial fraction of the observed abundances of disequilibrium species at $p < 350$ mbar in Jupiter. Such an enrichment in the upper tropospheric concentrations of species such as CO, HCN, and hydrocarbons such as C_2H_2 increases the likelihood that they will be directly detected in the upper troposphere of Jupiter by the Galileo probe neutral mass spectrometer (Niemann *et al.* 1992). In the next chapter, we discuss our own attempts to detect CO and HCN in Jupiter and Saturn using the FTS.

6.5. Saturn PH_3 1-0 Observations

Although the $1-0$ rotational transition of PH_3 was not detectable in Jupiter, we did detect a very strong pressure-broadened (FWHM = 11.2 GHz) line while observing Saturn with the FTS in the 1300 μm filter on December 7, 1992 (UT). The line was so strong, in fact, that it was easily detected in less than half a minute of observation! Based on its central frequency, we identified it as the first rotational transition of PH_3 at 266.945 GHz. Before our next observing run, we acquired a new 16 bit A/D, improved the instrument's optical alignment, and removed several sources of electrical interference. As a result, we were able to reduce systematic noise and greatly improve the data quality. Observations on July 11, 1993 with the 1300 μm filter and 30″ Winston cone confirmed the December detection (the $\sim 30\%$ depth and 11 GHz width of the two observations were the same to within experimental

uncertainty) and provided the spectra we present here (published in Weisstein and Serabyn 1994). The average zenith optical depth through the Earth's atmosphere at 225 GHz was $\tau_{225\ \mathrm{GHz}} = 0.12$ for the Saturn observations (as measured by an on-site water vapor radiometer) and, a few hours later, $\tau_{225\ \mathrm{GHz}} = 0.19$ for observations of Venus (our calibration source).

In order to allow removal of instrumental and beam effects from our data, we observed Venus over the same airmass range as Saturn. Fortunately, on July 11, the angular diameter of Venus (17.6″) almost perfectly matched that of Saturn (18.3″ × 16.4″, for a geometric mean of 17.4″). This advantageous match in size allowed a direct division of the Saturn spectrum by that of Venus, obviating the need for detailed beam coupling measurements and calculations.

Since T_A^* differs from the disk-averaged brightness temperature by the multiplicative factor $\eta_c{}^{-1}$ according to (4.10), the beam coupling would normally have to be determined and removed. However, because the angular sizes of Venus and Saturn were so well matched during our observations, we were able to bypass the complications of beam coupling by simply dividing the two planetary spectra by each other, canceling out the coupling efficiency in the process. (This procedure works best if the Earth's atmospheric opacity is unchanged between the two planetary observations.) An additional advantage of the division is its elimination of residual optical standing waves remaining in the spectra.

This division process does not account for Saturn's rings (the sub-Earth latitude on Saturn was 13.1° on July 11). It also ignores differences between telescope coupling to the projected ellipse of Saturn's disk and the projected circle of Venus's. However, we expect the effects of Saturn's rings and oblateness to be rather small ($\sim 10\%$ and $< 1\%$, respectively) and therefore that the division provides a successful calibration to better than the 10% level. After division, the resultant spectrum

was scaled to an absolute brightness temperature scale using a linear fit to published continuum brightness temperatures for Venus (Table IX) at 150, 230, and 300 GHz by Ulich (1981), Clancy and Muhleman (1991), and Werner *et al.* (1978).

Table IX. Published measurements of the Venus brightness temperatures for millimeter wavelengths (frequencies above 90 GHz).

Frequency (GHz)	T_B (K)	Reference
142.9	300 ± 21.0	Ulich 1974
150.0	294 ± 22.0	Ulich 1981*
178.6	315 ± 13.8	Rowan-Robinson *et al.* 1978
230.0	280	Clancy and Muhleman 1985
230.0	288†	Clancy and Muhleman 1991*
300.0	276 ± 14.0	Werner *et al.* 1978*

*Used in the linear calibration fit

†Provides the best model fit to 1.3 mm CO spectra; no uncertainty quoted

The reduced spectra for Saturn and Venus in the standard units of T_A^* are shown in Fig. 6.8. A residual ripple due to multiple reflections in the Winston cone is present in both spectra, but the 267 GHz PH_3 line in Saturn stands out prominently. The 230 GHz CO $2-1$ line is also readily apparent on Venus, although it is quite narrow compared to the FTS's resolution.

Dividing the Saturn spectrum by that of Venus and normalizing as discussed above yields the final brightness temperature spectrum shown in Fig. 6.9, in which the region near the narrow Venusian CO line has been blanked. As can be seen in Fig. 6.9, the division was successful in eliminating most of the residual instrumental ripple. Of other expected lines in Saturn in the filter bandpass (Bézard *et al.* 1986), the 216 GHz H_2S line is not apparent, nor is the 230 GHz CO $2-1$ line (Figure 6.8a) or the 266 GHz HCN $3-2$ line.

We first compare our derived Saturn continuum brightness temperatures to previously published measurements. In spite of the variations introduced by a ring geometry which differs among the published observations, the agreement of our derived continuum level with previous broadband measurements is quite good. Fitting

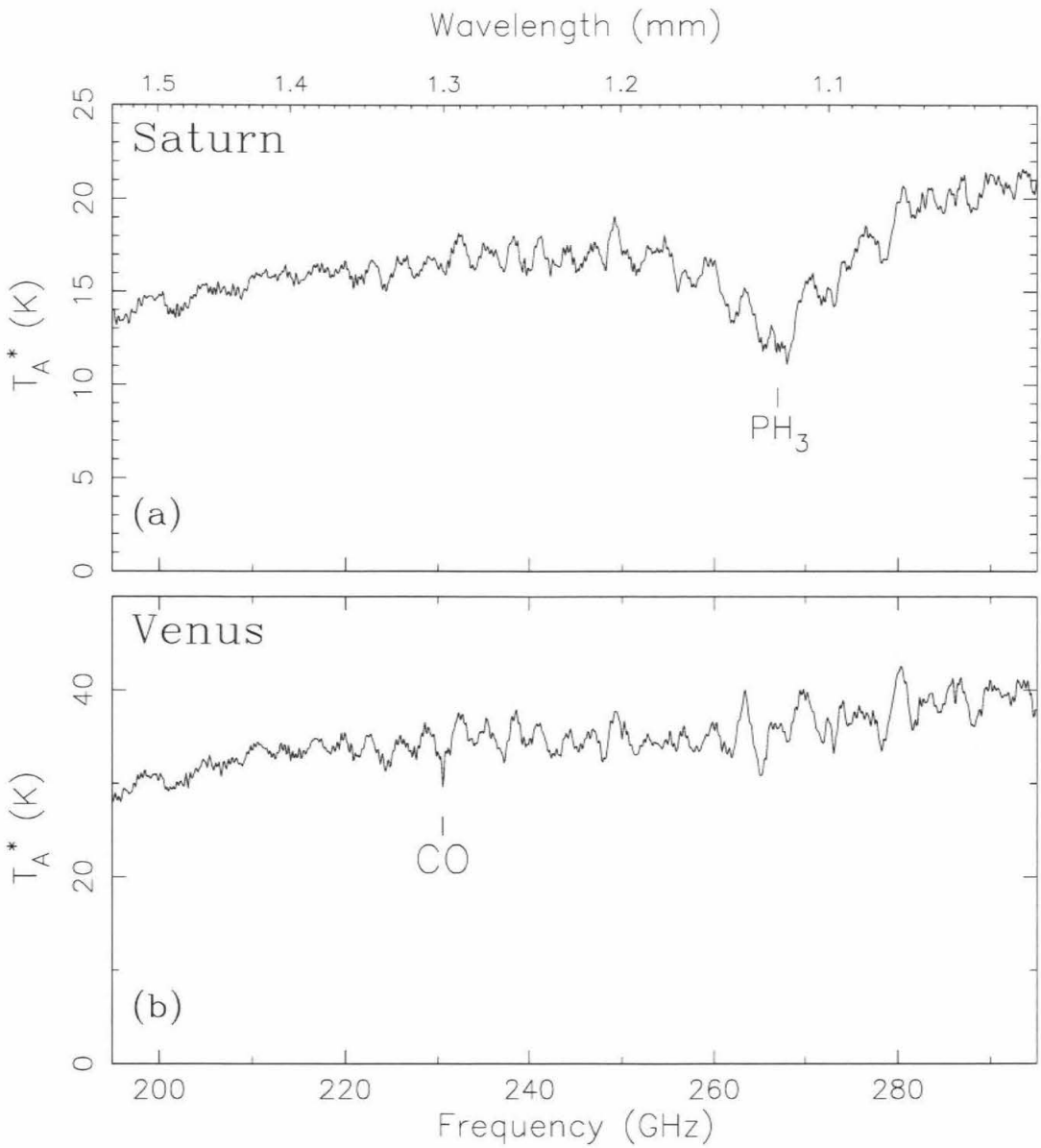

Figure 6.8. Atmospheric and hot spillover-corrected antenna temperatures measured in the 1300 μm filter in units of T_A^* for (a) Saturn, with a total of 48 scans "on" source, giving an "on" integration time of 35 minutes and (b) Venus, with a total of 40 scans taken over 29 minutes. The ripple visible over the entire passband results from reflective standing waves in the Winston cone light concentrator and is not removed by the usual calibration procedure for the 1300 μm filter.

a linear slope to the continuum, we obtain a saturnian brightness temperature of 139 K at 195 GHz (1.5 mm) and 148 K at 295 GHz (1.0 mm), consistent with the 137 $\pm$ 11 K saturnian system brightness temperature reported by Ulich (1981) at 150 GHz and the 145 $\pm$ 7 K temperature quoted by Werner *et al.* (1978) at 300 GHz, but

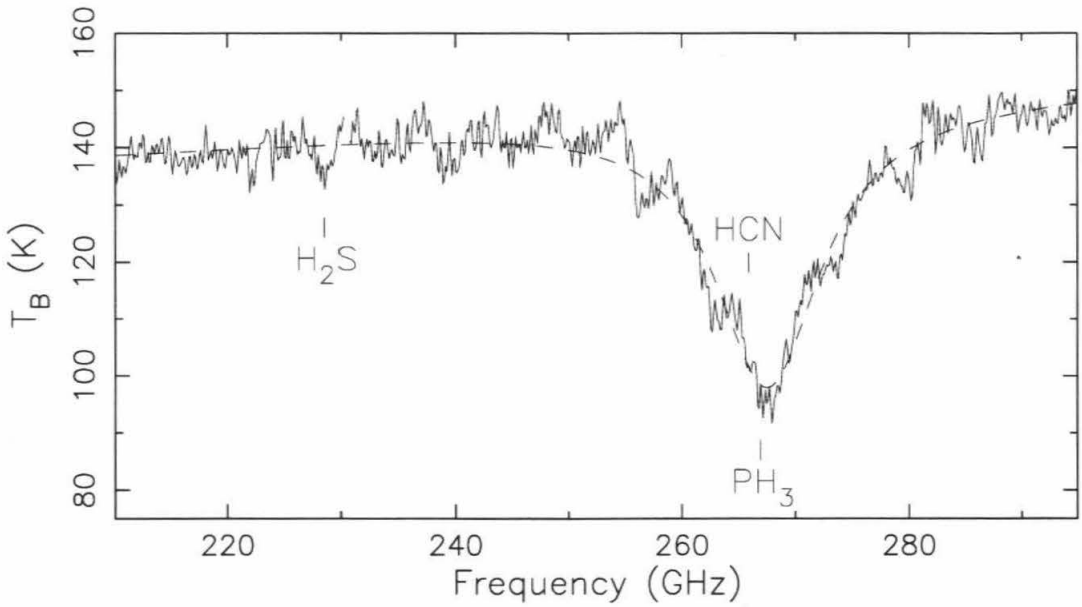

Figure 6.9. Solid line: calibrated Saturn brightness temperature spectrum: (6.8a) / (6.8b) $\times T_{\rm Venus}(\nu)$. Dashed line: Lorentzian best fit with linear baseline. The region near 230 GHz has been blanked to suppress the narrow CO absorption line observed in Venus (the calibration source), preventing it from appearing spuriously in the Saturn spectrum. The central frequencies of several lines with rotational transitions in the passband (which were not detected) are marked.

slightly larger than the 134.2 $\pm$ 3.2 K temperature given by Hildebrand *et al.* (1985) at 310 GHz.

There are a number of factors which could influence the continuum level and slope of our Saturn spectrum. The first, as already discussed, is the uncertainty present in the brightness temperature of Venus, the calibration source. In particular, the brightness temperature of Venus at 150 GHz (Ulich 1981) has an appreciable uncertainty and could potentially skew the slope used to convert the flux scale of Saturn to brightness temperature units. Secondly, the continuum level and slope are affected by the contribution of ring emission, which itself has a slight (but poorly determined) slope (Muhleman and Berge 1982). A third factor is the approximation $B_{\rm hot} \approx B_{\rm sky}$ used to derive (4.10), which will not be correct if there is a small difference between $T_{\rm sky}$ and $T_{\rm hot}$. In light of these uncertainties, we adopt 144 K—the average measured continuum temperature—as our best estimate of Saturn's brightness temperature

(including ring contributions) in the 195 to 295 GHz frequency range.

Since Doppler broadening is negligible (making consideration of a Voigt profile unnecessary), we first fit a Lorentzian lineshape with a linear baseline to the PH_3 line (Figure 6.9) using a nonlinear least squares algorithm. We fit the spectrum (1) allowing all parameters (line center, width, and depth; continuum average and slope) to vary, and (2) with the line center fixed at the PH_3 transition frequency (dashed curve in Figure 6.9). The two fits both gave a FWHM of 11.2 GHz, a line center depth of 48 K ($\sim$ 34% of the continuum, giving a brightness temperature at line center of $\sim$ 98 K), and an integrated area of 840 K GHz. When the line center frequency was allowed to vary, the solution converged to $\nu_0 = 267.5$ GHz. Because of the small resultant frequency offset from the true line center ($< 5\%$ of the line's FWHM and < 3 resolution elements) and accompanying agreement to better than 1% in both FWHM and depth between the two trials, the derived line parameters appear to be quite reliable.

In order to determine the PH_3 mole fraction indicated by our data, we used our radiative transfer code to generate model spectra for various PH_3 mole fractions and cutoff pressures. In this model, ring absorption and emission are included to generate a disk averaged brightness temperature for Saturn and its rings. The disk averaged continuum brightness temperature predicted by this Saturn model is 137 K at 200 GHz, falling slightly to 136 K at 295 GHz. These model temperatures are reasonably close to the measured $\sim$ 144 K temperature, although the continuum slope of the model (which is rather sensitive to the assumed frequency dependence of the ring brightness temperatures) is appreciably smaller than that measured. In addition to agreeing well with our observations, the model is also consistent with the predictions of other published Saturn models. In fact, when we suppress disk averaging and ring contributions to our model, we obtain brightness temperatures within several K of

those predicted by the model of Lellouch *et al.* (1984) at our frequencies.

Potential uncertainties in our Saturn whole disk brightness temperature model include the assumed NH_3 mixing ratio, uncertainties in the NH_3 inversion lineshape and Saturn pressure-temperature profile, and inaccuracies inherent in ring modeling. Because NH_3 is the primary opacity source in the continuum of Saturn near 200 GHz, the NH_3 distribution determines the continuum level. However, since tropospheric NH_3 is assumed to follow a saturation law down to the base of the NH_3 cloud, and because the atmospheric optical depth at frequencies between 195 and 295 GHz exceeds unity while still in the saturation region of NH_3 (Grossman 1990), varying the NH_3 mole fraction has a negligible effect on the model continuum brightness temperature. Similarly, despite variations in the atmospheric pressure-temperature profile of up to 10 K with latitude (Prinn *et al.* 1984, Lindal *et al.* 1985), the model brightness temperature is almost independent of the particular profile chosen. The explanation lies once again in the NH_3 saturation law, which allows the NH_3 cloud to move in altitude in response to a temperature offset to a new pressure which corresponds to the original temperature (Grossman 1990). Unlike the NH_3 mixing ratio and pressure-temperature profile, the nature of the model used to characterize emission and absorption by the rings is capable of producing appreciable ($\lesssim 10\%$) differences in whole disk model brightness temperatures, as are different assumptions about the lineshape of the far NH_3 inversion linewings (Fig. 5.6b). Although our simple ring model appears to match our observations adequately, better experimental measurements of the NH_3 inversion lineshape would be very helpful.

We concentrate now on the distribution of PH_3 in Saturn's atmosphere. Because PH_3 is destroyed by UV photolysis in the upper atmosphere, there is reason to believe that there exists some altitude above which all PH_3 is effectively destroyed. We call the pressure corresponding to this altitude the PH_3 cutoff pressure, p_c, and

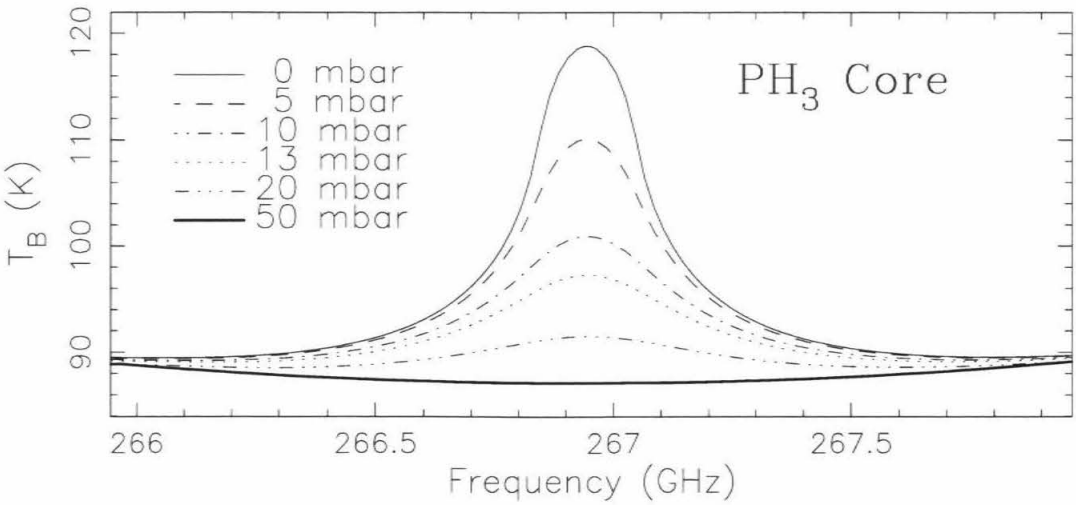

Figure 6.10. Model PH_3 central line cores for various atmospheric cutoff pressures. The line cores have been convolved to our instrumental resolution of 205 MHz.

assume PH_3 is present only at pressures $p > p_c$. Since Saturn's atmosphere has a temperature inversion at ~ 60 mbar, any PH_3 present at pressures less than 60 mbar would be seen as an emission spike at line center (superimposed on PH_3 absorption in the wings). No such emission core is observed in our data, so comparison with models generated for various cutoff pressures (Fig. 6.10) indicates that, in order for the emission spike not to have been detectable ($\leq 3\sigma$), $p_c \gtrsim 13$ mbar. This result is consistent with the UV observations of Winkelstein *et al.* (1983), which imply an absence of PH_3 above the 25 mbar level.

Finally, we discuss the actual pressure-broadened lineshape of PH_3. The high PH_3 absorption coefficient near line center makes Saturn's atmosphere highly opaque, so brightness temperature measurements near line center probe the atmosphere at pressures only slightly greater than the true cutoff pressure (note that the value for p_c given above is a lower limit only). In the troposphere, the depth of the absorption becomes smaller as p_c (and the corresponding temperature) is increased. The observed central line depth is therefore a good indicator of the atmospheric cutoff level. Models

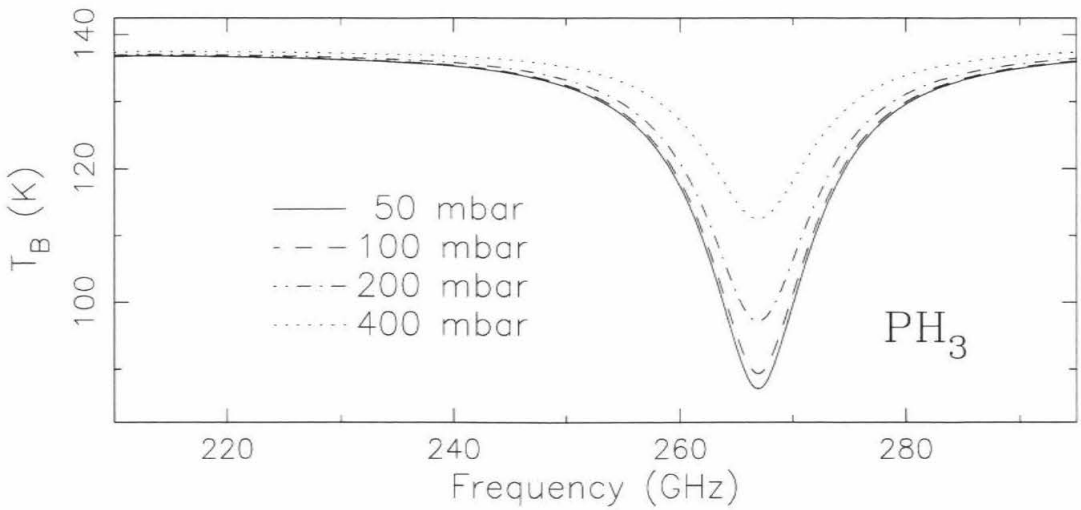

Figure 6.11. Saturn models for various atmospheric cutoff pressures near and below the tropopause. In the troposphere, the line depth increases as the cutoff pressure is moved to higher altitudes (cooler temperatures). The best-fit to the observations is 100 mbar (dashed curve).

with PH_3 cutoff pressures in the range 50-400 mbar were investigated (Fig. 6.11). A cutoff pressure of 100 mbar was found to reproduce the observed line depth most accurately but, allowing for uncertainties in the data, models with p_c up to 140 mbar are capable of reproducing the observed line depth. For larger p_c, the predicted line depths are too small to agree with our measurements. Combining with the previous results, we thus find 13 mbar $< p_c <$ 140 mbar.

Using our best value of p_c = 100 mbar, we ran models for a suite of PH_3 mole fractions, each assumed to be constant at pressures $p > p_c$. PH_3 is expected to undergo rapid depletion with altitude, resulting in a depletion scale height of $\sim$ 3.5 km for an eddy diffusion coefficient of $K \sim 10^4$ cm^2 s^{-1} (Kaye and Strobel 1984). Since the depletion scale height is small compared to the pressure scale height of $\sim$ 40 km (and because the ripples remaining in the data after calibration relative to Jupiter likely make attempts at more detailed modeling futile), the simplest PH_3 model, consisting of a constant mixing ratio below the cutoff pressure ($\sim$ pressure of peak photodissociation), is expected to provide an adequate fit to our observations. In light

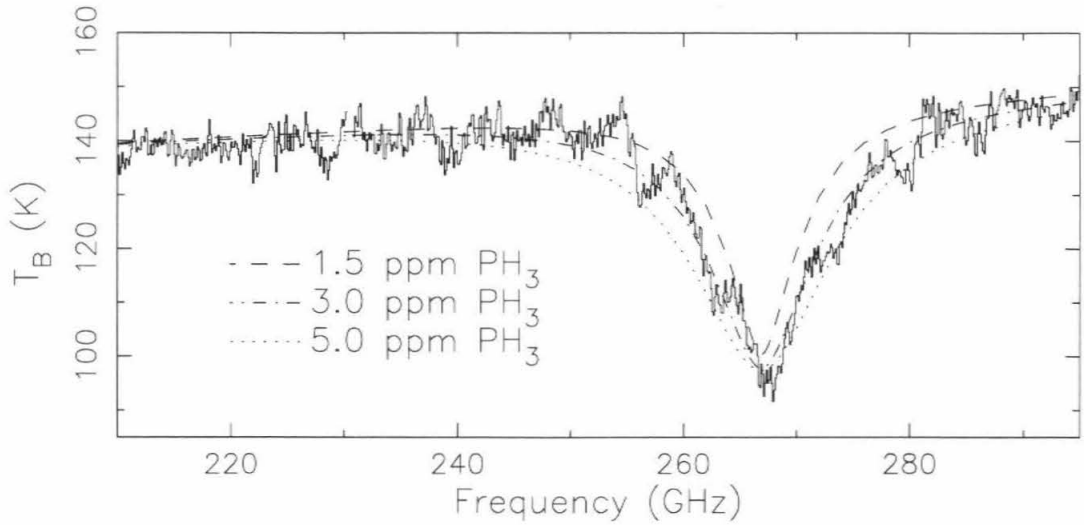

Figure 6.12. Saturn spectrum calibrated in units of brightness temperature, with superimposed model predictions for 1.5, 3.0, and 5.0 ppm PH_3. The region immediately surrounding 230 GHz has been blanked to remove the effects of the narrow CO line observed in Venus.

of the slight continuum slope difference between our nominal model and observations, we removed linear baselines from the disk average brightness temperatures generated by our model and reinserted baselines matching the measured Saturn spectrum.

As revealed by Fig. 6.12, which shows model curves for three PH_3 mole fractions superimposed on the Saturn spectrum, the observed *linewidth* is quite sensitive to the abundance of PH_3 because of opacity in the line wings. The observed PH_3 linewidth therefore provides a robust indicator of PH_3 mole fraction. By performing chi-squared tests of the fits, we obtained a best-fit PH_3 mole fraction of 3.0 ppm (see Table X). Based on the sensitivity of the fit to the model mole fraction, we estimate the uncertainty in our PH_3 determination to be $\sim \pm 1.0$ ppm.

Table X. Chi-squared residuals for various PH_3 fits to the $1-0$ line in Saturn with a 100 mbar cutoff.

PH_3 Mole Fraction (ppm)	Line Depth (K)	FWHM (GHz)	χ^2 (K^2)
1.5	44.5	7.50	2.58
2.0	46.2	8.80	1.62
2.8	47.4	10.7	1.13
3.0	47.6	11.2	1.11
3.2	47.7	11.6	1.13
4.0	48.1	13.2	1.45
5.0	48.2	14.9	2.10
Noll and Larson*	46.0	10.9	1.38

*1 ppm for 78 mbar $< p <$ 400 mbar, 7 ppm for $p >$ 400 mbar

Because the temperature line-broadening exponent for the 267 GHz PH_3 transition has not been measured in the laboratory, our models assumed the same exponent as for NH_3 (Berge and Gulkis 1976), $n = 0.67$. We also investigated models using values of n ranging from 0.5 to 1.0. The change in linewidth obtained by varying n in our model yielded PH_3 mixing ratio retrievals which differed from our nominal 3.0 ppm by $\pm$ 0.3 ppm, much less than our estimated uncertainty of $\pm$ 1.0 ppm (see Table XI) and negligible when combined with it in quadrature. Therefore, our determination of the PH_3 mole fraction in Saturn is rather insensitive to the precise numerical value of n.

Table XI. Best-fit PH_3 mole fractions in Saturn for various temperature broadening exponents n.

PH_3 Temperature Broadening Exponent	Best-fit Mole Fraction (ppm)
0.50	3.3
0.60	3.1
0.67	3.0
0.80	2.7
0.90	2.6

With a PH_3 mole fraction of 3.0 ppm, the pressures at which PH_3 absorption occurs are illustrated in the weighting function plots shown in Figure 6.13. In the continuum ($\Delta\nu = 10\alpha$; Figure 6.13a), almost all emission comes from NH_3 inversion

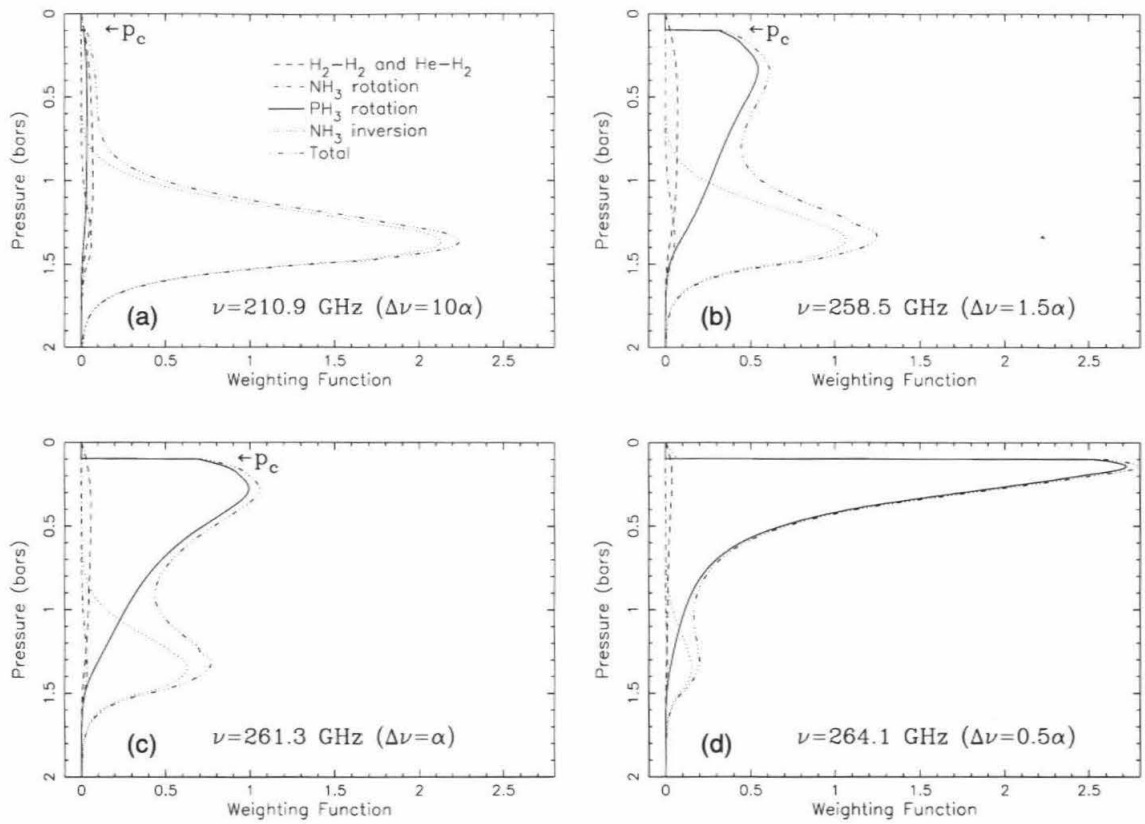

Figure 6.13. Saturn weighting functions for (a) 210.9 GHz ($\Delta\nu = 10\alpha$), (b) 258.5 GHz ($\Delta\nu = 1.5\alpha$), (c) 261.3 GHz ($\Delta\nu = \alpha$), and (d) 264.1 GHz ($\Delta\nu = 0.5\alpha$), where α is the Lorentzian HWHM and $\Delta\nu$ is the frequency offset from the PH_3 line center. The discontinuity evident in the PH_3 weighting function slope at $p_c = 100$ mbar results from our assumed PH_3 cutoff level.

line wings at a pressure of $\sim$ 1.4 bar. Near the PH_3 line center, on the other hand, the line originates from higher up, as a result of the large PH_3 opacity. Very close to line center at $\Delta\nu = 0.5\alpha$ (Figure 6.13d), the weighting function peaks at roughly 150 mbar, but at one half width away from line center at $\Delta\nu = \alpha$ (Figure 6.13c), we see to several hundred mbar. At $\Delta\nu = 1.5\alpha$ (Figure 6.13b), the PH_3 weighting function is decreasing in strength and moving downward, so the contribution from NH_3 dominates the weighting function (although PH_3 contributes down to $\sim$ 1 bar). The predominant contributions to PH_3 opacity therefore arise from pressures of $\sim$ 100-1000 mbar, varying across the line profile. Because all these contributions to Saturn's opacity arise above the cloud decks (which form at pressures $>$ 1.4 bar), we

need not consider the effects of clouds.

6.6. Saturn PH_3 3-2 Observations

We observed Saturn at the CSO on June 22, 1994 using the broad 350 μm filter and 20″ Winston cone, obtaining 61 "on" scans with a resolution 197 MHz. Because the on-site water vapor radiometer was down for repairs, the terrestrial atmospheric optical depth was not measured. However, observations of Jupiter on the 21st and 22nd suggest that weather was poorer on the 22nd. Nevertheless, we detected a *very* broad absorption centered near the PH_3 $3-2$ transition frequency of 800 GHz. We observed the Moon over a similar airmass range with the intention of using it as a division calibrator in order to remove residual atmospheric effects in the T_A^* spectrum. However, the slightly different airmasses of the Moon and Saturn resulted in differing spectral slopes near the edges of atmospheric windows (where transmission through the Earth's atmosphere falls off rapidly).

Since preserving the lineshape of the extremely broad PH_3 feature is essential in order to be able to scale the the raw Saturn spectrum shown in Fig. 6.14 to brightness temperature units, we did not divide by the Moon. The T_A^* spectrum is shown in Fig. 6.14, where the region from 830-845 GHz (which is obscured by an atmospheric O_2 line and an O_3 bandhead) has been blanked, and features in the 880-890 GHz region (discussed in the following chapter on the FTS Jupiter/Saturn submillimeter line survey) appear to correspond to the $10-9$ transition of HCN. The best-fit Lorentzian+linear baseline fit to the broad absorption feature over the frequency range 800-900 GHz (shown as the dotted line in Fig. 6.14) clearly shows the observed PH_3 line to be asymmetrical, presumably due to the low-frequency cutoff in atmospheric transmission. The Lorentzian has an apparent FWHM of 31 GHz and an absorption of $\sim 25\%$ at line center.

Because beam coupling measurements have not yet been completed, it is not

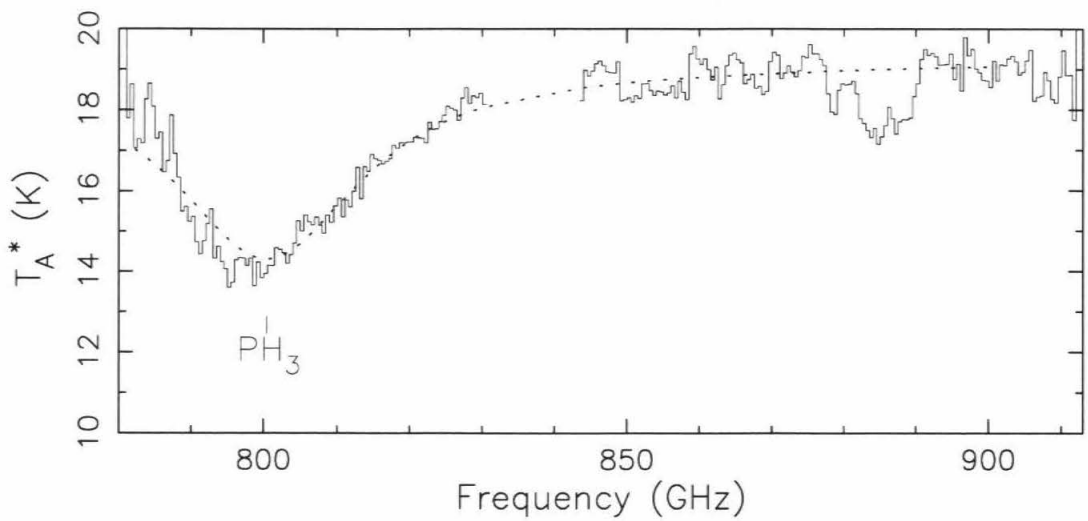

Figure 6.14. Saturn 350 μm spectrum divided by a Moon spectrum. The average central frequency of the $K = 0$, 1, and 2 transitions of the $J = 3 - 2$ PH_3 line is marked. The dotted line is a best-fit Lorentzian+linear baseline for the region 800-900 GHz, excluding the region near 880-890 GHz.

yet possible to convert the observed spectrum to an absolute temperature scale directly. Unfortunately, the atmospheric cutoff at 800 GHz means that we have no information on the continuum level on the low-frequency side of the line. Although we could use the spectrum obtained in the 450 μm filter to estimate the low frequency continuum level, this approach is not reliable because the baseline slopes between filters show a tendency to change discontinuously between filters.

The PH_3 distribution inferred from the 267 GHz $J = 1 - 0$ line would produce a line with a FWHM of 58 GHz and an absorption at line center of 31%. If less PH_3 were actually present, the line width would decrease. However, as long as a cutoff occurs at or above the tropopause, the PH_3 line core will be optically thick at line center for any (constant) concentration $\gtrsim 0.5$ ppm and would therefore reach the cold trap (tropopause) temperature of 82 K (Fig. 6.15), giving roughly the same absorption depth for any reasonable concentration. The observed absorption depth of 25% seems to imply that the line is not saturated at center, but the continuum may be hard to estimate given the large width of the PH_3 line. In order to match the observed

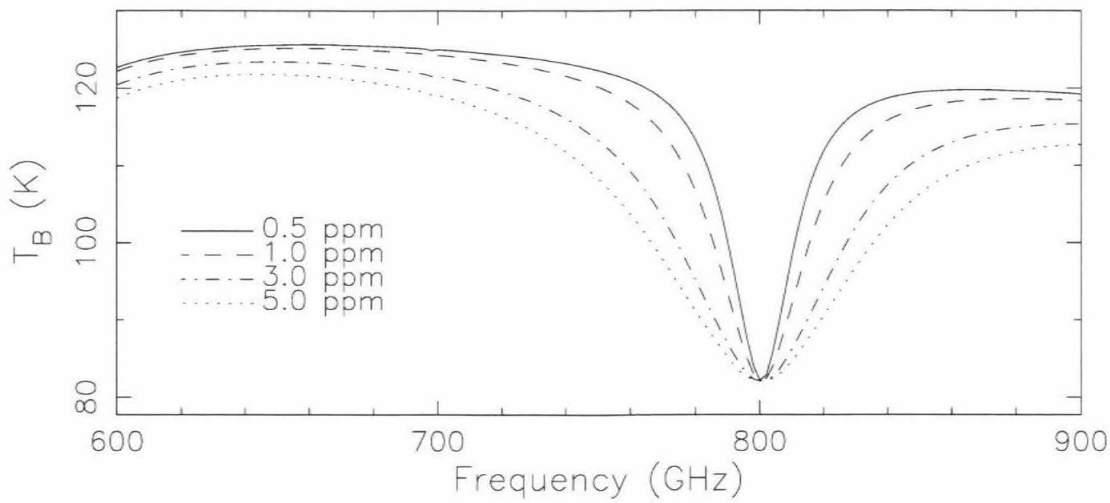

Figure 6.15. Radiative transfer models of Saturn assuming a range of constant PH_3 mole fractions with a cutoff at 100 mbar.

line width using a Lorentzian lineshape, a concentration of < 1 ppm is then needed according to our radiative transfer models. However, such a distribution results in a $1-0$ line with an integrated line area too small to be consistent with the measured low frequency line. Discrepancies between the assumed and actual lineshape parameters, including the *assumption* of a Lorentzian lineshape and use of the $J = 1 - 0$ line broadening coefficient (the only one for which laboratory measurements are available) for the $3 - 2$ line, may account for some of this mismatch.

6.7. Conclusions on PH_3 in Saturn

By comparing the width of the observed PH_3 $J = 1 - 0$ transition in Saturn with that modeled for various abundances using a radiative transfer code, we obtain an estimate of the saturnian PH_3 mole fraction of 3.0 ± 1.0 ppm in the pressure range from $\sim$ 1 bar to 100 mbar (assuming a constant mole fraction at pressures greater than a $\sim$ 100 mbar cutoff pressure). This abundance represents an enrichment of more than 5 times the solar value of $(P/H)_\odot = 2.7 \times 10^{-7}$ (Anders and Grevesse 1989) and is larger than the saturnian PH_3 abundance derived from previous infrared

measurements at these pressures. This abundance also represents a factor of ~ 5 enrichment over the mole fraction derived for Jupiter using the $3-2$ line. While Jupiter's smaller phosphorus abundance might be partially explained by Jupiter's greater gas retention during its formation, it seems likely that other factors, such as the convective transport rate from the deep atmosphere, may play a role. The non-detection of a narrow stratospheric emission core at the line center of the $J = 1-0$ PH_3 rotational transition in Saturn provides a lower limit on the PH_3 cutoff pressure in Saturn's stratosphere of at least 13 mbar, consistent with a low stratospheric PH_3 mixing ratio. The depth of the absorption line also places an upper limit of 140 mbar on the PH_3 cutoff pressure, with 100 mbar providing the best fit to our observations. Although we have also detected the PH_3 $J = 3-2$ line in Saturn, the extreme width of the line combined with its unfortunate position relative to a strong terrestrial H_2O feature have thus far precluded a quantitative analysis.

A summary of saturnian PH_3 abundances inferred by various observers is given in Table XII. Most infrared observations of Saturn prior to 1984 were at wavelengths of 3 and 10 μm. These observations sampled the saturnian atmosphere at pressures of $p \sim$ 400-700 mbar and obtained PH_3 abundances between 0.8 and 2.0 ppm (summarized in Prinn *et al.* 1984). However, measurements by Bézard *et al.* (1987) at 5 μm—a more transparent region of the spectrum—suggested that the PH_3 concentration was significantly higher at the $\sim$ 4 bar level. Similarly, Noll and Larson (1990) reported a best fit to 3 and 10 μm infrared observations—taking into account evidence for higher abundances at the pressures sampled by 5 μm measurements—with a PH_3 mole fraction of 1 ppm for 78 mbar $< p <$ 400 mbar and 7^{+3}_{-2} ppm for $p >$ 400 mbar (where the transition pressure is that of the upper cloud in their two-cloud model). However, the model of Noll and Larson was not optimized for the upper troposphere (i.e., that portion of the atmosphere above the base of the NH_3 clouds at pressures

$\leq$ 1.4 bar).

Table XII. Published saturnian PH_3 mole fractions* from infrared/millimeter observations.

PH_3 Mole Fraction (ppm)	Pressures Probed (mbar)	λ (μm)	Instrument	Reference
$\gtrsim 0.8^{\dagger}$	400-700	10	CFWS	Gillet and Forrest 1974
> 0.2	400-700	10	CGS	Bregman *et al.* 1975
0.9	500-1000	3	FTS	Larson *et al.* 1980
1.6	1000-3200	5	FTS	Larson *et al.* 1980
> 0.8	400-700	10	CGS	Tokunaga *et al.* 1980, 1981
1.0	400-700	10	IRIS	Hanel *et al.* 1981b
1.3 ± 0.8	400-700	10	IRIS	Courtin *et al.* 1984
$0.6^{+0.6}_{-0.3}$	< 100	100	CGS	Haas *et al.* 1985, 1986
$5.0^{\ddagger}$	4000	5	FTS	Bézard *et al.* 1987
3.0	1000-3200	5	FTS	Noll 1987
$7.0^{+3.0}_{-2.0}$	> 400	5	FTS	Noll and Larson 1990
3.0 ± 1.0	100-1000	1100	FTS	Weisstein and Serabyn 1994

*concentrations given relative to the hydrogen abundance have been converted assuming an H_2 mole fraction of 0.963

†tentative detection

‡this best current value (Bézard, pers. comm. 1994) is slightly higher than the published 4.0 ppm

CFWS: cooled filter-wheel spectrometer

CGS: cooled grating spectrometer

FTS: Fourier transform spectrometer

IRIS: Voyager infrared interferometer spectrometer (an FTS)

Infrared observations suffer from a lack of prominent PH_3 features, making it difficult to isolate PH_3 emission from that due to other continuum sources. An exception is the 1972 cm^{-1} Q-branch observed at 5 μm in Saturn by Bézard *et al.* (1987). Comparison with the laboratory measurements of Tarrago *et al.* (1992) allowed these authors to derive a PH_3 mole fraction of $\sim$ 5 ppm in the deep saturnian atmosphere. However, the analysis of 5 μm observations of Saturn is complicated by their sensitivity to reflected solar flux from a few hundred millibars in addition to thermal radiation from several bars. Noll and Larson used micro-windows in the 2000-2160 cm^{-1} region to determine the 7 ppm lower tropospheric PH_3 mole fraction for their model. Although Noll and Larson were able to fit portions of their spectrum (which contains nearly 2000 PH_3 lines) quite well, they had difficulty matching the entire

spectrum, possibly as a result of the discontinuous vertical mole fraction profile they used. Finally, infrared abundance inversions are sensitive to assumptions about cloud heights and structure. All these factors conspire to make an unambiguous estimate of the true PH_3 mixing ratio from infrared measurements very difficult, although these measurements do give convincing evidence for a drop in PH_3 abundance with increasing altitude.

Millimeter measurements avoid the complications inherent in infrared work because they are sensitive only to thermal emission from the upper troposphere (pressures < 1.4 bar; see Fig. 6.13) and are unaffected by reflected solar flux (which is negligible at millimeter wavelengths). The presumed "upper cloud" at 400 mbar (Tomasko *et al.* 1984) can also be ignored since its opacity is negligible at wavelengths longer than infrared. The constant PH_3 mole fraction of 3.0 ± 1.0 ppm which we derive is intermediate to the 3/10 μm and 5 μm-derived values discussed above. However, this is not due to our sampling of pressures intermediate to the two IR bands, since the central portion of the 267 GHz PH_3 line arises from higher in the atmosphere than do the IR lines. As a result, our measurements imply a PH_3 mole fraction in the upper troposphere of Saturn which is considerably larger than the previously published values.

In order to make a more direct comparison of our observations with the two-step PH_3 abundance profile derived by Noll and Larson (1990), we also ran atmospheric models using the profile suggested by these authors. We found that a mole fraction of 1 ppm for 78 mbar $< p <$ 400 mbar and 7 ppm for $p >$ 400 mbar resulted in a PH_3 line width somewhat too narrow and a line depth too small to be consistent with our observations (Figure 6.16), as confirmed by a chi-squared test (see Table X). However, the difference from our best one-step model is not large. It should in principle be possible to model the PH_3 line with various abundance profiles and

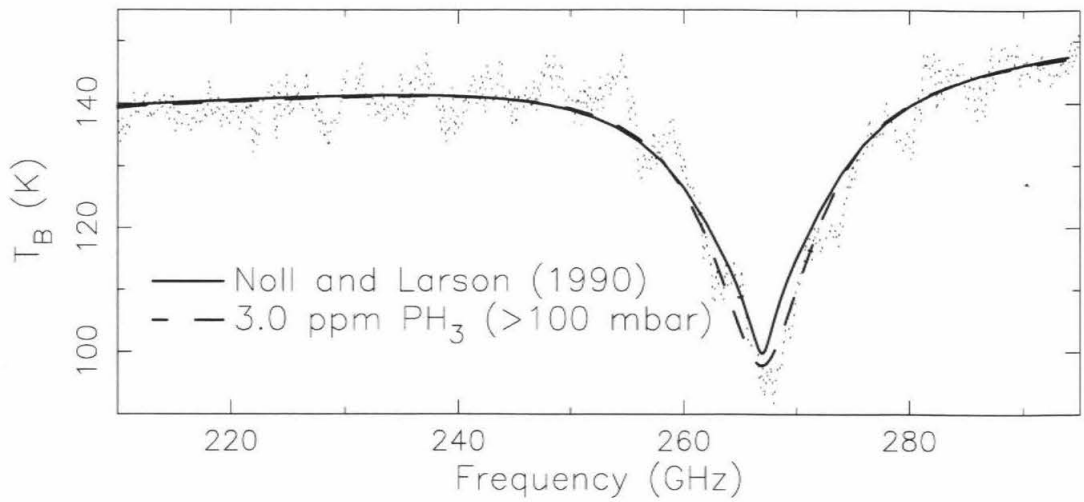

Figure 6.16. Dotted line: data from Fig. 6.9. Solid line: model spectrum for the mixing ratio given by Noll and Larson (1990), 1 ppm for 78 mbar $0 < p < 400$ mbar, 7 ppm for $p > 400$ mbar. Dashed line: model spectrum for a constant PH_3 mixing ratio of 3.0 ppm for $p > 100$ mbar (central curve from Fig. 6.12).

to use chi-squared testing to determine the profile matching our observations most closely. For example, we could use more complicated exponential profiles such as those adopted by Tokunaga *et al.* (1979), Tokunaga *et al.* (1980), Haas *et al.* (1985), or Griffith *et al.* (1992). Unfortunately, although the central portion of the observed PH_3 absorption line can be fit fairly cleanly, the remnant ripple evident in Fig. 6.9 would make it difficult to distinguish small differences in the lineshape, implying that our data do not yet warrant a parameterization beyond the first-order one-step approximation. The simple one-step PH_3 model we use is already consistent with a convective origin for tropospheric PH_3 in Saturn, since convection should result in a well-mixed, nearly constant tropospheric PH_3 mixing ratio up to the level at which PH_3 is most effectively destroyed by photodissociation, making it adequate for our analysis. Until further progress is made in the analysis of the $J = 3 - 2$ line near 800 GHz, or in reducing the Winston cone-induced ripple in the 1300 μm filter, more detailed modeling does not appear warranted for Saturn.

Finally, we address the question of time dependence. The "Great White Spot" equatorial atmospheric disturbance that occurred in Saturn in late September of 1990 (Westphal *et al.* 1992) may have resulted in an increase in the transport of PH_3 to the atmospheric levels at which we observed it. Because we have no data prior to December 1992, we are unable to compare observations before and after the event in order to address this possibility. However, our 1300 μm observations with the FTS indicate that no substantial change has occurred in the millimeter spectrum of Saturn between December 1992 and September 1995.

Chapter 7

Jupiter and Saturn Submillimeter Line Surveys

"'Yes indeed,' said the unicorn. ... 'What can we measure? ... We are experts in the theory of measurement, not its practice.'"

—J. L. Synge *(Kandelman's Krim)*

7.1. Introduction

In addition to NH_3 and PH_3, other molecules expected to play an important chemical role in the atmospheres of Jupiter and Saturn are H_2O, H_2S, HCN, HCP, CH_4, CH_3D, and CO. Additional possible constituents of jovian atmospheres include the hydrogen halides HBr and HCl and the alkali hydrides LiH and NaH. Of the molecules just listed, the submillimeter transitions of NH_3, H_2O, and CH_4 cannot be observed from the ground because NH_3 and H_2O are obscured by the Earth's atmosphere and CH_4 has only extremely weak transitions. However, the remainder of these species have rotational transitions lying at the millimeter and submillimeter wavelengths accessible to ground-based observation. The presence of appreciable quantities of any of these molecules in the tropospheres of the giant planets would therefore result in absorption features at their rotational transition frequencies, and the lineshapes of such features could be inverted to derive the atmospheric concentration (and, in the best of circumstances, the vertical distribution) of the detected molecules.

Because the intensities of molecular rotational transitions increase with frequency as J^3 for linear molecules, where J is the rotational quantum number, the highest frequency lines usually provide the tightest constraints. However, the higher frequency lines fall in poorer atmospheric transmission windows, and so a combination of large line absorption and optimal atmospheric transmission is needed to provide

the tightest constraints.

We used the FTS to survey the spectra of Jupiter and Saturn in all available submillimeter atmospheric windows between 300 and 1000 GHz (1000 and 300 μm). The molecules which were searched for include the saturated molecules PH_3 and H_2S, the hydrogen halides HCl and HBr, the alkali hydrides LiH and NaH, as well as HCN and HCP. The strong absorption feature detected in both Jupiter and Saturn at 800.5 GHz, corresponding to the $J = 3 - 2$ transition of PH_3, has already been discussed. Features coincident with the $J = 1 - 0$ transition of HCl and the $10 - 9$ transition of HCN were also tentatively observed in Saturn. No other molecules were detected in either planet, setting stringent limits on most of the species listed above. Several of these limits are the first observational constraints on these molecules in Jupiter and Saturn, and most of the remainder are substantial improvements over existing limits.

For the most part, the limits are lower in Saturn than in Jupiter, primarily as a result of Saturn's weaker gravity. Because the column mass abundance σ_c above a pressure p is given by $\sigma_c = p/g$ (where g is the gravitational acceleration), the column abundance for a fixed minor species concentration above a given pressure level is larger in Saturn than in Jupiter. The major continuum opacity source in both planets is NH_3, which condenses deeper in Saturn due to colder tropospheric temperatures. As a result, optical depth unity is reached at roughly the same pressure in Jupiter and Saturn (Figs. 5.10a-b), but the latter's gravity is 2.5 times weaker. Minor species are therefore detectable at smaller concentrations in Saturn than in Jupiter. In practice, Saturn's smaller flux decreases the signal-to-noise ratios of observations, canceling out this effect to some extent.

7.2. Observations

We observed Jupiter and Saturn at the CSO on June 21-24, 1994 (UT) using the FTS. For these broadband observations, we used two broad bandpass metal-

mesh filters which cover the high frequency 350 and 450 μm atmospheric windows in their entirety. Our molecular line search made use of these 350 μm and 450 μm filters, as well as the standard CSO 600 and 800 μm filters. Table XIII summarizes the observations obtained in each filter for both planets and the Moon (which was used as a division calibrator; see below). The number of scans in individual filters was selected in order to yield comparable RMS noise in each filter. Fig. 7.1 plots again the atmospheric transmission above Mauna Kea for 1 mm precipitable H_2O (Fig. 7.1a), together with the normalized transmissions of our suite of filters (Fig. 7.1b) and model spectra of Jupiter (Fig. 7.1c) and Saturn (Fig. 7.1d). In Figs. 7.1c and 7.1d, the FTS observations to be discussed in detail below have been scaled to and superposed on these model spectra in order to provide an overview of the observational frequency coverage. The higher noise apparent in the Saturn spectrum relative to Jupiter results from a combination of poorer atmospheric transmission and smaller planetary flux.

Table XIII. Summary of the observations constituting the FTS Jupiter and Saturn submillimeter line survey.

Filter (μm)	Date	Jupiter			Moon		
		UT	Airmass	"On" Scans	UT	Airmass	"On" Scans
800	June 23, 1994	09:41-09:56	1.83-1.97	6	13:25-13:28	1.97-1.98	2
600	June 24, 1994	06:42-09:29	1.18-1.74	48	09:35-09:43	1.43-1.45	4
450	June 21, 1994	09:05-09:37	1.50-1.68	8	10:32-10:46	1.59-1.65	4
350	June 21, 1994	07:57-08:36	1.26-1.36	8	08:46-08:52	1.31-1.32	2

Filter (μm)	Date	Saturn			Moon		
		UT	Airmass	"On" Scans	UT	Airmass	"On" Scans
800	June 24, 1994	11:40-18:20	1.13-1.92	80	07:54-08:02	2.09-2.18	2
600	June 23, 1994	12:34-18:45	1.13-1.92	111	11:37-11:40	1.40-1.40	2
450	June 21, 1994	12:58-16:04	1.15-1.41	6	10:32-10:46	1.59-1.65	2
350	June 22, 1994	12:40-18:15	1.13-1.60	61	08:42-08:56	1.34-1.34	2

For these observations, the instrumental field of view was defined by a 20″ aperture Winston cone. Since the CSO's main beam HPBW varies from 20″ at 345 GHz to 7.3″ at 950 GHz, the FTS has a spatial resolution decreasing from 24″ to 19″

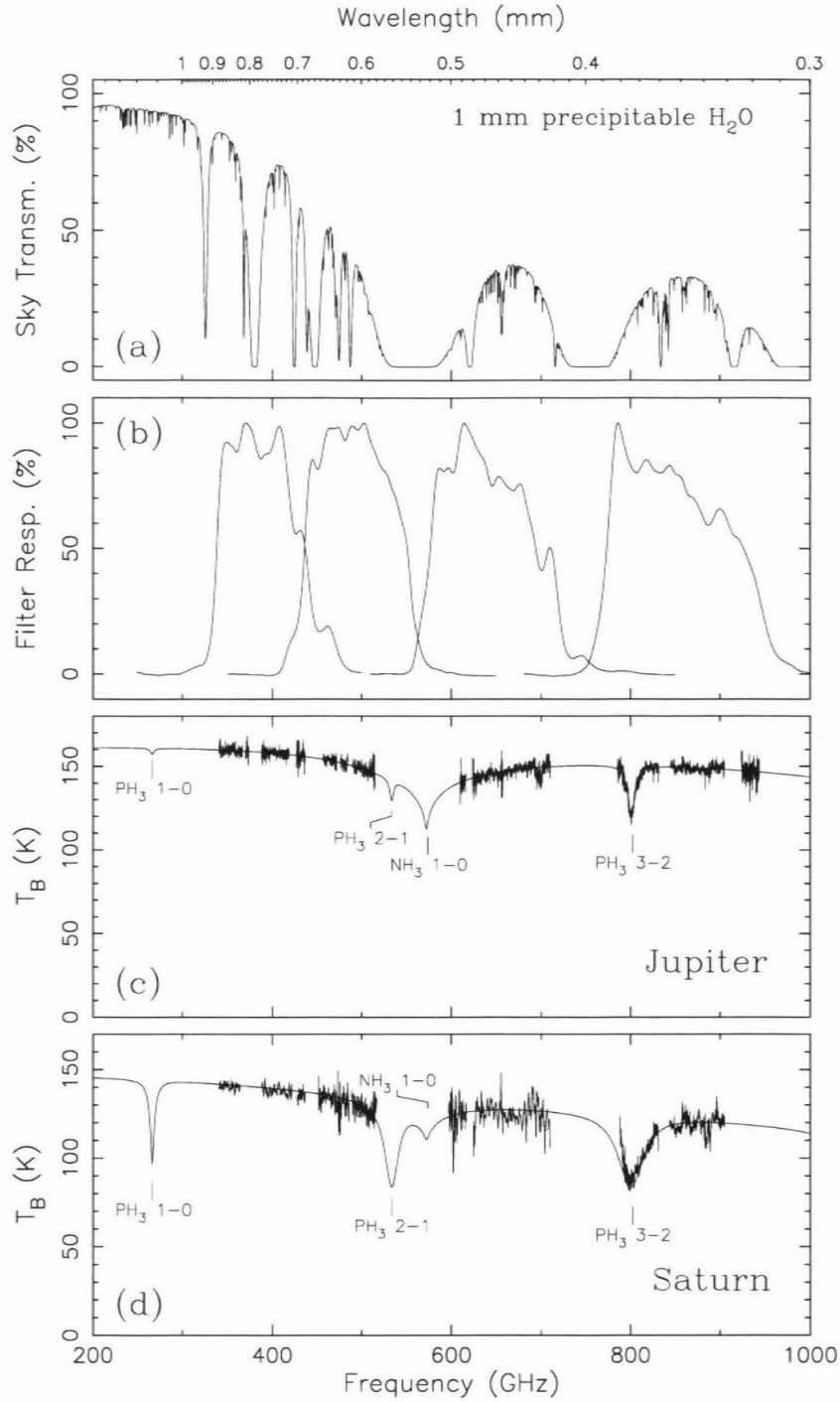

Figure 7.1. (a) Model atmospheric transmission above Mauna Kea for 1 mm precipitable H_2O, generated using the program **AT** (Grossman 1989). (b) The set of four filters used for the Jupiter/Saturn submillimeter line survey. From left to right, they are referred to in the text as the 800 μm, 600 μm, 450 μm, and 350 μm filters. (c) Radiative transfer model spectrum of Jupiter with FTS data superposed. The raw data (0.2 GHz resolution) has been scaled to lie along the model continuum, but the signal-to-noise ratio is preserved, illustrating the frequency range covered and the relative noise in each of the atmospheric windows. (d) Radiative transfer model spectrum of Saturn with FTS data superposed in like fashion, except that the 450 μm ($\sim$ 600 – 700 GHz) data have been binned to 0.5 GHz.

over this frequency range (Serabyn and Weisstein 1996). The size of Jupiter during the observations was 41.3″ × 38.6″, and of Saturn, 17.6″ × 15.7″.

7.3. Calibration

The resultant Jupiter and Saturn spectra obtained in each filter were divided by a spectrum of the Moon obtained over a similar airmass range (see Table XIII). This ratioing procedure divides out the Moon coupling efficiency (that fraction of the forward beam's solid angle which hits the Moon) and nearly eliminates residual terrestrial ozone features which were not completely removed by the T_A^* calibration procedure (which works perfectly only for an isothermal atmosphere). Even so, the division is not perfect, with a number of small ozone features remaining in the spectra.

Because humid weather in a subsequent observing run prevented completion of beam coupling measurements necessary to directly convert our observations to an absolute brightness temperature scale, we instead numerically scaled from the Jupiter/Moon and Saturn/Moon ratio spectra using the continuum level provided by our jovian planet radiative transfer model. The radiative transfer calculation was done using the Planck law, and the output intensity was converted to the blackbody (or "brightness") temperature T_B corresponding to the calculated intensity. Next, we fit piecewise linear baselines to the measured planetary continua in each of our measured spectra, and to the synthetic spectra given by our model. We then rescaled the observed spectra by the ratio of the continua so that the data continuum levels matched those of the models. The overall results are shown in Figs. 7.1c and 7.1d. These figures summarize the observations, but the absolute temperature scale on the vertical axes should not be construed to imply that our data has been absolutely calibrated. The temperature scale in Figs. 7.1c and 7.1d is based on radiative transfer modeling and was not derived from observation.

For small absorption features superposed on continuum emission, this proce-

dure preserves the line/continuum ratio since beam coupling affects the spectrum at each frequency by a given scaling factor which is independent of the relative importance of line absorption and continuum emission at that frequency. The scaling procedure does remove intrinsic information on absolute planetary fluxes, but allows a straightforward comparison of observations with radiative transfer models. In the absence of calibrated beam coupling measurements (which we continue to pursue), and given that the uncertainties on existing submillimeter Jovian brightness temperature measurements are comparable to the estimated uncertainties in radiative transfer models (due to uncertainties in line parameters and spectral lineshapes, especially for NH_3), the above scaling procedure gives sufficiently accurate continuum temperatures to allow the determination of accurate upper limits.

7.4. Results/Upper Limits

Table XIV lists, in alphabetical order, the molecular species considered in this paper which have submillimeter transitions falling within one or more of our filter bandpasses. Column 1 lists the names of the molecules, and column 2 gives their electric dipole moments μ (in Debye). The range of frequencies over which RMS noise was computed for the highest signal-to-noise transition of each molecule is given in column 3, and column 4 gives the RMS noise over this frequency range. The frequency range must be chosen carefully for transitions falling near the edge of an atmospheric window so as to include as much bandpass as possible while excluding frequencies strongly affected by atmospheric absorption. Column 5 presents the 3σ upper limit obtained from our FTS measurements for the mole fraction of each undetected species (discussed in detail below) and the best-fit concentrations for the detected molecules. Column 6 gives the best previously available observational upper limits.

Table XIV. 3σ upper limits for various molecular species in Jupiter and Saturn.

Jupiter

Species	μ (D)	Freq. Range (GHz)	RMS (K)	FTS Upper Limit (or mole fraction)	Previous Best Limit (or mole fraction)
CH_3D	0.0056	690.0-710.0	4.6	$< 8.8 \times 10^{-5}$	$= 1.6 - 2.4 \times 10^{-7}$
CO	0.1098	800.0-815.0	2.8	$< 1.3 \times 10^{-7}$	$= 1.0 - 1.6 \times 10^{-9}$
H_2S	0.974	680.0-694.0	2.6	$< 2.9 \times 10^{-8}$	$< 3.3 \times 10^{-8}$ (a)
HBr	0.828	490.0-510.0	2.7	$< 7.0 \times 10^{-9}$	—
HCl	1.109	623.7-630.0	5.2	$< 5.0 \times 10^{-9}$	—
HCN, condens.	2.984	870.0-900.0	2.3	$< 2.0 \times 10^{-9}$	—
HCN, no condens.	2.984	870.0-900.0	2.3	$< 3.0 \times 10^{-10}$	$= 2^{+2}_{-1} \times 10^{-9}$ (b)
HCP	0.039	665.0-681.0	1.7	$< 2.2 \times 10^{-8}$	—
LiH	5.882	870.0-905.0	2.4	$< 1.1 \times 10^{-11}$	—
NaH	6.7	860.0-880.0	2.0	$< 8.0 \times 10^{-12}$	—
PH_3	0.574	—	—	$= 6.0 \times 10^{-7}$ (c)	$= 2.6 - 9.3 \times 10^{-7}$

Saturn

Species	μ (D)	Freq. Range (GHz)	RMS (K)	FTS Upper Limit (or mole fraction)	Previous Best Limit (or mole fraction)
CH_3D	0.0056	455.0-473.0	3.6	$< 3.6 \times 10^{-6}$	$= 3.9 \pm 2.5 \times 10^{-7}$
CO	0.1098	340.0-364.0	1.5	$< 3.3 \times 10^{-8}$	$= 1.0 \pm 0.3 \times 10^{-9}$
H_2S	0.974	675.0-693.0	9.0	$< 1.6 \times 10^{-8}$	$< 2.0 \times 10^{-7}$
HBr	0.828	490.0-510.0	4.0	$< 1.1 \times 10^{-9}$	—
HCl	1.109	624.1-635.0	10.2	$= 1.1 \times 10^{-9}$	—
HCN, condens.	2.984	348.0-360.0	1.9	$< 1.5 \times 10^{-8}$ (d)	—
HCN, no condens.	2.984	348.0-360.0	1.9	$< 4.0 \times 10^{-10}$ (e)	$< 7 \times 10^{-9}$
HCP	0.039	345.0-364.0	1.7	$< 5.0 \times 10^{-9}$	—
LiH	5.882	880.0-892.0	7.0	$< 1.2 \times 10^{-11}$	—
NaH	6.7	855.0-880.0	3.5	$< 5.0 \times 10^{-12}$	—
PH_3	0.574	—	—	$= 3.0 \times 10^{-6}$ (f)	$= 0.9 - 10.0 \times 10^{-6}$

Notes.

In column 5, an '=' indicates an FTS detection, while a '<' indicates an upper limit. In column 6, an '=' indicates a previous detection, a '<' indicates a previous upper limits, and an '—' indicates a molecule for which no previous limit or detection exists.

[a] This value is a 1σ limit.

[b] This observation is apparently in error.

[c] The 0.6 ppm concentration quoted here is derived from the $J = 3 - 2$ line.

[d] The line is so broad that this limit is questionable. If present, the line might have been removed by baseline rescaling.

[e] This upper limit is the concentration best matching the observing spectral feature at the frequency of the HCN $10 - 9$ transition. The lack of detectable HCN features in lower frequency windows give a more stringent upper limit of $< 1.1 \times 10^{-10}$.

[f] The 3 ppm concentration quoted here is derived from the $J = 1 - 0$ line at 267 GHz (Weisstein and Serabyn 1994).

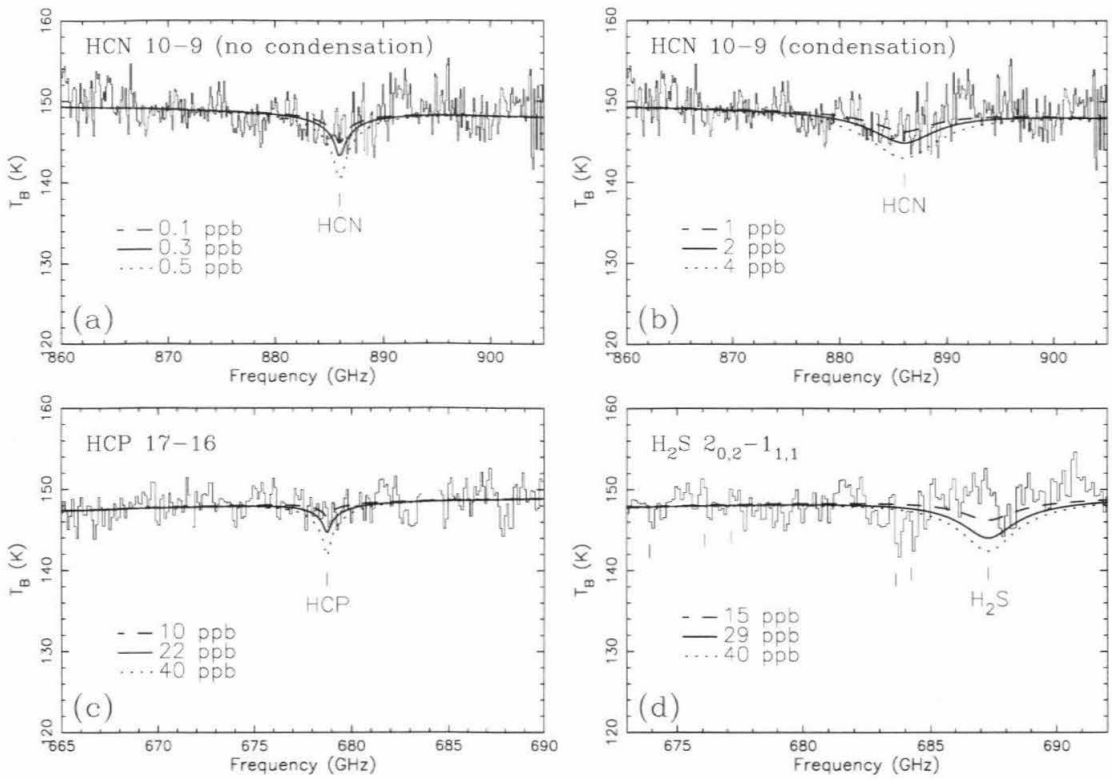

Figure 7.2. Jupiter non-detections. The histograms are the observed spectra at 200 MHz resolution, and the curves are radiative transfer models convolved to the instrumental resolution of 200 MHz. The middle (solid) model curves give the 3σ upper limits. (a) HCN with no condensation. (b) HCN including condensation. The terrestrial O_3 features at 883 and 889 GHz were not included in the spectral RMS and have been blanked in Figs. 7.2a and 7.2b. (c) HCP. (d) H_2S. Residual O_3 features near 684 GHz have been ticked.

7.4.1 HCN

Our observations covered the $4-3$ (354.5 GHz), $8-7$ (708.9 GHz), $9-8$ (797.4 GHz), and $10-9$ (886.0 GHz) transitions of the HCN molecule. None of these lines were detected in Jupiter. In Saturn, a feature is present at the frequency of the $10-9$ transition (Fig. 7.4), but no other HCN lines were detected. We therefore computed models to estimate the HCN concentration required to produce the observed line in Saturn and to place upper limits on the HCN concentrations based on the non-detections in Jupiter and Saturn. The models assumed broadening coefficients as measured by Rohart *et al.* (1987) for $HC^{15}N$.

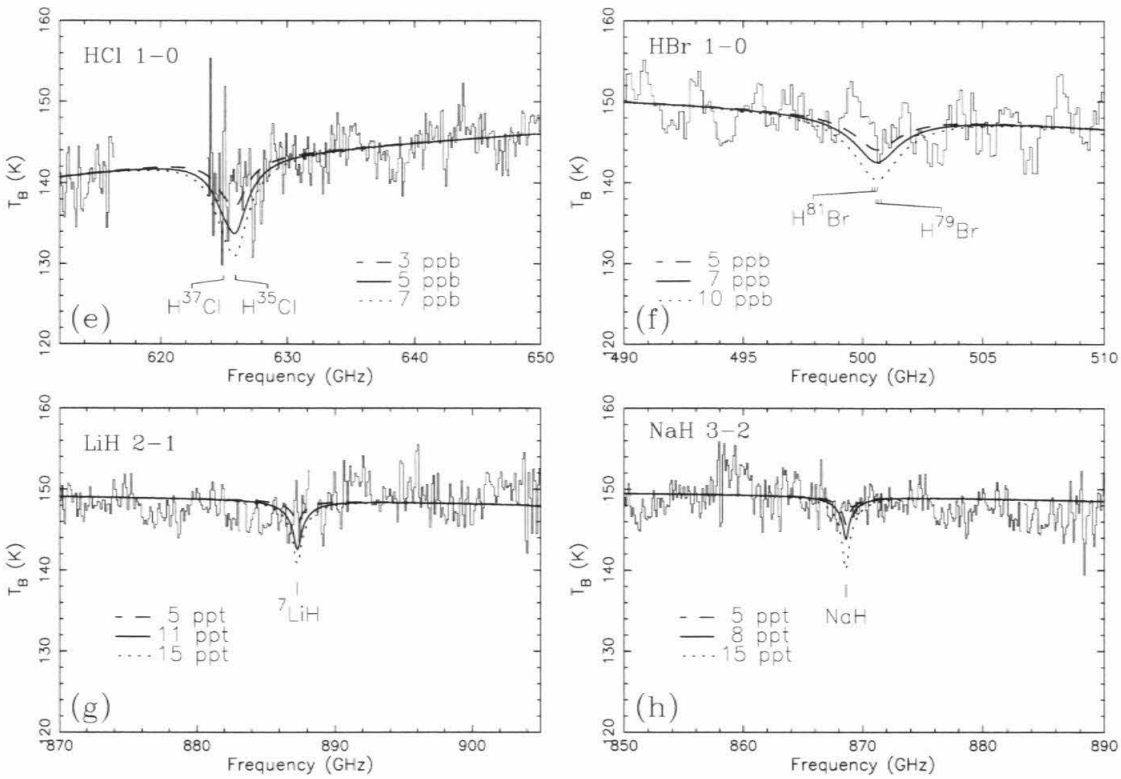

Figure 7.2. Jupiter non-detections, con't. (e) HCl. The frequencies obscured by a terrestrial H_2O feature centered at 620.7 GHz, in the middle of the bandpass, have been blanked, but result in greatly increased noise near the H_2O feature at 625 GHz. (f) HBr. The 2 GHz ripple results from reflective standing waves which did not divide out in this frequency range. (g) LiH. A strong O_3 feature near 889 GHz has been blanked. (h) NaH.

$$\Delta\nu = p_{H_2}(4260 \text{ MHz/bar})\left(\frac{300 \text{ K}}{T}\right)^{0.76} + p_{He}(1425 \text{ MHz/bar})\left(\frac{300 \text{ K}}{T}\right)^{0.66}. \quad (7.1)$$

We first consider upper limits derived from our non-detections, deferring for the moment discussion of the $10-9$ line in Saturn. In Jupiter, the non-detection of the $10-9$ rotational transition of HCN sets the most stringent upper limit, while for Saturn, the $3-2$ is the most definitive. For a constant HCN mole fraction in the stratosphere and troposphere, the 3σ upper limit is 0.3 ppb for Jupiter (Fig. 7.2a), and 0.1 ppb for Saturn (Fig. 7.3a). If we consider the more realistic case of condensation in the upper atmosphere, we obtain limits of 2 ppb (Jupiter; Fig. 7.2b) and $\sim$ 15 ppb (Saturn; Fig. 7.3b) in the deep atmosphere below the condensation level. In the

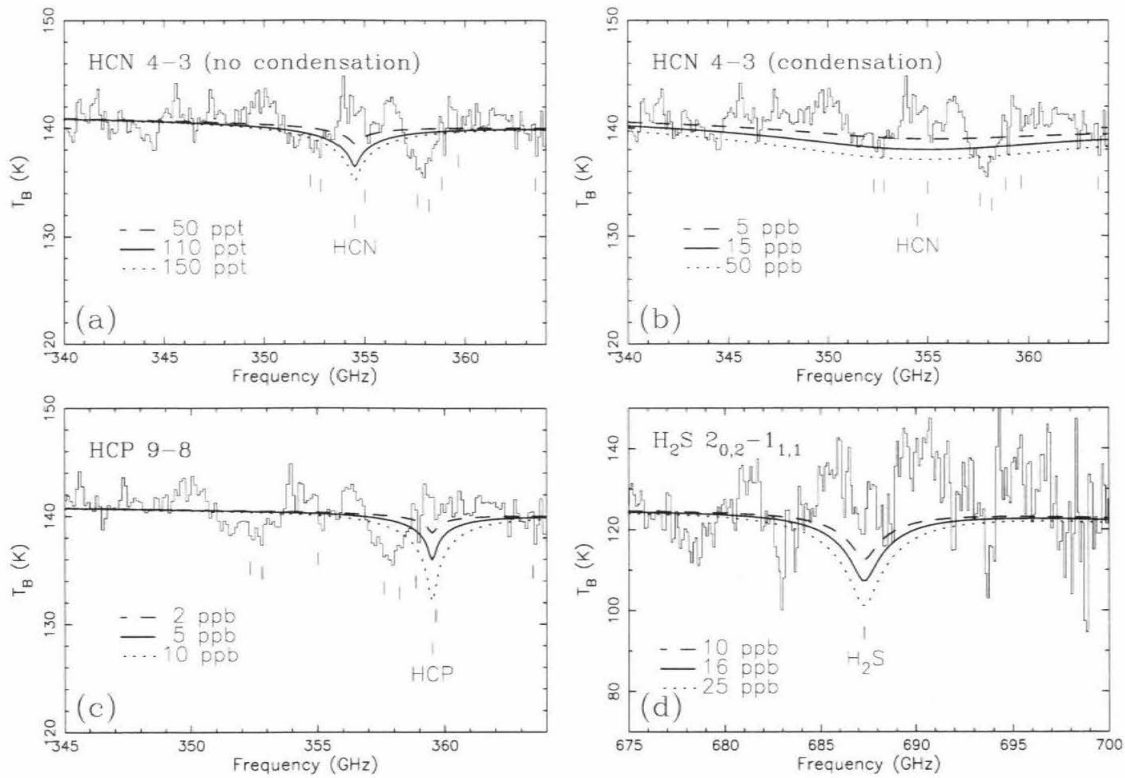

Figure 7.3. Saturn non-detections. The histograms are the observed spectra and 200 MHz resolution, and the curves are radiative transfer models convolved to the instrumental resolution of 200 MHz. The middle (solid) model curves give the 3σ upper limits, except for HCl, where it gives the model consistent with a 3σ detection. (a) HCN, not including condensation. (b) HCN with condensation. (c) HCP. Terrestrial O_3 features with strengths $> 10^{-4}$ nm^2 MHz and excitation temperatures < 1000 K have been ticked in Figs. 7.3a-7.3c. (d) H_2S. The increased noise at high frequencies occurs near the edge of the atmospheric window.

case of Saturn, however, the line is so broad that it is quite difficult to separate HCN line wing emission from the continuum, a problem exacerbated by the baseline fitting and rescaling procedure discussed above which has been applied to the spectrum. Furthermore, the limits in the case of HCN condensation are subject to rather large uncertainties because the HCN vapor pressure is highly sensitive to temperature near its saturation point (Bézard *et al.* 1995). Not only are the temperature profiles known to vary spatially (and probably temporally as well), but the saturation vapor law is also poorly determined. The HCN vapor pressure measurements used here are those of Small, which have been fit by Atreya (1986) with an equation of the form $V_p = a - b/(T - c)$, where V_p is vapor pressure. However, Small's data only

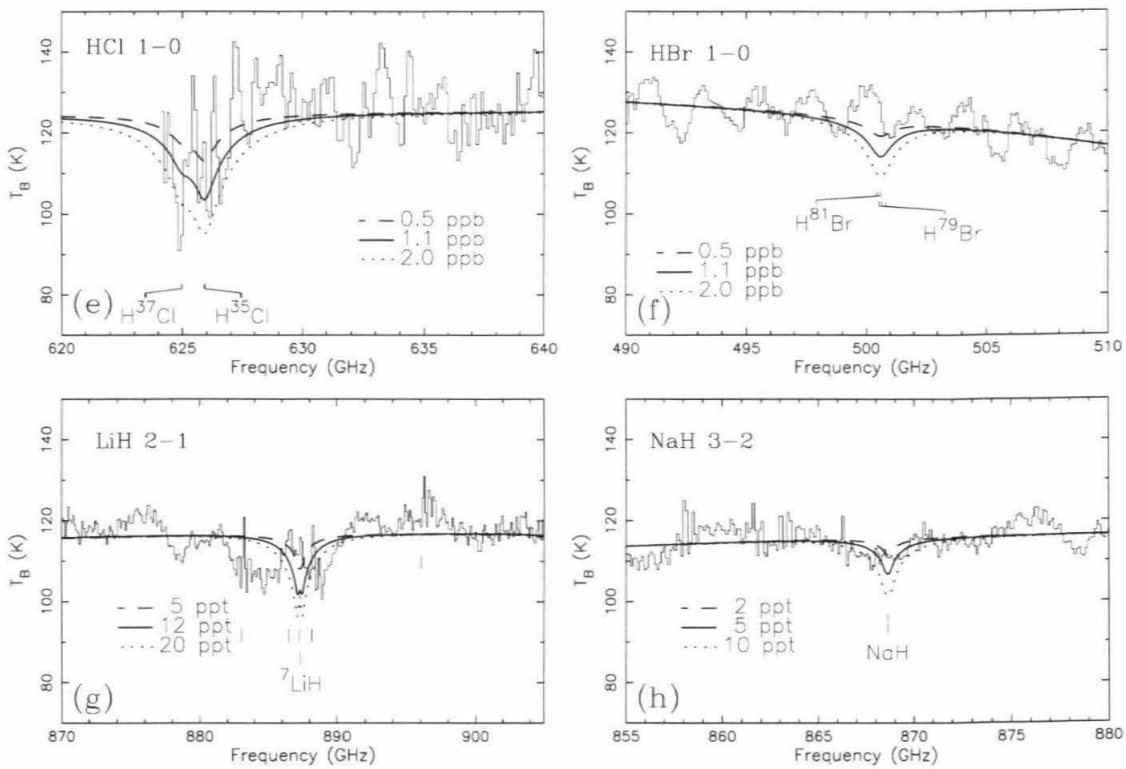

Figure 7.3. Saturn non-detections, con't. (e) HCl. The frequencies obscured by a terrestrial H_2O feature centered at 620.7 GHz, in the middle of the bandpass, have been blanked, but result in greatly increased noise near this feature. As can be seen by comparison with the middle model curve, the spectrum is consistent with an HCl detection at a concentration of 1.1 ppb. (f) HBr. The 2 GHz ripple results from reflective standing waves which did not divide out in this frequency range. (g) LiH. A small emission core arises from stratospheric LiH in the atmospheric model. The baseline in the 880-890 GHz frequency range is noticeably disturbed by either an instrumental ripple, terrestrial weather variations, or perhaps an unknown line in Saturn. The frequencies of strong O_3 transitions have been indicated with tick marks. (h) NaH. The baseline in this frequency range is also somewhat ripply.

extend down to a temperature of 202 K, and so the curve is an extrapolation at lower temperatures.

We now turn to the 885.97 GHz HCN $10 - 9$ transition in Saturn. As can be seen in Fig. 7.3g (to be discussed in more detail in §7.4.5), which shows the relevant spectral region, the baseline between 880 and 890 GHz is not flat—the spectrum is consistent with two to three broad absorption features, or a single even broader absorption with a superposed baseline ripple. In Jupiter (Fig. 7.2g) no analogous feature is present. This suggests that the spectral dips originate in Saturn's spectrum and are not an artifact produced by terrestrial absorption features not entirely removed

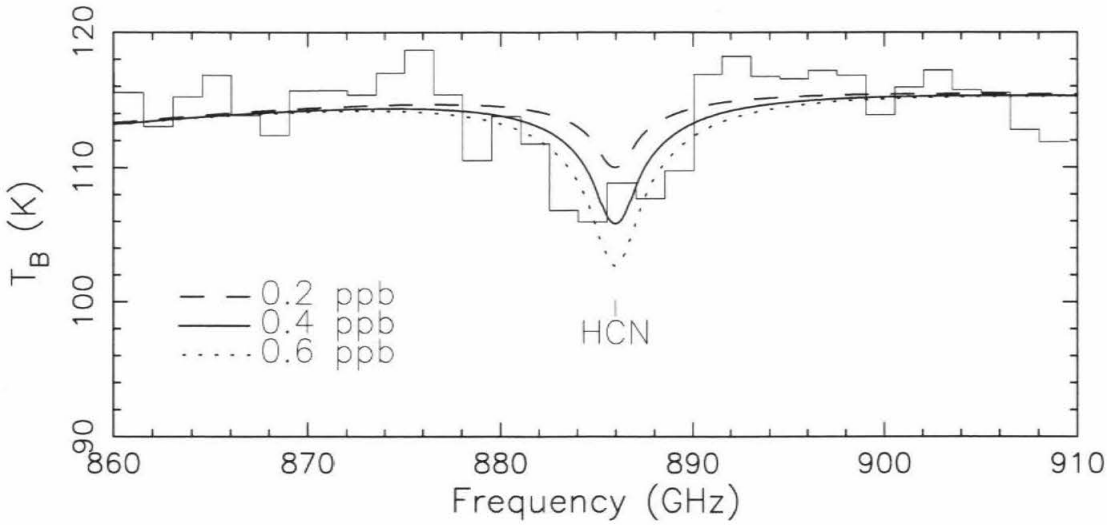

Figure 7.4. Observed Saturn spectrum (histogram curve) in the spectral region corresponding to the 10 – 9 transition of HCN, rebinned to 1.5 GHz channels, and model spectra for 0.2, 0.4, and 0.6 ppb HCN (smooth curves). The binned spectrum has *not* been divided by the Moon, but has been scaled to the continuum level of the radiative transfer models. In the model spectra, HCN has been distributed with a constant mole fraction throughout the stratosphere and troposphere. The model spectra have also been convolved to a resolution of 1.5 GHz. A mole fraction of 0.4 ppb HCN fits the observed spectrum best.

by the calibration procedure. This conclusion is further bolstered by the fact that recent re-observations of Saturn in the relevant 350 μm filter consistently show a broad absorption in the same frequency region. In order to improve the signal-to-noise ratio and to better accentuate broad features, we thus re-binned our 0.2 GHz spectral resolution data to a resolution of 1.5 GHz. Fig. 7.4 shows the prominent absorption feature which results.

The broad absorption line evident in in Fig. 7.4 is centered at 887.0 GHz (as obtained by fitting a Lorentzian lineshape), in reasonable but not perfect agreement with the HCN 10 – 9 transition frequency. We thus also searched the line catalog of Pickett *et al.* (1992) for additional line candidates centered near 886 GHz, but no plausible nearby transitions were found, making HCN the best candidate for producing the observed feature (see however §7.4.5 for a discussion of LiH). As models which include HCN condensation produce lines too broad and shallow to reproduce

the observed feature, we ran radiative transfer models using a variety of constant HCN mole fractions to determine the possible effect of HCN on this part of the spectrum. As shown in Fig. 7.4 (where the superposed model spectra have been convolved a resolution of 1.5 GHz, corresponding to the bin size of the data), a mole fraction of 0.4 ppb HCN gives good agreement with the data. This value is four times the upper limit obtained from non-detections of the lower frequency HCN lines, implying that the lower frequency transitions (and the $3-2$ line in particular; see Fig. 7.3a) should have been observable if HCN were distributed with a constant HCN mole fraction.

We attempted to resolve this discrepancy by considering models in which HCN was restricted to a vertical layer characterized by a given concentration, cuton pressure, and cutoff pressure. Surprisingly, no combination of these parameters was capable of reproducing the required contrast in line area between the $3-2$ non-detection and the possible $10-9$ feature. In fact, all models gave very similar absolute depths for the two lines, although the continuum levels at 350 and 880 GHz differ from one another by $\sim$ 30 K (and arise from different pressure levels). Given the conflict between the low abundance limit obtained from the $3-2$ line and the higher concentration implied by the observed $10-9$ feature, the detection of HCN in Saturn cannot yet be considered certain, and so we adopt the $10-9$ best-fit concentration of 0.4 ppb as the overall upper limit for a constant troposphere and stratosphere HCN profile in Saturn. Despite the difficulty of reaching a unique interpretation of our Saturn HCN data, the 0.4 ppb limit still provides a considerable improvement over the best published infrared upper limit.

HCN can be produced by equilibrium chemistry in the deep troposphere of Jupiter (Fegley and Lodders 1994), by coupled photochemistry of CH_4 and NH_3 in the upper troposphere (Kaye and Strobel 1984), or by a combination of the two. Chemical models of Jupiter predict upper tropospheric HCN concentrations of 0.6-2.6

ppb for eddy diffusion coefficients in the range $10^7 - 10^9$ cm^2 s^{-1} (Fegley and Lodders 1994). However, photochemistry can also produce concentrations in the same range if vertical mixing is slow ($K \sim 10^4$ cm^2 s^{-1}) in the upper troposphere. Our upper limit of 2 ppb on Jupiter can therefore not rule out either process.

Our HCN upper limit on Jupiter is, however, inconsistent with the reported HCN detection on Jupiter by Tokunaga *et al.* (1981). These authors identified three infrared lines which they interpreted as arising from tropospheric HCN at a concentration of 2^{+2}_{-1} ppb. Condensation of HCN was ignored in their model, which also neglected possible emission due to stratospheric HCN. In contrast, our "no condensation" profile assumes a constant HCN mole fraction in the stratosphere as well as the troposphere. This allows the existence of an emission core, which decreases the line depth when convolved to our instrumental resolution, hence providing a more conservative upper limit. Our HCN upper limit of 0.3 ppb limit in the absence of condensation is significantly lower than the Tokunaga *et al.* (1981) value, and we therefore believe that the detection reported by Tokunaga *et al.* (1981) was likely spurious. This conclusion is further supported by a recent remeasurement and reassessment of the purported infrared detections by Bézard *et al.* (1995), who found no features at the transition frequencies observed by Tokunaga *et al.* (1981). Based on these non-detections, Bézard *et al.* (1995) have obtained an HCN upper limit of 1.0 ppb, ignoring condensation. (A weaker limit of 6.0 ppb results if condensation is included.) It therefore appears that HCN is significantly less abundant in the upper atmosphere of Jupiter than reported in the work of Tokunaga *et al.* (1981). It also appears that submillimeter observations are capable of providing the tightest constraints on high dipole moment molecules such as HCN in the Jovian planets.

7.4.2 HCP

The HCP molecule, a disequilibrium species in the atmospheres of the giant

planets expected to form from the photodissociation products of CH_4 and PH_3 (Kaye and Strobel 1984), has many rotational transitions in our spectral bands. Based on our non-detections of the HCP $9-8$ (359.5 GHz), $10-9$ (399.4 GHz), $12-11$ (479.3 GHz), $16-15$ (638.9 GHz), $17-16$ (678.8 GHz), and $22-21$ (878.0 GHz) lines, we are able to place 3σ upper limits of 22 ppb and 5.0 ppb on its mole fraction in the upper atmospheres of Jupiter (Fig. 7.2c) and Saturn (Fig. 7.3c), respectively. For Jupiter, the best limit is obtained for the $17-16$ line, while the $9-8$ line provides the tightest constraint for Saturn. In the absence of laboratory data, we assumed the same broadening coefficient of 2100 MHz/bar and temperature exponent of 0.6 as for CO (see below). Our Jupiter limit is higher than the $\sim$ 9 ppb predicted by photochemical models of Kaye and Strobel (1984) and assumed in the radiative transfer models of Bézard *et al.* (1986). However, our 5 ppb limit for Saturn is smaller than this value, indicating that existing photochemical models predict an excess of HCP for this planet.

7.4.3 H_2S

Despite the many strong millimeter-submillimeter lines which should betray the presence of H_2S in Jupiter's and Saturn's atmospheres, this molecule remains undetected, presumably because it is removed by the formation of NH_4SH clouds in their deep atmospheres and exists in equilibrium only at unobservable levels beneath this cloud deck (Atreya 1986). Although H_2S has been suggested as a cloud chromophore in Jupiter (Lewis and Prinn 1970), its lack of detection calls this hypothesis into question. Unsuccessful searches in Jupiter have been carried out by Larson *et al.* (1984) in the infrared and Joiner *et al.* (1992) in the millimeter. The best current upper limit in Jupiter is that of Larson *et al.* (1984), 33 ppb at the 1σ level. In the case of Saturn, Owen *et al.* (1977) give an upper limit of 200 ppb.

In our FTS spectra, we searched for but did not find the strong $2_{2,1}-2_{1,2}$

(505.6 GHz), $4_{4,1} - 4_{3,2}$ (650.4 GHz), and $2_{0,2} - 1_{1,1}$ (687.3 GHz) H_2S transitions in Jupiter and Saturn. In our models, we used a line broadening of

$$\Delta\nu = p_{H_2}(1960 \text{ MHz/bar}) \left(\frac{300 \text{ K}}{T}\right)^{0.67} + p_{He}(1425 \text{ MHz/bar}) \left(\frac{300 \text{ K}}{T}\right)^{0.67}, \quad (7.2)$$

where the broadening coefficient for H_2S-H_2 was taken as that found for the 216 GHz line by Joiner *et al.* (1992), the H_2S-He broadening coefficient was taken from the measurement of the 168 GHz line by Willey *et al.* (1989), and the temperature exponent was taken as 0.67 following Joiner *et al.* (1992). Modeling of the $2_{0,2} - 1_{1,1}$ line assuming H_2S to be uniformly mixed in the upper troposphere gives a 3σ upper limit of 29 ppb in Jupiter (Fig. 7.2d) and 16 ppb in Saturn (Fig. 7.3d). These values are 30% smaller than the 1σ limit obtained by Larson *et al.* in Jupiter and more than an order of magnitude smaller than Owen *et al.*'s value in Saturn. For both planets, our new limits are more than three orders of magnitude smaller than the meteoritic sulfur abundance of 33 ppm (Anders and Grevesse 1989). This large depletion is consistent with the removal of sulfur as NH_4SH in the deep atmospheres, and further lessens the likelihood that H_2S is a significant contributor to cloud coloration.

7.4.4 Hydrogen Halides

In Jupiter and Saturn, the major halide reservoirs at the temperatures of the deep troposphere (> 400 K) are expected to be the hydrogen halides (Fegley and Lodders 1994). The fundamental $J = 1 - 0$ rotational transitions of both HBr and HCl fall within available atmospheric windows. (The fundamental transition of the lightest halogen halide, HF, falls at 1232 GHz, well above the highest frequency submillimeter atmospheric window.) These transitions are both hyperfine triplets, but the components are closely spaced in frequency. The HBr molecule exists in two isotopic forms, $H^{79}Br$ and $H^{81}Br$, with transitions falling at 500.6 GHz, while the HCl molecule exists as either $H^{35}Cl$ or $H^{37}Cl$, with transitions at 625.9 and 625.0 GHz,

respectively. Solar system isotopic ratios are $^{79}Br/^{81}Br = 1.02$ and $^{35}Cl/^{37}Cl = 3.1$ (Anders and Grevesse 1989). Because of the small separation in the isotopomer transition frequencies and the large pressure-broadening produced in the atmospheres of Jupiter and Saturn, tropospheric lines of each pair of isotopomers are expected to be blended together. (Stratospheric emission spikes, if present, would be well-separated.)

In FTS observations at the appropriate frequencies, we did not detect HBr or HCl in Jupiter or HBr in Saturn, but *did* tentatively detect HCl in Saturn. For the non-detections, we have determined upper limits for the molecular abundances. We have also modeled HCl in Saturn in order to determine the abundance giving the best match to our data. In our models, we used an HCl pressure-broadening coefficient of 2013 MHz/bar as measured for the $J = 4 - 3$ rotational transition in an N_2 atmosphere at ambient temperature and a pressure of $6 - 8$ torr (Chance *et al.* 1986), and a temperature exponent of $n = 0.85$, as determined for the 3.5 μm infrared $1 \leftarrow 0$ band by Bellard *et al.* (1985). In the absence of laboratory data, these same parameters were also used for the $J = 1 - 0$ transition of HBr. Based on the non-detection of an absorption feature, we derive a 3σ upper limit of 5 ppb for total HCl (both isotopomers) in Jupiter's troposphere (Fig. 7.2e). Assuming a temperature-broadening exponent of $n = 0.85$, we also place an upper limit of 7.0 ppb for HBr in Jupiter (Fig. 7.2f) and 1.1 ppb in Saturn (Fig. 7.3f). Neither the HCl nor the HBr limit is sensitive to the exact value used for n, and both remain unchanged if $n = 0.6$ is used instead.

For Saturn, our spectrum is consistent (at the 3.5σ level) with an absorption feature corresponding to a tropospheric HCl mole fraction of 1.1 ppb (Fig. 7.3e). Despite the atmospheric cutoff near 624 GHz (at the edge of a terrestrial water line) and resultant high noise near this cutoff, this absorption feature is present in data taken both on June 21 and June 24 (although atmospheric transmission was inferior

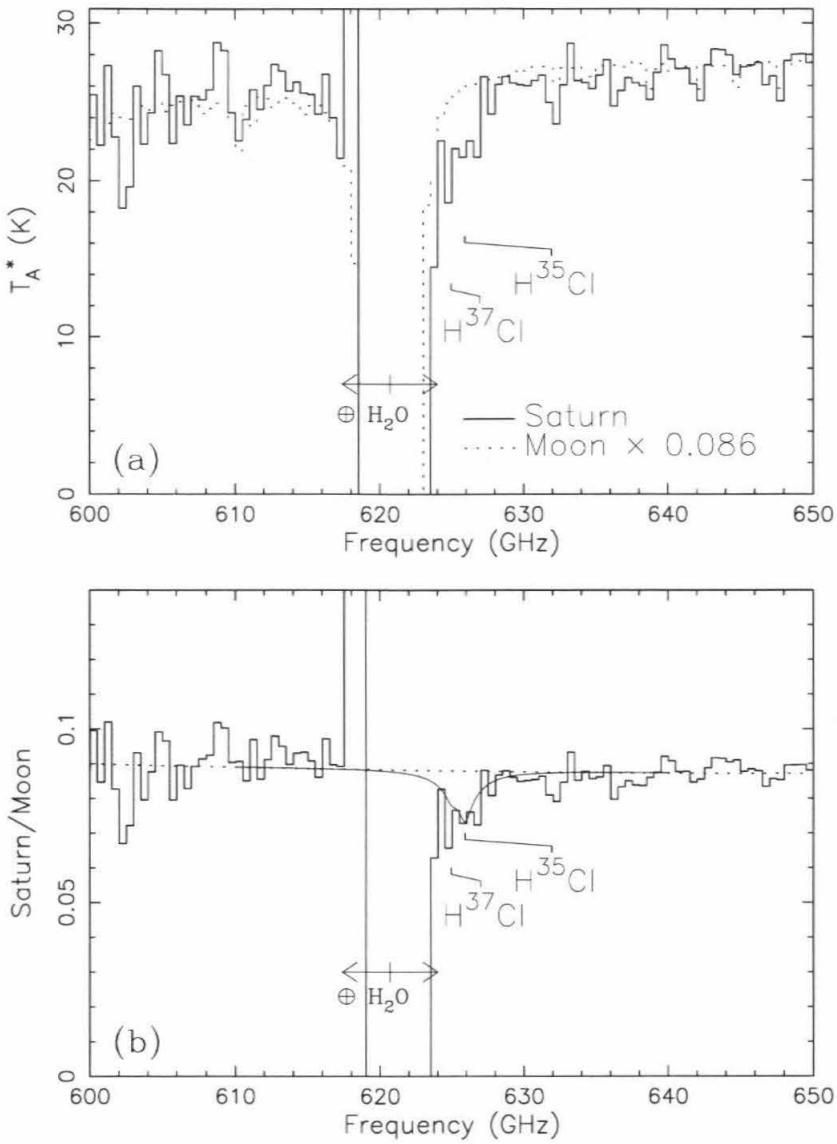

Figure 7.5. (a) Superposed Saturn and Moon spectra binned to 0.5 GHz channels, with the rotational transition frequencies of the HCl isotopomers indicated. The Moon has been scaled by a constant factor to place it on the same vertical scale. The baselines for both spectra are quite flat away from the 620.7 GHz H_2O line. An absorption feature near the HCl transition frequency at 625 GHz appears in the Saturn spectrum, but not the Moon spectrum. The terrestrial atmospheric transmission cuts off due to H_2O between 616.9-624.5 GHz, as marked. (b) Ratio of the spectra shown in (a) (solid histogram), a smooth fit to the baseline (dotted curve), and a model spectrum containing 1.1 ppb HCl (solid curve). The absorption feature at 625 GHz is well-matched to the frequency of the HCl $1-0$ rotational transition.

on the 24th relative to the 21st), but absent in Moon spectra taken the same nights, suggesting that it is real. Spectra from June 21 which show an absorption near 625 GHz in Saturn but no such feature in the Moon are presented in Fig. 7.5a. In this

figure, both spectra have been binned to 0.5 GHz spectral channels to reduce random noise, and the Moon spectrum has been scaled by a factor of 0.086 to allow a direct comparison with the Saturn spectrum. The absorption feature stands out strongly in the Saturn/Moon ratio spectrum shown in Fig. 7.5b, which has also been binned to 0.5 GHz. We therefore tentatively report the detection of HCl in Saturn at the 1.1 ppb level. Additional observations are planned to confirm this identification.

These results represent the first spectroscopic upper limits or detections obtained for halides in the atmosphere of any giant planet. Our Cl limit in Jupiter and detection in Saturn are factors of 66 and 300 smaller, respectively, than the meteoritic Cl mole fraction of 332 ppb (Anders and Grevesse 1989), indicating that Cl is strongly depleted in both planets. At the cold temperatures of the upper jovian tropospheres, halides are predicted to be removed as ammonium halide condensates (Fegley and Lodders 1994). The strong depletions indicated by our upper limit in Jupiter and tentative detection in Saturn are consistent with condensation. However, the tentative detection of HCl in Saturn suggests that vertical mixing may be rapid enough in this planet to maintain a small reservoir of HCl in equilibrium with the expected NH_4Cl condensate. For Br, on the other hand, our upper limits are greater that the solar value of 0.71 ppb (Anders and Grevesse 1989), so a comparison with solar abundance is not yet possible. However, the current Saturn HBr limit of 1.1 ppb is within a factor of 1.5 of the solar Br value.

7.4.5 Alkali Hydrides

In the upper tropospheres of Jupiter and Saturn, the group IA (alkali) metals have recently been predicted to be removed by the condensation of sulfides (Fegley and Lodders 1994). At higher temperatures, the major alkali gases are halides and hydroxides. The alkali hydrides NaH and KH (but not LiH) are also expected to form in the deep troposphere, but the predicted mole fractions are quite small (Fegley and

Lodders 1994). As a result, despite their large rotational dipole moments (e.g., 6.7 D for NaH and 5.882 D for LiH), metal hydrides are unlikely to be present in great enough quantities to produce observable spectral features. Identification of KH is also made difficult by the lack of published frequencies for its rotational transitions. Meteoritic abundances of Li and Na are 3.4 ppb and 3.4 ppm, respectively (Anders and Grevesse 1989), and we emphasize that the *solar* Li abundance is actually a factor of 140 smaller than the meteoritic value due to nuclear processing.

LiH exists as the isotopomers ^{6}LiH and ^{7}LiH, with ^{7}Li/^{6}Li = 12.3 (Anders and Grevesse 1989). The rotational transitions of LiH and NaH which fall in available atmospheric windows are ^{7}LiH $2-1$ and NaH $3-2$, occurring at frequencies 887.2 GHz and 868.6 GHz, respectively. (The ^{6}LiH $2-1$ transition at 905.7 GHz is well-separated from ^{7}LiH transition and expected to be much weaker because of the large ^{7}Li/^{6}Li isotopic ratio.) As anticipated, no line is apparent in the vicinity of these frequencies, allowing us to place 3σ upper limits of 11 ppt for (total) LiH in Jupiter (Fig. 7.2g), and 12 ppt in Saturn (Fig. 7.3g). For NaH, the 3σ limits are 8 ppt in Jupiter (Fig. 7.2h) and 5 ppt in Saturn (Fig. 7.3h). The LiH and NaH limits are more than two and five orders of magnitude, respectively, below meteoritic abundances of the respective alkalis, and are therefore consistent with condensation of these alkali hydrides. In the absence of laboratory measurements, pressure broadening of 2000 MHz/bar and a temperature exponent of 0.6 were adopted and hyperfine splitting ignored in the radiative transfer calculations.

The analysis of the Saturn spectrum shown in Fig. 7.3g is complicated by the presence of strong absorptions on either side of the ^{7}LiH transition frequency. As discussed in §7.4.1, the most likely candidate for these excursions below a constant baseline is a broad HCN $10-9$ absorption at 886.0 GHz, which has been corrupted by baseline ripple. Because we have not been able to reconcile the strength of this

apparent HCN feature with much weaker lower frequency HCN lines in Saturn—and because the width of the expected LiH line is much narrower than the breadth of the absorption feature presumably due to HCN—our LiH upper limit in Saturn has been computed using several simplifying assumptions. We did not superimpose an LiH line on an HCN absorption, but simply found the LiH mole fraction which would have produced an observable line, assuming no HCN, and treating the possible HCN absorption as noise. This assumption yields a rather conservative upper limit.

7.4.6 Molecules with Small Rotational Dipole Moments (CO and CH_3D)

The small rotational dipole moments of CO and CH_3D (0.1098 D and 0.0056 D, respectively) relative to their strong vibrational dipole moments render submillimeter searches of the Jovian planets inferior in sensitivity to those made at infrared wavelengths. In particular, while CO has been detected on Jupiter (Noll *et al.* 1988, Bjoraker *et al.* 1986) with a mole fraction of 1.0-1.6 ppb and on Saturn (Noll *et al.* 1986, Noll and Larson 1990) with a mole fraction of 0.7-1.3 ppb, our non-detections of the CO $3-2$ (345.8 GHz), $4-3$ (461.0 GHz), $6-5$ (691.5 GHz), and $7-6$ (806.7 GHz) lines only yield a 3σ upper limit of 130 ppb on Jupiter (based on the highest frequency line) and 33 ppb on Saturn (based on the $3-2$ line). In our model, the broadening coefficient was taken as 2100 MHz/bar and the temperature exponent as $n = 0.6$ (Noll *et al.* 1988). Similarly, while CH_3D has been detected in infrared observations (Bjoraker *et al.* 1986, Kunde *et al.* 1982, Drossart *et al.* 1982) at a concentration of $0.16-0.24$ ppm in Jupiter and at $0.14-0.64$ ppm in Saturn (Fink and Larson 1978, Courtin *et al.* 1984, Noll and Larson 1990), we did not detect the $2-1$ (465.2 GHz) or $3-2$ (697.8 GHz) lines, and are only able to set an upper limit of 88 ppm in Jupiter (based on the $3-2$ line) and 3.6 ppm in Saturn (based on the $2-1$ line). These values were derived assuming the same broadening coefficient and temperature exponent as for CO.

7.5. Conclusions

Our measurements set an upper limit of 0.3 ppb on the HCN mole fraction in Jupiter if HCN is distributed with a constant mixing ratio. This concentration is significantly lower than the purported infrared detection of Tokunaga *et al.* (1981). We have apparently detected the $10 - 9$ transition of HCN in Saturn. However, because this concentration is in conflict with the low abundance limit obtained from the $3 - 2$ line, the detection of HCN in Saturn cannot yet be considered certain, and so we adopt the $10 - 9$ best-fit concentration of 0.4 ppb as the overall upper limit for a constant troposphere and stratosphere HCN profile in Saturn. If condensation of HCN is included, the deep tropospheric HCN limits are increased to 2 ppb for Jupiter and $\sim$ 15 ppb for Saturn. We set a tropospheric HCl upper limit of 5 ppb in Jupiter, and have tentatively detected this molecule at a mole fraction of 1 ppb in Saturn. We set HBr upper limits of 7 ppb in Jupiter and 1.1 ppb in Saturn. To our knowledge, these are the first spectroscopic limits on the halides in any jovian planet. They indicate that Cl is strongly depleted relative to the solar abundance in the upper tropospheres of Jupiter and Saturn, but the tentative detection of HCl on Saturn suggests that vertical transport is rapid compared to the chemical lifetime of HCl. We also obtain upper limits of 29 ppb (Jupiter) and 16 ppb (Saturn) for H_2S (the latter is an order of magnitude improvement over existing measurements), and 22 ppb (Jupiter) and 5 ppb (Saturn) for HCP. For Saturn, this is nearly a factor of two smaller than the value suggested by photochemical models of Kaye and Strobel (1984). Finally, we obtain upper limits of 11 ppt (Jupiter) and 12 ppt (Saturn) for LiH, and 8 ppt (Jupiter) and 5 ppt (Saturn) for NaH. These are the first tropospheric upper limits to be placed on alkali metals in the troposphere of the Jovian planets, and indicate that both Li and Na are strongly depleted relative to meteoritic abundances.

Chapter 8

Uranus and Neptune

"I knew a mathematician who said, 'I do not know as much as God, but I know as much as God did at my age.'"

—Milton Shulman

8.1. Introduction

Thermodynamic equilibrium models predict that CH_4 and NH_3 should be the primary carbon and nitrogen reservoirs in Uranus and Neptune (Marten *et al.* 1993), as well as in Jupiter and Saturn (Fegley and Lodders 1994). Although both of these molecules condense in the upper tropospheres of Uranus and Neptune, CH_4 has been detected spectroscopically in both planets, and the presence of NH_3 is inferred indirectly based on the observed centimeter-wavelength continuum temperatures (Hofstadter and Muhleman 1988, de Pater *et al.* 1991). The detection of thermochemically unstable carbon- and nitrogen-bearing species such as CO and HCN (or more exotic species such as PH_3, GeH_4, and AsH_3) in the upper atmospheres of the jovian planets therefore reveals the existence of significant disequilibrium processes.

Convective mixing and stratospheric photochemistry of infalling material are the two most commonly invoked processes for explaining observations which are incompatible with equilibrium chemistry models. If the source of a disequilibrium species is convective mixing from below, the molecule is said to have an internal origin. Similarly, if disequilibrium species or their precursors enter an atmosphere from the top (e.g., via infalling meteorites (Moses 1992) or the loss to the upper atmosphere of ionized particles trapped in the magnetosphere after escaping from a close-orbiting satellite), they are said to be of external origin. Observations can potentially distinguish between these two mechanisms by inferring a vertical distribution which may

be incompatible with one or the other. For species which are determined to originate internally, determination of a vertical abundance profile can also provide constraints on the eddy diffusion coefficient, which is potentially very useful for the testing of interior models.

In Jupiter and Saturn, CO, PH_3, GeH_4, AsH_3, and many other disequilibrium species have been detected. Most are believed to have an internal origin. In Uranus and Neptune, all these molecules (including HCN) are expected to condense out in the cold tropospheres *with the exception of CO* (Bézard *et al.* 1986). However, kinetics arguments suggest that relatively small tropospheric CO concentrations of less than 1 ppb should be expected in Uranus and Neptune (Fegley and Prinn 1986), making these molecules very difficult to detect. It was therefore a great surprise when the narrow ($\lesssim$ 30 MHz) and weak ($\sim$ 0.1-0.6 K) stratospheric emission core of CO was detected at the ppm level in Neptune by Marten *et al.* (1993) using the CSO and JCMT. The CO line core was subsequently re-measured by Rosenqvist *et al.* (1992) using the IRAM 30-m telescope. If the CO molecule has an internal origin, these detections require eddy diffusion coefficients which are several orders of magnitude higher than predicted by mixing length theory (which appears to work reasonably well for Jupiter and Saturn), unless H_2O in Neptune is enhanced by a factor of $\gtrsim$ 200 over solar (Lellouch *et al.* 1994).

More surprising still was the detection of HCN line cores in Neptune by the same authors, despite the fact that the saturation vapor pressure of HCN indicates that it should condense at the cold temperatures of the lower stratosphere and upper troposphere of Neptune. As a result of condensation, HCN should exist at concentrations 22 orders of magnitude smaller than observed!

Neither CO nor HCN was seen in Uranus, allowing Marten *et al.* (1993) to place a stratospheric upper limit of 30 ppb for CO and 0.1 ppb for HCN, while

Rosenqvist *et al.* (1992) derived upper limits 40 ppb for CO and a much weaker limit of 15 ppb for HCN.

8.2. Previous Observations of CO and HCN in Neptune

Marten *et al.* (1993) observed CO $2-1$ (at the CSO), CO $3-2$ (at the JCMT), and HCN $4-3$ (at both the CSO and JCMT), Rosenqvist *et al.* (1992) detected CO $2-1$ and HCN $3-2$, and Lellouch *et al.* (1994) subsequently re-observed HCN $3-2$ in the Neptunian stratosphere. Based on their measurements, Marten *et al.* (1993) derived a CO mixing ratio (assumed to be uniformly mixed in the stratosphere and troposphere) of 1.2 ± 0.4 ppm, and an HCN mixing ratio (between 0.003-30 mbar) of 1.0 ± 0.3 ppb HCN. Rosenqvist *et al.* (1992) derived somewhat different values of 0.65 ± 0.35 ppm CO (between 1-200 mbar), and 0.30 ± 0.15 ppb HCN (between 0.3-3.5 mbar). In a paper discussing new HCN measurements, assessing the earlier detections, and developing a rather extensive photochemical model, Lellouch *et al.* (1994) found 0.32 ± 0.08 HCN ppb at 2 mbar with an exponential falloff scale height of 250^{+750}_{-110} km in the 0.1-3.0 mbar region. They ascribed reasons for the differing CO and HCN concentrations obtained by Rosenqvist *et al.* (1992) and Marten *et al.* (1993) to a combination of observational differences, higher Marten *et al.* (1993) model continuum temperatures, and neglect of limb emission in the model of Marten *et al.* (1993). Because all of these factors happen to push the concentrations of Marten *et al.* (1993) in the same direction, a relatively large discrepancy resulted.

Based solely on the high-resolution small-bandpass heterodyne stratospheric observations, it was not possible to make a clear case in favor of a purely internal or external source for either CO or HCN in Neptune. Estimates of external oxygen sources seem to be several order of magnitude too low to account for the observed CO concentrations (Rosenqvist *et al.* 1992), but thermochemical transport models predict abundances at least a factor of 30 smaller than observed (Fegley and Prinn

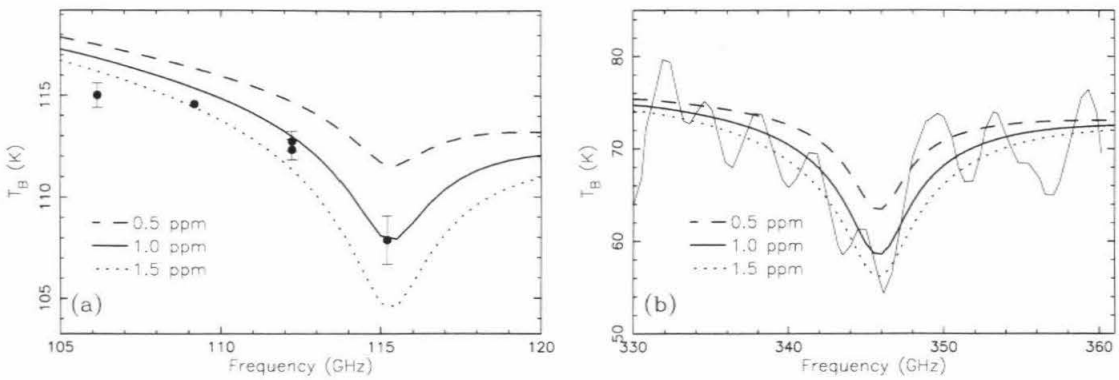

Figure 8.1. (a) Plateau de Bure interferometer CO $1-0$ measurements of Guilloteau *et al.* (1993). The model spectra superposed on the data points were generated by our own radiative transfer model, which gives slightly warmer temperatures than predicted by the model of Marten *et al.* (1993) (which is plotted in Guilloteau *et al.* 1993). (b) JCMT FTS CO $3-2$ measurements of Naylor *et al.* (1994). The spectrum has been scaled by a constant factor 0.9 in order to bring the continuum into agreement with our radiative transfer model. The spectral resolution of the FTS data is 1.8 GHz, to which our model CO spectra have also been convolved.

1986). For HCN in Neptune, Marten *et al.* (1993) favored internal origin (impact of galactic cosmic rays on upwelling N_2), Rosenqvist *et al.* (1992), an external origin (transport of neutral N from Triton followed by ionization and trapping in Neptune's magnetosphere), and Lellouch *et al.* (1994), a combination of the two. An internal origin could explain the lack of CO and HCN detections in Uranus, since this planet is thought to have a smaller interior heat source than Neptune, therefore inhibiting strong convection (Guillot *et al.* 1994; but see also Guillot 1995). However, the lack of a Triton-like satellite as an external N source for Uranus could also be responsible for the lack of observed stratospheric HCN. While HCN should condense in the upper troposphere of Neptune, making it difficult to observe, the question of an internal versus external origin for CO in Neptune could be resolved by the detection of tropospheric CO absorption lines.

Because tropospheric lines are much too wide to be detected using the ~ 1 GHz bandpasses of heterodyne receivers, other techniques are required. By tuning the IRAM Plateau de Bure interferometer to four discrete frequencies spaced 3 GHz apart between 106 and 115 GHz (in double sideband mode), Guilloteau *et al.* (1993) made

a tentative detection of a $5.3 \pm 0.8\%$ absorption feature in Neptune at the frequency of the CO $1 - 0$ transition (Fig. 8.1a). Based on their observations, these authors derived a tropospheric abundance between 0.6 and 1.5 ppm, with 0.6 ppm giving the best fit. Unfortunately, the three frequencies falling on the putative CO linewing were all on a single side (lower frequencies) of the line center (since terrestrial atmospheric absorption prevents observations on the other side), so a rise in temperature on the high frequency side of line was not observed (Fig. 8.1a).

A second measurement of tropospheric CO in Neptune was made with the JCMT FTS at a resolution of 1.8 GHz. In this measurement, Naylor *et al.* (1994) spectroscopically detected a wide absorption feature coinciding with the CO $J = 3 - 2$ transition frequency of 345 GHz (Fig. 8.1b). Their data was consistent with a tropospheric CO mixing ratio of 0.7-1.3 ppm, in agreement with the stratospheric values inferred by Rosenqvist *et al.* (1992) and Marten *et al.* (1993). Unfortunately, the spectra of both Uranus and Neptune obtained by Naylor *et al.* (1994) suffer from very large instrumental ripples across the entire bandpass (Fig. 8.1b). The ripples are especially worrisome because the absorption feature identified as CO appears to correspond very closely to two ripple periods. In addition, the data reduction technique described by Naylor *et al.* (1994) does not correct for atmospheric or filter transmission, and therefore does not provide a continuum level with which to compare their absorption feature. (The spectrum falling outside the frequencies plotted in Fig. 8.1b is essentially a filter transmission curve with superposed terrestrial atmospheric absorption.) The continuum level of the published spectrum of Naylor *et al.* (1994) was therefore determined from the Uranus radiative transfer model of Marten *et al.* (1993). In order to bring the continuum level of the (arbitrarily scaled) spectrum of Naylor *et al.* (1994) into agreement with our own radiative transfer model, the spectrum shown in Fig. 8.1b has been scaled by a constant factor 0.9.

Because of the limitations in the observations of Guilloteau *et al.* (1993) and Naylor *et al.* (1994), we believe that additional well-calibrated measurements of Neptune are called for in order to definitively establish the depth and width of the tropospheric CO line. Low frequency observations in the 1300 μm window can also search for the $J = 1 - 0$ line of PH_3, the $J = 3 - 2$ line of HCN, and the 216 and 300 GHz transitions of H_2S. In a rapidly convecting troposphere, PH_3 could be transported up to observable levels, and would be detectable in the tropospheres of Uranus and Neptune assuming a mole fraction higher than $\sim$ 10 ppb (Bézard *et al.* 1986). However, both PH_3 and HCN should condense in the upper atmospheres of Uranus and Neptune, rendering them potentially difficult to observe and, due to the lack of low-temperature vapor pressure measurements, hard to accurately model.

8.3. FTS Observations

We first observed Uranus and Neptune on July 22-24, 1995 (UT) (Encrenaz *et al.* 1996). Celestial mechanics made this a propitious time to observe because, in addition to Uranus and Neptune, Mars and the Moon were also available as flux calibrators. Because of their weak fluxes (which decrease as a function of frequency), Uranus and Neptune were observed in the 1300 μm atmospheric window using the 30″ Winston cone. However, because of poor atmospheric transmission ($\tau_{225\ \mathrm{GHz}} = 0.08$-0.16 on July 22 and 0.09-0.11 on July 24) resulting from relative high humidity (28-30% and 25-36%, respectively), the 1300 μm Neptune flux levels were not consistent between the two nights. We therefore re-observed Uranus and Neptune on September 19, 1995 using the 1300 μm filter only. On this night, both zenith optical depth ($\tau_{225\ \mathrm{GHz}} = 0.02$-0.06) and humidity (14-16%) were much lower, giving low-noise data with antenna temperatures comparable to the July data for Uranus, and the average of the two July nights for Neptune.

During the September observing run, we collected a total of 82 two-sided scans

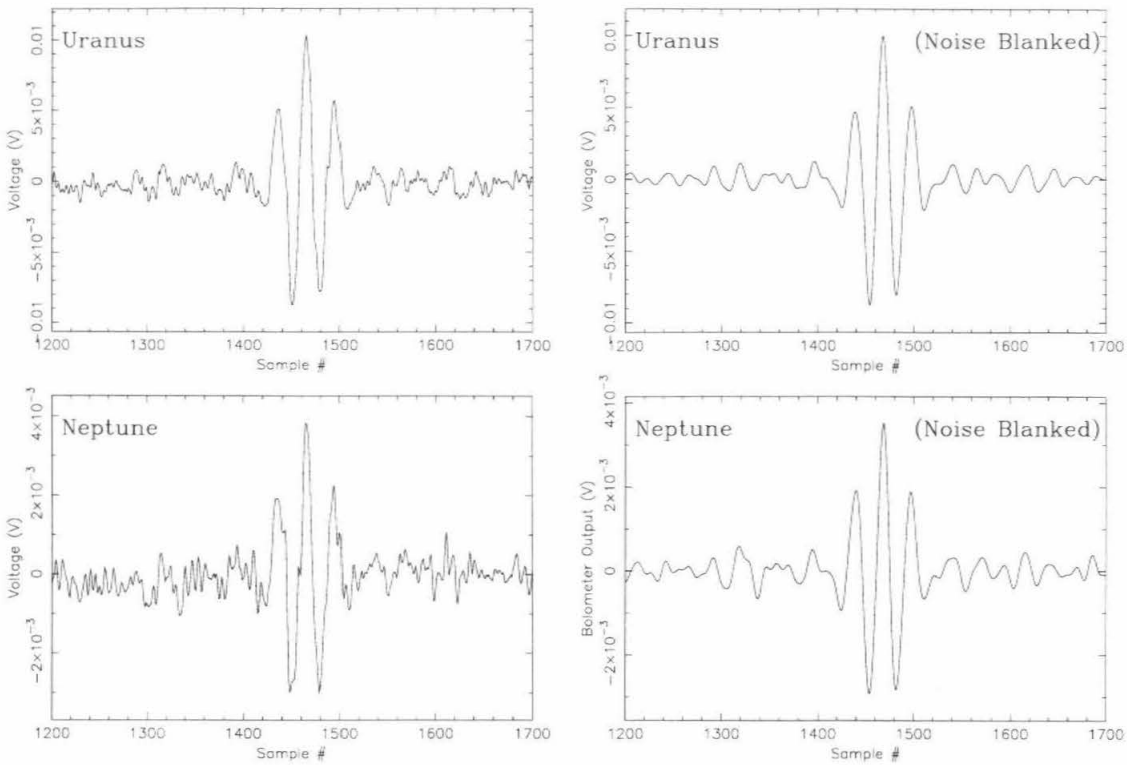

Figure 8.2. Interferograms of Uranus and Neptune. The plots on the left are raw "on"−"off" interferograms. The plots on the right have been Fourier transformed, frequencies below 100 and above 600 GHz have been blanked, and the resultant spectra inverse Fourier transformed.

of Uranus and 282 of Neptune over a 3 hour period. The scan length was kept to a short 5.9 cm, giving a resolution of only 3.1 GHz, but reducing the length of time between "on" and "off" scans. At the time of observation, Uranus and Neptune had equatorial diameters (at the 1 bar level) of 3.67″ and 2.30″, respectively. Fig. 8.2 shows the on−off difference interferograms obtained by averaging all the Uranus and Neptune scans and their corresponding off scans. Note the small amplitude of the difference interferograms (10 mV for Uranus and 4 mV for Neptune) compared to the $\sim$ 1 V of the sky ("off") interferogram. The plots on the left show raw measured interferograms, while the plots on the right show the interferograms obtained after blanking of high- and low-frequency noise falling outside the filter bandpass. (The blanking was done in spectral space, and the resulting spectra then inverse transformed.) The result of this procedure is interferograms corresponding to the sig-

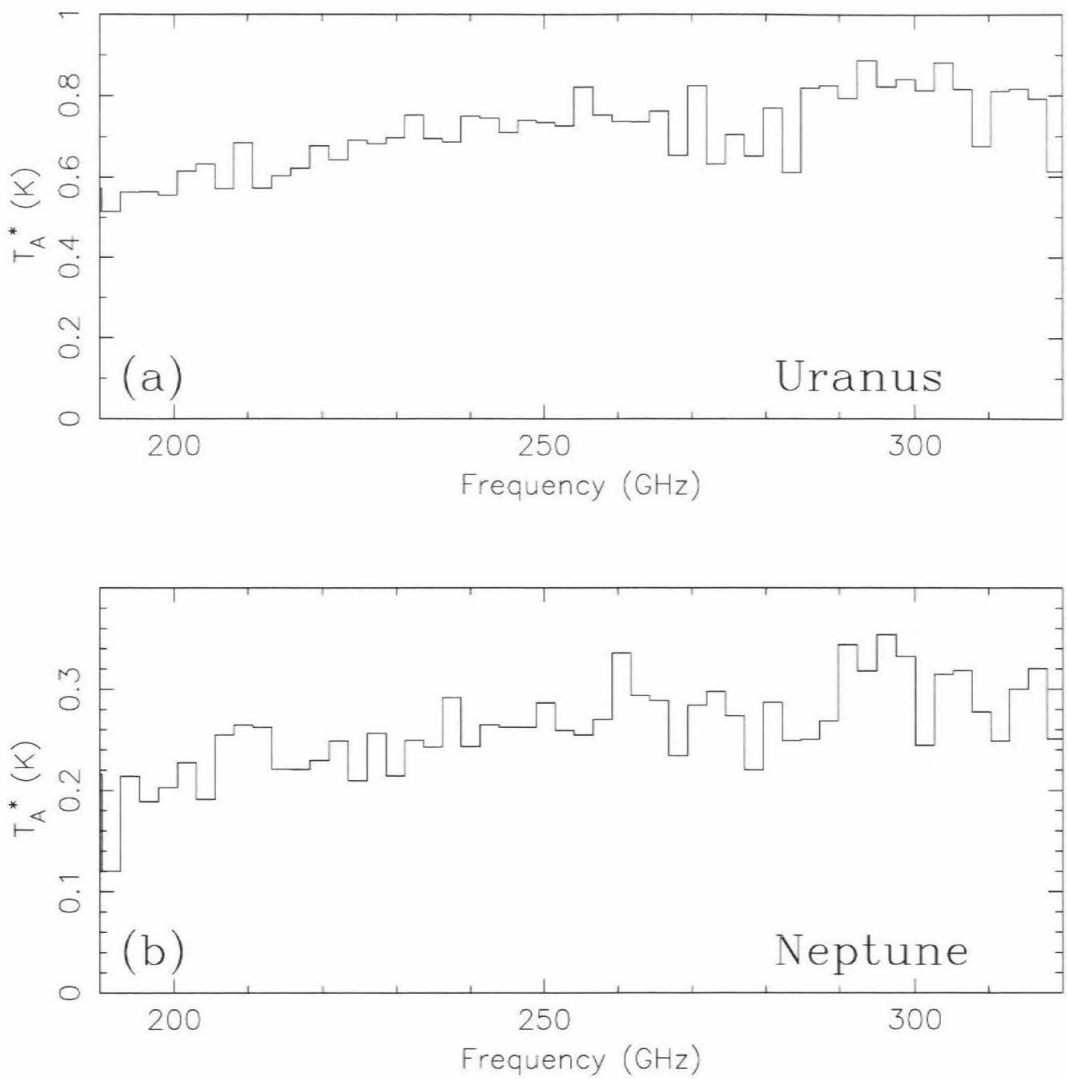

Figure 8.3. FTS spectra of (a) Uranus and (b) Neptune obtained in the 1300 μm filter in uncalibrated T_A^* units. Observational resolution is 3.1 GHz.

nal which would have been measured if more restrictive bandpass filtering had been performed prior to the A/D.

Fig. 8.3 shows the spectra obtained by Fourier transforming and processing the interferograms of Fig. 8.2. The signal-to-noise ratio is ~ 20 for Uranus and ~ 10 for Neptune between 200 and 250 GHz. Although the 1300 μm window includes transitions of CO $2-1$ (230 GHz), HCN $3-2$ (266 GHz), PH_3 $1-0$ (267 GHz),

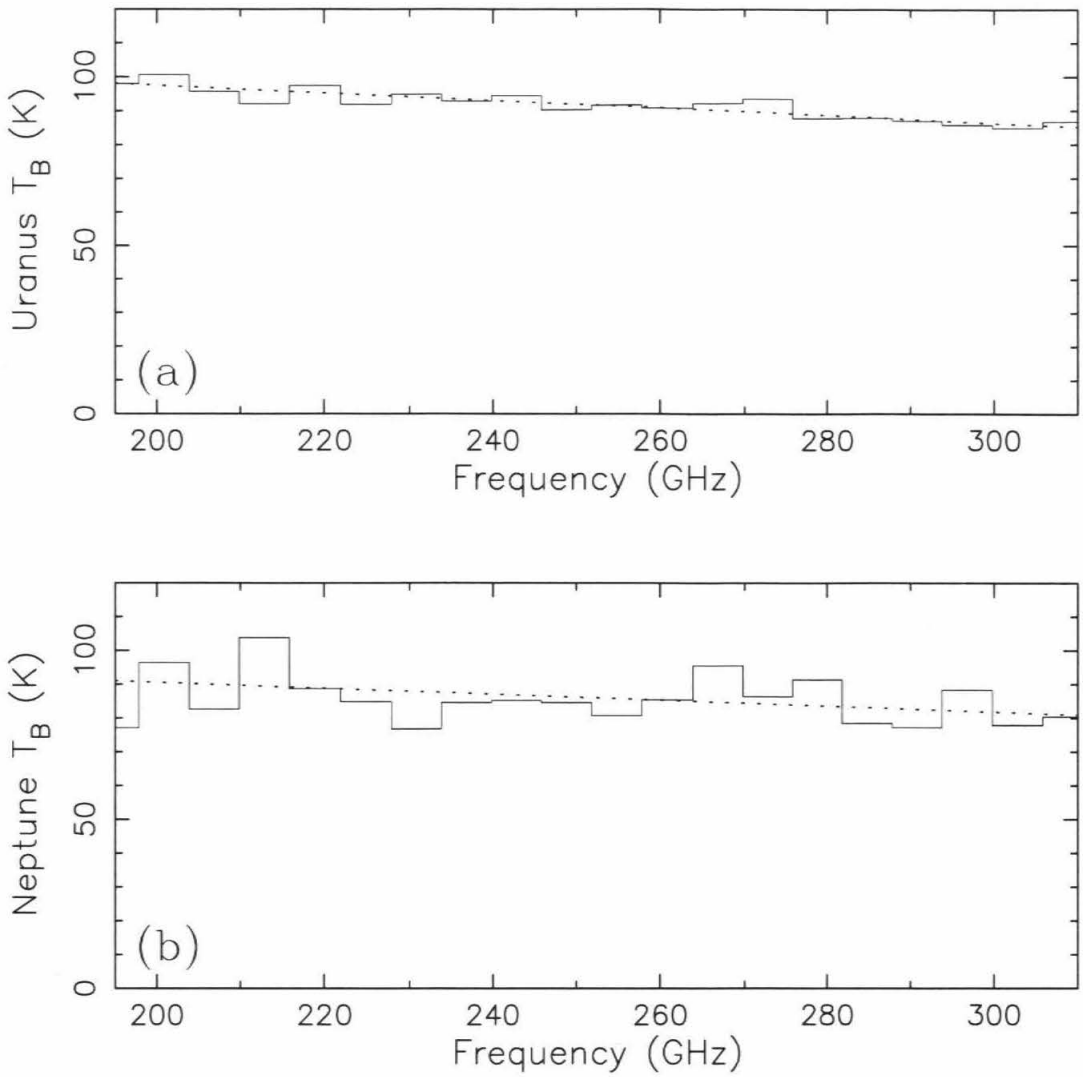

Figure 8.4. Continuum temperatures for (a) Uranus and (b) Neptune. The histogram-like curve is the FTS measurements, which have been calibrated using Mars observations, the Mars thermal model of Rudy (1987), and the disk sizes of Mars, Uranus, and Neptune. Also plotted are the filter measurements of Griffin and Orton (1993) (dashed lines) and the brightness temperatures predicted by our radiative transfer model (dotted lines).

and transitions at 216 and 300 GHz due to H_2S, none of these molecules was detected in either planet. In addition to placing upper limits on the potential abundances of the undetected molecules, the measurement of the continua of Uranus and Neptune has allowed the whole disk Neptune/Uranus temperature ratio—as well as absolutely calibrated temperatures of Uranus and Neptune separately—to be determined.

Prior to analysis of Uranus and Neptune spectra for spectral lines, it was necessary to first convert the observations in Fig. 8.3 to an absolute temperature scale using Mars as a calibrator. The procedure is described in Serabyn and Weisstein (1996), and the final results are reproduced in Fig. 8.4. Using this spectroscopic technique, as opposed to the wide-band filter measurements of previous observations, whole disk average temperatures very close to those of Griffin and Orton (1993) were obtained between 200-300 GHz (Serabyn and Weisstein 1996).

8.4. Upper Limits

In this section, radiative transfer models for various molecular species of interest are presented for Uranus and Neptune. As in Chapter 7, the mole fraction giving an absorption line corresponding to a 3σ detection threshold (after convolution to the instrumental resolution of 3.1 GHz) is identified as the 3σ upper limit. The analysis presented below represents an initial analysis of these spectra. The data have been further analyzed by Encrenaz, Serabyn, and Weisstein (1996), who obtain virtually identical limits on CO and PH_3. In the analysis of Encrenaz *et al.* (1996), however, the spectra were processed at a degraded resolution of 6 GHz in order to provide the greatest possible signal-to-noise ratio for broad tropospheric lines. Encrenaz *et al.* (1996) also did not place upper limits on HCN, although they did consider H_2S.

8.4.1 CO

In Neptune, radiative transfer models set a 3σ upper limit of 1.4 ppm on the tropospheric CO abundance (Fig. 8.5a). (Encrenaz *et al.* 1996 set a slightly more stringent upper limit of 1.0 ppm by folding the spectrum about the CO line center.) Although CO was not detected with our FTS, the 1.4 ppm upper limit is consistent with the low- to mid-range of the 0.6-1.5 and 0.7-1.3 ppm CO concentrations reported by Guilloteau *et al.* (1993) and Naylor *et al.* (1994), respectively. While these previous

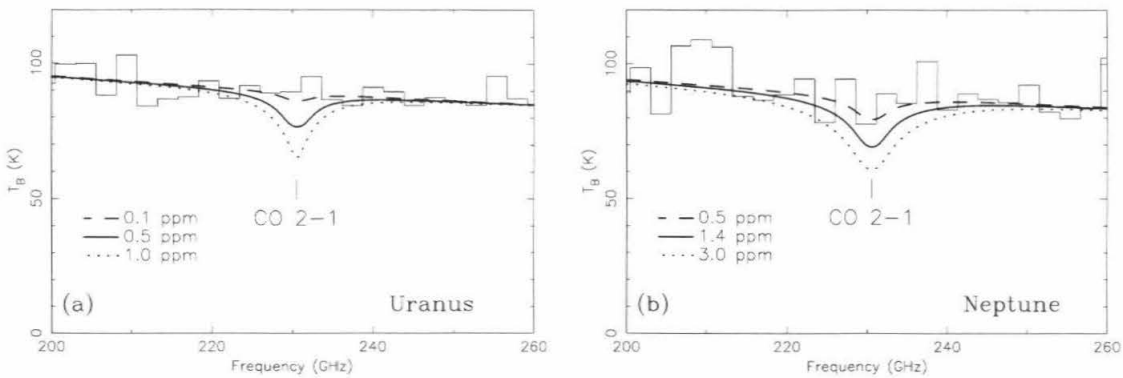

Figure 8.5. (a) Uranus and (b) Neptune spectra scaled to the continuum temperature given by our radiative transfer, together with three model CO lines. The 3σ upper CO limits (solid curves) are 0.5 ppm in Uranus and 1.4 ppm in Neptune.

measurements were unable to constrain the abundances responsible for the observed spectral features to better than a factor of $\sim$ 2 due to lack of knowledge of the continuum level, the upper limit obtained here unambiguously indicates that the tropospheric CO concentration cannot be as high as 1.4 ppm. Although the non-detection does not allow any new conclusions about the origin of CO in Neptune to be drawn, future observations using stronger, higher frequency transitions of CO may provide more conclusive information.

In Uranus, the upper limit obtained on the tropospheric CO abundance is 0.5 ppm (Fig. 8.5b). This is the first upper limit to be placed on tropospheric CO in Uranus.

8.4.2 PH_3

Because PH_3 is expected to condense in the upper tropospheres of Uranus and Neptune at altitudes above the $\sim$ 1.5 bar level, gaseous PH_3 can exist only in the deep tropospheres in the absence of supersaturation. As a result, PH_3 lines are expected to be very highly pressure broadened ($\sim$ 50 GHz) and very weak, making them almost impossible to detect. Fig. 8.6 shows model spectra containing 1 and 10 ppm PH_3, superposed on the observed spectra of Uranus and Neptune (which

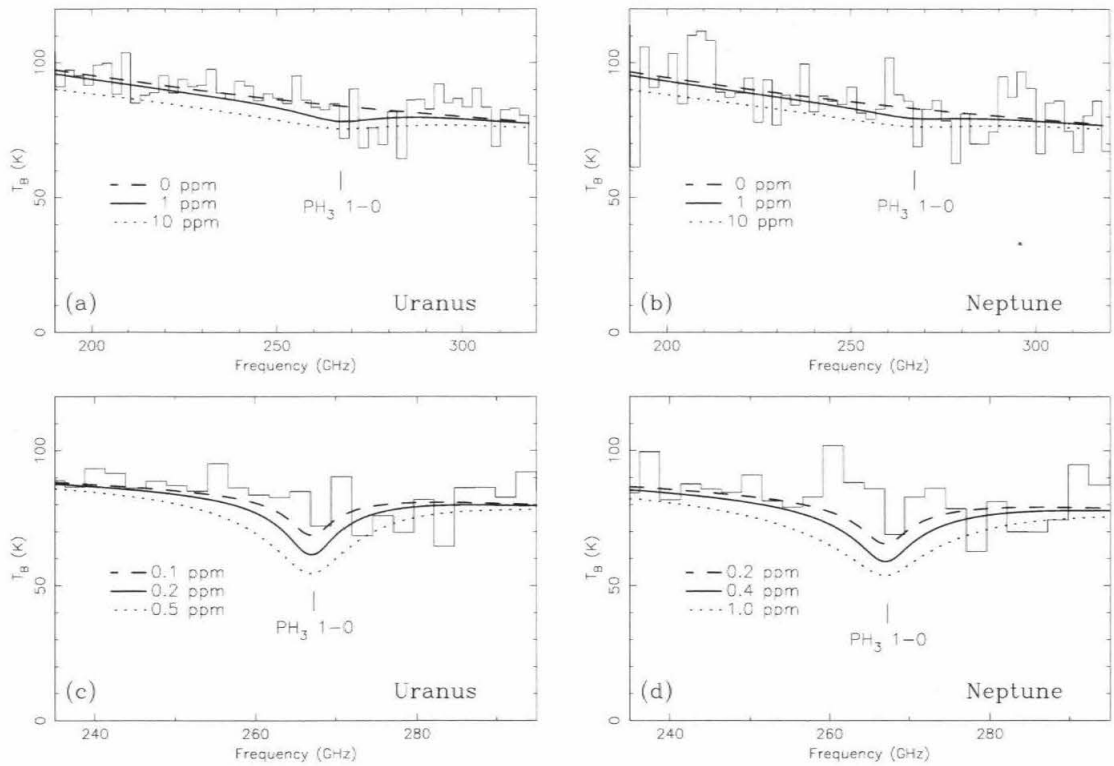

Figure 8.6. Uranus and Neptune spectra scaled to the continuum temperature given by our radiative transfer model. Model PH_3 lines are superposed. Because PH_3 is expected to condense in the upper tropospheres of Uranus and Neptune, it can exist in gaseous form only at deep levels and is therefore highly pressure broadened. In fact, with condensation, the line is predicted to be so wide and weak in both (a) Uranus and (b) Neptune, that no upper limit can be placed on PH_3 in either planet. However, if condensation is ignored, then the line forms higher up and is therefore stronger and narrower. In the absence of condensation, upper limits of 0.2 ppm are obtained in (c) Uranus and 0.4 ppm in (d) Neptune. In (c) and (d), the model spectra have been convolved to the instrumental resolution of 3.1 GHz.

have been scaled to the continuum level of our radiative transfer models). Because of the extreme width of the lines in Figs. 8.6a and 8.6b, it is not possible to place an upper limit on PH_3 if it does follow the assumed saturation vapor pressure law (Orton and Kaminski 1989). However, since the cold temperatures of the lower stratosphere and upper troposphere of Neptune (and Uranus) can severely limit the effectiveness of homogeneous nucleation to the point that particle formation will not occur until large supersaturations are achieved (Moses *et al.* 1992), we also computed models for PH_3 assuming that condensation did not occur. Although foreign condensation nuclei or ions can also act as nucleation centers, heterogeneous nucleation is difficult

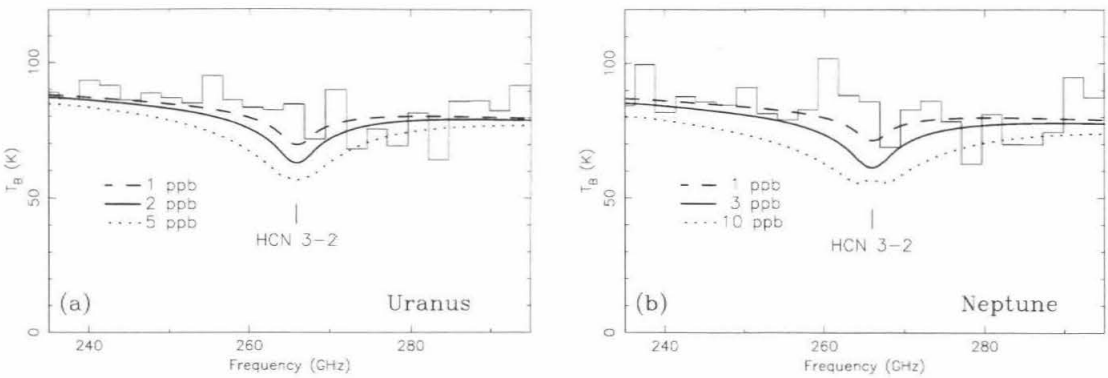

Figure 8.7. (a) Uranus and (b) Neptune spectra scaled to the continuum temperature given by our radiative transfer with model HCN lines superposed. The solid lines are the 3σ upper limits with saturation ignored.

to model due to the complicating effects of chemistry and mixing, and also as a result of insufficiently complete laboratory measurements (Moses *et al.* 1992). If PH_3 were to exhibit strong supersaturation such that its mole fraction were roughly constant in the upper tropospheres of Uranus and Neptune, it would likely be detectable. Our non-detection of spectral features due to PH_3 therefore allows us to obtain upper limits of 0.2 ppm in Uranus and 0.4 ppm in Neptune for a constant tropospheric PH_3 mole fraction, ruling out strong supersaturation in both planets in the presence of substantial convective transport.

8.4.3 HCN

HCN is expected to condense above the $\sim$ 5 bar level in the tropospheres of Uranus and Neptune, even deeper than PH_3. Since the 266 GHz weighting functions for Uranus and Neptune have almost no contribution at such deep levels and because tropospheric HCN lines originating from such levels would be pressure broadened to fantastic widths, HCN is not expected to be observable in the troposphere. However, if we assume HCN does not condense, upper limits of 2 ppb and 3 ppb are obtained for Uranus and Neptune (Fig. 8.7). These upper limits are considerably larger than the observed stratospheric HCN mole fraction of 0.3 ppb in Neptune, so our sensitivity

to tropospheric HCN is insufficient to distinguish between an internal and external origin for this molecule.

8.5. Conclusions

Our observations at 1300 μm did not succeed in detecting CO in Neptune, despite the fact that the observations were obtained under very favorable weather conditions. The observations of Guilloteau *et al.* (1993) and Naylor *et al.* (1994) can therefore not be confirmed, although our FTS measurements do reveal that the tropospheric CO concentration must lie below 1.4 ppm in Neptune. The best way to do to improve this limit is to re-observe Uranus and Neptune using the CSO FTS in the 800 μm window. Since CO line strength increases with increasing quantum number, measurements of the $3-2$ line under requisite good weather conditions should yield improved sensitivity. We hope to make these new measurements in the near future.

Our observations did not detect tropospheric CO in Uranus, nor PH_3 or HCN in either Uranus or Neptune. We obtained a tropospheric upper limit of 0.5 ppm CO in Uranus, the first tropospheric upper limit to be placed on CO in this planet. Although condensation of PH_3 and HCN would render these molecules unobservable in Uranus and Neptune, we have obtained upper limits in the case of extreme supersaturation with an assumed constant tropospheric mixing ratio. For Uranus, we derive upper limits of 0.2 ppm (PH_3) and 2 ppb (HCN), and for Neptune, we derive 0.4 ppm (PH_3) and 3 ppb (HCN).

Chapter 9

Conclusions

"A really good scientist is one who knows how to draw correct conclusions from incorrect assumptions."

—Otto Frisch *(What Little I Remember)*

"What is the meaning of it? ... It must tend to some end, or else our universe is ruled by chance, which is unthinkable. But what end? That is the great standing perennial problem, to which human reason is as far from an answer as ever."

—Sir Arthur Conan-Doyle *(The Adventure of the Cardboard Box)*

"There is no conclusion. What has concluded that we might conclude in regard to it? There are no fortunes to be told, and no advice to be given. Farewell."

—William James

"Plain stupidity is the only thing that can give them such assurance."

—Franz Kafka *(The Trial)*

9.1. Summary

The construction of a Fourier transform spectrometer operating at millimeter-submillimeter wavelengths has opened up the previously unexplored submillimeter waveband to intermediate resolution planetary spectroscopy. Using our FTS, extensive intermediate resolution (0.2-3.0 GHz) observations of the tropospheres of Jupiter, Saturn, Uranus, and Neptune have been made for the first time. These observations have detected wide, pressure-broadened lines of PH_3 in Jupiter and Saturn, and have also provided tight limits on the abundances of many undetected species in all four jovian planets.

The detection of PH_3 in Jupiter and Saturn has provided information about this species' vertical distribution which is roughly compatible with the "deep" ($\gtrsim 0.5$ bar) mole fractions derived from infrared observations, but appears to imply a more rapid falloff in Jupiter's upper troposphere than predicted by existing measurements and photochemical models. The derivation of new upper limits for H_2S, HBr, HCl, HCN, HCP, LiH, and NaH provides chemical constraints on the upper tropospheres

of Jupiter and Saturn. In particular, the strong depletion of HCl relative to the solar abundance is consistent with the low-temperature condensation of Cl as NH_4Cl in the upper tropospheres of Jupiter and Saturn, although the tentative detection of HCl in Saturn suggests that vertical mixing may be vigorous enough to maintain a reservoir of HCl in equilibrium with the expected NH_4Cl condensate. Likewise, Li and Na are strongly depleted, consistent with possible condensation as Li_2S and Na_2S. The depletion of H_2S on Jupiter and Saturn is consistent with condensation of NH_4SH, and makes a significant role for sulfur compounds as chromophores in the jovian planets unlikely. Our upper limit for HCN in Jupiter is 7 times smaller than the concentration derived from the only claimed detection to date, suggesting that this measurement may be in error (in the absence of temporal variations). FTS observations have also provided a 3σ upper limit of 1.4 ppm CO on Neptune, and 0.5 ppm on Uranus. Although both Guilloteau *et al.* (1993) and Naylor *et al.* (1994) have previously reported detections of CO at the 0.5-1.5 ppm level, the potential for systematic instrumental effects in both of these observations strongly supports the need for independent confirmation.

9.2. Future Work

Although a great deal of jovian planet spectra have been obtained, there is still much left to do. We anticipate that future FTS observations with longer integration times will provide even tighter constraints on tropospheric concentrations of molecules in the tropospheres of Jupiter and Saturn. In addition, our measurements of Uranus and Neptune have thus far only covered the lowest frequency 1300 μm filter, so observations at higher frequencies (where rotational line strengths are expected to be stronger) can yield better constraints on tropospheric CO.

A major observational project currently in its early stages is the determination of accurately calibrated submillimeter continuum temperatures for all the planets,

especially Jupiter and Saturn, at relatively high resolution. Wide-band bolometric measurements have provided the best continuum temperature results so far, but the large widths of the filter bandpasses combined with the often poorly known filter transmission functions can render these results inaccurate. In particular, the presence of strong absorption features (such as the tropospheric lines of PH_3 in Jupiter and Saturn or CO in Neptune) in the filter passband can render bolometric results in error by several percent, in addition to the errors already introduced by a fluctuating atmosphere and calibration inaccuracies. With a resolution of 200 MHz, the FTS avoids these pitfalls by resolving pressure-broadened atmospheric lines and accurately determining the shape of the filter bandpass. Furthermore, unlike the chopping method employed by bolometric observers, the On/Off/Hot observing technique used by the FTS effectively measures and removes atmospheric absorption, making spectra more insensitive to changes in atmospheric opacity and airmass. The 10.4 meter CSO dish also gives much better source coupling than available in earlier measurements using smaller telescopes (such as Hildebrand *et al.* 1985). FTS measurements can, in theory, yield calibrated continuum temperatures which are accurate to within a few percent, superior to those obtained to date with bolometric measurements, although systematic uncertainties due to unknown surface properties of Mars, the primary calibration source, will still remain.

Calibration is very difficult at millimeter/submillimeter wavelengths, primarily because the telescope beam pattern must be known with high accuracy. Changing emission and absorption by the temporally varying Earth's atmosphere also complicate measurements. Since the absorption by the Earth's atmosphere also changes as a function of airmass, bolometric observations must observe both source and a calibrator at the same position on the sky. In practice, observations are often made over a range of airmasses such that source and calibrator have the same "average" airmass.

One or more planets are usually used as primary flux standards because their intrinsic brightnesses can be estimated *a priori* with the aid of thermal models. Planets are the only bodies bright enough at submillimeter wavelengths to provide good flux calibrators, and the most accurate flux models can be constructed for planets with solid surfaces and tenuous atmospheres. Mars and the Moon are therefore the compact and extended calibrators of choice. Both Moon and planetary observations are necessary in order to extricate the beam coupling efficiency and Moon coupling (Kutner and Ulich 1981) from measurements of different sized planetary disks. The best existing thermal models for these bodies are the Rudy Mars model (Rudy 1987) and the Kiehm Moon model (developed for COBE calibration and available on-line at JPL). These models give absolute surface brightness temperatures which, in their range of applicability, are accurate to within $\sim 5-10\%$ and $\sim 1\%$ over all seasons/phases of Mars and the Moon, respectively. Calibration of high-quality submillimeter continuum temperatures would therefore also involve use of these thermal models and consideration of what, if any, modifications are required at submillimeter wavelengths.

Additional modeling of the PH_3 profile in Jupiter is needed in order to interpret the inferred falloff in PH_3 abundance in Jupiter's upper tropopause. This can be done using the newest incarnation of the Caltech/JPL jovian photochemistry and transport model, which now includes the capability of including Rayleigh scattering. Earlier modeling attempts with a previous version of the photochemical model appeared to demonstrate that the PH_3 profile can provide useful constraints on Jupiter's tropospheric eddy diffusion coefficient.

Finally, there are several instrumental improvements which could be made to the FTS itself. By encasing the FTS in vacuum jacket, differential phase errors caused by water vapor passing through the interferometer's two arms could be eliminated. Because the quality of spectra we obtain appears to be better correlated with

ground-level humidity than zenith opacity, we believe that this modification could greatly improve the quality of our spectra, especially during less-than-ideal weather. Another useful modification would be to fold the optical path length traversed by the phase-shifted beam by a factor of two or three. This modification would achieve high enough resolution to allow spectroscopic studies of narrow CO lines in the atmospheres of Venus and Mars, which we can currently detect, but do not have sufficient resolution to allow inversion for vertical abundance profiles. High resolution would also allow broadband line searches for undetected millimeter-submillimeter transitions of molecules such as SO, SO_2, HCl, or H_2SO_4 in the atmosphere of Venus.

Appendix A: Beamsplitter Transmission Function

"Just think, the definitions and deductive methods which everyone learns, teaches, and uses in mathematics, the paragon of truth and certitude, lead to absurdities! If mathematical thinking is defective, where are we to find truth and certitude?"

—David Hilbert

The transmission of a dielectric beamsplitter is most simply calculated in the approximation that the dielectric slab is infinite in extent. The geometry is then that of a Fabry-Perot étalon. Let a wave with electric field amplitude E_0 impinge obliquely on a slab of thickness d with index of refraction n immersed in a medium with index of refraction $n_0 < n$ (Figure A.1).

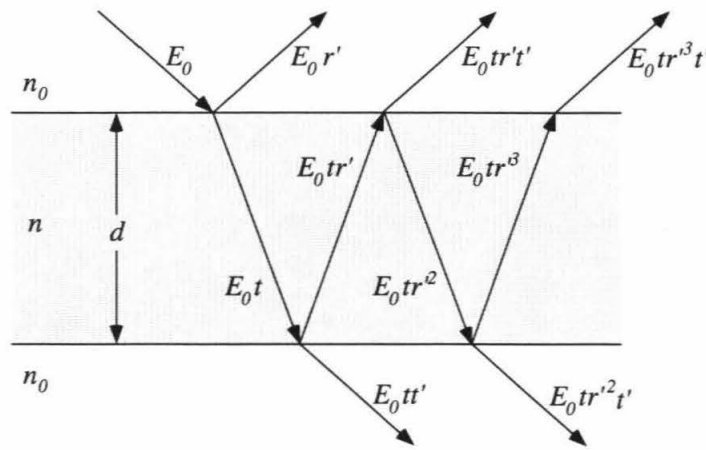

Figure A.1. Ray diagram for a Fabry-Perot étalon.

Let r and t be the internal amplitude reflection and transmission coefficients and r' and t', the external amplitude reflection and transmission coefficients. Then the electric field amplitudes of the reflected rays are

$$\begin{aligned} E_{1r} &= E_0 r \\ E_{2r} &= E_0 t r' t' e^{-i\delta} \\ E_{3r} &= E_0 t r'^3 t' e^{-2i\delta} \\ E_{nr} &= E_0 t r'^{(2n-3)} t' e^{-(n-1)i\delta}, \end{aligned} \tag{A.1}$$

where the phase difference between adjacent reflected rays is

$$\delta = 2\phi - \phi_0. \tag{A.2}$$

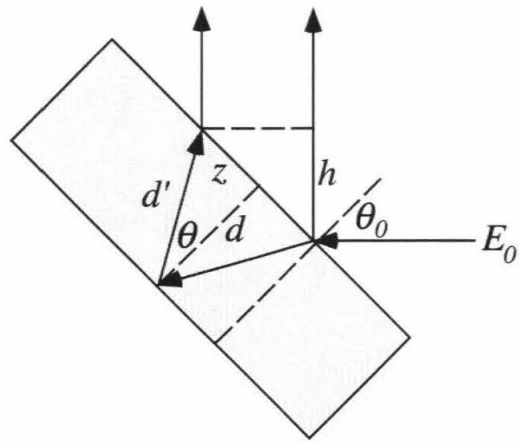

Figure A.2. Diagram showing two adjacent parallel reflected rays emerging for a Fabry-Perot étalon. An analogous diagram holds for the transmitted rays.

Referring to Fig. A.2,

$$\phi = d'k = \frac{n}{n_0} d'k_0 \tag{A.3}$$

is the phase advancement for one pass through the slab, and

$$\phi_0 = hk_0 \tag{A.4}$$

is the phase advancement in air which the reflected ray undergoes in "catching up" to perpendicular of the transmitted ray at the point where it exits the slab. k_0 is the wavenumber in medium n_0. A minus sign has been explicitly added to ϕ_0 since it is the *difference* of the phases between adjacent rays which is significant. Consulting Figure A.2 gives

$$z = d\tan\theta \tag{A.5}$$

$$d' = \frac{d}{\cos\theta} = \frac{d}{\sqrt{1-\sin^2\theta}} \tag{A.6}$$

$$h = 2z\sin\theta_0 = 2d\tan\theta\sin\theta_0, \tag{A.7}$$

where θ and θ_0 are connected by Snell's law,

$$n_0\sin\theta_0 = n\sin\theta. \tag{A.8}$$

Plugging (A.3) through (A.7) into (A.2) and using (A.8) gives

$$\begin{aligned}\delta &= \frac{(2d'n - hn_0)k_0}{n_0} = \frac{2\pi}{n_0\lambda_0}\left(\frac{2dn}{\cos\theta} - 2dn_0\tan\theta\sin\theta_0\right)\\ &= \frac{4\pi d}{n_0\lambda_0}\left(\frac{n}{\cos\theta} - n_0\tan\theta\sin\theta_0\right) = \frac{4\pi d}{n_0\lambda_0}\frac{n - n_0\sin\theta\sin\theta_0}{\cos\theta}\\ &= \frac{4\pi d}{n_0\lambda_0}\frac{1}{\sqrt{1-\sin^2\theta}}\frac{n^2 - nn_0\sin\theta\sin\theta_0}{n}\\ &= \frac{4\pi d}{nn_0\lambda_0}\frac{1}{\sqrt{1-\frac{n_0^2}{n^2}\sin^2\theta_0}}(n^2 - {n_0}^2\sin^2\theta_0) = \frac{4\pi d}{\lambda_0}\sqrt{\left(\frac{n}{n_0}\right)^2 - \sin^2\theta_0}. \quad (A.9)\end{aligned}$$

If the beamsplitter is at a $\theta_0 = 45°$ angle to the incident ray, then $\sin\theta_0 = 1/\sqrt{2}$ and (A.9) becomes

$$\delta = \frac{4\pi d}{\lambda_0}\sqrt{\left(\frac{n}{n_0}\right)^2 - \frac{1}{2}}. \quad (A.10)$$

Now combine the Stokes Relations,

$$r' = -r \quad (A.11)$$

$$1 - r^2 = tt' \quad (A.12)$$

to obtain the identity

$$tr't' = -r(1 - r^2). \quad (A.13)$$

If the parallel reflected rays in Figure A.2 are brought to a focus, the total electric field is given by summing (A.1) over orders to obtain

$$\begin{aligned}E_r &= \sum_{n=1}^{\infty} E_{nr} = \{r + r'tt'e^{-i\delta}[1 + (r'^2e^{-i\delta}) + (r'^2e^{-i\delta})^2 + \ldots + (r'^2e^{-i\delta})^{n-2}]\}E_0\\ &= \left[r + r'tt'e^{-i\delta}\sum_{n=0}^{\infty}(r'^2e^{-i\delta})^n\right]E_0 = \left(r + r'tt'e^{-i\delta}\frac{1}{1 - r'^2e^{-i\delta}}\right)E_0\\ &= \frac{r(1 - e^{-i\delta})}{1 - r^2e^{-i\delta}}E_0, \quad (A.14)\end{aligned}$$

where (A.13) has been used in the last step. The complex amplitude reflection coefficient is therefore

$$\mathcal{R}_p \equiv \frac{E_r}{E_0} = \frac{\sqrt{R_p}\,(1 - e^{-i\delta})}{1 - R_pe^{-i\delta}}, \quad (A.15)$$

where

$$R_p \equiv r^2 \tag{A.16}$$

is the Fresnel reflection coefficient for polarization p (either $\perp$ or $\|$),

$$R_{\|} = \left(\frac{\varepsilon \cos\theta - \sqrt{\varepsilon - \sin^2\theta}}{\varepsilon \cos\theta + \sqrt{\varepsilon - \sin^2\theta}} \right)^2 \tag{A.17}$$

$$R_{\perp} = \left(\frac{\cos\theta - \sqrt{\varepsilon - \sin^2\theta}}{\cos\theta + \sqrt{\varepsilon - \sin^2\theta}} \right)^2, \tag{A.18}$$

and ε the dielectric constant. Similarly, the electric fields of the transmitted rays in Fig. A.1 are

$$\begin{aligned} E_{1t} &= E_0 tt' \\ E_{2t} &= E_0 tt' r'^2 e^{-i\delta} \\ E_{3t} &= E_0 tt' r'^4 e^{-2i\delta} \\ E_{nt} &= E_0 tt' r'^{2(n-1)} e^{-(n-1)i\delta}. \end{aligned} \tag{A.19}$$

Bringing the transmitted rays to a focus and again using (A.13) gives the total transmitted electric field

$$E_t = \sum_{n=1}^{\infty} E_{nt} = \frac{tt'}{1 - r^2 e^{-i\delta}} E_0 = \frac{1 - r^2}{1 - r^2 e^{-i\delta}} E_0. \tag{A.20}$$

The complex amplitude transmission coefficient is therefore

$$\mathcal{T}_p \equiv \frac{E_t}{E_0} = \frac{1 - R_p}{1 - R_p e^{-i\delta}}. \tag{A.21}$$

If the reflected and transmitted rays are now allowed to reflect off two mirrors M1 and M2 at distances $l_1/2$ and $l_2/2$ from the beamsplitter (the optical path lengths l_1 and l_2 are twice as large), and then recombined and focused (Fig. A.3), the total emerging electric field is

$$\begin{aligned} E_p &= \mathcal{T}_p E_r e^{ikl_1} + \mathcal{R}_p E_t e^{ikl_2} = E_0 \frac{(1 - R_p)\sqrt{R_p}\,(1 - e^{-i\delta})}{(1 - R_p e^{-i\delta})^2} (e^{ikl_1} + e^{ikl_2}) \\ &= E_0 e^{ik(l_1 + l_2)/2} \frac{(1 - R_p)\sqrt{R_p}\,(1 - e^{-i\delta})}{(1 - R_p e^{-i\delta})^2} [e^{ik(l_1 - l_2)/2} + e^{-ik(l_1 - l_2)/2}] \\ &= E_0 e^{ik(l_1 + l_2)/2} \frac{(1 - R_p)\sqrt{R_p}\,(1 - e^{-i\delta})}{(1 - R_p e^{-i\delta})^2} 2\cos(\tfrac{1}{2} k \Delta l), \end{aligned} \tag{A.22}$$

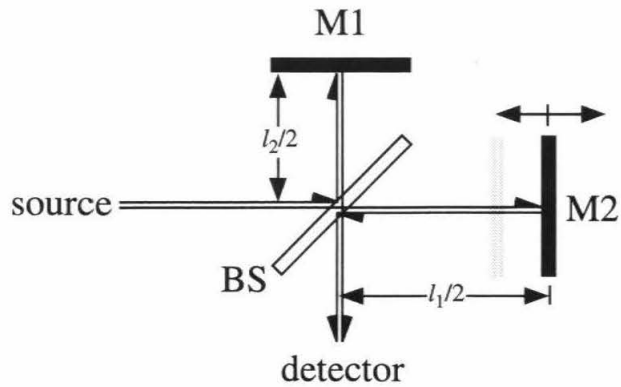

Figure A.3. Ray paths for the perpendicular beams which are split by the beamsplitter (BS), reflected off the mirrors M1 and M2, and then recombined. The optical paths are twice the physical separations of the mirrors since the rays travel this distance once in each propagation direction.

where

$$\Delta l \equiv l_1 - l_2. \tag{A.23}$$

Now use the identities

$$|1 - R_p\epsilon^{-i\delta}|^2 = 1 + {R_p}^2 - 2R_p\cos\delta = (1 - R_p)^2 + 4R_p\sin^2(\tfrac{1}{2}\delta) \tag{A.24}$$

$$|1 - \epsilon^{-i\delta}|^2 = 4\sin^2(\tfrac{1}{2}\delta) \tag{A.25}$$

to obtain

$$\begin{aligned} I_{k,p}(\Delta l) &= \tfrac{1}{2}c\epsilon_0|E_p|^2 \\ &\propto \tfrac{1}{2}|E_p|^2 = \tfrac{1}{2}|E_0|^2\left\{\frac{4(1 - R_p)^2R_p\sin^2(\frac{1}{2}\delta)}{[(1 - R_p)^2 + 4R_p\sin^2(\frac{1}{2}\delta)]^2}\right\}4\cos^2(\tfrac{1}{2}k\Delta l) \\ &= \left\{\frac{16(1 - R_p)^2R_p\sin^2(\frac{1}{2}\delta)}{[(1 - R_p)^2 + 4R_p\sin^2(\frac{1}{2}\delta)]^2}\right\}\{\tfrac{1}{2}|E_0|^2[1 + \cos(k\Delta l)]\}, \end{aligned} \tag{A.26}$$

where c is the speed of light and ϵ_0 is the permittivity of free space. But (A.26) can be broken up into

$$I_{k,p}(\Delta l) \equiv T_p(k)J_p(k)\{\tfrac{1}{2}[1 + \cos(k\Delta l)]\}, \tag{A.27}$$

where $T_p(k)$ is the beamsplitter transmission function

$$T_p(k) \equiv \frac{16(1 - R_p)^2R_p\sin^2(\frac{1}{2}\delta)}{[(1 - R_p)^2 + 4R_p\sin^2(\frac{1}{2}\delta)]^2}, \tag{A.28}$$

$J_p(k) \equiv |E_0|_p^2$ is a term proportional to the incident flux, and $1 + \cos(k\Delta l)$ is an interference term. The expression for a single polarization then becomes

$$I_{k,p}(\Delta l) = T_p(k) J_p(k) \{\tfrac{1}{2}[1 + \cos(k\Delta l)]\}. \tag{A.29}$$

For an unpolarized source, $J_\perp(k) = J_\parallel(k) = J(k)/2$, so

$$\begin{aligned} I_k(\Delta l) &= [T_\perp(k) J_\perp(k) + T_\parallel(k) J_\parallel(k)] \tfrac{1}{2}[1 + \cos(k\Delta l)] \\ &= \{\tfrac{1}{2}[T_\perp(k) + T_\parallel(k)] J(k)\} \{\tfrac{1}{2}[1 + \cos(k\Delta l)]\}, \end{aligned} \tag{A.30}$$

and the net transmission is an average of the transmissions in each of the two polarizations,

$$\langle T(k) \rangle \equiv \tfrac{1}{2}[T_\perp(k) + T_\parallel(k)]. \tag{A.31}$$

Plugging (A.31) into (A.30) then gives

$$I_k(\Delta l) = \langle T(k) \rangle J(k) \{\tfrac{1}{2}[1 + \cos(k\Delta l)]\}. \tag{A.32}$$

Appendix B: Winston Cones

"Logic is invincible because in order to combat logic it is necessary to use logic."
—Pierre Boutroux

"You can only find truth with logic if you have already found truth without it."
—G. K. Chesterton

The equation of the surface of a Winston cone is given in (r', z') coordinates (Fig. B.1) by the normal form equation of a parabola,

$$(r' - r'_0)^2 = 4f(z' - z'_0). \tag{B.1}$$

From the geometry of Fig. B.1,

$$r'_0 = 0 \tag{B.2}$$

$$z'_0 = -f, \tag{B.3}$$

so (B.1) becomes

$$r'^2 = 4f(z' + f). \tag{B.4}$$

To express in (r, z) coordinates, rotate the axes to obtain

$$\begin{bmatrix} r \\ z \end{bmatrix} = \begin{bmatrix} \cos\theta & -\sin\theta \\ \sin\theta & \cos\theta \end{bmatrix} \begin{bmatrix} r' \\ z' \end{bmatrix} - \begin{bmatrix} a' \\ 0 \end{bmatrix}. \tag{B.5}$$

Inverting then gives

$$\begin{bmatrix} r' \\ z' \end{bmatrix} = \begin{bmatrix} \cos\theta & \sin\theta \\ -\sin\theta & \cos\theta \end{bmatrix} \begin{bmatrix} r + a' \\ z \end{bmatrix} = \begin{bmatrix} (r + a')\cos\theta + z\sin\theta \\ -(r + a')\sin\theta + z\cos\theta \end{bmatrix}. \tag{B.6}$$

Plugging (B.4) into (B.6) and simplifying gives

$$(r\cos\theta + z\sin\theta)^2 + a'r(1 + \sin\theta)^2 - 2a'z\cos\theta(1 + \sin\theta) - a'^2(3 + \sin\theta)(1 + \sin\theta) = 0. \tag{B.7}$$

With $r = \sqrt{x^2 + z^2}$, (B.7) is a fourth order surface. Such surfaces are difficult to manufacture, but techniques have been developed which allow Winston cones to be commercially produced at reasonable cost.

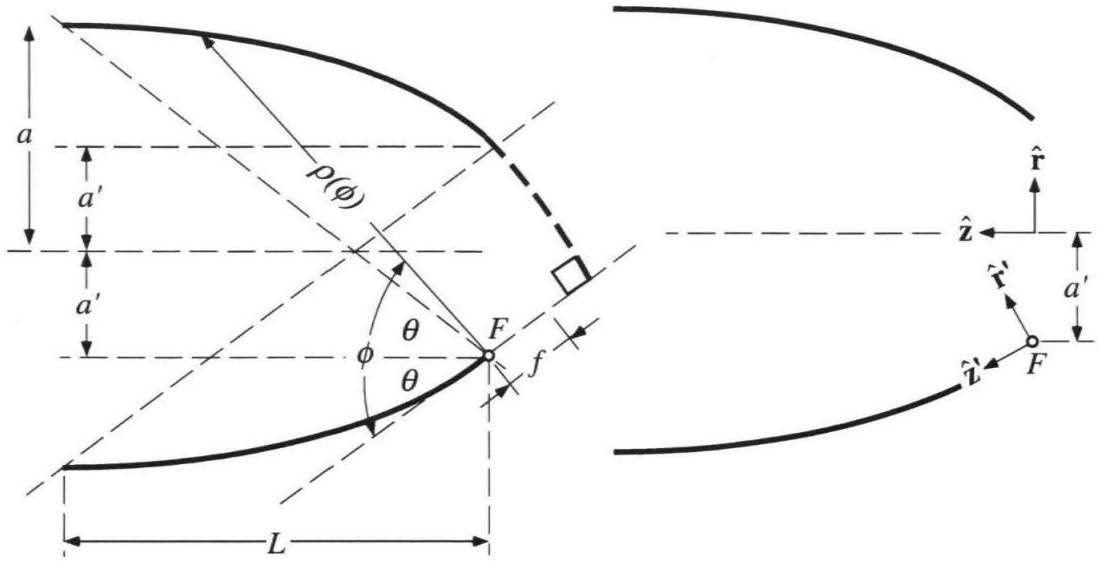

Figure B.1. Schematic diagram of a Winston cone light concentrator. The entrance and exit apertures are of radius a and a', respectively. F is the focus of the upper parabola segments, and f is its focal length. The length of the cone is L. The diagram on the right shows the origins and orientations of the focus-centered and symmetry axis-centered coordinate systems discussed in the main text.

Of the parameters a (entrance aperture radius), a' (exit aperture radius), f (focal length), L (cone length), and θ (opening half-angle), only two are independent. The equation of a parabola in polar coordinates centered at the focus F is

$$\rho(\phi) = \frac{2f}{1 - \cos\phi}. \tag{B.8}$$

Now, when $\phi = \theta + \pi/2$, the radius vector points in the $\hat{\mathbf{r}}$ direction and has length $2a'$, so

$$\rho(\theta + \tfrac{1}{2}\pi) = \frac{2f}{1 - \cos(\theta + \frac{1}{2}\pi)} = \frac{2f}{1 + \sin\theta} = 2a'. \tag{B.9}$$

Solving for f gives

$$f = a'(1 + \sin\theta). \tag{B.10}$$

From Fig. B.1,

$$\tan\theta = \frac{a + a'}{L}, \tag{B.11}$$

so

$$L = (a + a')\cot\theta. \tag{B.12}$$

The final relationship is derived from

$$\rho(2\theta) = \frac{2f}{1-\cos(2\theta)} = \sqrt{L^2 + (a+a')^2}, \qquad (B.13)$$

where the right-hand side of the equation follows from the Pythagorean theorem. Plugging in (B.10) and (B.12) then gives

$$\frac{2a'(1+\sin\theta)}{2\sin^2\theta} = (a+a')\sqrt{1+\cot^2\theta} = (a+a')\csc\theta. \qquad (B.14)$$

Solving for a' finally gives

$$a' = a\sin\theta. \qquad (B.15).$$

The Winston cone is there completely specified by the length L and the geometric field of view

$$\Theta_G \equiv 2\theta = 2\sin^{-1}\left(\frac{a'}{a}\right). \qquad (B.16)$$

Appendix C: Beam Coupling

"So far as the theorems of mathematics are about reality, they are not certain; so far as they are certain, they are not about reality."

—Albert Einstein

Approximating the telescope beam pattern by a Gaussian gives an area-normalized primary beam

$$P(\rho) = \frac{1}{2\pi\sigma^2} e^{-\rho^2/2\sigma^2}, \tag{C.1}$$

where ρ is the radial offset from beam center and

$$\sigma = \frac{HPBW}{2\sqrt{2\ln 2}} \tag{C.2}$$

is the Gaussian standard deviation, with HPBW the half-power beamwidth. (C.1) is normalized so that

$$\int_0^{2\pi} \int_0^{\infty} P(\rho)\rho \, d\rho \, d\theta = 1. \tag{C.3}$$

Let the beam center be pointed an angular distance R away from the center of a field of view of diameter Θ. In polar coordinates, the law of cosines relates R and ρ to the center of the field of view by

$$\rho^2 = R^2 + r^2 - 2Rr\cos\theta. \tag{C.4}$$

Therefore,

$$P(r,\theta) = \frac{1}{2\pi\sigma^2} e^{-R^2/2\sigma^2} e^{-(r^2 - 2rR\cos\theta)/2\sigma^2}. \tag{C.5}$$

The response of the instrument to a point source an angular distance R away from the pointing center is therefore given by integrating (C.5) over the Winston cone's circular field of view,

$$\begin{aligned} F(\sigma, R, \Theta) &= \int_0^{2\pi} \int_0^{\Theta/2} P(r,\theta) r \, dr \, d\theta \\ &= \frac{1}{\pi\sigma^2} e^{-R^2/2\sigma^2} \int_0^{\Theta/2} r e^{-r^2/2\sigma^2} \left(\int_0^{\pi} e^{rR\cos\theta/\sigma^2} \, d\theta \right) dr. \end{aligned} \tag{C.6}$$

But

$$I_0(x) = \frac{1}{\pi}\int_0^{\pi} e^{x\cos\theta}\, d\theta \qquad (C.7)$$

(Arfken 1985, p. 615), where I_0 is a zeroth order modified Bessel function, so

$$\int_0^{\pi} e^{rR\cos\theta/\sigma^2}\, d\theta = \pi I_0\left(\frac{rR}{\sigma^2}\right), \qquad (C.8)$$

and plugging (C.8) into (C.6) gives

$$F(\sigma, R, \Theta) = \frac{e^{-R^2/2\sigma^2}}{\sigma^2}\int_0^{\Theta/2} re^{-r^2/2\sigma^2} I_0\left(\frac{rR}{\sigma^2}\right) dr. \qquad (C.9)$$

Note that although this equation is functionally identical to the response of a Gaussian beam to a uniform brightness disk, for our instrument, (C.9) gives response function of the FTS to a *point source*. It must be convolved with the source brightness distribution to obtain the actual response of our instrument.

Although (C.9) cannot be integrated analytically, it gives a simple answer for a point source centered at $R = 0$. In this case, (C.9) simplifies to

$$F(\sigma, 0, \Theta) = \frac{1}{\sigma^2}\int_0^{\Theta/2} re^{-r^2/2\sigma^2}\, dr = 1 - e^{-\Theta^2/8\sigma^2}. \qquad (C.10)$$

In order to find the half-power beamwidth $W \equiv R_{1/2}$, set $F(\sigma, R, \Theta)$ equal to half of the peak beam response,

$$F(\sigma, W, \Theta) = \tfrac{1}{2}F(\sigma, 0, \Theta). \qquad (C.11)$$

Plugging in (C.9) and (C.10) gives

$$\frac{e^{-W^2/2\sigma^2}}{\sigma^2}\int_0^{\Theta/2} re^{-r^2/2\sigma^2} I_0\left(\frac{rW}{\sigma^2}\right) dr = \tfrac{1}{2}(1 - e^{-\Theta^2/8\sigma^2}), \qquad (C.12)$$

which can be solved by looking for the roots of

$$f(W) \equiv \frac{e^{-W^2/2\sigma^2}}{\sigma^2}\int_0^{\Theta/2} re^{-r^2/2\sigma^2} I_0\left(\frac{rW}{\sigma^2}\right) dr - \tfrac{1}{2}(1 - e^{-\Theta^2/8\sigma^2}). \qquad (C.13)$$

To solve using Newton-Raphson iteration, we also need the derivative df/dW, which is

$$\frac{df}{dW} = \frac{-We^{-W^2/2\sigma^2}}{\sigma^4}\int_0^{\Theta/2} re^{-r^2/2\sigma^2} I_0\left(\frac{rW}{\sigma^2}\right) dr + \frac{e^{-W^2/2\sigma^2}}{\sigma^2}\int_0^{\Theta/2} re^{-r^2/2\sigma^2}\frac{d}{dW}\left[I_0\left(\frac{rW}{\sigma^2}\right)\right] dr. \quad (C.14)$$

But

$$\frac{d}{dx}I_0(ax) = \tfrac{1}{2}a[I_{-1}(ax) + I_1(ax)] = aI_1(ax), \quad (C.15)$$

so

$$\frac{df}{dW} = \frac{1}{\sigma^2}\left\{\frac{e^{-W^2/2\sigma^2}}{\sigma^2}\left[\int_0^{\Theta/2} r^2 e^{-r^2/2\sigma^2} I_1\left(\frac{rW}{\sigma^2}\right) dr - W\int_0^{\Theta/2} re^{-r^2/2\sigma^2} I_0\left(\frac{rW}{\sigma^2}\right) dr\right]\right\}. \quad (C.16)$$

The derivative of f is therefore

$$\frac{df}{dW} = \frac{1}{\sigma^2}[F'(\sigma, R, \Theta) - WF(\sigma, R, \Theta)], \quad (C.17)$$

where

$$F'(\sigma, R, \Theta) \equiv \frac{e^{-W^2/2\sigma^2}}{\sigma^2}\int_0^{\Theta/2} r^2 e^{-r^2/2\sigma^2} I_1\left(\frac{rW}{\sigma^2}\right) dr. \quad (C.18)$$

Equation (C.13) can now be solved numerically for W, although care must be taken in evaluating F and F' since the $I_0(x)$ and $I_1(x)$ functions blow up for $x \gg n$. By using the asymptotic form

$$I_n(x) \approx \frac{1}{\sqrt{2\pi x}} e^x \quad (C.19)$$

for $x \gg n$, the integrals can be done acceptably. Therefore, with $x \equiv rR/\sigma^2$, the kernal of F becomes

$$K[F] = \frac{e^{-R^2/2\sigma^2}}{\sigma^2} re^{-r^2/2\sigma^2} I_0\left(\frac{rW}{\sigma^2}\right) \sim \frac{e^{-R^2/2\sigma^2}}{\sigma^2} re^{-r^2/2\sigma^2}\frac{e^{rR/\sigma^2}}{\sqrt{\frac{2\pi rR}{\sigma^2}}} = \frac{1}{\sigma\sqrt{2\pi R}} r^{-1/2} e^{-r^2/2\sigma^2} e^{(2rR-R^2)/2\sigma^2} = \frac{1}{\sigma\sqrt{2\pi R}} r^{-1/2} e^{-(R-r)^2/2\sigma^2}. \quad (C.20)$$

Similarly,

$$K[F'] \sim \frac{1}{\sigma\sqrt{2\pi R}} r^{1/2} e^{-(R-r)^2/2\sigma^2}. \qquad (C.21)$$

References

ANDERS, E. AND N. GREVESSE 1989. Abundances of the elements: Meteoritic and solar. *Geochim. Cosmochim. Acta* **53**, 197-214.

APPLEBY, J. F. AND J. S. HOGAN 1984. Radiative-convective equilibrium models of Jupiter and Saturn. *Icarus* **59**, 336-366.

ARFKEN, G. 1985. *Mathematical Methods for Physicists, 3rd ed.* Academic Press, Orlando, Flor.

ARMSTRONG, B. H. 1967. Spectrum line profiles: The Voigt function. *J. Quant. Spectrosc. Radiat. Transfer* **7**, 61-88.

ATREYA, S. K. 1986. *Atmospheres and Ionospheres of the Outer Planets and their Satellites.* Springer-Verlag, Berlin.

ATREYA, S. K. AND P. N. ROMANI 1985. Photochemistry and clouds of Jupiter, Saturn, and Uranus. In *Recent Advances in Planetary Meteorology* (G. E. Hunt, Ed.), pp. 17-68. Cambridge Univ. Press, Cambridge, England.

BACHET, G., E. R. COHEN, P. DORE, AND G. BIRNBAUM 1983. The translational-rotational absorption spectrum of hydrogen. *Can. J. Phys.* **61**, 591-603.

BAINES, K. H., M. E. MICKELSON, L. E. LARSON, AND D. W. FERGUSON 1995. The abundance of methane and ortho/para hydrogen on Uranus and Neptune: Implications of new laboratory 4-0 H_2 quadrupole line parameters. *Icarus* **114**, 328-340.

BELLARD, J., W. B. JOHNSTON, P. H. MOFFAT, AND D. T. LLEWELLYN-JONES 1985. Experimental determination of the temperature dependence of nitrogen-broadened line widths in the 1 — 0 band of HCl. *J. Quant. Spectrosc. Radiat. Transfer* **33**, 365-371.

BERGE, G. L. AND S. GULKIS 1976. Earth-based radio observations of Jupiter: Millimeter to meter wavelengths. In *Jupiter* (T. Gehrels, Ed.), pp. 621-692. Univ. of Ariz. Press, Tucson, Ariz.

BÉZARD, B., P. DROSSART, J. P. MAILLARD, G. TARRAGO, N. LACOME, G. POUSSIGUE, A. LEVY, AND G. GUELACHVILLI 1987. High resolution spectroscopy of Saturn at 5 μm. II. Cloud structure and gaseous composition. *Bull. Amer. Astron. Soc.* **19**, 849.

BÉZARD, B., D. GAUTIER, AND A. MARTEN 1986. Detectibility of HD and non-equilibrium species in the upper atmospheres of the giant planets from their submillimeter spectra. *Astron. Astrophys.* **161**, 387-402.

BÉZARD, B., C. GRIFFITH, T. OWEN, AND J. LACY 1995. Non-detection of hydrogen cyanide on Jupiter. *Icarus* **118**, 384-391, 1995.

BÉZARD, B., A. MARTEN, AND G. PAUBERT 1992. First ground-based detection of cyanoacetylene on Titan. *Bull. Amer. Astron. Soc.* **24**, 953-954.

BÉZARD, B., A. MARTEN, AND G. PAUBERT 1993. Detection of acetonitrile on Titan. *Bull. Amer. Astron. Soc.* **25**, 1100.

BÉZARD, B., P. N. ROMANI, B. J. CONRATH, AND W. C. MAGUIRE 1991. Hydrocarbons in Neptune's stratosphere from Voyager infrared observations. *J. Geophys. Res.* **96**, 18961-18975.

BIRNBAUM, G. AND E. R. COHEN 1976. Theory of line shape in pressure-induced absorption. *Can. J. Phys.* **54**, 593-602.

BJORAKER, G. L. 1985. *The Gas Composition and Vertical Cloud Structure of Jupiter's Troposphere Derived from 5 Micron Spectroscopic Observations.* Ph.D. thesis, Univ. of Ariz., Tucson, Ariz.

BJORAKER, G. L., H. P. LARSON, AND V. G. KUNDE 1986. The gas composition of Jupiter derived from 5-μm airborne spectroscopic observations. *Icarus* **66**, 579-609.

BORUNOV, S., V. DOROFEEVA, I. KHODAKOVSKY, P. DROSSART, E. LELLOUCH, AND T. ENCRENAZ 1995. Phosphorus chemistry in the atmosphere of Jupiter: A reassessment. *Icarus* **113**, 460-464.

BORYSOW, A. AND L. FROMMHOLD 1986. Theoretical collision-induced rototranslational absorption spectra for the outer planets: H_2-CH_4 pairs. *Astrophys. J.* **304**, 849-865.

BORYSOW, A. AND L. FROMMHOLD 1987. Collision-induced rototranslational absorption spectra of H_2-CH_4 pairs at temperatures from 50 to 300 K. *Astrophys. J.* **318**, 940-943.

BORYSOW, J., L. FROMMHOLD, AND G. BIRNBAUM 1988. Collision-induced rototranslational absorption spectra of H_2-He pairs at temperatures from 40 to 300 K. *Astrophys. J.* **326**, 509-515.

BOWDEN, M. D., B. W. JAMES, I. S. FALCONER, L. B. WHITBOURN, J. C. MACFARLANE, AND K. E. LESLIE 1991. High-frequency phase-modulated interferometer. *Optics Communications* **82**, 188-192.

BOYD, R. W. 1983. Thermal detectors. Ch. 13 in *Radiometry and the Detection of Optical Radiation*, pp. 211-223. Wiley, New York.

BRACEWELL, R. 1965. *The Fourier Transform and Its Applications.* McGraw-Hill, New York.

BRAULT, J. W. 1985. Fourier transform spectroscopy. In *High Resolution in Astronomy: 15th Advanced Course of the Swiss Society of Astronomy and Astrophysics* (A. Benz, M. Huber, and M. Mayor, Eds.). Geneva Observatory, Sauverny, Switzerland.

BREGMAN, J. D., D. F. LESTER, AND D. M. RANK 1975. Observation of the ν_2 band of PH_3 in the atmosphere of Saturn. *Astrophys. J. Let.* **202**, L55-L56.

BRIGGS, F. H. AND P. D. SACKETT 1989. Radio observations of Saturn as a probe of its atmosphere and cloud structure. *Icarus* **80**, 77-103.

CARLSTROM, J. E. AND J. ZMUIDZINAS 1996. Millimeter and submillimeter techniques. To appear in *Reviews of Radio Science 1993-1995* (W. R. Stone, Ed.). Oxford University Press, Oxford, England.

CHAMBERLAIN, J. E., G. W. CHANTRY, F. D. FINDLAY, H. A. GEBBIE, J. E. GIBBS, N. W. B. STONE, AND A. J. WRIGHT 1966. The spectral transmission at infra-red wavelengths of Michelson interferometers with dielectric film beam-dividers. *Infrared Phys.* **6**, 195-203.

CHAMBERLAIN, J. W. AND D. M. HUNTEN 1987. *Theory of Planetary Atmospheres.* Academic Press, New York.

CHANCE, K. V., I. G. NOLT, L. ZINK, D. A. JENNINGS, K. M. EVENSON, M. D. VANEK, AND J. V. RADOSTITZ 1986. Collisional broadening of HCl rotational transitions using tunable far-infrared radiation. *11th Conf. IR and Millimeter Waves*, Oct. 20-24, pp. 1-3, 1986.

CHANDRASEKHAR, S. 1960. *Radiative Transfer.* Dover Publ., New York.

CHANG, A. T. C. AND T. T. WILHEIT 1979. Remote sensing of atmospheric water vapor, liquid water, and wind speed at the ocean surface by passive microwave techniques from the Nimbus 5 satellite. *Radio Sci.* **14**, 793-802.

CLANCY, R. T. AND D. O. MUHLEMAN 1985. Chemical-dynamical models of the Venus mesosphere based upon diurnal microwave CO variations. *Icarus* **64**, 183-204.

CLANCY, R. T. AND D. O. MUHLEMAN 1991. Long-Term (1979-1990) Changes in the thermal, dynamical, and compositional structure of the Venus mesosphere as inferred from microwave spectral line observations of ^{12}CO, ^{13}CO, and $C^{18}O$. *Icarus* **89**, 129-146.

CLANCY, R. T. AND D. O. MUHLEMAN 1994. Ground-based microwave spectroscopy of the Earth's stratosphere and mesosphere. Ch. 7 in *Atmospheric Remote Sensing by Microwave Radiometry* (M. A. Janssen, Ed.). John Wiley & Sons, New York.

CLANCY, R. T., D. MUHLEMAN, AND G. BERGE 1990. Global changes in the 0-70 km thermal structure of the Mars atmosphere derived from 1975 to 1989 microwave spectra. *J. Geophys. Res.* **95**, 14543-14554.

CLANCY, R. T., D. MUHLEMAN, AND B. JAKOSKY 1983. Variability of carbon monoxide in the Mars atmosphere. *Icarus* **55**, 282-301.

COHEN, E. R., L. FROMMHOLD, AND G. BIRNBAUM 1982. Analysis of the far infrared H_2-He spectrum. *J. Chem. Phys.* **77**, 4933-4941.

CONNES, J. 1961. *Rev. Opt.* **40**, pp. 45, 116, 171, 231. Available in English translation as NAVWEPS Report No. 8099, NOTS TP3157, U.S. Naval Ordinance Test Station, China Lake, Calif.

CONNES, P., J. CONNES, AND J.-P. MAILLARD 1969. *Atlas des Spectres dans le Proche Infrarouge de Venus, Mars, Jupiter, et Saturne.* Edititions du Centre National de Recherche Scientifique, Paris.

CONRATH, B. P. AND P. J. GIERASCH 1984. Global variation of the para hydrogen fraction in Jupiter's atmosphere and implications for dynamics of the outer planets. *Icarus* **57**, 184-204.

CONRATH, B. J., D. GAUTIER, R. A. HANEL, AND J. S. HORNSTEIN 1984. The helium abundance of Saturn from Voyager measurements. *Astrophys. J.* **282**, 807-815.

COOLEY, J. W. AND J. W. TUKEY 1965. An algorithm for the machine calculation of complex Fourier series. *Math. Comput.* **19**, 297.

COURTIN, R., N. CORON, T. ENCRENAZ, R. GISPERT, P. BRUSTON, J. LEBLANC, G. DAMBIER, AND A. VIDAL-MADJAR 1977. Observations of giant planets at 1.4 mm and consequences on the effective temperatures. *Astron. Astrophys.* **60**, 115-123.

COURTIN, R., D. GAUTIER, A. MARTEN, B. BÉZARD, AND R. HANEL 1984. The composition of Saturn's atmosphere at northern temperate latitudes from Voyager IRIS spectra: NH_3, PH_3, C_2H_2, C_2H_6, CH_3D, CH_4, and the saturnian D/H ratio. *Astrophys. J.* **287**, 899-916.

DEBOER, D. AND P. STEFFES 1994. Laboratory measurements of the microwave properties of H_2S under simulated Jovian conditions with an application to Neptune. *Icarus* **109**, 352-366.

DE PATER, I. AND J. R. DICKEL 1982. VLA observations of Saturn at 1.3, 2, and 6 cm. *Icarus* **50**, 88-102.

DE PATER, I. AND S. MASSIE 1985. Models of the millimeter-centimeter spectra of the giant planets. *Icarus* **62**, 143-171.

DE PATER, I. AND M. RICHMOND 1989. Neptune's microwave spectrum from 1 mm to 20 cm. *Icarus* **80**, 1-13.

DE PATER, I., P. N. ROMANI, AND S. K. ATREYA 1991. Possible microwave absorption by H_2S gas in Uranus' and Neptune's atmospheres. *Icarus* **91**, 220-233.

DEAN, J. A. (Ed.) 1985. *Lange's Handbook of Chemistry, 13th ed.*, pp. 10-28 *et seq.* McGraw-Hill, New York.

DORE, P., L. NENCINI, AND G. BIRNBAUM 1983. Far infrared absorption in normal H_2 from 77 to 298 K. *J. Quant. Spectrosc. Radiat. Transfer* **30**, 245-253.

DOWLING, T. E., D. O. MUHLEMAN, AND G. L. BERGE 1987. Aperture synthesis observations of Saturn and its rings at 2.7-mm wavelength. *Icarus* **70**, 506-516.

Drossart, P., T. Encrenaz, V. Kunde, R. Hanel, and M. Combes 1982. An estimate of the PH_3, CH_3D, and GeH_4 abundances on Jupiter from the Voyager IRIS data at 4.5 μm. *Icarus* **49**, 416-426.

Drossart, P., T. Encrenaz, and A. Tokunaga 1984. Variability of phosphine on Jupiter from 5-μm spectroscopy. *Icarus* **60**, 613-620, 1984.

Drossart, P., E. Lellouch, B. Bézard, J.-P. Maillard, and G. Tarrago 1990. Jupiter: Evidence for a phosphine enhancement at high northern latitudes. *Icarus* **83**, 248-253.

Encrenaz, T. and M. Combes 1977. The far infrared spectrum of Saturn: Observability of PH_3 and NH_3. *Astron. Astrophys.* **61**, 387-390.

Encrenaz, T., M. Combes, and Y. Zeau 1978. The spectrum of Jupiter between 10 and 13 μ: An estimate of the Jovian $^{15}N/^{14}N$ ratio. *Astron. Astrophys.* **70**, 29-36.

Encrenaz, T., M. Combes, and Y. Zeau 1980. The spectrum of Jupiter between 8 and 9 μ: Estimates of the Jovian C/H and D/H ratios. *Astron. Astrophys.* **84**, 148-153.

Encrenaz, T., B. Bézard, J. Crovisier, A. Coustenis, E. Lellouch, S. Gulkis, and S. K. Atreya 1995. Detectibility of molecular species in planetary and satellite atmospheres from their rotational transitions. *Planet. Space Sci.* **43**, 1485-1516.

Encrenaz, T., E. Serabyn, and E. W. Weisstein 1996. Millimeter spectroscopy of Uranus and Neptune: Constraints on CO and PH_3 tropospheric abundances. In press in *Icarus*.

Epstein, E. E., M. A. Janssen, and J. N. Cuzzi 1984. Saturn's rings: 3-mm low-inclination observations and derived properties. *Icarus* **58**, 403-411.

Esposito, L. W., J. N. Cuzzi, J. B. Holberg, E. A. Marouf, G. L. Tyler, and C. C. Porco 1984. Saturn's rings: Structures, dynamics, and particle properties. In *Saturn* (T. Gehrels, Ed.), pp. 463-545. Univ. of Ariz. Press, Tucson, Ariz.

Fegley, B. Jr. 1994. Properties and composition of the terrestrial oceans and of the atmospheres of the Earth and other planets. In *AGU Handbook of Physical Constants* (T. Ahrens, Ed.). American Geophys. Union, Washington, DC.

Fegley, B. Jr. and K. Lodders 1994. Chemical models of the deep atmospheres of Jupiter and Saturn. *Icarus* **110**, 117-154.

Fegley, B. Jr. and R. G. Prinn 1986. Chemical models of the deep atmosphere of Uranus. *Astrophys. J.* **307**, 852-865.

Fink, U. and H. P. Larson 1978. Deuterated methane observed on Saturn. *Science* **201**, 343-345.

Forman, M. L., W. H. Steel, and G. A. Vanesse 1966. Correction of asymmetric interferograms obtained from Fourier spectroscopy. *J. Opt. Soc. Amer.* **56**, 59-63.

Gautier, D., B. J. Conrath, T. Owen, I. de Pater, and S. K. Atreya 1995. In *Neptune and Triton* (D. Cruikshank and M. S. Matthews, Eds.). In press, Univ. of Ariz. Press, Tucson, Ariz.

Gierasch, P. J. 1983. Dynamical consequences of orthohydrogen-parahydrogen disequilibrium on Jupiter and Saturn. *Science* **219**, 847-849.

Gillet, F. C. and W. J. Forrest 1974. The 7.5 to 13.5 micron spectrum of Saturn. *Astrophys. J.* **187**, L37-L38.

Goodman, G. C. 1969. *Models of Jupiter's Atmosphere.* Ph.D. thesis. Univ. of Illinois, Urbana, Ill.

Gordy, W. and R. L. Cook 1984. *Microwave Molecular Spectra, 3rd ed.* Wiley, New York.

GRIFFIN, M. J., P. A. R. ADE, G. S. ORTON, E. I. ROBSON, AND W. K. GEAR 1986. Submillimeter and millimeter observations of Jupiter. *Icarus* **65**, 244 -256.

GRIFFIN, M. J. AND G. S. ORTON 1993. The near-millimeter brightness temperature spectra of Uranus and Neptune. *Icarus* **105**, 537-547.

GRIFFITH, C. A., B. BÉZARD, T. OWEN, AND D. GAUTIER 1992. The tropospheric abundances of NH_3 and PH_3 in Jupiter's Great Red Spot, from *Voyager IRIS* observations. *Icarus* **98**, 82-93.

GROSSMAN, A. W. 1990. *Microwave Imaging of Saturn's Deep Atmosphere and Rings.* Ph.D. thesis. California Institute of Technology, Pasadena, Calif.

GROSSMAN, A. W., D. O. MUHLEMAN, AND G. L. BERGE 1989. High-resolution microwave images of Saturn. *Science* **245**, 1211-1215.

GROSSMAN, E. 1989. AT, atmospheric transmission software. Airhead Software, Boulder, Colo.

GUILLOT, T. 1995. Condensation of methane, ammonia, and water and the inhibition of convection in giant planets. *Science* **269**, 1697-1699.

GUILLOT, T., D. GAUTIER, C. CHABRIER, AND B. MOSSER 1994. Are the giant planets fully convective? *Icarus* **112**, 337-353.

GUILLOTEAU, S., A. DUTRY, A. MARTEN, AND D. GAUTIER 1993. CO in the troposphere of Neptune: Detection of the J=1-0 line in absorption. *Astron. Astrophys.* **279**, 661-667.

GURWELL, M. A. 1996. *Planetary Atmospheres: Probing Structure through Millimeterwave Observations of Carbon Monoxide.* Ph.D. thesis, California Institute of Technology, Pasadena, Calif.

GURWELL, M. A. AND D. O. MUHLEMAN 1996. CO on Titan: Evidence for a well-mixed atmosphere. *Submitted to Icarus.*

GURWELL, M. A., D. O. MUHLEMAN, K. P. SHAH, G. L. BERGE, D. J. RUDY, AND A. W. GROSSMAN 1995. Observations of the CO bulge on Venus and implications for mesospheric winds. *Icarus* **115**, 141-158.

HAAS, M. R., E. F. ERICKSON, D. GOORVITCH, D. D. MCKIBBIN, AND D. M. RANK 1985. Observations of the $J = 10$ manifold of the pure rotation band of phosphine on Saturn. *Icarus* **64**, 549-556.

HAAS, M. R., E. F. ERICKSON, D. GOORVITCH, D. D. MCKIBBIN, AND D. M. RANK 1986. Erratum to: Observations of the $J = 10$ manifold of the pure rotation band of phosphine on Saturn. *Icarus* **67**, 342.

HANEL, R. A., B. J. CONRATH, L. W. HERATH, V. G. KUNDE, AND J. A. PIRRAGLIA 1981a. Albedo, internal heat, and energy balance of Jupiter: Preliminary results of the Voyager infrared investigation. *J. Geophys. Res.* **86**, 8705-8712.

HANEL, R. A., B. J. CONRATH, F. M. FLASAR, V. G. KUNDE, W. MAGUIRE, J. C. PEARL, J. A. PIRRAGLIA, R. SAMUELSON, L. HEARTH, M. ALLISON, D. P. CRUIKSHANK, D. GAUTIER, P. GIERASCH, L. HORN, R. KOPPANY, AND C. PONNAMPERUMA 1981b. Infrared observations of the saturnian system from Voyager 1. *Science* **212**, 192-200.

HILDEBRAND, R. H. 1985. Erratum to: Throughput of diffraction-limited field optics system for infrared and millimetric telescopes. *Appl. Opt.* **24**, 616.

HILDEBRAND, R. H., R. F. LOWENSTEIN, D. A. HARPER, G. S. ORTON, J. KEENE, AND S. E. WHITCOMB 1985. Far-infrared and submillimeter brightness temperatures of the giant planets. *Icarus* **64**, 64-87.

HILDEBRAND, R. H. AND R. WINSTON 1982. Throughput of diffraction-limited field optics system for infrared and millimetric telescopes. *Appl. Opt.* **21**, 1844-1846.

HOFSTADTER, M. D. 1992. *Microwave Observations of Uranus.* Ph.D. thesis. California Institute of Technology, Pasadena, Calif.

HOFSTADTER, M. D., G. L. BERGE, AND D. O. MUHLEMAN 1990. Vertical motions in the Uranian atmosphere: An analysis of radio observations. *Icarus* **84**, 261-267.

HOFSTADTER, M. D. AND D. O. MUHLEMAN 1988. Latitudinal variations of ammonia in the atmosphere of Uranus: An analysis of microwave observations. *Icarus* **81**, 396-412.

HOLAH, G. D. 1982. Far-infrared and submillimeter-wavelength filters. Ch. 6 in *Infrared and Millimeter Waves* **6**. Academic Press, New York.

HOROWITZ, P. AND W. HILL 1990. *The Art of Electronics, 2nd ed.* Cambridge Univ. Press, Cambridge, England.

JOINER, J. AND P. S. STEFFES 1990. Modeling of the millimeter-wave emission of Jupiter utilizing laboratory measurements of ammonia opacity. *J. Geophys. Res.* **96**, 17462-17470.

JOINER, J., P. S. STEFFES, AND K. S. NOLL 1992. Search for sulfur (H_2S) on Jupiter at millimeter wavelengths. *IEEE Trans. Microwave Theory Tech.* **40**, 1101-1109.

KAKAR, R. K., J. W. WATERS, AND W. J. WILSON 1976. Venus: Microwave detection of CO. *Science* **191**, 379-380.

KAYE, J. A. AND D. F. STROBEL 1984. Phosphine photochemistry in the atmosphere of Saturn. *Icarus* **59**, 314-335.

KIEFFER, H. H., T. Z. MARTIN, A. R. PETEREFREUND, B. M. JAKOSKY, E. D. MINER, AND F. D. PALLUCONI 1977. Thermal and albedo mapping of Mars during the Viking primary mission. *J. Geophys. Res.* **82**, 4249-4921.

KIM, S. J. AND T. OWEN 1983. PH_3 mixing ratio in the Great Red Spot. *Bull. Amer. Astron. Soc.* **15**, 832.

KNACKE, R. F., S. J. KIM, S. T. RIDGWAY, AND A. T. TOKUNAGA 1982. The abundances of CH_4, CH_3D, NH_3, and PH_3 in the troposphere of Jupiter derived from high-resolution 1100-1200 cm^{-1} spectra. *Astrophys. J.* **262**, 388-395.

KUNDE, V., R. HANEL, W. MAGUIRE, D. GAUTIER, J. BALUTEAU, A. MARTEN, A. CHEDIN, N. HUSSON, AND N. SCOTT 1982. The tropospheric gas composition of Jupiter's North Equatorial Belt (NH_3, PH_3, CH_3D, GeH_4, H_2O) and the Jovian D/H isotopic ratio. *Astrophys. J.* **263**, 443-467.

KUTNER, M. L., L. MUNDY, AND R. J. HOWARD 1984. Interpretation of absolute line intensities on the NRAO 11 meter and other millimeter wave telescopes. *Astrophys. J.* **283**, 890-894.

KUTNER, M. L. AND B. L. ULICH 1981. Recommendations for calibration of millimeter-wavelength spectral line data. *Astrophys. J.* **250**, 341-348.

LANDRY, B., M. ALLEN, AND Y. L. YUNG 1991. Troposphere-stratosphere interactions in a one-dimensional model of Jovian photochemistry. *Icarus* **89**, 377-383.

LARSON, H. P., D. S. DAVIS, R. HOFMANN, AND G. L. BJORAKER 1984. The Jovian atmospheric window at 2.7 μm: A search for H_2S. *Icarus* **60**, 621-639.

LARSON, H. P., U. FINK, H. A. SMITH, AND D. S. DAVIS 1980. The middle-infrared spectrum of Saturn: Evidence for phosphine and upper limits to other trace atmospheric constituents. *Astrophys. J.* **240**, 327-337.

LARSON, H. P., U. FINK, AND R. R. TREFFERS 1977. Phosphine in Jupiter's atmosphere: The evidence from high-altitude observations at 5 micrometers. *Astrophys. J.* **211**, 972-979.

LELLOUCH, E. *et al.* 1994. Millimeter-wave observations of the Jupiter/Comet Shoemaker-Levy 9 collision from IRAM 30-m telescope: CO, CS, and OCS. Abstract 02.03 in *Special Session on Comet Shoemaker-Levy 9; 26th Annual Meeting of the Division for Planetary Sciences, Oct. 31-Nov. 4, 1994. Washington, DC.*, p. 12.

LELLOUCH, E., M. BELTON, I. DE PATER, S. GULKIS, AND T. ENCRENAZ 1990. Io's atmosphere from microwave detection of SO_2. *Nature* **346**, 639.

LELLOUCH, E., F. COMBES, AND T. ENCRENAZ 1984. Microwave observations of Jupiter and Saturn. *Astron. Astrophys.* **140**, 216-219.

LELLOUCH, E., T. ENCRENAZ, AND M. COMBES 1984. The detectibility of minor atmospheric species in the far infrared spectra of Jupiter and Saturn. *Astron. Astrophys.* **140**, 405-413.

LELLOUCH, E., M. GÉRIN, F. COMBES, S. ATREYA, AND T. ENCRENAZ 1989. Observations of the J=1-0 CO lines in the Mars Atmosphere: Radiodetection of ^{13}CO and monitoring of ^{12}CO. *Icarus* **77**, 414-438.

LELLOUCH, E., J. J. GOLDSTEIN, J. ROSENQVIST, S. W. BOUGHER, AND G. PAUBERT 1994. Global circulation, thermal structure, and carbon monoxide distribution in Venus's mesosphere in 1991. *Icarus* **110**, 315-339.

LELLOUCH, E., G. PAUBERT, AND T. ENCRENAZ 1991. Mapping of CO millimeter-wave lines in Mars' atmosphere—the spatial variability of carbon-monoxide on Mars. *Planet. Space Sci.* **39**, 219-224.

LELLOUCH, E., P. N. ROMANI, AND J. ROSENQVIST 1994. The vertical distribution and origin of HCN in Neptune's atmosphere. *Icarus* **108**, 112-136.

LELLOUCH, E., D. STROBEL, M. BELTON, G. PAUBERT, G. BALLESTER, AND I. DE PATER 1994. Millimeter wave observations of Io's atmosphere: New data and new models. *Bull. Amer. Astron. Soc.* **26**, 1136.

LEWIS, J. S. AND R. G. PRINN 1970. Jupiter's clouds: Structure and composition. *Science* **169**, 472-473.

LEVY, A., N. LACOME, AND G. TARRAGO 1994. Temperature-dependence of collision-broadened lines of phosphine. *J. Molec. Spectrosc.* **166**, 20-31.

LIEBE, H. J. 1980. Atmospheric water vapor: A nemesis for millimeter wave propagation. In *Atmospheric Water Vapor* (Deepak *et al.*, Eds.), pp. 143-201. Academic Press, New York.

LIEBE, H. J. 1981. Modeling attenuation and phase of radio waves in air at frequencies below 1000 GHz. *Radio Sci.* **16**, 1183-1199.

LIEBE, H. J. 1985. An updated model for millimeter wave propagation in moist air. *Radio Sci.* **20**, 1069-1089.

LINDAL, G. F. 1992. The atmosphere of Neptune: An analysis of radio occultation data acquired with Voyager 2. *Astron. J.* **103**, 967-982.

LINDAL, G. F., J. R. LYONS, D. N. SWEETNAM, V. R. ESHELMAN, D. P. HINSON, AND G. L. TYLER 1987. The atmosphere of Uranus: Results of radio occultation measurements with Voyager 2. *J. Geophys. Res.* **92**, 14987-15001.

LINDAL, G. F., D. N. SWEETNAM, AND V. R. ESHLEMAN 1985. The atmosphere of Saturn: An analysis of the Voyager radio occultation measurements. *Astron. J.* **90**, 1136-1146.

LINDAL, G. F., G. E. WOOD, G. S. LEVY, J. D. ANDERSON, D. N. SWEETNAM, H. B. HOTZ, V. R. ESHLEMANM, AND G. L. TYLER 1981. The atmosphere of Jupiter: An analysis of the Voyager radio occultation measurements. *J. Geophys. Res.* **86**, 8721-8727.

LOEWENSTEIN, E. V. 1963. On the correction of phase errors in interferograms. *Appl. Opt.* **2**, 491-494.

LOEWENSTEIN, E. V. AND D. R. SMITH 1971. Optical constants of far infrared materials. I: Analysis of channeled spectra and application to mylar. *Appl. Opt.* **10**, 577-583.

MARTEN, A., R. COURTIN, D. GAUTIER, AND A. LACOMBE 1980. Ammonia vertical density profiles in Jupiter and Saturn from their radioelectric and infrared emissivities. *Icarus* **41**, 410-422.

MARTEN, A., C. DE BERGH, D. GAUTIER, J.-P. MAILLARD, P. DROSSART, B. L. LUTZ, AND G. S. ORTON 1994. Four micron high-resolution spectra of Jupiter in the North Equatorial Belt: H_3^+ emissions and the $^{12}C/^{13}C$ ratio. *Planet. Space Sci.* **42**, 391-399.

MARTEN, A., D. GAUTIER, M. J. GRIFFIN, H. E. MATTHEWS, D. A. NAYLOR *et al.* 1995. The collision of Comet Shoemaker-Levy-9 with Jupiter—Detection and evolution of HCN in the stratosphere of the planet. *Geophys. Res. Let.* **22**, 1589-1592.

MARTEN, A., D. GAUTIER, T. OWEN, D. B. SANDERS, H. E. MATTHEWS, S. K. ATREYA, R. P. J. TILANUS, AND J. R. DEANE 1993. First observations of CO and HCN on Neptune and Uranus at millimeter wavelengths and their implications for atmospheric chemistry. *Astrophys. J.* **406**, 285-297.

MARTEN, A., D. GAUTIER, L. TANGUY, A. LECACHEUX, C. ROSOLEN, AND G. PAUBERT 1988. Abundance of carbon-monoxide in the stratosphere of Titan from millimeter heterodyne observations. *Icarus* **76**, 558-562.

MARTIN, D. H. 1982. Polarizing (Martin-Puplett) interferometric spectrometers for the near- and submillimeter spectra. Ch. 2 in *Infrared and Millimeter Waves* **6**, 65-148. Academic Press, New York.

MASSIE, S. T. AND D. M. HUNTEN 1982. Conversion of *para* and *ortho* hydrogen in the Jovian planets. *Icarus* **49**, 213-226.

MERTZ, L. 1967. Auxiliary computation for Fourier spectroscopy. *Infrared Phys.* **7**, 17-23.

MEYER, W., L. FROMMHOLD, AND G. BIRNBAUM 1989. Rototranslational absorption-spectra of H_2-H_2 pairs in the far infrared. *Phys. Rev. A* **39**, 2434-2448.

MICHELSON, A. A. 1891. Visibility of interference-fringes in the focus of a telescope. *Phil. Mag.* **31**, 256-259.

MICHELSON, A. A. 1892. On the application of interference methods to spectroscopic measurements. *Phil. Mag.* **34**, 280.

MOSES, J. I. 1992. Meteoroid ablation in Neptune's atmosphere. *Icarus* **99**, 368-383.

MOSES, J. I., M. ALLEN, AND Y. L. YUNG 1992. Hydrocarbon nucleation and aerosol formation in Neptune's atmosphere. *Icarus* **99**, 318-346.

MUHLEMAN, D. O. AND G. L. BERGE 1982. Microwave emission from Saturn's rings. In *Planetary Rings* (A. Brahic, Ed.), pp. 57-70. I.A.U., Cepadues-Editions, Toulouse, France.

MUHLEMAN, D. O., G. L. BERGE, AND R. T. CLANCY 1984. Microwave measurements of carbon monoxide on Titan. *Science* **223**, 393-396.

NAYLOR, D.A., T. A. CLARK, AND G. R. DAVIS 1994. A polarizing Fourier transform spectrometer for astronomical spectroscopy at submillimeter and mid-infrared wavelengths. *SPIE* **2198**, 703-714.

NAYLOR, D.A., G. R. DAVIS, M. J. GRIFFIN, T. A. CLARK, D. GAUTIER, AND A. MARTEN 1994. Broad-band spectroscopic detection of the CO J=3-2 tropospheric absorption in the atmosphere of Neptune. *Astron. Astrophys. Let.* **291**, L51-L53.

NIEMANN, H. B., D. N. HARPOLD, S. K. ATREYA, G. R. CARIGNAN, D. M. HUNTEN, AND T. C. OWEN 1992. Galileo probe mass spectrometer experiment. *Space Sci. Reviews* **60**, 111-142.

NOLL, K. S., T. R. GEBALLE, AND R. F. KNACKE 1989. Arsine in Saturn and Jupiter. *Astrophys. J. Let.* **338**, L71-L74.

NOLL, K. S., R. F. KNACKE, T. R. GEBALLE, AND A. T. TOKUNAGA 1986. Detection of carbon monoxide in Saturn. *Astrophys. J. Let.* **309**, L91-L94.

NOLL, K. S., R. F. KNACKE, T. R. GEBALLE, AND A. T. TOKUNAGA 1988. The origin and vertical distribution of carbon monoxide in Jupiter. *Astrophys. J.* **324**, 1210-1218.

NOLL, K. S. AND H. P. LARSON 1990. The spectrum of Saturn from 1990 to 2230 cm^{-1}: Abundances of AsH_3, CH_3D, CO, GeH_4, NH_3, and PH_3. *Icarus* **89**, 168-189.

OEPTS, D. 1976. Fourier transform spectroscopy. Sec. 4.2 (Far Infrared and Submillimeter-Wave Regions), Ch. 4 (Molecular Spectroscopy) in *Methods of Experimental Physics* **13B** (D. Williams, Ed.), pp. 60-87. Academic Press, New York.

ORTON, G. S., M. J. GRIFFIN, P. A. R. ADE, I. G. NOLT, J. V. RADOSTITZ, E. I. ROBSON, AND W. K. GEAR 1986. Submillimeter and millimeter observations of Uranus and Neptune. *Icarus* **67**, 289-304.

ORTON, G. S. AND C. D. KAMINSKI 1989. An exploratory 5-μm spectrum of Uranus. *Icarus* **77**, 109-117.

ORTON, G., J. LACY, A. CASTILLO, J. ACHTERMAN, AND P. PARMAR 1992. Zonal-mean temperature structure, composition, and cloud properties of Jupiter in 1989 October from high-resolution spectroscopic thermal imaging. *Bull. Amer. Astron. Soc.* **24**, 1041.

ORTON, G. S., A. T. TOKUNAGA, AND J. CALDWELL 1983. Observational constraints on the atmospheres of Uranus and Neptune from new measurements near 10 μm. *Icarus* **56**, 147-164.

OWEN, T. *et al.* 1994. JCMT observations of the collision of Comet Shoemaker-Levy 9 with Jupiter. Abstract 03.03 in *Special Session on Comet Shoemaker-Levy 9; 26th Annual Meeting of the Division for Planetary Sciences, Oct. 31-Nov. 4, 1994, Washington, DC.*, p. 19.

OWEN, T., A. R. W. MCKELLAR, T. ENCRENAZ, J. LECACHEUX, C. DEBERGH, AND J. P. MAILLARD 1977. A study of the 1.56 μm band on Jupiter and Saturn. *Astron. Astrophys.* **54**, 291-295.

PENZIAS, A. A. AND C. A. BURRUS 1973. Millimeter-wavelength radio-astronomy techniques. *Ann. Rev. Astron. Astrophys.* **11**, 51-72.

PICKETT, H. M., R. L. POYNTER, AND E. A. COHEN 1981. Pressure broadening of phosphine by hydrogen and helium. *J. Quant. Spectrosc. Radiat. Transfer* **26**, 197-198.

PICKETT, H. M., R. L. POYNTER, AND E. A. COHEN 1992. Submillimeter, millimeter, and microwave spectral line catalogue. JPL Publ. 80-23, Rev. 3. JPL, Pasadena, Calif. The most recent version of catalog is available on the World Wide Web via `http://spec.jpl.nasa.gov`.

POYNTER, R. AND R. KAKAR 1975. The microwave frequencies, line parameters, and spectral constants for $^{14}NH_3$. *Astrophys. J. Sup.* **29**, 87-96.

PRINN, R. G., H. P. LARSON, J. J. CALDWELL, AND D. GAUTIER 1984. Composition and chemistry of Saturn's atmosphere. In *Saturn* (T. Gehrels and M. S. Matthews, Eds.), pp. 88-149. Univ. of Arizona Press, Tucson.

PRINN, R. G. AND J. S. LEWIS 1975. Phosphine on Jupiter and implications for the Great Red Spot. *Science* **190**, 274-276.

RIDGWAY, S. T., L. WALLACE, AND G. R. SMITH 1976. The 800-1200 inverse centimeter absorption spectrum of Jupiter. *Astrophys. J.* **207**, 1002-1006.

ROHART, F., D. DEROZIER, AND J. LEGRAND 1987. Foreign gas relation of the $J = 0 - 1$ transition of $HC^{15}N$. A study of the temperature dependence by coherent transients. *J. Chem. Phys.* **87**, 5794-5803.

ROSENKRANZ, P. W. 1994. Absorption of microwaves by atmospheric gases. Ch. 2 in *Atmospheric Remote Sensing by Microwave Radiometry* (M. A. Janssen, Ed.). Wiley, New York.

ROSENQVIST, J. E., LELLOUCH, P. N. ROMANI, G. PAUBERT, AND T. ENCRENAZ 1992. Millimeter-wave observations of Saturn, Uranus, and Neptune—CO and HCN on Neptune. *Astrophys. J. Let.* **392**, L99-L102.

ROWAN-ROBINSON, M., P. A. R. ADE, E. I. ROBSON, AND P. E. CLEGG 1978. Millimetre observations of planets, galactic and extra-galactic sources. *Astron. Astrophys.* **62**, 249-254.

RUBENS, H. AND R. W. WOOD 1911. Focal isolation of long heat-waves. *Phil. Mag.* **21**, 249-261.

RUDY, D. J. 1987. *Mars: High Resolution VLA Observations at Wavelengths of 2 and 6 cm and Derived Properties.* Ph.D. thesis. California Institute of Technology, Pasadena, Calif.

RUDY, D. J., D. O. MUHLEMAN, G. L. BERGE, B. M. JAKOSKY, AND P. R. CHRISTENSEN 1987. Mars: VLA observations of the northern hemisphere and the north polar regions at wavelengths of 2 and 6 cm. *Icarus* **71**, 159-177.

RUZE, J. 1966. Antenna tolerance theory—A review. *Proc. IEEE* **54**, 633-640.

SAKAI, H., G. A. VANASSE, AND M. L. FORMAN 1968. Spectral recovery in Fourier spectroscopy. *J. Opt. Soc. Amer.* **58**, 84-90.

SCHNOPPER, H. W. AND R. I. THOMPSON 1974. Fourier spectrometers. In *Methods of Experimental Physics*, **12A** (M. L. Meeks, Ed.), pp. 491-529. Academic Press, New York.

SERABYN, E., T. G. PHILLIPS, AND C. R. MASSON 1991. Surface figure measurements of radio telescopes with a shearing interferometer. *Appl. Opt.* **30**, 1227-1241.

SERABYN, E. AND E. W. WEISSTEIN 1995. Fourier transform spectroscopy of the Orion Molecular Cloud core. *Astrophys. J.* **451**, 238-251.

SERABYN, E. AND E. W. WEISSTEIN 1996. Measurements of planetary brightness temperature spectra at near- and sub-millimeter wavelengths with a Fourier transform spectrometer. To appear in *Appl. Opt.*

SERABYN, E., E. W. WEISSTEIN, AND D. C. LIS 1993. FTS atmospheric transmission measurements and observations of planetary atmospheres. Presented at the 1993 Zermat Conference.

SHAH, K. P. 1992. *Interferometric Observations of the J(0,1) Line on Venus: Upper Mesospheric Winds and CO Abundance.* Ph.D. thesis, California Institute of Technology, Pasadena, Calif.

SHAH, K. P., D. O. MUHLEMAN, AND G. L. BERGE 1991. Measurement of winds in Venus' upper mesosphere based on Doppler shifts of the 2.6-mm ^{12}CO line. *Icarus* **93**, 96-121.

SMITH, M. D. AND P. J. GIERASCH 1995. Convection in the outer planet atmospheres including ortho-para hydrogen conversion. *Icarus* **116**, 159-179.

SPILKER, T.R. 1993. New laboratory measurements on ammonia's microwave inversion spectrum, with implications for planetary atmospheres. *J. Geophys. Res.* **98**, 5539-5548.

STRANG, G. 1993. Wavelet transforms versus Fourier transforms. *Bull. Amer. Math. Soc.* **28**, 288-305.

STROBEL, D. F. 1977. NH_3 and PH_3 photochemistry in the Jovian atmosphere. *Astrophys. J. Let.* **214**, L97-L99.

TANGUY, L., B. BÉZARD, A. MARTEN, D. GAUTIER, E. GÉRARD, G. PAUBERT, AND A. LECACHEUX 1990. Stratospheric profile of HCN on Titan from millimeter observations. *Icarus* **85**, 43-57.

TARRAGO, G., N. LACOME, A. LEVY, G. GUELACHVILLI, B. BÉZARD, AND P. DROSSART 1992. Phosphine spectrum at 4-5 μm: Analysis and line-by-line simulation of $2\nu_2$, $\nu_2+\nu_4$, $2\nu_4$, ν_1, and ν_3 bands. *J. Molec. Spectrosc.* **154**, 30-42.

THOMPSON, L. A. 1990. Mylar as an optical window. *Publ. Astron. Soc. Pac.* **102**, 1086-1091.

THOMPSON, A. R., J. M. MORAN, AND G. W. SWENSON, JR. 1991. *Interferometry and Synthesis in Radio Astronomy.* Krieger Publ. Co., Malabar, Flor.

TOKUNAGA, A., S. BECK, T. GEBALLE, J. LACY, AND E. SERABYN 1981. The detection of HCN on Jupiter. *Icarus* **48**, 283-289.

TOKUNAGA, A. T., H. L. DINERSTEIN, D. F. LESTER, AND D. M. RANK 1980. The phosphine abundance on Saturn derived from new 10-micrometer spectra. *Icarus* **42**, 79-85.

TOKUNAGA, A. T., H. L. DINERSTEIN, D. F. LESTER, AND D. M. RANK 1981. Erratum to: The phosphine abundance on Saturn derived from new 10-micrometer spectra. *Icarus* **48**, 540.

TOKUNAGA, A. T., R. F. KNACKE, S. T. RIDGWAY, AND L. WALLACE 1979. High-resolution spectra of Jupiter in the 744-980 inverse centimeter spectral range. *Astrophys. J.* **232**, 603-615.

TOMASKO, M. G. 1974. Ammonia absorption relevant to the albedo of Jupiter. II. Interpretation. *Astrophys. J.* **187**, 641-650.

TOMASKO, M. G., R. A. WEST, G. S. ORTON, AND V. G. TEJFEL 1984. Clouds and aerosols in Saturn's atmosphere. In *Saturn* (T. Gehrels and M. S. Matthews, Eds.), pp. 150-194. Univ. of Arizona Press, Tucson, Ariz.

TOWNES, C. H. AND A. L. SCHAWLOW 1975. *Microwave Spectroscopy.* Dover Publ., New York.

TRAFTON, L. M. 1965. *A Study of the Energy Balance in the Atmospheres of the Major Planets.* Ph.D. thesis. California Institute of Technology, Pasadena, Calif.

ULICH, B. L. 1974. Absolute brightness temperature measurements at 2.1-mm wavelength. *Icarus* **21**, 254-261.

ULICH, B. L. 1981. Millimeter-wavelength continuum calibration sources. *Astron. J.* **86**, 1619-1626.

ULICH, B. L., J. R. DICKEL, AND I. DE PATER 1984. Planetary observations at a wavelength of 1.32 mm. *Icarus* **60**, 590-598.

ULICH, B. L. AND R. W. HAAS 1976. Absolute calibration of millimeter-wavelength spectral lines. *Astrophys. J. Supp.* **30**, 247-258.

VANASSE, G. A. AND H. SAKAI 1967. In *Progress in Optics*, **VI** (E. Wolf, Ed.). North Holland Publ., Amsterdam.

VAN VLECK, J. H. AND V. F. WEISSKOPF 1945. On the shape of collision-broadened lines. *Rev. Mod. Phys.* **17**, 227-236.

WATERS, J. W. 1976. Absorption and emission by atmospheric gases. In *Methods of Experimental Physics*, **12B** (M. L. Meeks, Ed.). Academic Press, New York.

WEISSTEIN, E. W. AND E. SERABYN 1994. Detection of the 267 GHz $J = 1-0$ rotational transition of PH_3 in Saturn with a new Fourier transform spectrometer. *Icarus* **109**, 367-381.

Weisstein, E. W. and E. Serabyn 1996. Submillimeter line search in Jupiter and Saturn. In press in *Icarus*.

Weisstein, E. W., E. Serabyn, and M. A. Allen 1996. Submillimeter detection of PH_3 in Jupiter and Jupiter's radiative-convective boundary. Submitted to *Icarus*.

Welford, W. T. and R. Winston 1989. *High Collection Nonimaging Optics*. San Diego: Academic Press.

Werner, M., G. Neugebauer, J. Houck, and M. Hauser 1978. One-millimeter brightness temperatures of the planets. *Icarus* **35**, 289-296.

Westphal, J. A., W. A. Baum, A. P. Ingersoll, C. D. Barnett, E. M. De Jong, G. E. Danielson, and J. Caldwell 1992. Hubble Space Telescope observations of the 1990 equatorial disturbance on Saturn: Images, albedos, and limb darkening. *Icarus* **100**, 485-498.

Whitbourn, L. B., J. C. Macfarlane, P. A. Stimson, B. W. James, and I. S. Falconer 1988. An experimental study of a CW optically pumped far infrared formic acid vapour laser. *Infrared Phys.* **28**, 7-20.

Whitcomb, S. E. and J. Keene 1980. Low-pass interference filters for submillimeter astronomy. *Appl. Opt.* **19**, 197-198.

Willey, D. R., T. M. Goyette, W. L. Ebenstein, D. N. Bittner, and F. C. De Lucia 1989. Collisionally cooled spectroscopy: Pressure broadening below 5 K. *J. Chem. Phys.* **91**, 122-125.

Winkelstein, P., J. Caldwell, S. J. Kim, M. Combes, G. E. Hunt, and V. Moore 1983. A determination of the composition of the saturnian stratosphere using the IUE. *Icarus* **54**, 309-318.

Winston, R. 1970. Light collection within the framework of geometric optics. *J. Opt. Soc. Amer.* **60**, 245-247.

Woody, D., D. Vail, and W. Schaal 1994. Design, construction, and performance of the Leighton 10.4-m diameter radio telescope. *Proc. IEEE* **82**, 673-686.

Wright, E. L. 1976. Recalibration of the far-infrared brightness temperatures of the planets. *Astrophys. J.* **210**, 250-253.

Wrixon, G. and W. Welch 1970. The millimeter wave spectrum of Saturn. *Icarus* **13**, 163-172.

Wrixon, G., W. Welch, and D. Thornton 1971. The spectrum of Jupiter at millimeter wavelength. *Astrophys. J.* **169**, 171-183.

Zharkov, V. N. and V. P. Trubitsyn 1978. *Physics of Planetary Interiors*. Pachart Publishing House, Tucson, Ariz.